Integral Quadratic Constraints and Safety Certificates for Uncertainty Characterization and Control Safety-Aware Filtering of Proximity Operations Between Satellites

by

Axel Garcia Burgos

B.S. Aerospace Engineering, Embry-Riddle Aeronautical University (2015)
S.M. Space Systems Engineering, The Skolkovo Institute of Science and Technology, (2017)

Submitted to the Department of Aeronautics and Astronautics
in partial fulfillment of the requirements for the degree of

Doctor of Philosophy in Aeronautics and Astronautics

at the

MASSACHUSETTS INSTITUTE OF TECHNOLOGY

May 2023

©2023 Axel Garcia Burgos. All Rights Reserved. The author hereby grants to MIT a nonexclusive, worldwide, irrevocable, royalty-free license to exercise any and all rights under copyright, including to reproduce, preserve, distribute and publicly display copies of the thesis, or release the thesis under an open-access license.

Authored by: Axel Garcia Burgos
Departmnent of Aeronautics and Astronautics, May 01, 2023

Certified by: Richard Linares
Associate Professor of Aeronautics and Astronautics
Thesis Supervisor

Certified by: Olivier L. de Weck
Professor of Aeronautics and Astronautics
Thesis Committee Member

Certified by: Christopher Jewison
Technical staff, The Charles Stark Draper Laboratory, Inc.
Thesis Committee Member

Certified by: Paul Cefola
Research Scientist, The State University of New York at Buffalo
Thesis Committee Member

Certified by: Felix R. Hoots
Aerospace Fellow, The Aerospace Corporation, Inc.
Thesis Committee Member

Certified by: Zachary Folcik
Technical staff, MIT Lincoln Laboratory
Thesis Committee Member

Certified by: Juan Felix San Juan-Diaz
Professor, SCoTIC-Universidad de La Rioja
Thesis Committee Member

Accepted by: Jonathan P. How
R. C. Maclaurin Professor of Aeronautics and Astronautics
Chair, Graduate Program Committee

Integral Quadratic Constraints and Safety Certificates for Uncertainty Characterization and Control Safety-Aware Filtering of Proximity Operations Between Satellites

by

Axel Garcia Burgos

Submitted to the Department of Aeronautics and Astronautics
on May 01, 2023, in partial fulfillment of the
requirements for the degree of
Doctor of Philosophy in Aeronautics and Astronautics

Abstract

Abstract

Techniques in robust optimization and formal verification methods are used (1) to examine the stability and robust performance of a satellite controller that considers six-dimensional, uncertain state, and often unmodeled dynamics during rendezvous and proximity operations, and (2) to explore the synthesis of control Lyapunov/barrier functions (CLFs/CBFs) using neural networks and stochastic gradient descent to provide safety-aware filtering for the fuel-optimal control policies. A linear quadratic regulator controller for a servicer satellite (Servicer) is analyzed via the dissipativity inequality principle and quadratic constraints. This method allows the capture of unmodeled dynamics to reduce system uncertainty of proximity operations among the Servicer, client satellite (Client), and unsafe regions (e.g., obstacle). The same controller is implemented with a finite time horizon (i.e., model predictive controller) to filter out unsafe control output during an autonomous inspection of a Client. This framework mitigates the collision risk based on integral quadratic constraints (IQCs) worst bounds recommendation, miss distance, Mahalanobis distance, and Probability of Collision (Pc) metrics. Innovative deterministic reachability methods based on integral quadratic constraints and neural Lyapunov functions are compared and connected. The novel contributions of this work focus on formulating mathematical safety guarantees, modeling controller output, and reducing uncertainty on system performance when designing fuel-optimal and safe maneuvers of Servicer around the Client while avoiding unsafe regions in LEO.

Acknowledgments

Studying at MIT AeroAstro has been a dream come true. I would like to thank my family for instilling in me the value of pursuing higher education, especially my twin brother, mother, and father. I dedicate this thesis to my twin brother Marcel, who has always gone every step of the way with me. I would like to thank the CROEM boarding school (i.e., teachers and peers) that I grew up with in Puerto Rico, as their intellect, curiosity and motivation for learning inspired me to relocate to the mainland U.S. for better aerospace opportunities at an early age. I also have to highlight my math and physics teachers for pushing me into participating in international olympiads, as those events shaped my competitive spirit and willingness to never stay within my comfort zone. Apart from all the key players during my childhood, I need to thank the NASA education office for all the K-12 programs I was able to participate in growing up for minorities interested in STEM; the Embry-Riddle (ERAU) supervisor (Dr. Luis Gonzalez) that NASA matched with my research interest during my undergraduate years; the ERAU undergraduate capstone advisors, Prof. Bogdan Udrea and Prof. Heidi Nykyri, for allowing me to work on NASA-sponsored research aligned to my specific interest at the time; and all the NASA scientists that supervised my work at the various NASA centers during my employment there, especially at NASA Goddard, where my interest in Guidance Navigation and Control (GN&C) for satellite started and my contributions made it to international space conferences. Lastly, a special thanks to Dr. Georgia De Nolfo, Dr. Giuseppe Cataldo, Dr. Irving Linares, Dr. Antti Pulkkinen, and Dr. Tupper Hyde for being key roles in my professional development during my time at Goddard.

There were several people at MIT that I truly need to highlight due to their support in my growth as an engineer and entrepreneur. I would like to thank Prof. Edward Crawley for giving me the opportunity to join the Space Systems Architecture lab five years ago, while I was a graduate student at Skoltech in Moscow, Russia. He and the MIT-Skoltech program shaped my entrepreneurial mindset and allowed me to discover the beauty of interdisciplinary research with practical applications into commercialization. Without a doubt, I owed to Crawley my MIT experience. Special thanks to Prof. Kerri Cahoy and Jason McKnight for supporting me during the admission process at MIT AeroAstro. To my first colleagues and friends at MIT, Markus Guester, Miles Lifson, Inigo del Portillo, Mark Sanchez Net, and Anne Collin, thanks for being so welcoming and exchanging ideas, sharing struggles and research motivation during the inception of my MIT journey. Especially you, Markus, as you have become a great friend throughout the years. I would also like to thank the entrepreneurial community at MIT for teaching me so much about creating successful startups. From coursework to MIT business competitions, I would like to thank the faculty and colleagues with whom I spent intense nights working on business ideas and pitch slides. To my co-founder, Shang Giao, for trusting me and my patented agrobeads technology to enter the agricultural market in China, I learned so much from you and wish we can keep collaborating in the future. To my colleagues, Miles Lifson and Mina Takla, for exploring the business concept idea of Safe Orbit and writing technical grants with me to fund this idea. You guys are brilliant! I would like to thank my current advisor, Prof. Richard Linares, for accepting me into the Astrodynamics, Space Robotics and Control Lab (ARCLab) as a doctorate-seeking student at

MIT AeroAstro. During my first semester at MIT, I had the privilege of attending his lectures, participating in his research projects, and engaging in drawing-on-board sessions with him, all of which allowed me to admire his creative thinking and systems engineering mindset. I am privileged to have so many excellent members on my PhD committee. Paul Cefola, Zachary Folcik, and Juan Felix San Juan Diaz, thanks for your patience when I was learning various methods of propagation and for sharing with me your expertise in semi-analytical theory and overall experience in the field of astrodynamics; thanks to my Draper advisor, Christopher Jewison, for your support navigating the MIT AeroAstro Ph.D. program, pushing me to reach my research milestones and providing technical feedback in safety verification of RPO controllers; thanks to Prof. Olivier De Weck for all the coursework offered in space systems engineering and your thought-provoking questions during my PhD meeting updates; and finally, thanks to Felix Hoots for sharing his experience when "thinking through astrodynamical equations" and simplifying convoluted concepts, and sharing with me his expertise in operational astrodynamics. I am very lucky to have acquired so much experience and feedback in every meeting of my research activities at MIT. Other engineers outside my committee were also very influential in my research development. I want to thank Micah Fry for his crash course on Integral Quadratic Constraints (IQC) theory and Prof. Alexander Megretski for expanding my understanding in this field. I also need to thank Prof. Chuchu Fan, Charles Dawson, and Mr. Francisco Camargo for their willingness to clarify questions on Lyapunov theory, neural nets and object-oriented programming to solve my technical problems. I want to thank all students of ARClab that made this experience fun during my journey at MIT – especially to you, Thomas Roberts, Daniel Jang, Miles Lifson, and Adriana Macieira Mitchell. You guys are the most sociable brilliant space engineers I know. Never change that personality!

Finally, I would like to thank the Draper Scholar Program and GEM Fellowship for providing funds during my graduate studies at MIT – especially GEM for offering key internships with MIT Lincoln Labs and Aerospace Corporation, which helped me identify the research gaps presented in my thesis. I would like to thank the Matthew Isakowitz Fellowship Program (MIFP) that provided me with employment at Planet Labs, where I discovered my passion for commercial space. Thanks to CEO Steve Isakowiz and the whole MIFP team for introducing me to the new era of commercial space. Thanks to that experience and my strong academic record, I was hired as a Flight Dynamics Engineer for Amazon's visionary Kuiper project. I consider this opportunity to be a starting point in my career, as it would allow me to apply and demonstrate the skills I acquired during my PhD studies at MIT.

Abstract

Techniques in robust optimization and formal verification methods are used (1) to examine the stability and robust performance of a satellite controller that considers six-dimensional, uncertain state, and often unmodeled dynamics during rendezvous and proximity operations, and (2) to explore the synthesis of control Lyapunov/barrier functions (CLFs/CBFs) using neural networks and stochastic gradient descent to provide safety-aware filtering for the fuel-optimal control policies. A linear quadratic regulator controller for a servicer satellite (Servicer) is analyzed via the dissipativity inequality principle and quadratic constraints. This method allows the capture of unmodeled dynamics to reduce system uncertainty of proximity operations among the Servicer, client satellite (Client), and unsafe regions (e.g., obstacle). The same controller is implemented with a finite time horizon (i.e., model predictive controller) to filter out unsafe control output during an autonomous inspection of a Client. This framework mitigates the collision risk based on integral quadratic constraints (IQCs) worst bounds recommendation, miss distance, Mahalanobis distance, and Probability of Collision (Pc) metrics. Innovative deterministic reachability methods based on integral quadratic constraints and neural Lyapunov functions are compared and connected. The novel contributions of this work focus on formulating mathematical safety guarantees, modeling controller output, and reducing uncertainty on system performance when designing fuel-optimal and safe maneuvers of Servicer around the Client while avoiding unsafe regions in LEO.

Contents

List of Figures

List of Tables

Nomenclature

Acronyms

ADCS Attitude Determination and Control Subsystem

ADRAS-J Active Debris Removal Astroscale Japan

C2E2 Compare Execute Check Engine

CA Closest Approach

CAPD Decomposed Reachability Analysis for Nonlinear Systems

CARA Conjunction Assessment Risk Analysis

CBF Control Barrier Function

CDR Critical Design Review

CLBF Control Lyapunov Barrier Function

CLF Control Lyapunov Function

CONOP Concept of Operation

CORA Continuous Reachability Analyzer

CPU Central Processing Unit

DART Demonstration of Autonomous Rendezvous Technology

ECI Earth Centered Inertial Coordinate System

ELSA-d End-of-Life Services by Astroscale-demonstration

ELSA-m End-of-Life Services by Astroscale- multiple

ESA European Space Agency

GA Gim-Alfriend

GEO Geosynchronous Equatorial Orbit

GN&C Guidance, Navigation, and Control

GPS Global Positioning System

HCW Hill-Clohessy-Wiltshire

HJB Hamilton-Jacobi-Bellman

HTV H-II Transfer Vehicle (HTV)

IPOPT Interior Point Optimizer

IQC Integral Quadratic Constraints

IR Infrared

ISS International Space Station

JPL Jet Propulsion Laboratory

KNITRO Nonlinear Interior Point Trust Region Optimization

KOZ Keep-out-Zone

LEO Low Earth Orbit (LEO)

Lidar Light Detection and Ranging

Linear Fractional Transformation LFT

Linear Time Invariant LTI

Linux Lovable Intellect Not Using XP

LOS Line-of-Sight

LPE Lagrange Planetary Equations

LQR Linear Quadratic Regulator

LVLH Local-Vertical-Local Horizontal

MATLAB Matrix Laboratory

MC Monte Carlo

MPC Model Predictive Control

NASA National Aeronautics and Space Administration

NLP Nonlinear Program

NORAD North American Aerospace Defense Command

OBC On-board Computing System

OD Orbit Determination

OS Operating System

PC Probability of Collision

PRISMA Italian for Hyperspectral PRecursor of the Application Mission

Proportional Derivative PD

QCQP Quadratically Constrained Quadratic Programs

QP Quadratic Program

R2BP Restricted Two Body Problem

RAM Random Access Memory

ROE Relative Orbital Element

RPO Rendezvous and Proximity Operations

RSO Resident Space Objects

RTOS Real-time Operating System

SGP4 Simplified General Perturbation 4

SGP4 Simplified General Perturbations Satellite Orbit Model 4

Single Input Single Output SISO

SNOPT Sparse Nonlinear Optimizer

SRP Solar Radiation Pressure

STM State Transition Matrix

TAM Total Addressable Market

TanDEM-X TerraSAR-X add-on for Digital Elevation Measurement

TCA Time of Closest Approach

TIRA Toolbox for Interval Reachability Analysis

TLE Two-Line Element

TPU Tensor Processing Units

TRL Technology Readiness Level

U.S. United States

USD United States Dollar

VNODE-LP Validated Numerical ODE through Literate Programming

Variables

$\boldsymbol{x} = [\boldsymbol{\rho}, \dot{\boldsymbol{\rho}}]$ Hill frame relative state

E Expectation operator

α, β Penalization variables

$\bar{P}_{k+1}$ Covariance Propagation

$\delta\bar{\boldsymbol{o}}\boldsymbol{e}_{nns} = (\delta\bar{a}, \delta\bar{\Psi}, \delta\bar{p_1}, \delta\bar{p_2}, \delta\bar{q_1}, \delta\bar{q_2}, \delta\bar{\Omega})$ Set of mean nearly-nonsingular differential equinoctial orbital elements

Δ_{IQC} Integral quadratic constraint operator

$\dot{\omega}_{x,y,z}$ Angular velocities derivatives

κ Bound

Ω Right Ascension of the Ascending Node (RAAN)

ω Argument of Perigee

$\omega_{x,y,z}$ Angular velocities

π Loss function

Ψ mean argument of latitude

ρ Local mass density of atmosphere

σ Quadratic function

θ Learning process parameter

θ_{roll}, θ_{pitch}, θ_{yaw} Roll, pitch, and yaw angles

A State Dynamics

a Semi-major axis

a_c Acceleration

a_{drag} Acceleration of Atmospheric Drag on Satellite

B Control Input

C_d Drag coefficient

d Displacement

e Orbit eccentricity

f True Anomaly

h Angular momentum of the reaction wheels

$h(x)$ Lyapunov function

i Inclination

$I_{x,y,z}$ Inertia moments

Isp Specific Impulse

J Total Inertia Matrix

J_2 Term that comes from an infinite series mathematical equation that describes the perturbational effects of oblation on the gravity of Earth.

p_1, p_2 Orbit inclination vector components

$P_{\boldsymbol{\rho\rho}}$ Relative position Covariance

$q(t)$ Vector component of the quaternions

q_1, q_2 Eccentricity vector components

R_u, R_x Weight matrices of controller

t Time

T_{drag} Torque produced from aerodynamic effects

T_{ext} Total external disturbance torque

T_{GG}	Torque produced from gravity gradient effects
T_r	Torque produced by radiation effects
$T_{x,y,z}$	Environment disturbance torque
u_{ref}	Control output of reference
v_0	Initial velocity
v_{rel}	Relative velocity of satellite and surrounding atmosphere
x_f	Final Position
x_{ref}	State reference
Q_i	Process noise covariance

Chapter 1

Introduction

1.1 Technical Innovations in Rendezvous & Proximity Operation (RPO) Missions

Rendezvous and proximity operations (RPOs) have been an essential aspect of space exploration and satellite activities since the 1960s, when the space race between the United States and the Soviet Union spurred the development of numerous technologies and missions [61]. As space exploration has evolved, RPO technologies have become increasingly important for maintaining and servicing satellites, as well as for addressing the growing issue of space debris. Despite the crucial role RPOs play in modern space activities, understanding of the technologies and methodologies underpinning these operations may not be widely understood. This introduction aims to provide a comprehensive overview of the key developments and challenges within the field of RPOs and to establish the context for the research presented in this thesis.

The International Space Station (ISS), which began construction in 1998, serves as a prime example of how RPOs have become essential for sustaining human presence and research activities in space [114, 59, 130]. Various satellite missions, such as the Northrop Grumman Cygnus, Space-X Dragon, and Japanese HTV, have been developed to perform rendezvous and docking operations with the ISS. These operations facilitate the delivery of supplies, equipment, and crew members to the ISS, and their safe return to Earth.

In recent years, there have been significant advances in autonomous docking technologies, such as the DART mission, which demonstrated the ability to dock autonomously with a satellite in 2005 [113]. Furthermore, developments in passively-safe and fuel-efficient transfers have enabled satellite formation flying operations, including the PRISMA and TanDEM-X demonstration missions in 2009 and 2010, respectively [22]. These advances have laid the groundwork for innovative services and missions, such as the Mission Extension Vehicle-1 & 2 (MEV-1 & 2) by Northrop Grumman, which aim to service aging satellites in geostationary Earth orbit (GEO) and extend their functional lifetimes.

The rapid growth of the private space industry has created new opportunities for companies to commer-

cialize RPO technologies and services. For example, Astroscale Inc., a global leader in RPO, launched the successful Elsa-d mission in 2021, demonstrating active debris docking and removal in low Earth orbit (LEO) [17]. Other upcoming Astroscale missions include the 2023 ADRAS-J, the 2024 Elsa-M, and the 2026 LEXI-P missions, each focusing on different aspects of RPOs, such as proximity operations, multi-client satellite retirement, and in-orbit servicing capabilities in GEO, respectively [69, 63, 17]. Smaller U.S. RPO-driven companies, such as Starfish, Kayhan Inc., Rogue Space, and VisSidus Technologies Inc., have also emerged and actively participate in the development of RPO technologies, presenting at academic conferences and competing for grants [134, 72, 101, 10]. This new commercial space race aims to capture a portion of the total addressable market (TAM) for in-orbit services, valued at 14.3 billion USD in 2022 [112].

The growing importance of RPOs in maintaining satellite operations and addressing space debris highlights the need for ongoing research and development in this field. This thesis focuses on addressing the challenges and opportunities presented by RPO technologies and aims to contribute to the development of novel methodologies and techniques to improve the safety, efficiency, and commercial viability of these essential space activities.

1.2 Research Motivation

As a result of the increasing demand for space-based services, the active satellite population is expanding at an exponential rate and is expected to grow by two orders of magnitude by 2030 [26]. This growth in space operations will require both increased spacecraft control autonomy and techniques to provide robust safety guarantees for satellite inspection, repair, debris retrieval/removal, and on-orbit assembly activities at various altitudes.

Because of atmospheric drag, the Earth's non-uniform nature of gravity effects, and overall model uncertainties performing these services become more challenging in LEO altitudes. Missions such as Elsa-d by Astroscale have successfully demonstrated satellite capture and deorbit technology in this regime. Moreover, future missions such as ClearSpace-1 and DeOrbit by ESA are also planned for active debris removal in LEO. The increasing demand for space-based services is leading to an exponential expansion of the active satellite population. However, ensuring the robustness and safety of on-orbit services, including satellite inspection, repair, debris retrieval/removal, and on-orbit assembly activities, has always been a crucial aspect of GN&C platforms. Previous missions, particularly those involving human crews, such as the International Space Station (ISS), required highly tailored analysis and algorithms to ensure the robustness and safety of the systems. Although these algorithms were never formally proven in an analytical framework to be robust and safe, they relied on Monte Carlo simulations and other forms of analysis. With the increasing volume of on-orbit services at various altitudes, there is a need to develop more formal techniques that guarantee safety in operations for a servicer spacecraft (Servicer), a client spacecraft (Client), and obstacle regions. Thus, maneuvering techniques such as Natural Motion Circumnavigation (NMC) must be designed with full

satisfaction of state and actuation constraints.

1.3 Problem Formulation

Currently, conjunctions involving two active satellites account for a relatively small portion of collision risk among trackable Low-Earth Orbit (LEO) resident space objects (RSOs). However, this risk is expected to increase significantly, particularly in the 450 km - 600 km altitude band [89]. Due to the congested environment at these altitudes, high-value assets, such as exquisite science satellites or GEO communication satellites, face unique challenges in maintaining safe and efficient operations. Although SpaceX and Amazon have adopted disposable satellite concepts for their LEO constellations, high value satellites still require a focus on robust techniques to ensure their longevity and performance in the dense LEO environment.

Although the proposed verification framework can be applied to any altitude, this thesis aims specifically to improve the robustness of GN&C systems for client inspection in LEO. The chosen altitude band is of particular interest due to the non-uniform nature of gravity effects, such as J_2 perturbations, which significantly impact the controller output during these operations. Atmospheric drag also contributes to disturbances that affect satellite controllers in LEO. A method of controller verification must provide robust guarantees of the keep-out zone (KOZ) and sun angle requirements among Servicer, Client, and an obstacle region, while taking into account the uncertainties, nonlinearities, and disturbances affecting the Servicer and Client states, as well as the Servicer thrust output. Figure 1-1 illustrates the Concept of Operations (CONOPs) of an RPO mission in LEO, focusing on improving the safety and operational efficiency of servicing high-value satellites in this densely populated and dynamically complex region.

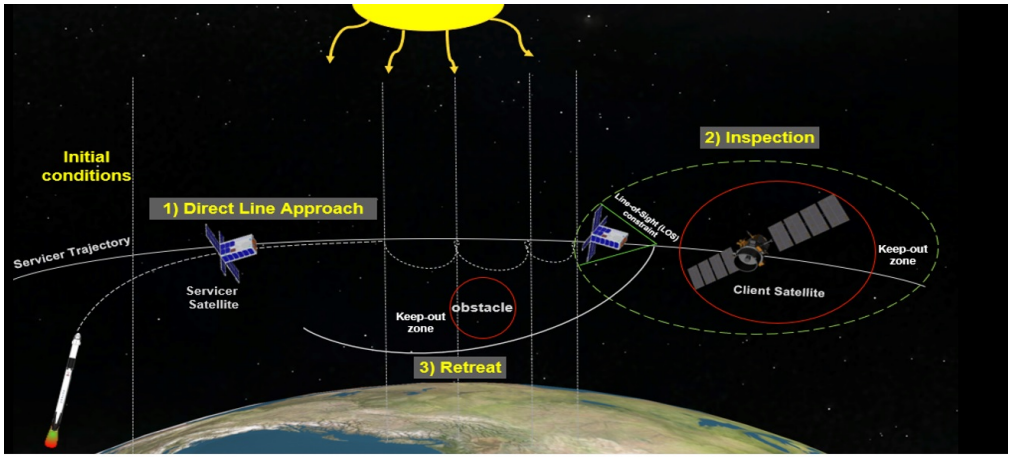

Figure 1-1: CONOPs: phases of an RPO mission (e.g., direct approach, inspection with a Line-of-Sight (LOS) cone constraint, and retreat maneuvers).

The list below describes the two problems motivating this research into safety assurance of control performance for low relative velocity encounters between satellites:

- Problem #1: Orbital Operations. Fly-bys with objects of low relative velocity occur more frequently due to congested altitudes near Earth [94]. As a result, more robust control verification methods will be required to ensure a safe separation among Servicer, Client, and Obstacle while accounting for uncertainties, nonlinearities, and disturbances in state and actuation.
- Problem #2: Rendezvous and Proximity Operations: Servicer inspecting a Client would require full satisfaction of mission requirements in the control strategy. These requirements consist of 1) inspection of a Client considering sun-angle constraints while respecting a KOZ away from Client/Obstacle, and 2) performing fuel-efficient maneuvers during each phase of the RPO mission. As a result, capturing the effects of nonlinear dynamics, exogenous disturbances, and path constraints is crucial for mission success.

To ensure safe servicing operations in the densely populated and dynamically complex region of space, it is crucial to have robust controllers that can capture nonlinear and time-varying dynamics and mission constraints. These controllers must be able to account for system uncertainties, nonlinearities, and disturbances, regardless of the design of the GN&C platforms used for various RPO missions. Standardizing these platforms through regulations would also facilitate performance analysis. However, achieving this task with fuel-efficient thrust engines presents a challenge, as the optimization variables require a complete control history of continuous and long-duration maneuvers that can last for hours or days. Therefore, managing satellite operations and collision avoidance at the scale projected for congested altitudes in low Earth orbit (LEO) will require robust, highly automated, and fuel-efficient maneuver planning. Such planning must avoid unsafe states, including those that arise from interactions between systems controlled by independent operators.

1.4 Summary of Thesis Contributions

The goal of this section is to describe the Ph.D. contributions towards closing the technical gap in the GN&C verification method for RPO missions. In this thesis, three research areas are connected: optimization techniques for fuel-optimal maneuvers, reachability techniques to characterize uncertainties, nonlinearities, and disturbances, and risk optimization techniques to minimize the risk of collision between satellites. This section also includes a roadmap of the chapters found in this thesis.

1.4.1 Contributions

- Contribution #1: Deterministic reachability technique to analyze robustness of GN&C systems. This contribution consists of a framework capable of generating uncertainty bounds for state-related out-

put (i.e., Servicer relative position/pointing attitude with Client) by performing reachability analysis deterministically for closed-loop controllers. The innovative reachability technique captures state and actuation uncertainties and nonlinearities, and attitude disturbances affecting the control output of the Servicer with respect to the Client.

- Contribution #2: Methodology that combines deterministic reachability (contribution #1) and neural Lyapunov functions to increase safety in the design of autonomous GN&C systems. This contribution consists of developing fuel-optimal control methods with safety-aware filtering techniques (i.e., via control barrier/Lyapunov functions) that can handle nonlinear and time-varying dynamics and constraints, such as a Line-of-sight (LOS) cone constraint when the Servicer is at closest approach to Client for inspection, and a collision avoidance constraint (KOZ) in case the Servicer's planned trajectory intersect with obstacle region.

1.4.2 Thesis Roadmap

The research motivation and problem formulation are described in the first chapter. This thesis begins its literature review, second chapter, by presenting a brief history of verification methods. The issues with these methods for RPO control design are explained and linked to the Ph.D. contributions. The review then introduces the two areas explored in this thesis. In the third chapter, the innovative methodology of the GN&C verification platform is described. This includes the fundamental theory of formal methods and robust optimization techniques used in this research. In the fourth chapter, the results of these techniques applied to the RPO mission are shown. The fifth chapter states the conclusions regarding risks and the significance of this research for the astrodynamics community, the overall summary, and future work. The appendix describes the derivation of some of the dynamics, code, and IQC classes used in this thesis. References appear at the end. The thesis roadmap can be seen in Figure 1-2.

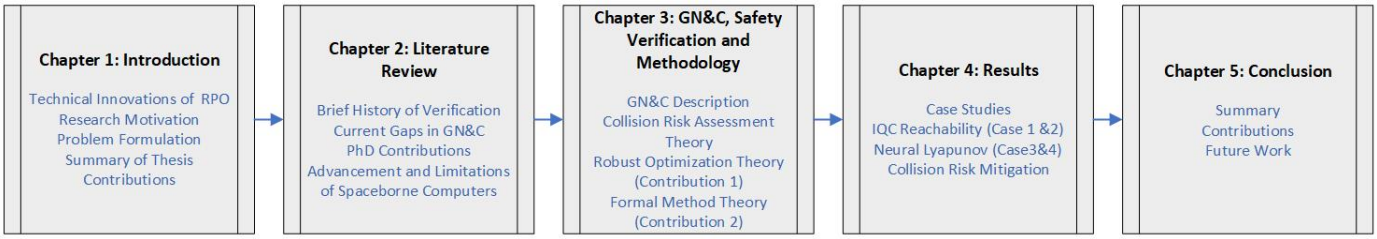

Figure 1-2: Thesis Roadmap.

Overall, three main areas of research were explored to improve controller performance during RPO missions. The first research area explores the Integral Quadratic Constraints (IQCs) theory as an innovative technique to reduce system uncertainties while validating the safety of controllers with a feedback control law. The second research area explores learning-based functions in formal methods to create barrier certificates for more robust control policies. The third describes how these two methods can reduce collision risk

metrics between the servicer, client, and obstacle region. The goal of this approach would be to enforce not only fuel optimality but also safety guarantees of satellite operations in real-time (e.g., collision avoidance applications). Although the focus of this thesis is on LEO altitudes, these contributions can be applied to higher altitudes such as GEO or even, if adjusted correctly, to cis-lunar space as well.

Chapter 2

Literature Review

This review of the literature provides a comprehensive overview of the current state-of-the-art in control verification for RPO design, including formal and optimization methods for safety guarantees, fuel-efficient trajectories, controller types, and current limitations of spaceborne computers. Through an examination of the technical issues found in the literature and the current work conducted by researchers, this review highlights the limitations of the current state-of-the-art and identifies the need for more sophisticated and robust verification methods. The PhD contributions presented in this thesis address these limitations by proposing new techniques for control verification that improve the safety and efficiency of RPO missions, particularly those operating in densely populated and dynamically complex regions of space.

2.0.1 Brief History of Verification Methods

French mathematician Comte de Buffon pioneered the field of statistical sampling to obtain approximate solutions to problems in 1777. He originated the famous 'Buffon's needdle' experiment consisting of estimating the probability that a needle would lie across a line between two wooden strips on his floor, and then proved the relationship of this experiment with the estimation of π in the 18th century [140]. His contributions motivated research in probability and estimation. However, complex applications using this technique were not feasible until the Electronic Numerical Integrator and Computer (ENIAC), one of the earliest digital computer used in the 20th century [84]. Although other physicists contributed to the development of numerical simulations (e.g., Manhattan Project for the development of atomic bombs), John Von Neumann was the first to successfully perform stochastic simulations, which became essential in the new era of digital computing technology for simulating large complex physical systems [84]. With the advancement of digital computers in the 20th century, advanced methodologies for Monte Carlo algorithms were framed for robust analysis of safety-critical systems [140, 15]. In addition, in 1977, the American computer scientist Leslie Lamport, from the Digital Equipment Corporation, designed the first algorithmic correction of a multiprocess program [73]. Since then, formal methods for safety assessment were further developed and the first reachability analysis

technique was published in 1978 for the analysis and verification of communication protocols [53]. In the same decade, robust control techniques were also developed for analyzing the stability of linear systems with control feedback and able to account for model uncertainty. The Russian mathematician Yakubovich pioneered the theory of analyzing complex combinations of signals affecting a given dynamical system, which allowed the study of control performance for safety-critical schemes [87, 65]. Consequently, MIT professor A. Megretski pioneered the merging of three research fields – input-output theory, absolute stability theory, and the robust control field – into a unified framework called Integral Quadratic Constraints (IQCs) with the theoretical contributions from Yakubovich in 1997 [111].

2.0.2 Current Gap in GN&C Verification Methods of Onboard Algorithms for RPO Mission

Many satellite operators rely on Global Positioning System (GPS) receivers for on-board relative navigation algorithms. While new developments in low-power GPS receivers can provide highly accurate real-time positioning measurements for low-Earth orbit (LEO) satellites [71], the availability of real-time GPS data is not always guaranteed due to factors such as signal blockage and interference. In situations where real-time GPS data is not available, satellite operators may use a conventional backup strategy that involves using NORAD Two Line Elements (TLEs), which are uplinked from ground stations and propagated with an orbit propagator such as the Simplified General Perturbations Satellite Orbit Model 4 (SGP4) [97]. However, this approach can result in errors of up to 10 km for TLEs that are two days old [86]. Although a semi-analytic propagator from the last known accurate state can be used to improve the accuracy of TLE-based navigation, it is important to note that this approach also has limitations due to uncertainties in the orbit dynamics model and atmospheric drag. Nonetheless, the use of TLEs for onboard state estimation remains a viable option for satellite operators as a backup to GPS-based navigation in situations where other measurement techniques, such as laser ranging and RF ranging, are not available or feasible. Table 2.1 below provides relevant information on the most common GPS receivers used in small spacecraft.

Table 2.1: GPS Receivers for Small Spacecraft [20]

Model	Accuracy(m)	Manufacturer
COM-1289	1.2	Eurotech
Explorer	15	General Dynamics
OEM719	1.5	Novatek
GPS-kit	1.5	GomSpace
SGR-Ligo	5	Surrey Satellite Technology
piNAV-NG	10	SkyFox Labs

The availability of real-time GPS data for RPO missions in low Earth orbit (LEO) varies depending on the specific class of traffic. Although most large and medium-sized spacecraft likely have GPS onboard, small satellites and CubeSats may not have GPS receivers due to size, cost, or power constraints. However, precision ephemeris for both objects are critical for RPO missions, regardless of their size, and whether they are cooperative or non-cooperative. In addition, avoiding debris is a crucial part of satellite operations and

should be considered a general mission requirement. While satellite radar altimeters can provide real-time positioning accuracy of a few centimeters [147], these devices can be expensive or too large for Servicers in LEO. Optical vision sensor systems, such as lidar and IR-cam, can be used as auxiliary information sources to improve navigation performance in GPS-denied environments. These systems can provide relative range and bearing measurements between two objects, which can be used to estimate the relative position and velocity of the Servicer with respect to the Client. However, it is important to note that distinguishing between trackable and non-trackable debris can be challenging and may require more sophisticated sensing and detection technologies. Consequently, improving the accuracy in the tracking of debris is another issue in RPO control, but it is not included as a research objective in this thesis. As a result, solving this problem becomes crucial for spaceflight sustainability due to the rapid growth of satellites at orbital altitudes in LEO.

Verification methods to improve current practice have been researched and explored as a result. Numerical simulations have been proposed for the study of safety-critical systems of space missions since the late 20th century. The most popular method has been the use of stochastic sampling (i.e., Monte Carlo) algorithms for providing mission-critical software assurance for spacecraft (e.g., Parker Solar Probe, Europa Clipper, Mars 2020, James Webb Space Telescope) [11, 34]. Since then, numerical simulations have been used to plan maneuvers of satellites in relative navigation with other satellites, applying robust techniques in linear programming via the Monte Carlo approach [94, 116, 132]. This method has been further applied to the probability of collision forecast between two satellites, given a set of initial states and associated covariances [85]. Although this technique has been useful for planning RPO controllers, repetitive algorithms are computationally inefficient and do not scale well with increasing parameters in the optimization variables. Due to time-varying constraints and unmodeled disturbances from real-time operations, this technique does not offer safety guarantees in the verification methods of RPO controllers.

Since 2008, reachability analysis has been used to provide safety guarantees in control design in the field of space situational awareness. Numerous tools exist to calculate the reachable set of hybrid nonlinear systems, including CORA [8], Flow* [24], C2E2 [35], VNODE-LP [96], CAPD [51], DynIbx [122], and TIRA [90]. These tools are designed to compute the over-approximation of the interval of reachable sets, but they are limited in scale to state spaces of up to four dimensions due to the exponential growth of finding the solution of the Hamilton-Jacobi-Bellman (HJB) equation, which is needed in deterministic reachability problems [81]. Furthermore, these tools break when analyzing ill-conditioned systems (i.e., a small variation in the input argument changes the output value significantly), which is often the case with satellite equations of motion [141]. Regardless of the limitations in scale, several authors have contributed to and published reachability analysis using these tools for control verification of satellites. For example, Marcus Holzinger from the University of Colorado at Boulder analyzed the reachable set and control laws for a single satellite with the goal of performing low-thrust transfers from LEO to GEO altitudes [58]. Dr. Dan Xue from Tsinghua University derived the reachable domain for a single impulsive satellite transfer maneuver as well [145]. Dr. Christopher Jewison from the Draper Laboratory also used deterministic reachability using simplified

assumptions of relative motion for a docking application [60]. In recent years, stochastic reachable sets have been used to tackle higher-dimensional problems targeting rendezvous and docking satellite applications [109]. Given the uncertainty in the dynamics, any insight from this reachable set becomes probabilistic, and as a result, hard guarantees of safety for reaching a desired state cannot be given. Consequently, a robust framework for analyzing RPO controllers that have high dimensionality and are ill-conditioned, via the deterministic reachability technique, is not yet available for safety-critical systems in satellite operations. Combining safety guarantees with reachability techniques for mission analysis in proximity operations is a technical gap in RPO GN&C design.

2.0.3 Innovations in Control Design for RPO Missions

Model Predictive Control (MPC) provides a way to calculate optimal trajectories by minimizing a cost function in real-time [120]. MPC has enabled the planning of online optimization strategies for operations of collision avoidance for low-thrust fuel-efficient transfers for satellite formation flying such as the TanDEM-X and PRISMA demonstration missions [22]. MPC has also offered insight on fuel-efficient satellite maneuvers considering unmodeled disturbances with adaptive algorithms applied to MPC schemes [43]. Innovative approaches to increase the robustness of MPC to enable its use in real-time include the tube-based approach, a framework published for RPO control strategies in 2018 [83]. This technique permits accounting for a particular realization of the uncertainty due to the nonlinearities at each time step. This approach conserves the computational effort reduction of linear MPC while allowing for a time-varying control law, where the feedback gain matrix is evaluated offline. As a result, system constraints are tightened to allow the trajectories of the uncertain system, affected by disturbance, to lie in a tube centered on the nominal trajectory. A recent paper (2020) from Prof. Frank Allgöwer and his Ph.D. candidate Lukas Schwenkel showed that tube-based MPC controllers cannot provide robust constraint satisfaction or stability of unmodeled dynamics, delays, or any other dynamic uncertainty beyond linear constrained systems [128]. The limitations of the various MPC schemes used in RPO design are summarized as follows:

- A major drawback of an MPC architecture is the black-box nature of optimization-based controllers, which makes safety analysis difficult. This issue applies to linear and nonlinear MPCs.
- There are no capabilities for guaranteeing the safety, stability, or recursive feasibility of robust MPCs beyond the linear case [13]. This issue applies to tube-based and nonlinear MPCs.
- Model uncertainty (e.g., atmospheric drag, J_2) is often multiplicative in the dynamics, but robust MPCs are typically limited to additive uncertainty [13, 79]. This issue applies to tube-based and nonlinear MPCs.
- Optimization engines used to solve constraints and cost functions are not qualified for safety-critical systems. This issue applies for linear, tube-based, and nonlinear MPCs [25].

- MPCs are computationally expensive, making it difficult to achieve high control frequencies in practice [78]. This issue applies to nonlinear MPCs.

To overcome these issues and guarantee the safety of using computationally efficient MPCs (i.e., linear, tube-based MPCs) in RPO design, formal methods, and robust optimization theory can be applied to guarantee long-term safety in the face of both unplanned maneuvers by other spacecraft and time-varying, nonlinear perturbations and constraints. Min-Max MPC schemes are not included in this thesis due to the extremely conservative control policies and a small domain of feasibility [110].

2.0.4 PhD Contributions in GN&C Verification for RPO Missions

In formal methods, Lyapunov functions can be applied, which originated in 1940 when a Japanese mathematician, Nagumo, provided a theorem proving necessary and sufficient conditions for set invariance [95]. This technique is based on encoding information about long-term safety into local information about a scalar function [9]. As a result, Lyapunov functions have been developed to guarantee the forward invariance of a subset of the dynamical system's state space [117]. Unfortunately, barrier functions are notoriously difficult to synthesize analytically for systems with complex dynamics or subject to uncertain disturbances. As a result of that, recent trends in safety analysis have included the use of neural networks for learning Lyapunov and barrier certificate functions [2, 27]. In recent years, neural certificates have been used for nonlinear control verification in applications ranging from robot locomotion [21] and flight through propeller wash [133] to decentralized multi-agent control [108]. As a result, another contribution in this thesis targets the use of control barrier/Lyapunov (CLBF/CBF) functions for safety-aware filtering of RPO control policies to achieve safety guarantees. The novelty in this approach is capturing the nonlinear and time-varying dynamics of low relative velocity encounters in proximity operations while ensuring safety guarantees in the satellite RPO MPC design. A paper that motivates this research area can be found in [31], which applies learning-based (CLBF/CBF) functions for a linear and time-invariant approximation of satellite relative motion to perform a docking procedure with state and angle constraints. However, this paper does not capture the complex physical environment (i.e., time-varying, nonlinear, and unmodeled uncertainties) and mission requirements (i.e., fuel-optimal maneuvers, and path/angle constraints) for providing robust safety guarantees. Recent neural Lyapunov tools have become open source, but are limited in the synthesis of nonlinear dynamics with robust guarantees [115, 21]. A CBF/CLBF toolbox capable of handling nonlinear dynamics and mission constraints has become available in [31], and the author of this thesis has developed this tool for GN&C verification of satellite RPO MPC design.

In addition to formal methods, optimization techniques play an important role in characterizing uncertainties and improving system performance [87, 65]. IQCs are inequalities used to describe the possible combinations of signals within a given dynamical system [111] and are explored in this thesis because they allow representations of relationships between processes, evolving in a complex dynamical system, in a closed form expression that is useful for safety analysis. Furthermore, innovative techniques are being published to

facilitate a systematic, scalable, and efficient analysis of robustness and performance [138, 102, 99]. IQCs have been applied to multivariable systems such as microgrid voltage control systems [123], distributed control systems [36], and even manufacturing, due to the high dimensionality of the multivariable process [93]. Aerospace applications have also been impacted by IQCs. Recent research explores the IQC approach to validate a Doppler estimator for a novel inertial navigation system where reliable and robust navigation is needed [41]. Other papers apply the IQC framework to achieve high pointing performance for spacecraft stability [106] and to achieve high performance attitude for a geostationary control platform [33]. Furthermore, IQC theory has been applied to characterization of complete uncertainty quantification, and to analysis for aircraft flight controllers with a focus on simplified longitudinal aircraft models [100] and time-varying multipliers [39]. However, reducing model uncertainties of RPO autonomous control schemes via IQCs has not yet been fully explored. Two of the most recent papers that inform this thesis for safety certification of RPO MPC controllers show important benefits of applying IQCs [129] and merging both IQC and Lyapunov functions techniques [131] to analyze robustness in control design. The goal of these contributions is to be able to account for model uncertainty due to time-varying, nonlinear dynamics, path, and angle constraints, and increase robustness from black-box autonomous RPO control systems (i.e., MPC schemes). In collaboration with the MIT Lincoln Laboratory, a framework has been created to analyze robust performance of synthesized controllers via the IQC approach. The open-source IQC toolbox from the Lincoln Laboratory [40] is capable of both modeling and analyzing uncertain/nonlinear systems, which can be modeled as an interconnection of a linear time-varying system (i.e., describing the nominal system), and a structured set of bounded operators Δ (i.e., describing the system's uncertainties and nonlinearities). Innovative aspects of this toolbox are modeling of time-varying systems, and this platform has been upgraded by the author to perform reachability analysis for safety GN&C verification of RPO missions. Other tools exist but they are not as developed (i.e., are incapable of handling time-varying systems or reachability analysis) [98, 88, 115]. Table 2.2 shows a comparison of the safety verification methods discussed so far, and the benefits of using IQC for existing reachability techniques.

Table 2.2: Comparison of verification methods of spaceflight GN&C platforms for RPO mission

Techniques	Capable of handling actuation uncertainty and nonlinear dynamics	Fast & Low-cost Operation	Robustness	Scalable
Monte Carlo Simulations	✓	✗	✗	✗
Deterministic reachability tools (HJ)	✗	✗	✓	✗
Stochastic reachability tools	✓	✗	✗	✗
Onboard planning algorithms (i.e., MPC)	✗	✓	✓	✗
IQC	✓	✓	✓	✓

The innovative techniques described in Table 2.2 refer to the deterministic reachability method applied to satellite GN&C platforms via IQCs. This first contribution is described in great detail in later chapters. Figure 2-1 below shows the same techniques being compared in terms of control robustness vs. computational time, as described in the literature. The goal of IQCs is to increase the robustness of the system while reducing the computational time during reachability analysis. This contribution would enable faster safety checks on the state output produced by the GN&C platform.

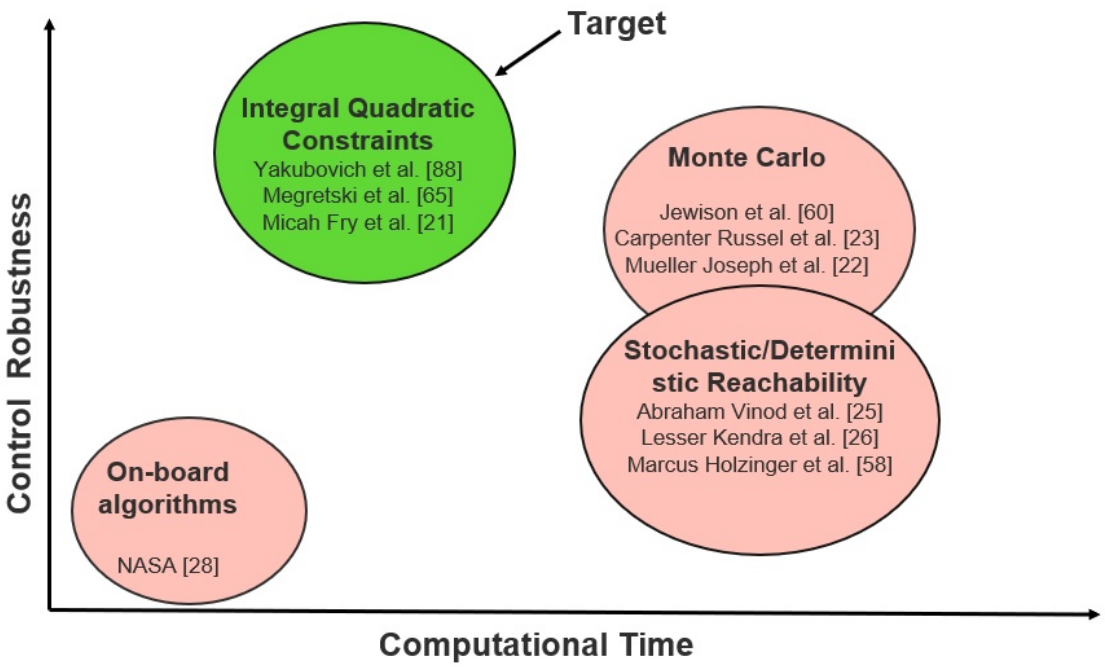

Figure 2-1: Comparison of reachability techniques: control robustness vs. computational time

This second contribution focuses on the development of fuel-optimal and robust GN&C platforms for RPO missions. There are two popular methods for developing control techniques for fuel-optimal maneuvers: indirect vs direct methods. Hamiltonian-based approaches (i.e. indirect methods) are the most accurate methods to achieve fuel-optimal trajectories [37]. However, the implementation of path and angle constraints with Hamiltonian techniques has not yet been fully explored operationally. Some of these constraints involve the Servicer docking with the Client within a certain angle (i.e., line-of-sight (LOS) requirements) or performing RPO maneuvers considering a keep-out zone. As these Hamiltonian approaches require extensive mathematical formulations to derive path and angle constraints– which are difficult in practice to formulate– direct methods (i.e., non-Hamiltonian techniques) are often used to enforce angle and path constraints [16] in optimization methods. In a direct collocation method, the state and control are parameterized at an appropriately chosen set of discrete points along the time interval of interest [4]. The continuous optimal control problem is then transcribed to a finite-dimensional nonlinear program (NLP). The resulting NLP can then be solved using well-known software such as SNOPT, IPOPT, and KNITRO [103]. Direct collocation methods were originally developed as h methods (such as Euler or Runge-Kutta methods), where the time interval of interest is divided into a mesh and the state is approximated using a fixed degree polynomial in each mesh interval. These direct methods have the limitation of reducing the accuracy of the optimal solution generated by these algorithms (i.e., bounding state and constraint by some threshold [139]). Our goal is to develop these controllers with safety guarantees that can handle nonlinear dynamics, path, and angle constraints for performing various rendezvous and proximity operation (RPO) maneuvers.

Table 2.3: Benefits of using CBFs/CLFs to existing optimization techniques described in the literature for RPO missions.

Techniques	Capable of incorporating nonlinear dynamics & uncertainties	Fast & Low-cost Operation	Safety Guarantees (i.e., path constraints)	Scalable (Centralized Controllers)
Onboard algorithms	❌	✅	❌	❌
Hamiltonian Approach (e.g., primer vector, sliding mode control)	❌	✅	❌	❌
Non-Hamiltonian Approach (e.g., GPOPS, MPC, adaptive control)	❌	❌	✅	❌
Control Barrier/ Lyapunov Functions + Controller	✅	✅	✅	✅

In Figure 2-2, it is shown that control barrier/Lyapunov functions will not always generate the most fuel-optimal solutions, but the most robust in terms of safety. The trade-off between safety and fuel consumption will be described in more detail in the results chapter.

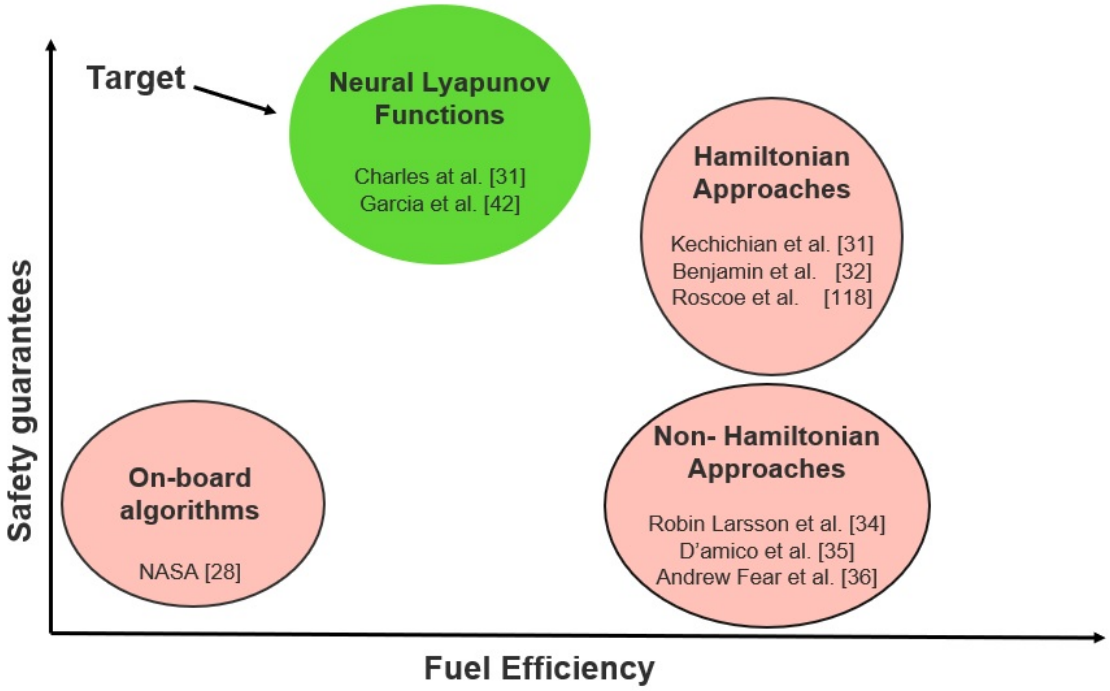

Figure 2-2: Comparison of control techniques: fuel efficiency vs. safety guarantees.

The theory behind control barrier/Lyapunov functions will enforce safety while the controller is providing a fuel-optimal trajectory. Both the safety filter and the nominal controller output are subject to a quadratic program (QP) solver to provide fuel-optimal trajectory maneuvers that satisfy safety requirements. In the next chapters, we will show how this method captures the uncertainty of the dynamical model to ensure long-term safety. The key advantage of this method is that the safety filter can be applied to both direct and indirect optimization techniques.

2.0.5 Advancement and Limitations of On-board Computing Systems (OBC) for Spacecraft

Satellite on-board computers are responsible for handling ground-based telecommands, providing ground telemetry, processing on-board data, and controlling the spacecraft platform and payload devices [77]. The spacecraft OBC usually has at least a processor, random access memory (RAM), read-only memory for boot code, mass memory, data bus interfaces, and a power supply. Perhaps, unlike many other embedded computers, some parts of the onboard computer may be redundant to circumvent possible hardware malfunction.

On-board software can be divided into three parts: hardware driver software that provides abstractions of the underlying hardware, an operating system (OS) that provides task and resource management, and application software that provides mission-specific functionality [76]. Typical OS selections have included real-time operating systems (RTOS) such as RTEMS and VxWorks, though some simpler onboard software

may not need an operating system at all.

Linux kernels have been available for spacecraft OBCs since 2002, providing operating system facilities such as virtual memory, processes, communication sockets, and files. The kernel is responsible for driving the devices, managing input-output access, scheduling processes, enforcing memory sharing, and handling signals [77]. One of the main benefits of this operating system is freedom in selecting the hardware platform. This is because Linux OS has many communication protocols and standards, making interfacing with external devices easier than with other operating systems. Table 2.4 shows a list of various Linux onboard computers with their specifications.

Table 2.4: Specifications of Linux OBCs [76]

Component	Volatile Memory (RAM)	Non-Volatile Memory	Power
LEON-3FT SPARC V8	625 MB	625 MB	20 W
Qualcomm SDA845 SoC	3.5 GB	128 GB	4.5 W
Dual core Freescale 2020 Power PC	512-1000 MB	256 GB	40 W
FreeScale e500 PowerPC	1.317 GB	4 GB	25 W

An important limitation of onboard computers regarding GN&C elements, even in Linux OS, results from the lack of RAM/Memory and CPU power to run real-time computations of nonlinear programs (e.g., IPOPT). There are other components that OBCs should interface with and provide power to, and RPO GN&C algorithms are a small portion of the operations handled by this onboard computer. Another limitation is that not all solvers that are embedded in direct optimization methods to solve for fuel-optimal trajectories as part of the GN&C algorithms, and their libraries, are compatible with Linux platforms. Indirect methods have been validated for real-time operations in a NASA CubeSat platform [119] but these algorithms do not handle path and angle constraints as with direct methods. Another point to consider is that RAM/memory and CPU power are largely dependent on the size of the spacecraft [48]. Consequently, even if there are sufficient capabilities to run sufficiently powerful OBCs with these algorithms onboard, not all spacecraft will have enough power to interface with these onboard computers. As a result, the advancement in Linux OS onboard spacecraft would enable the contributions of this thesis (i.e., integral quadratic constraints and control barrier/Lyapunov functions applied to GN&C) to run smoothly, with the appropriate hardware, in real-time applications onboard spacecraft. For now, the intended use of these contributions is for GN&C verification offline, which provides safety checks prior to embedding these algorithms in spaceborne computers. Exploring reachability, barrier functions, and integral quadratic constraints in more depth and applying them to real scenarios of proximity operations can reduce system uncertainty by characterizing the physical environment and updating control policies to satisfy state and actuator constraints. The current state-of-the-art in hardware motivates this possibility. Both research areas could lead to significant contributions in the field of control and astrodynamics, and shrink the current technical gap regarding safety certifications of RPO controllers.

Chapter 3

GN&C Description, Safety Verification & Methodology

This chapter starts with a description of the functionality of the GN&C algorithms, RPO mission phases, sets of equations of relative motion, orbital frames, and sensor suite. It then introduces the two control laws selected for the RPO scenarios shown in this thesis. The attitude determination and control subsystem is described as well as as a description of the disturbances, uncertainties, and nonlinearities affecting the control output. The core mathematics of the collision risk minimization metrics are introduced. Finally, an overview of robust optimization and formal methods is presented. These two concepts serve as the foundation for the proposed methodology to shrink the gap of safety verification of RPO GN&C platforms.

3.1 Guidance, Navigation, and Control (GN&C)

The following architecture represents the Guidance, Navigation and Control onboard the Servicer. In this thesis, a lidar sensor model provides azimuth/elevation, which is fed into the navigation Kalman filter to smooth out noise generated by the lidar measurements. Quaternions/Euler angles are simulated for pointing accuracy during each phase of the simulation. The guidance contains the dynamics for the various phases of the RPO mission, and the control algorithms enable a feedback control law for each phase. The maneuver plan is then fed into the actuation device to move the plant (i.e., the Servicer). The state machine logic for abort maneuvers and emergency transfers [126] is outside the scope of this thesis. Figure 3.1 shows the logic of a standard GN&C platform. The first goal of this thesis is to capture the disturbances, uncertainties, and nonlinearities that are not modeled within the GN&C scheme due to the simplification of the dynamics used in the onboard computer of the Servicer. The second goal is to develop a fuel-optimal control with safety guarantees considering various constraints and unknown disturbances affecting the Servicer and Client.

RPO missions work by tracking the location of a moving Servicer and Client in space, performing ma-

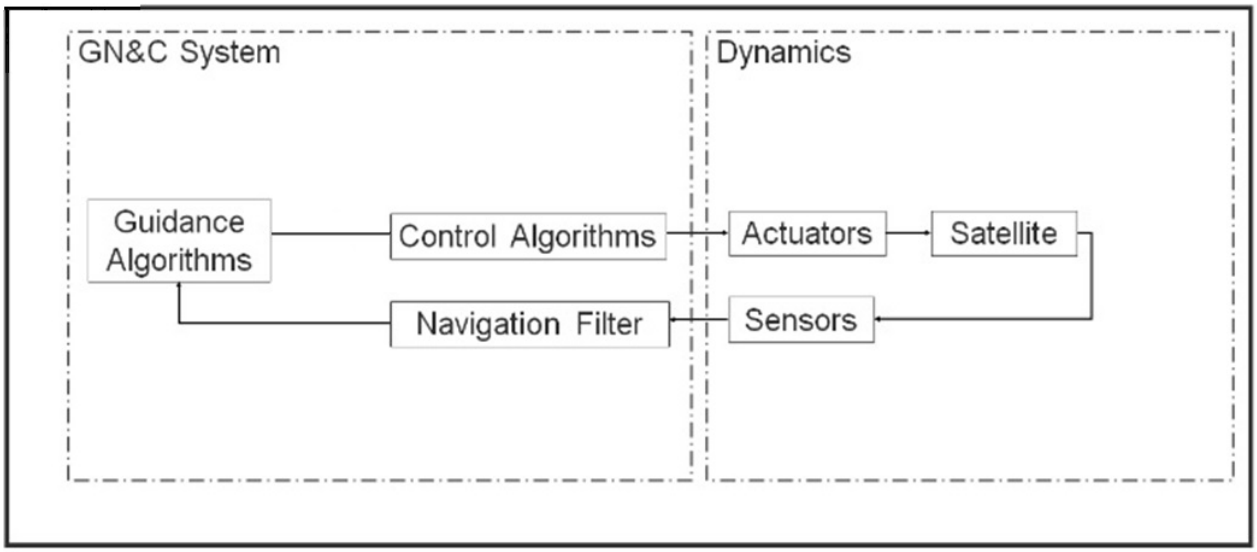

Figure 3-1: Standard GN&C Platform.

neuvers so that the Servicer gets closer to the Client, and then finally performing inspection or docking maneuvers based on the application. A spacecraft GN&C includes three elements: navigation for tracking the current location of the Servicer, using navigation sensors for state information, guidance for directing the Servicer toward the Client, and control for applying guidance commands to the Servicer. The following list shows a description of each of these elements.

- The guidance component involves the current location and trajectory of the Servicer towards a designated maneuver phase, as well as the desired changes in its velocity, rotation and acceleration to follow this path. The guidance algorithm includes the dynamics for the direct line, inspection, and retreat phases, as discussed in the next section.

- The navigation component involves the location and velocity of the Servicer (its state vector) and its attitude (angular position in space). Sensors and actuator are used to obtain satellite state information and control output, respectively. In this thesis, a lidar sensor is used to collect state measurements, and a Kalman filter is applied to smooth out the noise generated sensor measurements and control decisions from the spacecraft actuation.

- The control component involves the application of steering controls needed to execute guidance commands while maintaining platform stability and smooth travel among the various phases in the RPO mission. Linear Quadratic Regulator (LQR) and Model Predictive Control (MPC) are used for the case studies presented in this thesis.

The next section will describe the mission phases for the selected RPO mission.

3.2 RPO Mission Phases

The most common RPO maneuvers and their dynamical equations can be found in [144]. Table 3.1 describes the selected mission with various RPO maneuvers executed throughout the simulated phases of this mission.

Table 3.1: Phases of RPO Mission. Total Duration: 1.94 hrs [143]

Phases	Time Duration (seconds)
Direct Approach	[0-1000]
Inspection Mode	[1200-1700]
Positioning	[1700-4100]
Closest Approach	[4100-5700]
Retreat	[5700-7000]

The first maneuver is a direct approach maneuver to get closer to a Client. This approach is a closed-loop maneuver in which the Servicer moves in a straight line in Local-Vertical-Local-Horizonal (LVLH) frame following a trapezoidal velocity profile. This means that each segment has a phase of constant acceleration, then a phase of constant velocity, and last, another phase of constant deceleration. The acceleration utilized during the first and last phases is the same, but opposite in sign. The satellite moves a defined distance, starting and ending at zero velocity. This line approach is performed along the +R-bar direction; however, the system is capable of performing this maneuver in any arbitrary direction. As this segment behaves in a rectilinear fashion, the following kinematic formulas can be used: The overall distance of the segment is represented in Equation (3.1) as

$$x = ||x_f - x_0|| \tag{3.1}$$

where x_f is the position (m) at the end of the maneuver and x_0 is the initial position (m).Similarly, Equation (3.2) shows the reference velocity as

$$\dot{x}_r = v_0 + a_c \Delta t d \tag{3.2}$$

where v_0 is the initial velocity (m/s), a_c is the acceleration (m/s^2), Δt is time (s) and d is the displacement (m). The reference acceleration is given in Equation (3.3) as

$$\ddot{x}_r = a_c d \tag{3.3}$$

The guidance algorithms used in the inspection mode, positioning, closest approach and retreat phases are modeled through satellite equations of motion (EOM) to represent the Servicer maneuvers. The next section discusses the various sets of satellite EOM used in the RPO mission.

3.2.1 Satellites' Relative Motion Embedded in the GN&C Platform

The following list describes the most common relative satellite equations of motion applied to the guidance algorithms for the phase maneuvers onboard the RPO GN&C platform. Due to limitations with computing power onboard satellites, the controller is limited to a closed-form, linearized and averaged orbital dynamics

expression, which is shown in the fourth chapter, as a control state-form representation.

- Hill-Clohessy-Wiltshire (HCW) [66]: The dynamics are expressed in relative position and velocity as a state vector. This model is not accurate for large separations. It also assumes a circular reference orbit around the Client and neglects orbital perturbations.

- Tschauner–Hempel Linearized Equations of Relative Motion in Elliptic Reference Orbit [74]: This linearization assumes that two objects are proximate in position and velocity, but it does not require any assumption about the eccentricity of the orbit. It contains time-varying coefficients for radial distance, angular velocity, and acceleration as the target's spacecraft trajectory (i.e., with respect to the Servicer) varies with time.

- D'amico Relative Orbital Elements (ROEs) [28]. These relative state dynamics are usually preferred in the RPO control problem. This method is conservative in nature as it enforces the constraint of anti-parallelism of the eccentricity and inclination vectors between the Servicer and Client. This set of dynamics is not used in this thesis because although it enforces a passively safe trajectory, fuel consumption is not optimal in the overall approach.

- Modified form of Lagrange's Planetary Equations (LPEs) for J_2 [118]. The same formulation presented in that paper, but with equinoctial variables, was applied here and taken from the Gim-Alfriend paper published in 2005 [47]. This model was used during the synthesis of control barrier/Lyapunov functions and the feedback control law in the fourth chapter of this thesis.

- Gauss's Variational Equations, Including J_2 and Atmospheric Drag [135]: The advantage of using this method over the Cartesian formulations is that not only are the linearization errors much smaller, but also each orbital element can be controlled independently. When navigating in absolute navigation, this model is used to recover the state transition matrix from mean to osculating terms, as stated by the Gim-Alfriend method [46].

The Lagrange Planetary Equations (LPEs) relative equation of motion [80] with equinoctial variables is implemented in the control scheme for this thesis. The convenience of deriving the relative equation of motion based on the relative orbital elements (ROEs) allows the ROE to vary slowly with time, and also allows for perturbations to be more conveniently included. Gim and Alfriend [46] first developed the relative equations of motion including the first-order secular and osculating J_2 perturbation in arbitrarily eccentric orbits, in which a J_2-perturbed state transition matrix (STM) was derived by using the relationship between the relative state and the ROE, and a curvilinear coordinate system is used instead of the rectilinear coordinate frame to obtain more accurate results [146]. Although this thesis focuses on LEO operations, the set of equinoctial variables eliminates singularities in the inclination/eccentricity vectors for an operational RPO controller for any altitude (i.e., not just available for LEO applications). This control setup of the relative equations of motion between the Servicer and the Client, applying LPE dynamics, will be discussed in more detail in a

later section of this chapter. The orbital frames are introduced next, as this thesis includes several mission phases in which these frames become relevant.

3.2.2 Orbital Frames

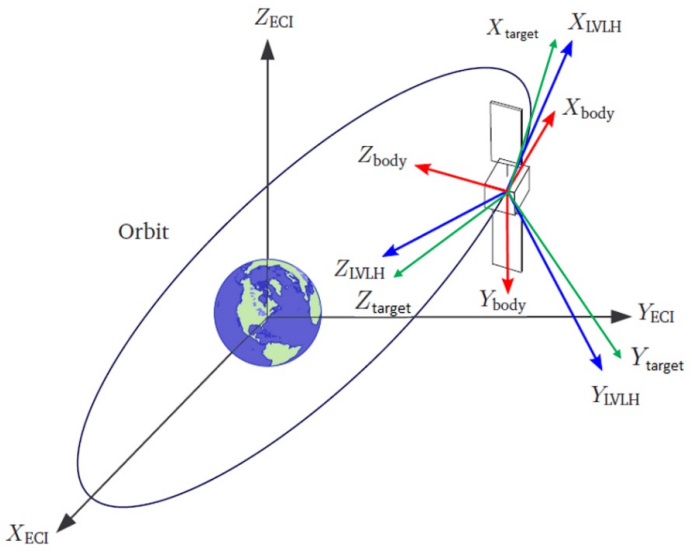

Figure 3-2: Illustration of a general spacecraft formation with out-of-plane relative motion.

Figure 3-2 shows a graphical representation of the various orbital frames used in this thesis. During the various phases of RPO missions, three main reference frames [**?**] are usually used to express the motion of the Servicer trajectory with respect to the Earth or the relative trajectory of the Servicer with respect to the Client.

- Earth-Centered Inertial Coordinate System (ECI): This reference frame has its origin in the center of the Earth, where a Cartesian coordinate system is defined with (X_{ECI}) pointing towards the vernal equinox, (Z_{ECI}) coinciding with the north pole axis, and (Y_{ECI}) perpendicular to the previous two.

- Local-Vertical-Local Horizontal (LVLH): This frame is centered on the spacecraft, with one axis directed toward the center of the Earth (Z_{LVLH}), another one normal to the orbital plane (Y_{LVLH}), and the last perpendicular to the previous two (X_{LVLH}). This frame is orbit fixed.

- Spacecraft Body Frame: The spacecraft body-fixed frame is a rotating reference frame centered on the center of mass of the spacecraft, with its axes parallel to the body's principal axis of inertia. The Client reference is centered on the spacecraft, and the frame is used to determine the orientation of the satellite.

These frames would be used through the RPO mission phases presented in this thesis.

3.3 Sensor Suite

Navigation sensors include GPS when the Servicer is in absolute navigation (i.e., navigating with respect to the Earth rotating frame) or optical sensors, such as lidar, Infrared camera, and visual camera when Servicer is navigating relative to another object (e.g., Client), usually within 250 meters.

In this thesis, a lidar model is used to provide relative position, bearing angle and range measurements, and a Kalman filter, which employs an algorithm that uses a series of measurements observed over time, containing noise, and produces estimates of unknown variables that tend to be more precise than those based on a single measurement alone [68].

Covariance Prediction

The most fundamental information for the collision risk is the covariance of the Client's and Servicer's state uncertainties. This research focuses on the relative state covariance and does not consider the individual covariances of the two objects for risk assessment purposes.

Based on the latest navigation solution, the Client must evaluate the risks associated with the predicted future relative trajectory. When no measurements are taken, the covariance evolves according to the dynamics. The GA-STM [46] is used to propagate the Hill frame relative state covariance. The covariance propagated by the natural dynamics is

$$\begin{aligned} P(t) &\equiv E\left[(\boldsymbol{x}(t)-\bar{\boldsymbol{x}}(t))^T(\boldsymbol{x}(t)-\bar{\boldsymbol{x}}(t))\right] \\ &= \Phi_{J2}(t,t_0)\cdot P(t_0)\cdot \Phi_{J2}^T(t,t_0) \end{aligned} \tag{3.4}$$

where E is the expectation operator, $\boldsymbol{x} = [\boldsymbol{\rho}, \dot{\boldsymbol{\rho}}]$ is the Hill frame relative state, $\bar{\boldsymbol{x}}$ is its mean, and $\Phi_{J2} = \partial \boldsymbol{x}(t)/\partial \boldsymbol{x}(t_0)$ is the linear mapping between the relative states through GA-STM in equinoctial variables [47].

The Servicer's maneuvers have execution noises. As a result, the Gates' maneuver model, which accounts for maneuver execution errors [44], is used. At the time of a continuous maneuver, the following maneuver covariance is added.

$$P_{\boldsymbol{\Delta V}} = [\sigma_s^2(\Delta V)^2 + \sigma_r^2]\hat{\boldsymbol{v}}\hat{\boldsymbol{v}} + [\sigma_p^2(\Delta V)^2 + \sigma_a^2](I - \hat{\boldsymbol{v}}\hat{\boldsymbol{v}}) \tag{3.5}$$

where $\hat{\boldsymbol{v}} = \boldsymbol{\Delta V}/|\boldsymbol{\Delta V}|$. With the natural dynamics, the covariance grows over time, and the growth in the in-track direction is especially significant. During RPO, it is reasonable to assume that the servicer spacecraft has constant access to the navigation solutions. Thus, it is practical to make covariance predictions assuming some measurement updates.

The relative position bearing angle measurement by optical imagers and range measurements is considered.

$$\boldsymbol{Y}_{\text{optical}} = \left[\arctan\left(y/x\right), \arctan\left(z/\sqrt{x^2+y^2}\right)\right] \tag{3.6}$$

$$Y_{\text{range}} = |\boldsymbol{\rho}| \tag{3.7}$$

The measurement models have corresponding noise covariance R. The contribution of the future measurements on the covariance is incorporated by assuming that the measurements are taken at the maximum likelihood state, linearizing the measurement models. The Joseph formulation of the Kalman filter covariance update equations is used [127].

$$P_k = (I - K_k \cdot \tilde{H}_k) \cdot \bar{P}_k \cdot (I - K_k \tilde{H}_k)^T + K_k \cdot R_k \cdot K_k^T \tag{3.8}$$

$$K_k = \bar{P}_k \cdot \tilde{H}_k^T \cdot [\tilde{H}_k \cdot \bar{P}_k \cdot \tilde{H}_k^T + R_k]^{-1} \tag{3.9}$$

where the subscript k indicates k-th measurement update, $\bar{P}$ is the a priori covariance, and $\tilde{H}$ is the measurement partial.

Finally, in order to keep the predicted covariance more realistic, process noise is included. The noise acceleration is assumed to be a piecewise constant white Gaussian sequence $\boldsymbol{u}(t_i)$ rather than a process [127]. The covariance propagation equation has an additional noise contribution.

$$\bar{P}_{k+1} = \Phi_{J2}(t_{k+1}, t_k) \cdot P_k \cdot \Phi_{J2}^T(t_{k+1}, t_k) + \Gamma(t_{k+1}, t_k) \cdot Q_k \cdot \Gamma^T(t_{k+1}, t_k) \tag{3.10}$$

where Q_i is the process noise covariance

$$E[\boldsymbol{u}(t_i)\boldsymbol{u}(t_j)] = Q_i \delta_{ij} \tag{3.11}$$

and Γ is the process noise transition matrix.

This covariance prediction enables the computation of collision risk. As a result, this thesis includes collision risk assessment capabilities (i.e., Miss and Mahanalobis distances, and 2D PC metrics) to validate safety of the GN&C platform onboard Servicer during the closest approach to obstacle or Client. The ultimate goal of this thesis is to upgrade the GN&C platform to be robust in terms of state output, fuel optimality, and safety. This goal is achieved by applying two methods: integral quadratic constraints during forward-reachability, including sensor measurements and noise, to analyze worst-case output; and control barrier/Lyapunov functions to improve the robustness of fuel-optimal controllers. Figure 3-3 shows the overall framework.

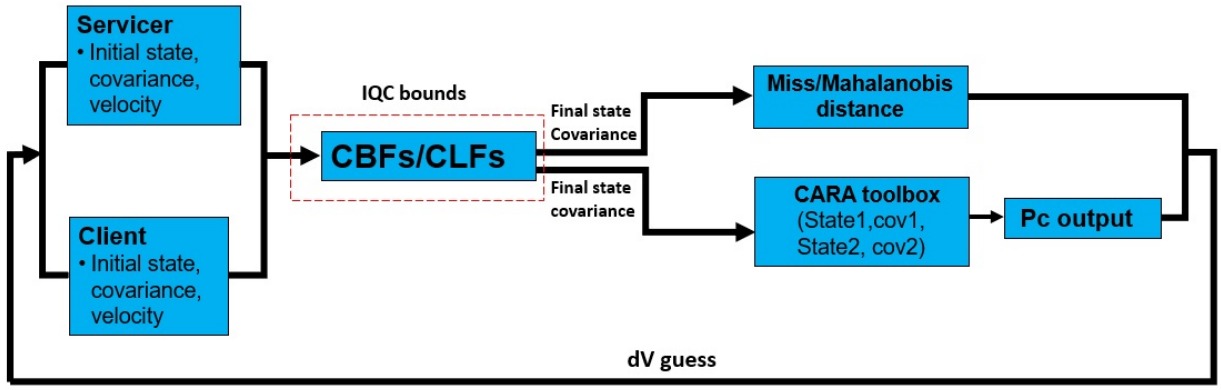

Figure 3-3: Design of Robust GN&C Platform.

The architecture above shows that if the IQC bounds exceed the safety threshold specified by miss distance, Mahanalobis distance and PC computations, another initial guess for dV maneuver recommendation would be provided to minimize the collision risk. The next section discusses in more detail the overall software architecture created for this platform.

3.4 Robust GN&C Software Architecture Description

The software architecture consists of four modules: GN&C, neural Lyapunov, IQC-reachability, and collision risk assessment, as shown in Figure 3-4. All four modules are implemented in Python version 3.9, with some wrapper functions for the MATLAB dependencies of the IQC-reachability module. The source code for the IQC-reachability module's first version was obtained from the author's colleague, Dr. Micah Fry, a former control engineer from the MIT Lincoln Laboratory.

The platform requires initial state conditions, an initial guess of delta-V, Client initial position, mission duration, and integration step for the Servicer in relative or absolute frames (i.e., ECI/LVLH), depending on the RPO scenario of interest. The physical environment quantities, such as atmospheric drag, J_2, and sensor noise, along with the associated covariance of the uncertainty of the initial conditions for Servicer and Client, are included in the parameter file. The sequencer file contains the RPO phases' logic (e.g., direct approach, inspection phase, and retreat) with the actions for collecting measurement frequency updates. The main.py file expects the number of Monte Carlo runs and associated seeds (if multiple scenarios are run in parallel). The simulation's speed depends on the number of cores of the local machine.

A pose estimator that uses lidar measurements generates relative state measurements, and the navigation module filters out the noise from these measurements. The navigation output feeds into the guidance and control algorithms to calculate the state and thrust outputs through the RPO mission phases. The neural Lyapunov module takes inputs from main.py to synthesize robust barrier/Lyapunov functions that are fed into the quadratic program to provide a solution that is both fuel-optimal and safe, based on Lyapunov safety conditions. The output of both control algorithms (neural Lyapunov + controller and standalone

controller) is compared and updated (if the standalone controller does not meet Lyapunov conditions for safety guarantees).

The IQC reachability method generates worst-state bounds of uncertainties using the inputs from main.py file. Both outputs, neural Lyapunov + controller and IQC bounds, are stored, added together, and fed into the collision risk assessment for worst-case analysis using the PC, Mahanalobis, and miss-distance metrics. The parameter file includes physical environment quantities such as atmospheric drag, J_2, and sensor noise, and the associated covariance of the uncertainty of the initial conditions for Servicer and Client.

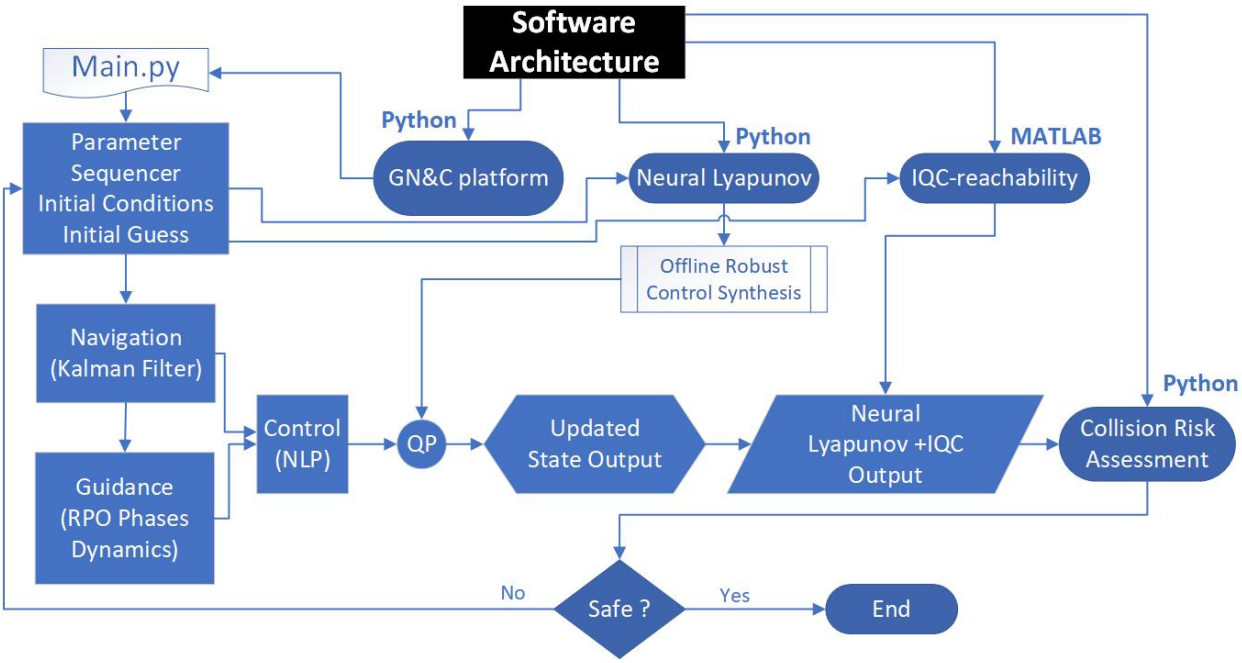

Figure 3-4: Software Integration of the Robust GN&C Platform.

The goal of this platform is to create an iterative loop of initial guesses for delta-v or state initial conditions to improve the robustness of GN&C platforms. This loop will continue until the safety threshold is satisfied by performing safety validation via the collision risk assessment module. The control submodule varies depending on the control design law used in the RPO scenarios. For instance, the LQR method is used when designing the PD control type for attitude, whereas the model predictive control is used to calculate fuel-optimal maneuvers. The next section describes the control design methods integrated into this software architecture.

3.5 RPO Controllers

A typical approach in control design relies on designing a controller, running Monte Carlo simulations, and studying simulation output to identify which design parameters (denoted as R_x and R_u matrices in this thesis) should be used to provide information about the stability of the controller. These steps are followed

by implementing the controller on virtual environments and the physical system to determine performance and re-tune parameters if needed. The goal of the next chapters is to propose innovative techniques that could certify these controllers as safe for various orbital scenarios without the need for the computationally expensive Monte Carlo approach. The next two subsections will introduce controllers used onboard spacecraft.

3.5.1 Linear Quadratic Regulator (LQR)

The LQR approach is based on the search of the trade-off between the regulation performance of the states and the control effort, and is formulated in Equation (3.12) below as

$$\begin{aligned} & J = \int_0^\infty \left(\tfrac{1}{2}(x - x_{ref})^T R_x (x - x_{ref}) + \tfrac{1}{2}(u - u_{ref})^T R_u (u - u_{ref}) \right. \\ \text{s.t.} \quad & \dot{x} = Ax(t) + Bu(t) \quad y = \quad Cx + Du, \end{aligned} \tag{3.12}$$

where the requirement of performance, $J \geq 0$, implies that both R_x and R_u are positive definite matrices penalizing state errors and thruster efforts. The A (state matrix), B (input matrix), C (output matrix), and D (direct transmission matrix) represent the state space realization of the system, x is the measured state, u is the actuation effort, and R_x and R_u are initially approximated by Bryson's rule as in [42]. The variables x_{ref} and u_{ref} represent the reference trajectories for the inspector satellite. The goal of this control strategy is to satisfy a feedback control law such that the minimum $u_{final} = -kx$ is found, where k is the optimal gain matrix and x is the final state (goal). This control is used for the IQC reachability analysis for the guidance, and a PD control law, for the attitude control of the Servicer. These are case studies (1 and 2) presented in the next chapter of this thesis.

3.5.2 Model Predictive Controller (MPC)

Linear Model Predictive Controller is an extension to the linear-quadratic regulator (LQR), which comes from optimal control theory [62]. This control algorithm is based on the numerical solution of an optimization problem online with actuator and/or state constraints, which is useful for trajectory planning and obstacle avoidance applications. MPC relies on the concept of receding horizon optimal control derivation. According to this approach, at time t, we solve to find the optimal control sequence over a finite future horizon of N steps as shown in Figure 3-5.

Applying this formulation to satellite navigation, the receding horizon control strategy would replan the route of the satellite dynamics and the corresponding maneuver actions periodically, finding the overall set of actions over a time horizon, applying the first and then replanning for the next step [62].

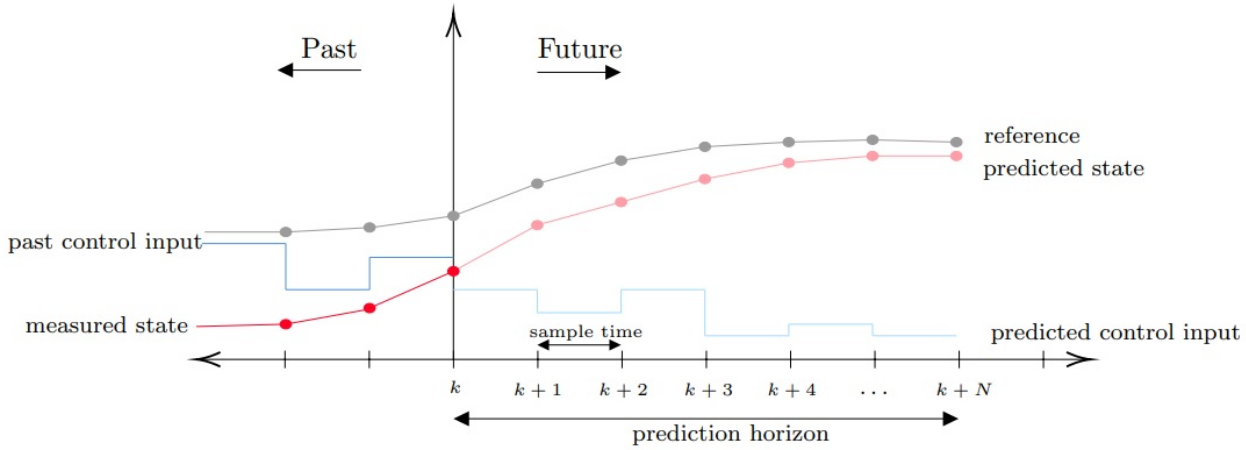

Figure 3-5: A visualization of model predictive control [66]. At the current sample time k, a sequence of control inputs are calculated that minimize the error between the predicted state and the reference trajectory over the prediction horizon N. This process is repeated every sampling instant, whereby the prediction horizon continuously recedes by one step.

A simple MPC example is used to introduce the controller and is mathematically represented as follows:

$$\begin{aligned} x(k+j+1|k) &= Ax(k+j|k) + Bu(k+j|k) \\ x(k|k) &= x(k) \\ z(k+j|k) &= Cx(k+j|k) \\ |u(k+j|k)| &\leq u_m, |x(j)| \leq x_m \end{aligned} \tag{3.13}$$

where $x(k|k)$ and $x(k+j|k)$ are the set-point (reference) and output vectors predicted for a future sample $j+k$, respectively, but calculated at the current sample k, $j = 1, ..., N$), $u(k+j|k)$ represents the decision variables control input increments on the control horizon, A and B are the state dynamics and control input (i.e., time-invariant but time-varying dynamics are also possible), respectively, C is the measurement of our sensors or relative distance between two satellites, and u and x represent the actuators and state, respectively.

The LQR controller is used to validate the reachability method via IQCs while the MPC controller is used to validate the safe and fuel-efficient RPO maneuvers via the neural Lyapunov method. The reason for this is that IQC solves Ricatti inequalities within the control scheme for robustness characterization, bounding the energy of the system and incorporating various sources of uncertainty affecting that system. This computation, if applied to each time step through the whole simulation, would take too long to characterize MPC schemes. For that reason, we only applied IQCs to MPC schemes at specific times (i.e., closest approach to Debris or Client) in the case studies presented in this thesis. The attitude determination and control subsystem is introduced next, as this thesis includes a performance analysis of the control attitude pointing of the Servicer with respect to the Client.

3.6 Attitude Determination and Control Subsystem

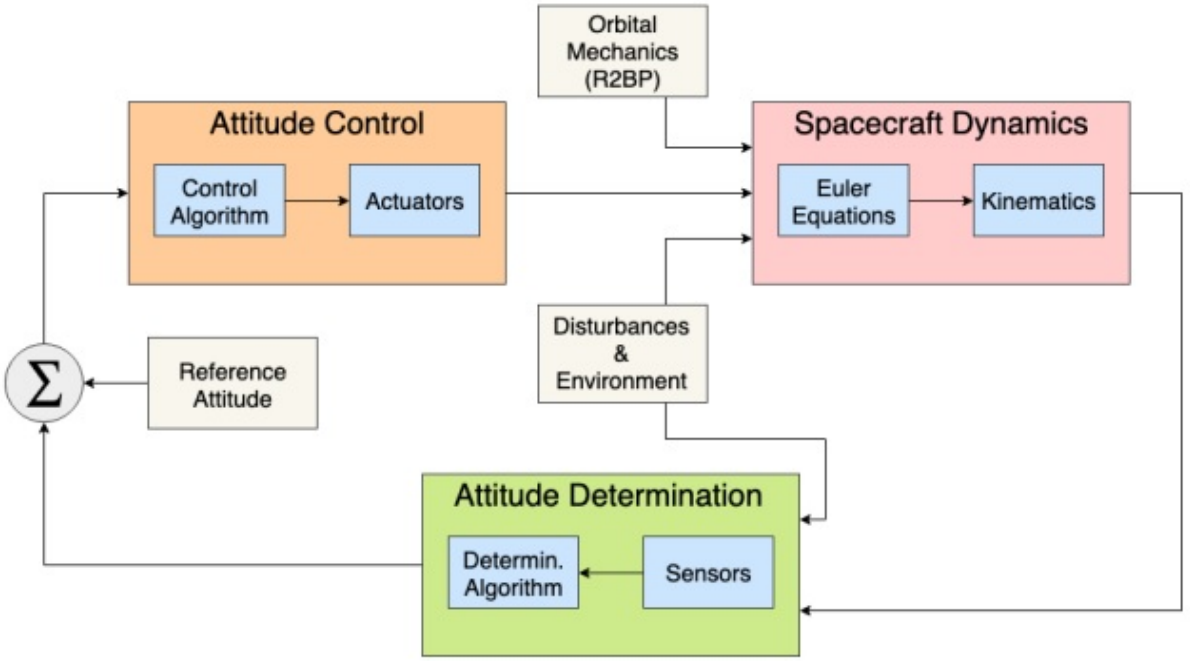

Figure 3-6: ADCS block diagram taken from [75].

Figure 3-6 shows the logic scheme for the Attitude Determination and Control Subsystem (ADCS) implemented in this thesis to demonstrate performance analysis of the control orientation of the Servicer with respect to a Client. The following equations describe the dynamics and kinematics for controlling the orientation of the Servicer. The orbital dynamics of the Servicer is described by the use of equations derived from the restricted two-body problem model (R2BP). The computation of the attitude motion of the Servicer is based on the unconstrained Euler equations describing the rotation of a rigid body in the spacecraft body frame as shown in Equation (3.14).

$$\begin{aligned} I_x\dot{\omega_x} + (I_z - I_y)\omega_z\omega_y &= u_x + T_x \\ I_y\dot{\omega_y} + (I_x - I_z)\omega_x\omega_z &= u_y + T_y \\ I_z\dot{\omega_z} + (I_y - I_x)\omega_y\omega_x &= u_z + T_z \end{aligned} \tag{3.14}$$

where $I_{x,y,z}$ represent the inertia moments, $\omega_{x,y,z}$ are the angular velocities, $\dot{\omega}_{x,y,z}$ their derivatives, $u_{x,y,z}$ represent the control actions, and $T_{x,y,z}$ is the environment disturbance torque acting on the Servicer.

It is possible to obtain the relative attitude of the Servicer, with respect to the ECI reference frame, by integrating the angular velocities. Attitude kinematics are fulfilled using quaternions (discussed in a later chapter) as attitude parameters. These dynamics can be represented as shown in Equation (3.15).

$$\frac{d(q_0,q)^T}{dt} = \frac{1}{2}\begin{bmatrix} 0 & -w_x & -w_y & -w_z \\ w_x & 0 & w_z & w_y \\ w_y & -w_z & 0 & w_x \\ w_z & w_y & -w_x & 0 \end{bmatrix} [q_0(t), q(t)]^T \tag{3.15}$$

where $q_0(t)$ is the scalar component, $q(t)$ is the vector component of the quaternions, and the 4×4 matrix represents the skew symmetric matrix [56].

The reaction wheel actuation can also be modeled as in Equation (3.16).

$$\dot{\omega} = -J^{-1}(\omega \times J\omega) - J^{-1}(\omega \times h) + J^{-1}T_w + J^{-1}T_e \tag{3.16}$$

where J is the total inertia matrix of the Servicer including the reaction wheel, h is the angular momentum of the reaction wheels, T_w is the torque produced by the reaction wheels' acceleration and T_{ext} is the external disturbance torque.

The angular momentum of the reaction wheels is given as in Equation (3.17).

$$\dot{\omega} = -T_w \tag{3.17}$$

The disturbances affecting the attitude dynamics as well as the uncertainties and nonlinearities caused by the simplified relative equations of motion need to be modeled and captured for robustness guarantees in GN&C platforms.

3.7 Modeling Disturbances, Uncertainties and Nonlinearities

There are environmental disturbances, such as the aerodynamic effects, gravity gradient effects, and solar pressure effects, which perturb the attitude motion [64]. The total external disturbance torque in the Servicer body reference frame is given by Equation (3.18)

$$T_{ext} = T_{drag} + T_{GG} + T_R \tag{3.18}$$

where T_{drag} denotes the torque produced from aerodynamic effects, T_{GG} denotes the torque produced from gravity gradient effects, and T_r denotes the torque produced by radiation effects.

The total external disturbance torque is modeled as the alignment errors of each component and bounded via the proposed contributions. The various phases of this RPO mission can be represented in Figure (3-7).

Due to the linearization and averaged satellite equations of motion (LPE dynamics) that constitute the guidance algorithms, one of the outputs used by the controller, the full effects of J_2 gravity perturbation is usually truncated to first-order dynamics [134]. The reference trajectory inside the controller uses a semi-analytical approximation to model the J_2 effects.

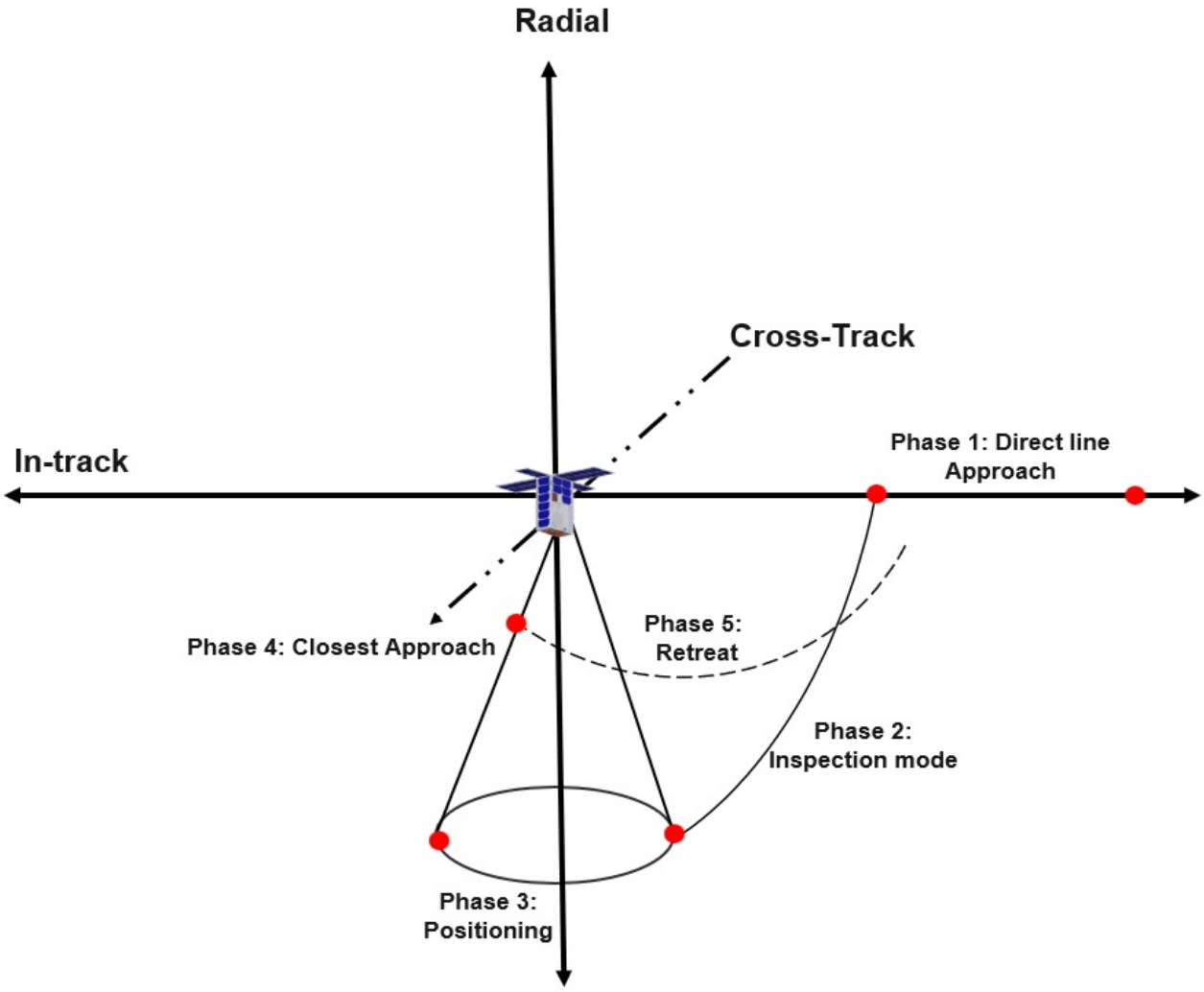

Figure 3-7: CONOPs: phases of the RPO mission (direct approach, inspection through Line-of-Sight (LOS) cone constraint, and retreat maneuvers).

Other uncertainties that affect the control design can be found in Table 3.2 below:

Table 3.2: Uncertainties captured in the control scheme

Uncertainty	Characterization
Actuation	JPL papers [18, 57, 1, 32]
Initial Conditions	Orbital Perturbation chapter [92]
Sensor Noise	Lidar specifications [134]

Cold-gas thrusters are selected as the primary engine devices for the RPO maneuvers in this work. Cold gas propulsion, which relies on the process of controlled ejection of compressed liquid or gaseous propellants to generate thrust, is usually used for proximity operations [121]. Thrust output varies from 0.1 mN to 1 N ranges with uncertainty commanded thrust output up to 5% [70].

Cold-gas thrusters are selected as the primary engine devices for RPO maneuvers in this work due to their simplicity, reliability, and safety. Cold gas propulsion relies on the process of controlled ejection of

compressed liquid or gaseous propellants to generate thrust, and is typically used for proximity operations [121]. The thrust output of cold-gas thrusters can vary from 0.1 mN to 1 N, with commanded thrust output uncertainty of up to 5% [70]. Additionally, cold-gas thrusters do not require combustion or other complex components, making them a low-cost and low-maintenance option for RPO missions. While other propulsion systems, such as chemical propulsion, can provide higher specific impulse and greater maneuverability, these systems often require more complex hardware and can be more expensive to develop and operate. Therefore, cold-gas thrusters are a suitable choice for RPO maneuvers, but constrained to certain Servicer sizes, in situations where precise maneuvering and safety are of utmost importance.

In addition, Hall and ion thrusters are usually selected as the secondary actuation devices for position-keeping maneuvers during RPO missions. The typical thrust output varies from 200 mN to 600 mN. For the Hall thruster design, the power supply normally regulates the discharge current between the anode and the cathode. It is found in [1] that the actual beam current, beam energy, and beam species mix, all of which influence the thrust along with the specific impulse (Isp), depend on plasma and thermal processes in the thruster. The efficiencies of each of these species multiply to give the total thruster efficiency. To obtain the uncertainty, all these efficiencies need to be modeled to calculate the thrust, as shown in [57].

However, the biggest source of uncertainty for ion engines comes from understanding how the current is distributed among the emitters. At JPL, Dr. Ziemer has developed expertise in ion engines and has collected very accurate measurements of current and voltage, but with the drawback of combining their measurements and uncertainty in the hydraulic impedance (these are pressure-fed capillary emitters) between all the emitters that run in parallel. Although there is some uncertainty about emitter and thruster-level alignment as well, the expected value was found to be small [32]. Furthermore, Dr. Ziemer found that a significant amount of the error of controlling the test mass "quietly" (which includes sensing noise, modeling errors, etc.) came from rounding off the thrust commands to the thrusters [32]. That is, while the controller calculated the required thrust levels with double-precision floating-point numbers, those were rounded down to the integer-level commands that were limited due to communication and thruster control bandwidth and precision. In the end, the uncertainty of the sensor calibration and this error from rounding the commands contributed significantly to the overall uncertainty in their model predictions versus performance analysis. Characterizing actuation uncertainty is extremely important to incorporate safety guarantees in RPO missions. The next section describes collision risk metrics used to improve safety in satellite operations.

3.8 Collision Risk Minimization

For risk evaluation, three different metrics are used. The simplest metric is the miss distance or the L_2-norm of the relative position ρ. Another useful distance metric is the Mahalanobis distance in position space $\sqrt{\boldsymbol{\rho} \cdot P_{\boldsymbol{\rho}\boldsymbol{\rho}}^{-1} \cdot \boldsymbol{\rho}}$ where $P_{\boldsymbol{\rho}\boldsymbol{\rho}}$ is the relative position covariance. This thesis only focuses on the position space to gain insight into the instantaneous collisional risks. Another class of risk metrics is the probability of

collision (PC). The probability of collision is a common metric used in collision avoidance (CA) for measuring the conjunction risk and one of the most important pieces of data that is evaluated by the NASA CARA Operators [54]. PC is widely used, but needs to be interpreted properly to be used responsibly. If an object's state is poorly known (high covariance), a low PC can correspond to insufficient information rather than low risk of collision. Relying on a PC threshold for maneuvers without considering the quality of corresponding covariance information is therefore ill-advised. Therefore, it is important to consider these cases and understand the accuracy of the PC metric when evaluating the risk of collision. Currently, three PC categories exist: red or high risk, amber or moderate risk, and green or low risk. Operationally, a conjunction event is tracked over time for a few days before the TCA. If the PC is consistently in the red zone, or is increased from the amber to red zone, necessary steps are taken to generate an avoidance maneuver plan. The ultimate go/nogo decision for the execution of a planned avoidance maneuver is a function of many other factors, such as the miss distance magnitude, including its relative components, consistency of the orbit determination (OD) solutions, and operational considerations of the effect of avoidance maneuver on the core mission. Others have also argued that the estimated miss distance is a better alternative for minimizing the risk of a conjunction event [136].

Nevertheless, PC remains one of the most important parameters operationally for adjudicating conjunction events and deciding whether a mitigation action is necessary. Moreover, with the increased adaptation of ground-based or on-board autonomous CA processes, more and more satellite operators are relying heavily on easily quantifiable metrics, such as Pc, to make decisions on conjunction avoidance actions. New emerging techniques in quadratically constrained quadratic programs (QCQPs) are being considered in RPO missions as well [107, 14, 104]. This technique is an optimization technique in which both the objective function and the constraints are solved through a quadratic program more efficiently, which is key in real-time operations.

The next section describes the relationship between the two fundamental theories used for the PhD contributions of this thesis.

3.9 Relationship between Integral Quadratic Constraints and Control Barrier/Lyapunov Functions

The use of integral quadratic constraints and control barrier/Lyapunov functions in GN&C spacecraft systems design can be connected with the dissipativity principle, a concept in control theory that characterizes systems that can store and dissipate energy. In particular, these two methods exploit the benefits of the properties of quadratic functions to generate worst-case performance analysis while accounting for disturbances, uncertainties and nonlinearities often ignored in the design of GN&C spacecraft systems.

Integral quadratic constraints (IQCs) provide a framework for analyzing and designing feedback control systems that account for uncertain and nonlinear dynamics. IQCs enable the use of Lyapunov theory and linear matrix inequalities to design robust controllers that guarantee stability and performance in the presence

of uncertainties and nonlinearities. Control barrier/Lyapunov functions (CBFs/CLFs) provide a complementary approach that enforces safety constraints by designing controllers that ensure that the system remains within a safe set of states, even in the presence of disturbances and uncertainties. CBFs/CLFs can also be used to ensure that the system reaches a desired goal while avoiding unsafe states.

By leveraging these methods, GN&C systems can be designed with robustness and safety guarantees that account for the inherent uncertainties, nonlinearities, and disturbances in the system. This is particularly important in the context of RPO missions, where precise control and safety are critical for successful and safe operation of the Servicer and Client spacecraft.

3.10 Robust Optimization

Robust optimization is a subset of optimization theory and has become a method of choice for optimization under uncertainty in many fields, including aerospace [40]. In this section, the theoretical background of the IQC framework, which combines aspects of robust optimization, input-output theory, and absolute stability theory, is presented for the reader's benefit.

3.10.1 Contribution 1: Evaluating Controller Performance and Stability via Integral Quadratic Constraints

IQCs offer a framework for representing various elements of a dynamical system (e.g., non-linear, time-varying, uncertain, or distributed) to aid in rigorous analysis of robust stability and performance [65]. Based on Megretski's lectures from MIT [111], these techniques can be employed to derive optimization-based algorithms for the certification of stability and robustness of specific feedback systems. This concept is applied to improve safety operations in proximity operation among the Servicer, Client and Debris objects. The following items describe the benefits of using IQC properties:

- To exploit structural information about satellite dynamics,
- To characterize properties of external perturbation signals, and
- To analyze combinations of several perturbations, applied control and external perturbation signals.

The goal of this contribution is to synthesize a controller that minimizes closed-loop robust performance metrics. These metrics include establishing L2 gain bounds, disturbances, and other system properties that could reduce the uncertainty of a system output [138]. The basic properties of IQCs are explored in the next section.

Background

In robustness analysis, it is natural to assume that the dynamics G(s) are known, and ϕ describes the challenging aspects of the dynamics (i.e., nonlinear, time-varying, or uncertain) components of the system.

A system of equations (3.19) represents the feedback interconnection of a single input single output (SISO) linear time-invariant (LTI) system.

$$\begin{cases} \dot{x} = Ax + Bw \\ w = \phi(Cx) \end{cases} \tag{3.19}$$

where A, B, C are given real matrices $det(sI - A) \neq 0$ for Re(s) $\geq$ 0, G(s) = C(sI - A)$^{-1}$ B is the transfer function of the LTI system, and $\phi : \mathbb{R} \to \mathbb{R}$ is such that $\phi(0) = 0$ and $\phi \in$ [0,1]. The analysis objective is to establish global asymptotic stability of the equilibrium point at x= 0. In order to model the system as an IQC, we recognize the exact model S of the dynamical system and specify the objective as an IQC to be established for S. We then apply IQC analysis to the system in Eq 3.19 and define S as the behavioral model in terms of signals w and x:

$$S = [w; x] : \dot{x} = Ax + Bw, \& w = \phi(Cx) \tag{3.20}$$

This system is often represented as a linear fractional transformation (LFT), which is graphically represented in Figure 3-8. For a set S of d-dimensional signals $q = q(t)$, an IQC is defined by a quadratic form σ.

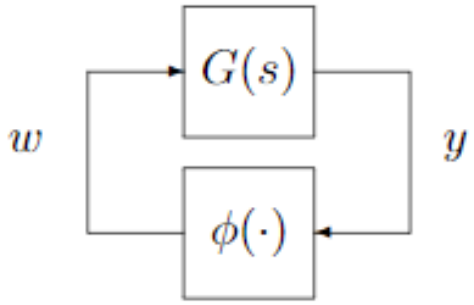

Figure 3-8: Graphical representation of IQC as an LFT.

This quadratic function representation is important for practical feasibility as it permits checking for positive semi-definiteness of linear combinations for different σ values. This is useful for control performance analysis. Defining the states of a lower bound $\kappa = \kappa(q(0))$ for the integrals of σ(q(t)) over long intervals of time: a complete IQC $\succ 0$ on S means existence of a continuous function $\kappa : \mathbb{R}^d \to \mathbb{R}_+$ such that $\kappa(0) = 0$ and

$$\int_0^T \sigma(q(t))\, dt \geq -\kappa(q(0)) \tag{3.21}$$

$\forall$ q $\in$ S and T $\geq$ 0, while a conditional IQC $\sigma \triangleright 0$ on S states that

$$\int_0^T \sigma(q(t))\, dt \geq -\kappa(q(0)) \tag{3.22}$$

$\forall$ signals q $\in$ S of finite energy.

In addition, the robust L_2 induced performance metric is a bound on the ratio between the energies of a system's output signal and the system's input signal [40]. We can combine this metric with IQC to define the robust L2-to-Euclidean performance, which is a bound on the ratio between the Euclidean norm of a system's output (at a specific time) and the system's input signal energy as shown in Equation (3.23).

$$\text{Robust } \ell_2\text{-to-Euclidean norm: } \kappa \in \mathbb{R}_+ \text{ such that } ||e||_{\ell_2} < \kappa ||u_{control}||_{\ell_2}, \tag{3.23}$$

where $e = (P, \Delta)u_{control}$ for any admissible Δ. This metric is capable of maintaining a bound on a system's output at a specific time, given a bound on the input signal's energy. This can be measured with IQC analysis by creating and analyzing a finite-horizon system whose output is zero at any time except for the desired instance. Figure 3-9 shows an example of this metric applied at a specific instance during a simulated natural motion circumnavigation RPO scenario.

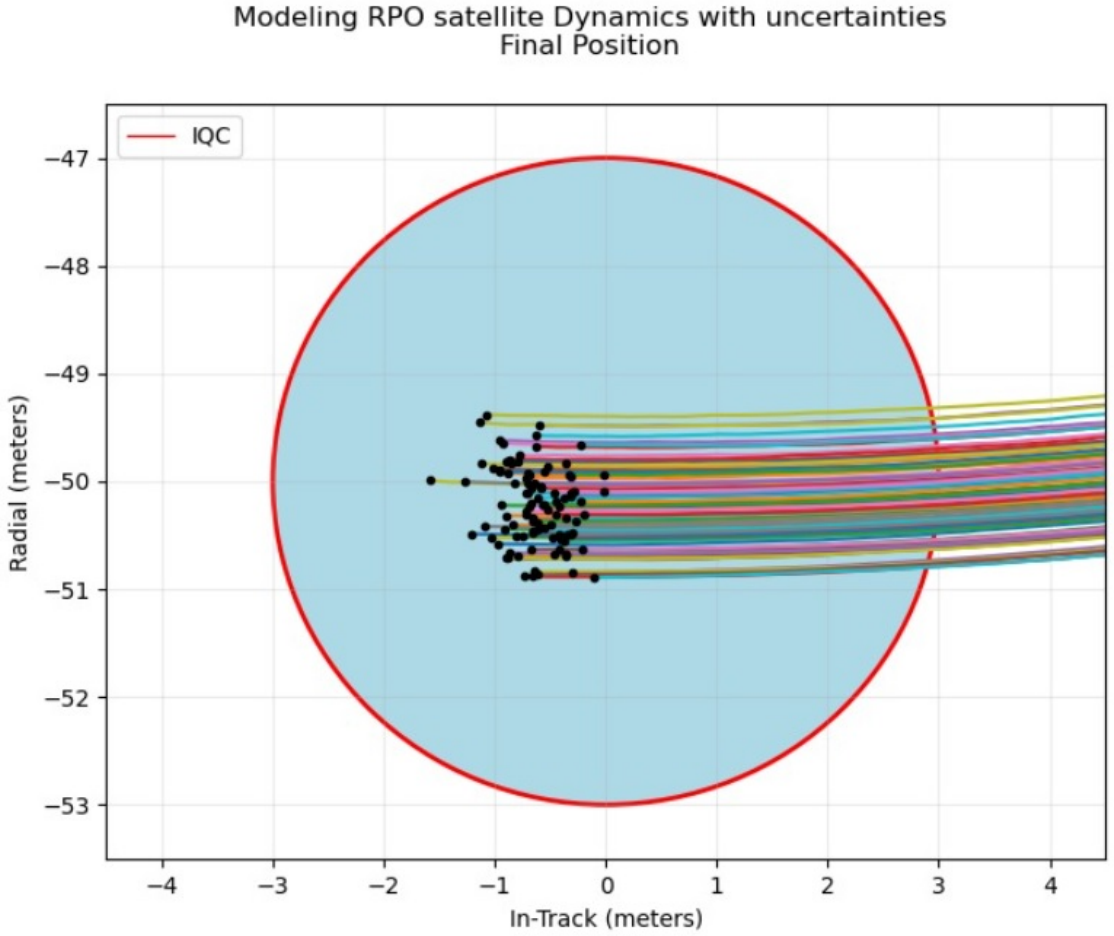

Figure 3-9: 1000 Monte Carlo runs and the IQC analysis showing the worst-state bound at the time of final position of the circumnavigation RPO scenario.

The bound is obtained by conducting IQC analysis on the uncertain system and then multiplying the resulting L2-to-Euclidean norm by the bound on the admissible disturbance's energy. In 3D representation,

the 1000 Monte Carlos runs and the worst-case performance of the final position are shown in Figure 3-10 below:

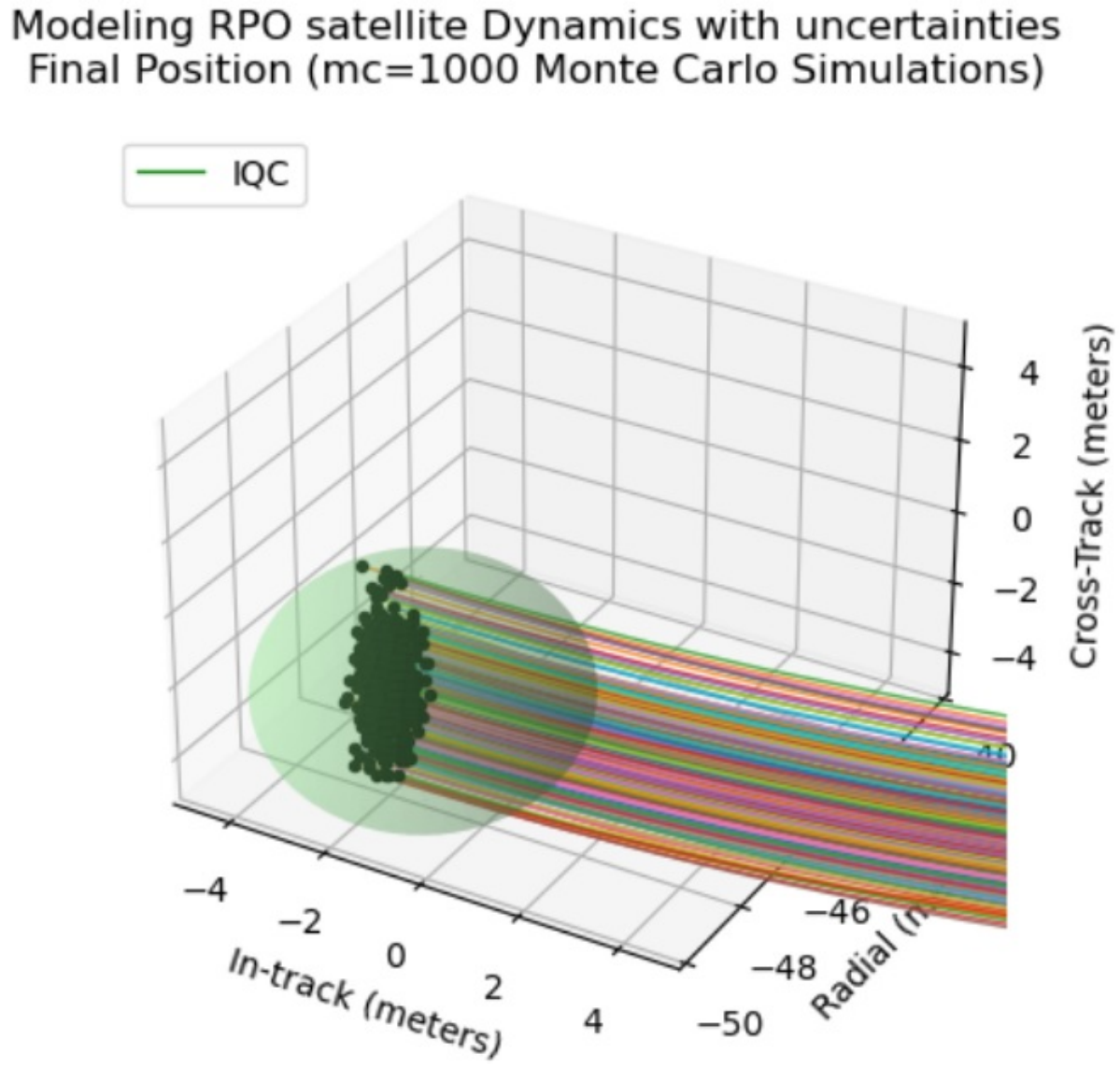

Figure 3-10: 3D representation of RPO worst-case final positions during 1000 MC runs and IQC uncertainty bound at the time of final position of the RPO circumnavigation scenario.

One can think of a complete IQC $\succ 0$ as an implicit dissipation inequality $\sigma(q(t)) \geq dV(x_h(t))/dt$ where $x_h = x_h(t)$ is the hidden state of the system and $V = V(x_h)$ is an unknown non-negative storage function satisfying an upper bound $V(x_h(0)) \leq \kappa(q(0))$. Not only does IQC analysis incorporate static and dynamic time-invariant uncertainties, but it can also consider time-varying uncertainties (i.e., rate-bounded and arbitrarily fast), nonlinear uncertainties (i.e., sector-bounded, norm-bounded, slope-restricted, and passive), and a variety of delay uncertainties [39]. By modeling the system as an LFT on uncertainties, IQC analysis is capable of determining an upper bound on the worst-case performance of any system, thereby providing a more efficient method of parameter-tuning than using the Monte Carlo approach. Because IQC theory is well-suited for a large suite of uncertainty types (e.g., modeling sensor noise as a class of white signal [99] (see appendix for IQC derivation), this framework provides assessments on a closer approximation of the physical system and can flexibly include or remove uncertainties in the analysis.

3.11 Formal Methods

In contrast to other design systems, formal methods use mathematical proof as a complement to system testing in order to ensure correct behavior [131]. One of the techniques in formal methods is to use barrier certificates, which are powerful algorithms for system verification. For the benefit of the reader, an introduction to Lyapunov stability and control barrier function theories will be summarized in this section.

3.11.1 Contribution 2: Certifying Safe Controllers via Synthesis of Control Barrier and Lyapunov Functions

The complete theory of control barrier functions based on Lyapunov theory can be found here [31]. A summary of the theorems most relevant to this method is presented below.

Dynamical System

Let us consider the behavior of dynamical systems of the form

$$\dot{x} = f(x, u) \tag{3.24}$$

where x $\in X \subseteq \mathbb{R}^n$ is the state u $\in U, \subseteq \mathbb{R}^m$ is the input, and $f : X \times U \to X$ is the flow map, which we assume to be locally Lipschitz in x and u. The sets X and U represent the sets of admissible state and control inputs, respectively. Often, we will consider a restricted (but still quite general) class of dynamics known as control-affine dynamics shown in Equation (3.25):

$$\dot{x} = f(x) + g(x)u \tag{3.25}$$

where $g : \mathbb{R}^n \to \mathbb{R}^{m \times n}$ is also assumed to be locally Lipschitz. We focus only on the continuous-time case. In the context of a dynamical system of this form, the control engineer's task is to find a feedback controller $\pi : X \to U$ such that the control input $u = \pi(x)$ imparts to the closed loop system $\dot{x} = f_c(x) = f(x, \pi(x))$ certain desirable properties (e.g., stability). In general, π may be a function of time and state, as in trajectory-tracking control. For clarity, we consider the case where the state x is fully observable. When designing a controller, our goals as control engineers are to ensure that the system's behavior achieves objectives such as stability, robust performance, and safety.

To prove that a closed-loop (i.e. autonomous) system is stable, we turn to one of the most widely known types of certificate: the Lyapunov function. A continuously differentiable function $V : X \to \mathbb{R}$ is a Lyapunov function if it satisfies Equation (3.26):

$$\begin{aligned} V(x_g) &= 0 \\ V(x) &> 0 \quad \forall x \in X \\ \frac{d}{dt}(V(x)) &\leq 0 \quad \forall x \in X \end{aligned} \tag{3.26}$$

where $X_g \subseteq X$ represents the goal of the controller (i.e., a point or region) and $\frac{d}{dt}(V(x)) = \nabla V(x) f_c(x)$ is the Lie derivative of V along the closed-loop dynamics f_c. There are several theorems in [31] that prove the stability of a closed-loop system with these Lyapunov functions.

More specifically, if we focus on the dynamics that can be expressed in a control affine system, as shown in Eq. (3.26), a Control Lyapunov Function (CLF), $X : \mathbb{X} \to \mathbb{R}$ certifies the asymptotic stabilization of a system about x_g as Equation (3.27) shows.

$$\begin{aligned} V(x_g) &= 0 \\ V(x) &> 0 \quad \forall x \in X \\ \inf_u [L_f V(x) + L_g V(x) u] &\leq 0 \quad \forall x \in X \end{aligned} \tag{3.27}$$

where $L_f V$ and $L_g V$ denote the Lie derivatives of V along f and g, respectively. Once the CLF is found, a set of admissible control inputs for each state can be represented as $K_{CLF} = u : L_f V(x) + L_g V(x) u \leq 0$. Any policy π that chooses control inputs from these sets will necessarily stabilize the system. Since these conditions are linear in u, a common choice is a quadratic program (QP) that finds the smallest-magnitude control such that $u \in K_{CLF}$.

This theory can be extended to the safety of barrier certificates useful for identifying unsafe sets and guaranteeing that a dynamical system will never enter an unsafe region. These type of functions are called Control Barrier Functions (CBFs). If there exists a strictly increasing scalar function $\alpha : \mathbb{R} \to \mathbb{R}$ such that

$\alpha(0) = 0$ and $\frac{d}{dt}(h(x)) \leq -\alpha(h(x))$, then h is a barrier function for the closed-loop system, $\dot{x} = f_c(x)$. The third condition from Eq. (3.27) can be modified for a barrier function h

$$\inf_u [L_f h(x) + L_g h(x)u + \alpha h(x))] \leq 0 \quad \forall x \in X \tag{3.28}$$

This condition is affine in u, allowing a CBF to be used in a quadratic program with a controller for safety and stability considerations.Figure 3-11 shows a visual representation of the relationship between control barrier and Lyapunov functions.

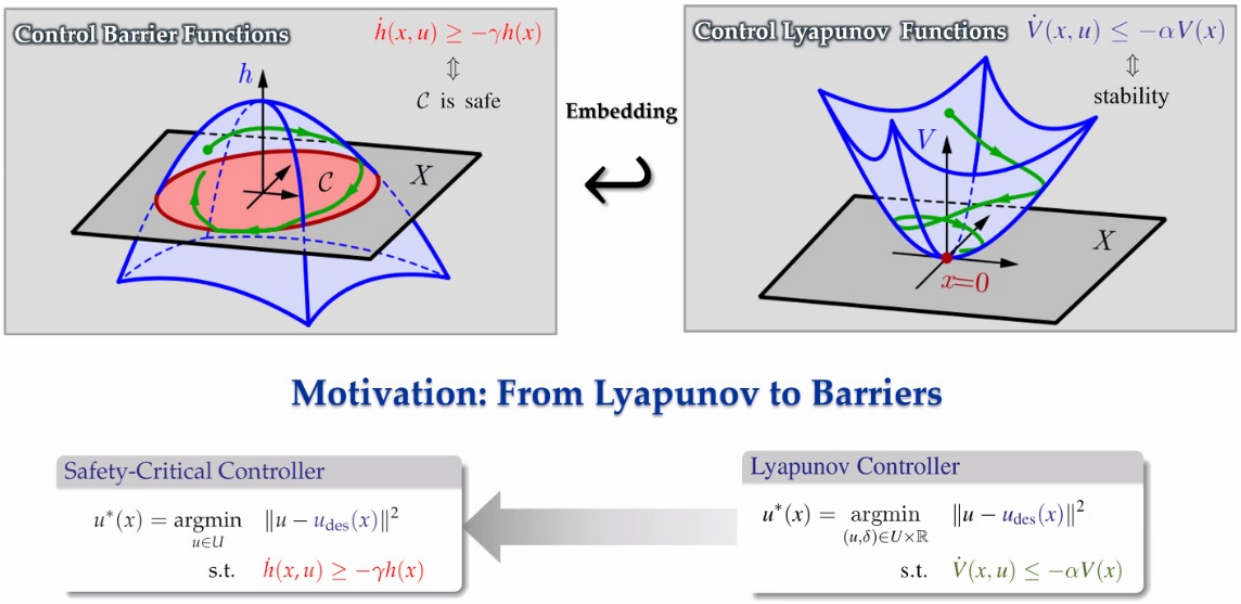

Figure 3-11: 3D representation of control barrier and Lyapunov functions [9].

This novel approach combine the stability criteria from Lyapunov certificates and the safety component of barrier functions to synthesize control Lyapunov barrier functions (CLBFs). This concept encapsulates both properties of CLF and CBF, and enforces stability of a controller towards a specific location while filtering the control output to stay within some safety bounds specified by the control designer. This property becomes relevant during the inspection phase of RPO missions.

Synthesis of CLF and CBF

All of the certificates discussed above allow the control engineer to prove that the controller design is sound. However, these methods share a common drawback: there has historically been no general method for finding these certificates [31]. Although there are two other techniques to find these functions (i.e., sum-of-Squares [9] and simulation-guided [67]), learning-based functions work better for larger-dimensional systems. Table 3.3 below describes the advantages and limitations of these techniques.

Table 3.3: Three Methods to Synthesize Lyapunov Functions

Approach	Advantages	Limitations
Simulation-guided	Open and intuitive formulation	Not sound for black-box systems
Sum-of-Squares	Deterministic guarantees for known dynamics	Works for low-dimensional systems
Neural Lyapunov	Works for nonlinear and large-dimensional systems	Learn from samples

As a result, this thesis explores a learning-based approach to certificate synthesis when a controller is known and the designer's goal is to certify it for the closed-loop system. A visual representation of a control barrier function applied to a nominal LQR controller can be shown in Figure 3-12.

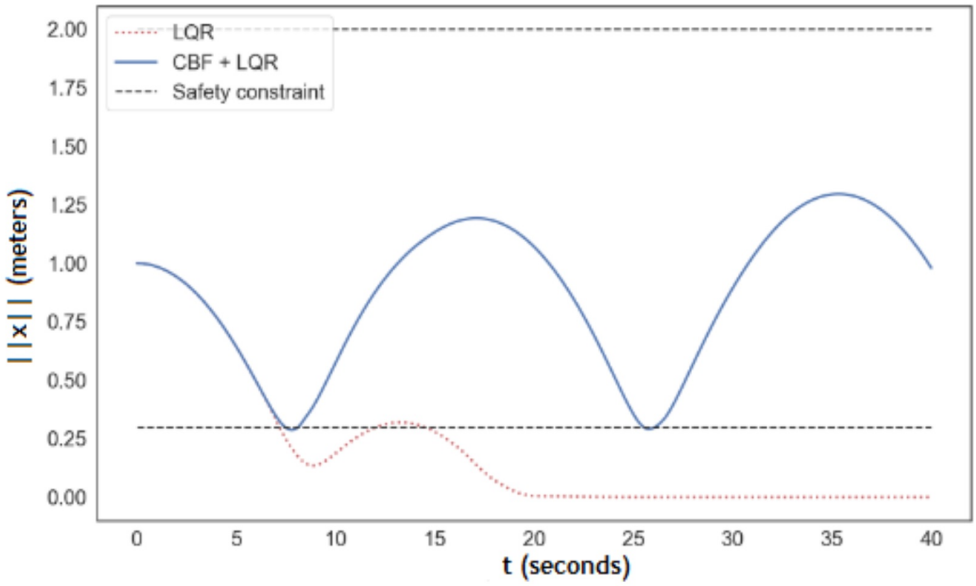

Figure 3-12: LQR filtered by the learned CBF, so that it satisfies the safety constraint (i.e., 0.3 m $<$ ||x||$<$2.0 m.

In this framework, the algorithm learns from the difference between the nominal controller and the Lyapunov model with real uncertainties. The certificate-based controllers can adjust for this difference at runtime.

Loss Function Definition

In order to apply Lyapunov safety conditions using a neural representation for V, two modifications must be made to accommodate the fact that neural networks are best suited for unconstrained optimization problems solved through stochastic gradient descent rather than constrained optimization [29]. Firstly, a penalty method is used to relax the constraints. Secondly, instead of imposing constraints universally (i.e., $\forall x \in X$), the evaluation is performed through a large, finite set of randomly sampled training points (x_1,x_2...,x_N) $\subset$ X. Each training point can be automatically labeled with a loss equivalent to the violation of the certificate conditions at that point. By averaging this loss across the entire training set, the empirical certificate loss is obtained, as shown in Equation (3.29), thus ensuring the feasibility of the constrained optimization problem.

$$L_V = \sum_{i \in I} \frac{\lambda_i}{N} \sum_{j=1}^{N} max(c_i(x_j, V), 0) \tag{3.29}$$

The optimization problem includes penalty weights α_i, which are tuned empirically as hyper-parameters to enforce constraint satisfaction. The constraints are incorporated as scalar penalties in the loss function, where empirical loss is different from true loss as it is evaluated at a limited number of points instead of the entire state space. The stochastic gradient descent can be used to minimize this empirical loss by adjusting the weights and biases of the neural network that represents V.

In addition, certificates impose constraints on the neural network structure, and hence, continuous-time certificates should be learned using networks with continuously-differentiable activation functions such as tanh, softplus, or the exponential linear unit (ELU). Secondly, there are several metrics of certificate quality that can be included as an objective for the certificate search, such as the size of the region-of-attraction certified by the resulting certificate or the size of the admissible control set K(x), the maximizing of which will yield a less-restrictive controller. Either objective could be incorporated into the certificate learning pipeline by adding an appropriately normalized term to the loss function, but care should be taken not to allow the neural certificate to overfit to this term at the expense of violating the certificate conditions [29]. The next section describes how the loss function is used to self-supervise both the certificate V and the control policy π.

Loss derivation for Lyapunov function

The aim of learning the CLF is to stabilize the system around x_0=[0,0]. To parameterize the CLF, V is represented by a neural network with hidden layers and the following empirical loss over $N = 10^6$ training points is minimized. The sample data is uniformly trained from the state space in all experiments. The

mathematical representation of the CLF loss can be seen in Equation (3.30).

$$\begin{aligned} L_V = \lambda_1 V(x_0) + \frac{\lambda_2}{N}\sum_{i=1}^{N} r(x_i) + \frac{\lambda_3}{N}\sum_{i=1}^{N} \max(L_f V(x_i) + L_g V(x_i) u_i, 0) \\ + \frac{\lambda_4}{N}\sum_{i=1}^{N} \max \frac{(V(x_i + \Delta t \dot{x}(x_i, u_i)) - V(x_i), 0)}{\Delta t} \end{aligned} \tag{3.30}$$

The solutions to the relaxed CLF QP at state x_i, including λ_1, λ_2, λ_3, λ_4, and $[r(x_i, u_i)]$, are incorporated into the optimization process with the penalty variables c_1 and λ_5 in the optimization of the loss function presented in Equation (3.31).

$$\begin{aligned} \min_{u} \quad & ||u||^2 + \lambda_5 r \\ \text{s.t.} \quad & L_f V(x) + L_g V(x) u \leq -cV(x) + r \\ & r \geq 0 \end{aligned} \tag{3.31}$$

$$\begin{aligned} \min_{u_k} \quad & J(x_k, u_k) = \textstyle\sum_{i=0}^{N-1}(||x_{i|k}||_Q) + (||u_{i|k}||_R) + \lambda \sum_{i=1}^{N} 1^T (H x_{i|k})_+ \\ \text{s.t.} \quad & x_{0|k} = x(t_k) \\ & x_{i+1|k} = A x_{i|k} + B u_{i|k} \\ & \hat{n}_{i|k}^T x_{i|k} \geq r_2, i = 0, ..., N \\ & |u_k|_\infty \leq u_{max} \end{aligned} \tag{3.32}$$

Additional approximations of the Lyapunov decrease conditions are included in the empirical loss through the third and fourth terms. Although strictly speaking, only the first two terms are necessary, these additional terms can aid the learning process.

3.11.2 Loss derivation for control barriers

A similar approach is adopted for learning a CBF as in the previous example, where h is defined as a neural network with hidden layers, $N = 10^6$ state space samples are taken, and the empirical loss function, shown in the Equation (3.33) below, is minimized.

$$\begin{aligned} \min_{u} \quad & ||\pi_{CBF} - \pi_{nominal}|| \\ \text{s.t.} \quad & L_f h(x) + L_g h(x) u \leq -h(x) \end{aligned} \tag{3.33}$$

where $\pi_{CBF} = \pi_{nominal} + \pi_{losses}$. The residue of π_{losses} is what the CBF function calculates during the learning process to complete the updated policy of the safe controller. The loss function π can be obtained by calling activating functions when learning the dynamics, with uncertain characteristics, and safety constraints of the various RPO scenarios. Eq. 3.34 describes the loss function:

$$L_V = \frac{\lambda_1}{N_{safe}} \sum_{i=1}^{N_{safe}} \max(0, h_\theta(x_i)) + \frac{\lambda_2}{N_{unsafe}} \sum_{i=1}^{N_{unsafe}} \max(0, -h_\theta(x_i)) + \frac{\lambda_3}{N} \sum_{i=1}^{N} r(x_i) + h_\theta^2(0). \tag{3.34}$$

The solutions to the relaxed CBF QP at state x_i, including λ_1, λ_2, λ_3, λ_4, and $[r(x_i, u_i)]$, are incorporated into the optimization process with the penalty variables c and λ_5 in the optimization of the loss function presented in Equation (**??**). The variable max represents the activation function used during the synthesis, and θ is the learning process parameter to improve the likelihood of satisfying the Lyapunov conditions. x_i, $1 \leq i \leq N$ are samples of the state vector. Consequently, the Lyapunov condition can be formulated as a cost function in Equation. (3.35) below:

$$\begin{aligned} \min_{r,u} \quad & ||u - u_0||^2 + \lambda_5 r \\ \text{s.t.} \quad & L_f h(x) + L_g h(x) u \leq -c \times h(x) + r \\ & r \geq 0 \end{aligned} \tag{3.35}$$

The rate of change of the Lyapunov function is what determines the safe and unsafe sets. Overall, this method would provide mathematical guarantees for the control system performance of RPO missions, accounting for unmodeled effects in relative motion dynamics, unanticipated maneuvers by the Client and Debris objects, path and angle constraints.

Chapter 4

Results

This chapter shows the results of and contributions of this thesis, which aims to shrink the gap in the safety verification method of RPO control design for LEO applications. The main objective of this chapter is to validate the proposed safety verification framework by proving the significance of this work in the field of spaceflight safety and autonomous operations for RPO missions. IQC reachability is introduced first, and then control barrier/Lyapunov functions are applied in later sections.

Competitive Advantage for the IQC-Reachability Framework

To solve problems that may be deterministic in principle, it is common practice to run repeated computational algorithms while considering uncertainties in parameters and initial conditions. This approach enables us to perform dispersion analysis. While this method can be useful to optimize controllers and to determine the amount of fuel usage needed to maintain a miss distance and PC thresholds, running these types of algorithms can take many days and does not provide robust guarantees for safety. This leads to a large computational burden even under simplified assumptions of satellite dynamics [39]. The main research question for this first contribution is: How can we guarantee robustness and stability in the control design while capturing model uncertainty and nonlinearities caused by environmental effects and hardware limitations? The performance of RPO controllers can be analyzed via the proposed IQC-reachability method to incorporate such guarantees. Figure 4-1 shows a graphical representation of the closed-loop controller that captures exogenous disturbances due to the physical environment (e.g., atmospheric drag, disturbance torque) and hardware limitations (e.g., sensor noise), uncertainties in actuation, and nonlinearities due to the first-order approximation of the effects J_2.

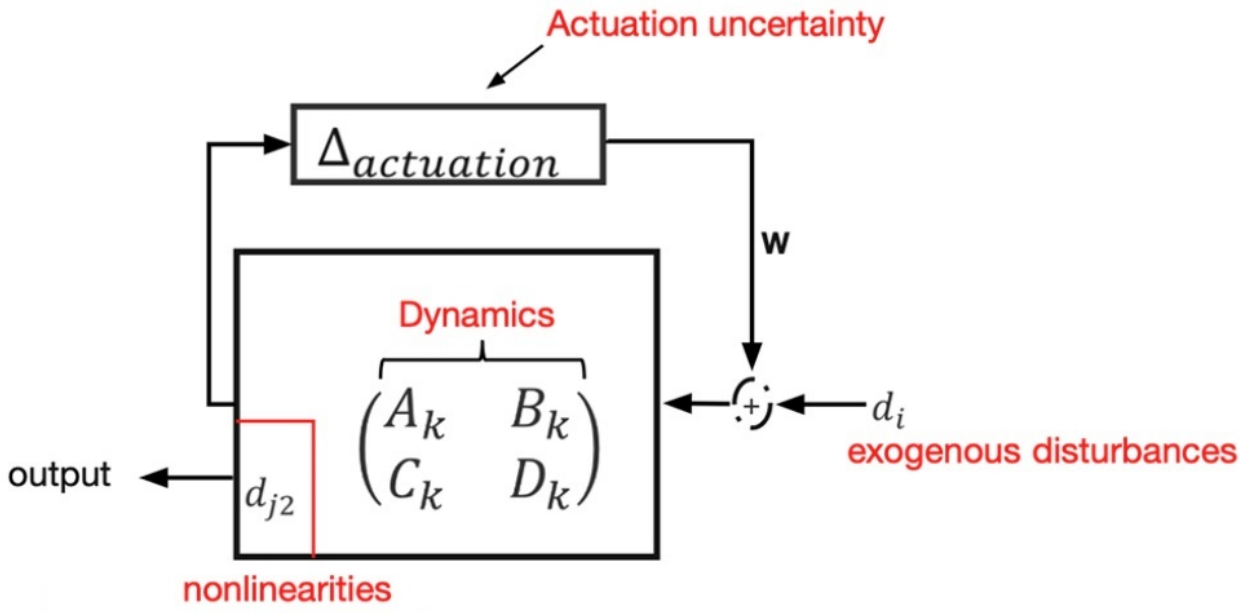

Figure 4-1: Uncertainty characterization in the control design. The actuation device uncertainties are captured as well as exogenous disturbances coming from perturbation effects (i.e., atmospheric drag, sensor noise, disturbance torque). The term d_{j_2} represents the nonlinearities due to the first-order approximation of J_2 gravity dynamics, and the output of this system represents the state uncertainty during forward-reachability analysis via IQCs.

The most common parameterization for the relative motion of two spacecraft is that of the relative Cartesian coordinates in the Hill frame $\mathcal{H} : \{\hat{\boldsymbol{h}}_1, \hat{\boldsymbol{h}}_2, \hat{\boldsymbol{h}}_3\}$ as shown in Figure 4-2. This is a rotating frame based on the reference orbit of the RSO where $\hat{\boldsymbol{h}}_1$ is the unit vector pointing in the direction of the RSO's position, $\hat{\boldsymbol{h}}_3$ is the orbit-normal unit vector in the direction of the *RSO* angular momentum vector, and $\hat{\boldsymbol{h}}_2 = \hat{\boldsymbol{h}}_3 \times \hat{\boldsymbol{h}}_1$ completes the right-handed system. The relative position vector of the servicer is defined by $\boldsymbol{\rho} = (x, y, z)^T$ with the relative velocity $\dot{\boldsymbol{\rho}} \triangleq {}^{\mathcal{H}}d\boldsymbol{\rho}/dt = (\dot{x}, \dot{y}, \dot{z})^T$, where ${}^{\mathcal{H}}d(\cdot)/dt$ denotes the time derivative taken in the rotating reference frame.

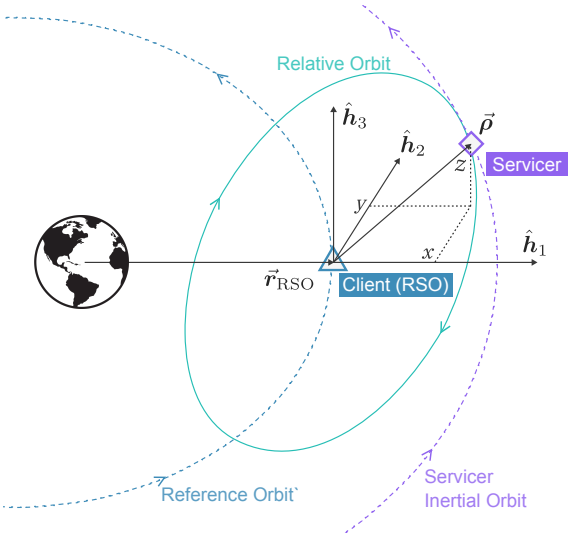

Figure 4-2: Illustration of a general spacecraft formation with out-of-plane relative motion.

The second most common parametrization used for formation design and modeling relative spacecraft dynamics is that of differential orbital elements, or simply the arithmetic difference between the servicer and reference orbital elements: $\delta \boldsymbol{oe} = \boldsymbol{oe}_{Servicer} - \boldsymbol{oe}_{RSO}$. This state representation is particularly useful for dynamics modeling in general due to the absolute orbital elements' slow rate of change, limited to the mean anomaly M or true anomaly f for unperturbed Keplerian motion, as compared to the relative Cartesian representation, which is composed of six so-called "fast variables" [124]. This thesis will specifically use the equinoctial variables as a set of orbital elements, $(a, \Psi, q_1, q_2, p_1, p_2)^T$, where a, Ψ, q_1, q_2, p_1, p_2 are defined in Equation (4.1) as follow:

$$\begin{aligned} a &= a \\ \Psi &= \Omega + \omega + f \\ q_1 &= e \sin(\omega + \Omega) \\ q_2 &= e \cos(\omega + \Omega) \\ p_1 &= \tan\left(\frac{i}{2}\right) \sin(\Omega) \\ p_2 &= \tan\left(\frac{i}{2}\right) \cos(\Omega) \end{aligned} \tag{4.1}$$

where a is the semimajor axis, Ψ is the mean argument of latitude, Ω is the right ascension of the ascending node, ω is the argument of perigee, f is the true anomaly, e is the orbit eccentricity, p_1 and p_2 are the orbit inclination vector components,and q_1 and q_2 are the eccentricity vector components. This set of equinoctial variables was chosen for its benefits of avoiding the singularity for circular orbits (when $e = 0$), equatorial

orbits (i.e., zero inclinations), as well as being extensively used throughout other bodies of work in the realm of relative spacecraft dynamics [47].

4.0.1 Formation Dynamics

This thesis leverages the analytical method developed by Gim and Alfriend [46], based on Brouwer's solution [19], which accommodates for an eccentric reference orbit and J_2 perturbation effects. While Brouwer's solution captures second-order secular and first-order periodic perturbations about a Keplerian reference orbit due to $J_2 - J_5$, the Gim-Alfriend (GA) method retains only the first-order secular J_2 terms. At the core of the GA method is the development of the state transition matrix (STM) for differential *mean* nearly non-singular equinoctial orbital elements given in Equation 4.2 below:

$$\delta\bar{\boldsymbol{oe}}_{nns}(t) = \bar{\boldsymbol{\phi}}_{J_2}(t, t_0)\delta\bar{\boldsymbol{oe}}_{nns}(t_0) \tag{4.2}$$

where $\delta\bar{\boldsymbol{oe}}_{nns} = (\delta\bar{a}, \delta\bar{\Psi}, \delta\bar{p_1}, \delta\bar{p_2}, \delta\bar{q_1}, \delta\bar{q_2}, \delta\bar{\Omega})^T$ represents the set of mean nearly non-singular differential equinoctial orbital elements of the servicer spacecraft with respect to the reference orbit; additionally, ($\bar{}$) and ($\tilde{}$) are used to distinguish between *mean* and *osculating* orbital elements. The GA method includes the full non-linear transformation between absolute mean and osculating elements,

$$\tilde{\boldsymbol{oe}}_{nns} = \bar{\boldsymbol{oe}}_{nns} - (J_2 R_e^2)\{\Delta\boldsymbol{oe}_{nns}^{(lp)} + \Delta\boldsymbol{oe}_{nns}^{(sp1)} + \Delta\boldsymbol{oe}_{nns}^{(sp2)}\} \tag{4.3}$$

the Jacobian for the mean to osculating transformation, $D(t)$:

$$D(t) = \frac{\delta\tilde{\boldsymbol{oe}}_{nns}}{\delta\bar{\boldsymbol{oe}}_{nns}} = I - (J_2 R_e^2)[D^{(lp)}(t) + D^{(sp1)}(t) + D^{(sp2)}(t)] \tag{4.4}$$

and Jacobian for the osculating differential orbital element to relative Cartesian Hill frame coordinates $(\boldsymbol{\rho}, \dot{\boldsymbol{\rho}})^T$:

$$\Sigma(t) \equiv \{A(t) + \alpha B(t)\} \tag{4.5}$$

where $\alpha = 3J_2 R_e^2$. The full GA STM for propagating the osculating relative Cartesian state in Hill frame coordinates is given by:

$$\Phi_{J_2}(t, t_0) = \{A(t) + \alpha B(t)\}D(t)\bar{\boldsymbol{\phi}}_{J_2}(t, t_0)D^{-1}(t_0)\{A(t_0) + \alpha B(t_0)\}^{-1} \tag{4.6}$$

where the analytical solution for the inverse of (4.5) is provided in the GA method and the first-order approximate inverse of (4.3)−(4.4) can be obtained by replacing J_2 with $-J_2$ in the Brouwer transformation and treating the osculating elements as the inputs [46, 7]. Equations (4.2)−(4.5) were modified to use the mean argument of latitude, Ψ, instead of the true argument of latitude, θ.

Finally, in order to include the control influence, $\boldsymbol{u}$, on the differential mean orbital elements, it can be

shown that

$$\delta\bar{\boldsymbol{\sigma}}\boldsymbol{e}_{nns}(t) = \bar{\boldsymbol{\phi}}_{J_2}(t,t_0)\delta\bar{\boldsymbol{\sigma}}\boldsymbol{e}_{nns}(t_0) + \int_{t_0}^{t} \bar{\boldsymbol{\phi}}_{J_2}(t,\tau)B(\tau)\boldsymbol{u}(\tau)d\tau \tag{4.7}$$

where $B(t)$ represents Gauss's variational equations (GVEs) evaluated on the reference orbit [118].

It is useful to note that, while this form of the GA method was used for the analyses throughout this thesis, there exist many alternative differential orbital elements-based formulations of the formation dynamics throughout the literature, as discussed in the introduction. Two variations of the GA method include the small-eccentricity version of (4.2)−(4.4) which can be used to save significant computational effort for formations in near-circular reference orbits, given by Alfriend and Yan [6]. The following sections will show how (4.7) is used to capture the formation dynamics during the control policy portion of the RPO missions, and the full GA STM from (4.6) is used to propagate the Hill frame relative Cartesian state-covariance for risk mitigation.

As a result, assuming that the differences between the Servicer's mean elements and the reference elements are small, the dynamics of the differential mean elements are found by linearizing Equation A.1 about the reference orbit:

$$\delta\dot{\bar{\boldsymbol{\sigma}}}\boldsymbol{e} = A\delta\bar{\boldsymbol{\sigma}}\boldsymbol{e} + Bu \tag{4.8}$$

The LQR is used to solve for the control solution of the feedback control system. The goal of this control strategy is to satisfy a feedback control law such that the minimum cost, $u_{final} = -kx$, is found, where k is the optimal gain matrix and x is the final state (goal).

4.1 Case Studies Framework

IQC analysis is applied to measure the robust performance of this LQR controller because it is capable of considering both numerous types of uncertainties and specifying characteristics of the system's exogenous disturbances. Analytical tools are used from the robust control literature [111] for such interconnections, and the approach is based on an IQC scheme for a robust control synthesis. The main research question can be divided into two and addressed in this section: (1) Is the system stable despite model uncertainties? and (2) Is the system robust despite model uncertainties and exogenous disturbances? Sensitivity studies are performed through IQC analysis to figure out worst-case magnitudes of uncertainties and disturbances for which the system is both unstable and weak. To answer the first question, controller weight matrices are tuned to stabilize a plant (i.e., Servicer) that considers first-order actuation model uncertainties. To answer the second question, IQC forward-reachability is used to inspect a high-value Client in LEO at 550 km. By performing this forward propagation through IQC, an uncertainty bound is found for reaching a desired state incorporating initial state uncertainty, satisfaction of an input/output performance metric, and

bounds for the physical disturbances of the environment in this orbital regime. The performance metric used is the L_2-induced norm chosen to account for the control effort performed by actuation (i.e., using cold-gas propulsion engines). An open-source library for operational flight dynamics applications (Orekit) [82] is employed to compare the designed control algorithms, using analytical formulas, with numerical propagation, which accounts for higher fidelity dynamics. Table 4.1 shows the Servicer specification. In addition, a debris object was added in these case studies to validate the IQC forward-reachability analysis framework.

Table 4.1: Servicer Specifications

Specifications	Values
Altitude	500 km
Initial Conditions (Cartesian/LVLH frame)	[0.0 m, -50.0 m, 0.0 m]
Uncertainty Initial Condition	X:[-0.0818 m, 0.020 m] Y: [-0.013 m, 0.013 m] Z: [-0.013 m, 0.013 m]
Alignment Error Bias Input	[0.10494 , 0 ,0, 0, 0.1049,0,0, 0,0.1049] deg^2,
Drag Coefficient	2.2
Mass	160 kg
Thruster Uncertainty	[-5% m/s^2 to 5% m/s^2]
Margin for uncertain orbital parameters due to 10% variation of geopotential	$\|\|10^{-3}\|\|$
Margin for Atmospheric Drag Uncertainties (m/s^2)	Drag is too small to be considered due to RPO mission duration (i.e., hours)

The Servicer inspecting the Client is assumed to have a dry mass of 160 kg, a drag coefficient of 2.2, and a drag area of 3 m^2. It is equipped with eight thrusters, including a mix of cold-gas and ion/Hall thrusters, to control movement in positive and negative directions along each axis. When making orbit corrections around the NMC, the Hall thrusters can deliver full thrust ranging from 392 to 397 mN at 6 kW, with a specific impulse of 100 seconds, offering fuel-efficient propulsion for orbit control. During guidance algorithm operations, cold gas is used, and a +/- 5% uncertainty in thruster output is assumed.

To compute the highest exogenous acceleration vectors affecting the controller at this orbital altitude, perturbation equations from [50] can be applied: Equation (16) for atmospheric drag and Equations (48-50) for the perturbing force due to Earth's oblateness (J_2). The NRLMSISE-00 density model [105] is utilized for maximum density calculations, using the solar and geomagnetic indices from the well-known Halloween storm condition in 2003 [49].

It is important to note that the linearized and averaged equations of motion neglect some terms. The Earth's gravity magnitude is 10^{-2}, and the J_2 term is 10^{-5}. The latter is a thousand times smaller, and as the gravity analytical expression only captures first-order J_2^2 terms, it becomes another thousand times smaller. Thus, the acceleration component due to the J_2 variation that is being ignored has a magnitude of $10^{-}8$ km/s^2. Table 4.2 shows the types of disturbances, uncertainties, and nonlinearities that were taken into account in the case studies presented in this chapter.

Table 4.2: IQC characterization of disturbances and uncertainties affecting LQR controller

Name of disturbances, uncertainties and nonlinearities (units)	Worst magnitude	IQC characterization
Sensor Noise (in hz)	White signal	IQC white class
Uncertain states (m)	$x_o = \Delta_3$	IQC $\Delta_{operator}$
Actuation uncertainty	$\Delta_3 = +/- 0.05$	IQC $\Delta_{actuation}$
Alignment error (deg^2)	Table 4.1	IQC Δ_{bias}

If the RPO mission were to last for an extended period (e.g., weeks or months), atmospheric drag would have a significant impact on the controller. The worst-case differential magnitudes' absolute values can be calculated, as referenced in [55], assuming the Client has a drag coefficient of 2.2 and a drag area of 5 m^2. Furthermore, uncertainty bounds were established under the premise that these perturbations affect the Servicer in both positive and negative directions. As atmospheric drag is highly diurnal and strongly influenced by solar activity, this disturbance can be modeled as a static LTI product. The Δ operator is used to constrain the actuation approximation error by a scalar κ, such that the L2-norm of Δ is less than or equal to κ. The disturbances influencing attitude control were taken from [75] and modeled as alignment error, as displayed in Table 4.1.

All the disturbances, uncertainties and nonlinearities caused by the geopotential model are characterized with the IQC operators. Nonlinearities due to neglected higher-order geopotential perturbations and periodic motion effects. The exogenous refer to the disturbances by atmospheric drag, gravity gradient effects, and solar pressure effects. Other characterization include the lidar model noise uncertainty and the actuation uncertainty based on selected actuation devices (e.g., cold-gas, ion engines, chemical propulsion).The nonlinearities due to Lagrange Planetary Equations (LPEs) dynamics approximation, and other uncertainties and disturbances can be captured with IQC theory.The reference trajectory uses a semi-analytical approximation in LPEs model neglects higher-order geopotential terms and first-order periodic terms (order J_2). The error in LPEs approximation model neglects geopotential terms and periodic of order up to $||10^{-3}||$. Figure 4-3 shows the overall framework of the IQC-based reachability method.

Equation 4.9 describes this characterization:

$$\begin{cases} \dot{x} = f(x(t)) + g(x(t))(u(t) + w(t)), \quad x(0) = x_0 \\ w = \Delta(u)(t) \end{cases} \tag{4.9}$$

where x $\in X \subseteq \mathbb{R}^n$ is the state u $\in U, \subseteq \mathbb{R}^m$ is the input, $f : X \times U \to X$ is the flow map (which it is assumed to be locally Lipschitz in x and u), and $g : \mathbb{R}^n \to \mathbb{R}^{m \times n}$ is also assumed to be locally Lipschitz.

4.1.1 Weight Tuning Algorithm

In regard to the first research question about the stabilization of the controller, Algorithm 1 was developed to tune the weight matrices, R_u and R_x, of the LQR scheme. State errors and control efforts were penalized given model uncertainties and performance criterion (J$\geq$ 0). As stated in Table 4.2, the actuation uncertainties as $\Delta_x = 0.05$, $\Delta_y = 0.05$, $\Delta_z = 0.05$ were assumed for utilization efficiencies described for cold-gas and Hall/ion

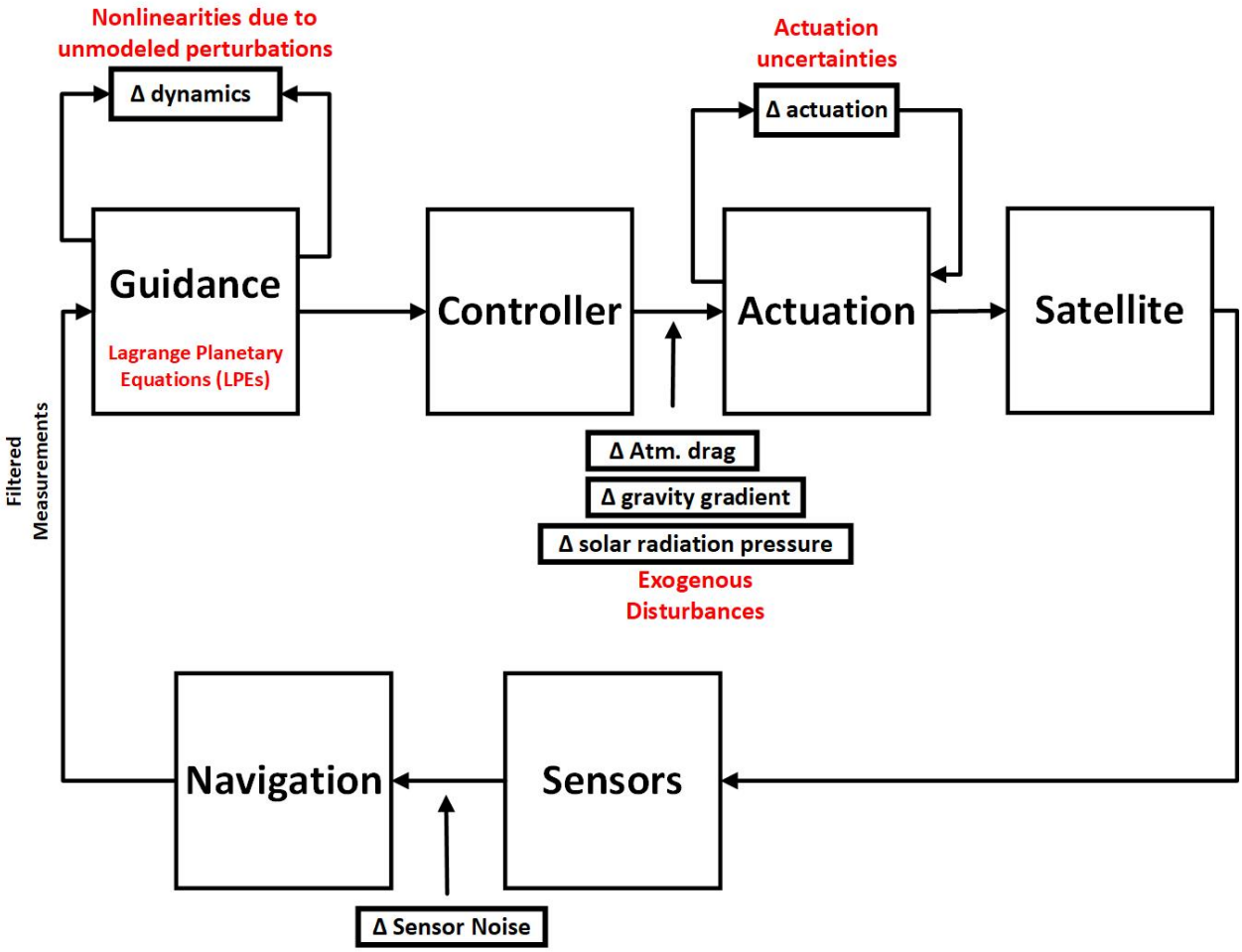

Figure 4-3: Illustration of the IQC framework capturing model disturbances, uncertainties & nonlinearities (J_2).

engines. These uncertainties represent thruster output in relation to commanded thrusts versus actual thrust values as shown in Figure 4-4.

The overall system model is balanced using the `balreal` function in MATLAB to compute a reduced-order approximation of the linear time invariant (LTI) model, thus helping to solve this ill-conditioned system. A modified procedure was implemented from [39] for tuning these matrices within the LQR control scheme and analyzed via the proposed IQC analysis framework.

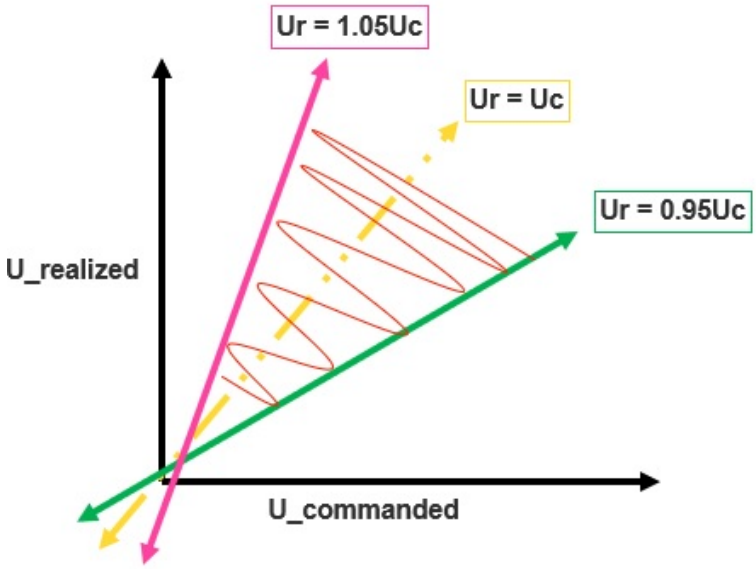

Figure 4-4: Actuation uncertainty. Uncertainties are shown in the radial, in-track and cross-track components.

Maximum units of 1 for each penalizing variable (α and β) were assumed. The minimum penalization variables for the required stabilization of the system are obtained as $\alpha = 0.2$ and $\beta = 1$ for the final controller. Figure 4-5 describes the case studies presented in this section where the Servicer trajectory is shown in a relative motion with respect to Client while considering a obstacle region. The obstacle is located at [-10 m, -35 m, 0 m] on the Cartesian plane.

The following case studies are considered in the next section:

- Case Study#1 focuses on IQC-based reachability to determine the worst-case state output of the Servicer during direct approach while considering a obstacle region and a trapezoidal guidance law.

- Case Study #2 focuses on IQC-based reachability during inspection phase (closest approach/attitude pointing requirements to Client).

4.2 IQC-based Reachability for RPO Mission

The following case studies will show the characterization of uncertainties and nonlinearities that are not currently captured in RPO control design. This characterization is performed by applying integral quadratic constraints to forward-reachability methods during maneuver phases of RPO missions.

Algorithm 1 IQC Analysis for tuning R_x and R_u

Require: Stable system $\dot{x}$=f(x,u,Δ)
Ensure: J $\geq$ 0
  α_0=0.1, β_0=0.1
  Δ_{x-y-z} =+/-0.5
  $R_x = \alpha I_{6,6}$
  $R_u = \beta I_{6,3}$
while Stable = False **do**
  if $\alpha < 1$ **then**
    $\alpha_0 + 0.01$
    if Stable=True **then** *StopLoop*
      if $\alpha = 1 \& \beta < 1$ **then** β_0+0.01,$\alpha = 0.1$
        if Stable=True **then**
          Stop Loop

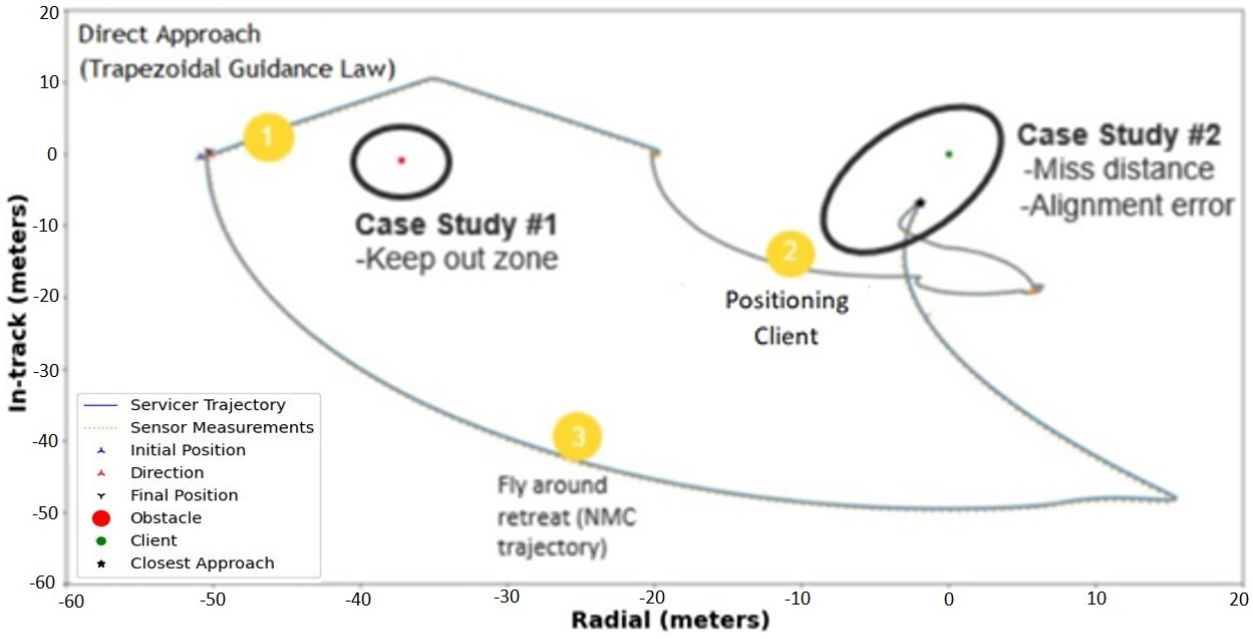

Figure 4-5: Servicer trajectory in relative motion with respect to Client (IR-plane)

4.2.1 Case Study 1: IQC-based Reachability during Direct Approach Phase (Collision Avoidance of Space obstacle)

The 3D Servicer trajectory for the entire duration of an RPO mission, 2D projections, sensor measurements from a lidar sensor, an obstacle region, and the Client are shown in Figure 4-6. The goal of this section is to verify control robustness such that the Servicer trajectory satisfies a keep-out zone (r_{min}) away from the

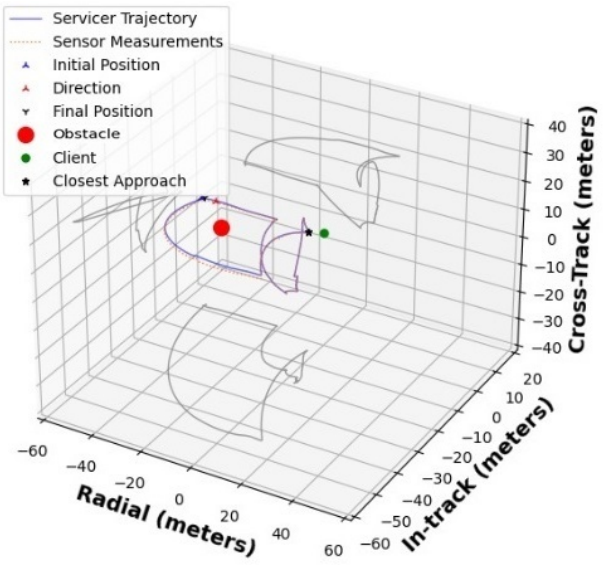

Figure 4-6: Servicer trajectory in relative motion with respect to Client (IR-plane)

obstacle region. The keep-out zone chosen for these case studies is 4 m radius centered around the obstacle as shown in Figure 4-7.

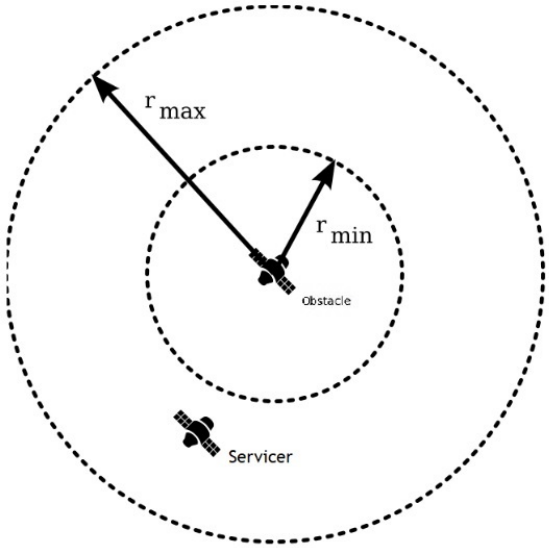

Figure 4-7: Keep-out Zone (KOZ) of Servicer to Client.

Because the obstacle object is located at [-10 m, -35 m, 0 m] and the Servicer at [0 m, -50 m, 0 m], a trapezoidal guidance law is designed to get closer to the Client during the direct approach maneuver. The Servicer then follows an inspection phase: positioning and closest approach maneuvers, and finally a retreat phase. First, the controller output is verified by comparing the reference trajectory with the truth dynamics modeled using numerical propagation as shown in Figure 4-8.

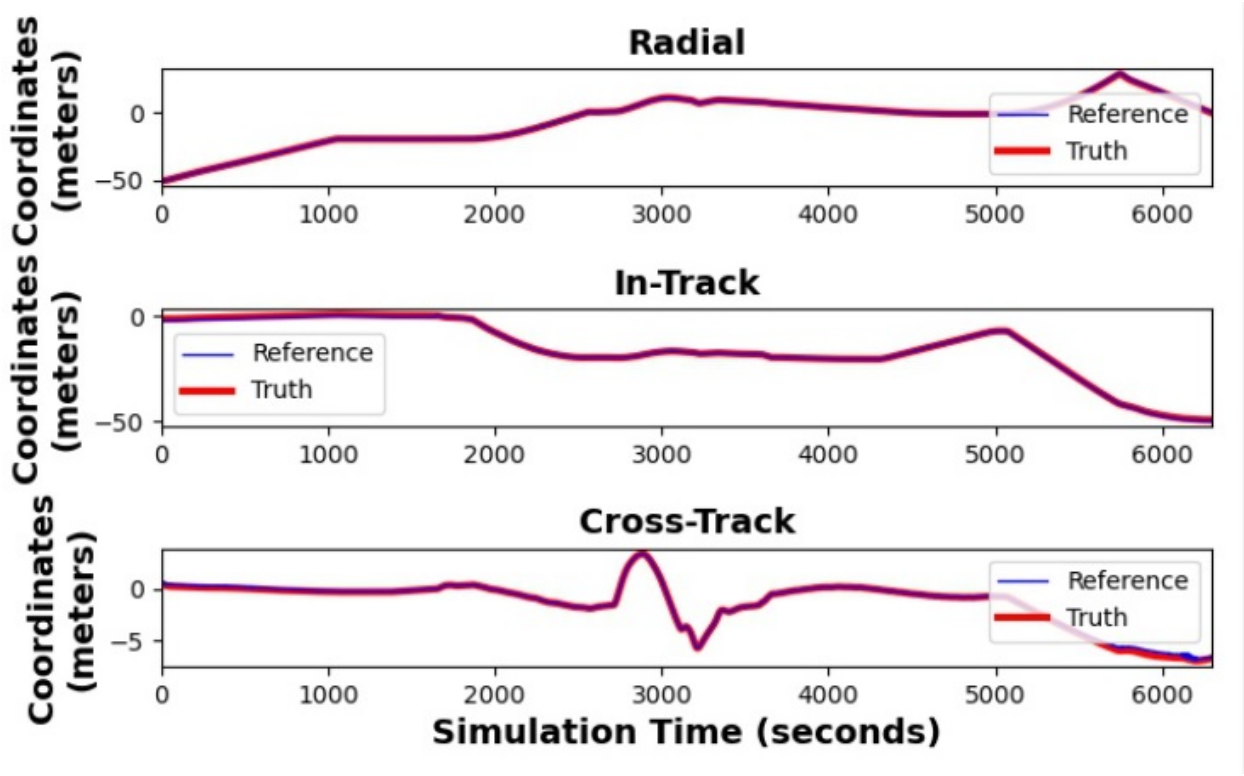

Figure 4-8: Reference vs. Truth trajectories.

The truth trajectory was generated using Orekit embedded in the control scheme. The reference is driven by Lagrange's analytical dynamics and embedded in two control laws: (1) a dV control law for reaching a desired trajectory, and (2) a closed-loop LQR control law for correcting state error. The errors between the reference and truth trajectories are shown in Figure 4-9.

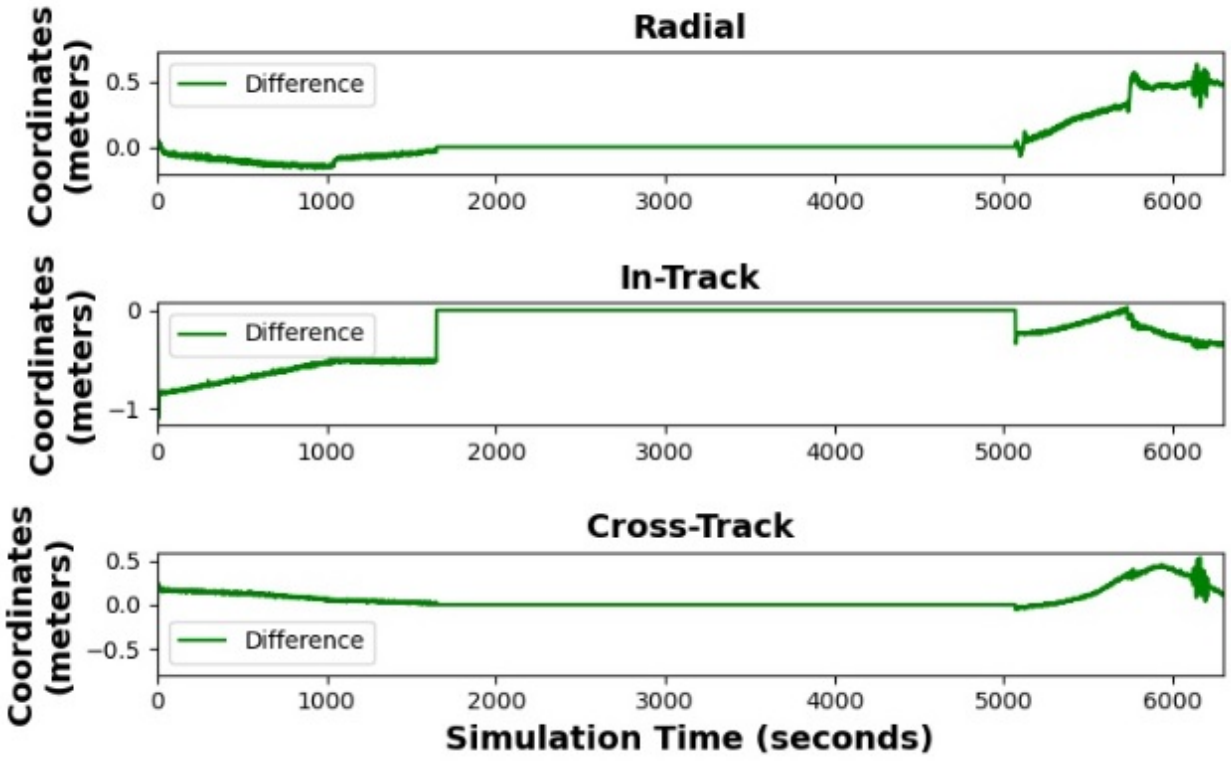

Figure 4-9: Difference (Reference vs. Truth) in trajectories.

4.2.2 Collision Avoidance Maneuver

Dispersion analysis was conducted by running 1000 trajectories of a trapezoidal guidance law via Monte Carlo runs. Figure 4-10 shows how these trajectories disperse and the IQC worst-uncertainty bound (green) grows at the time of closest approach (TCA) to the obstacle region, as shown in Figure 4-10.

The initial conditions and TCA to the obstacle can be seen in Figure 4-11. The distance variation of the initial condition and closest approach to the obstacle can be shown in Figure 4-12. The types of disturbances and uncertainties that were accounted for in the case studies presented in this chapter are broken down into uncertainty groups as shown in Tables 4.3, 4.4, and 4.5.

Table 4.3: Final Position's best/worst coordinates from mean-Truth and Cartesian distances for 1000 MC runs. The MC and IQC runs considered initial conditions and sensor noise uncertainties.

Metric	Radial (meters)	In-track (meters)	Cross-track (meters)	Cartesian distance (meters)
Best distance	-10	0.5	-0.8	10.04
Worst distance	-7	-0.3	0.3	7.01
IQC bound [+/−] from mean	[-12, -11]	[-0.1, 1.5]	[0.1,2]	[6.8,10.3]

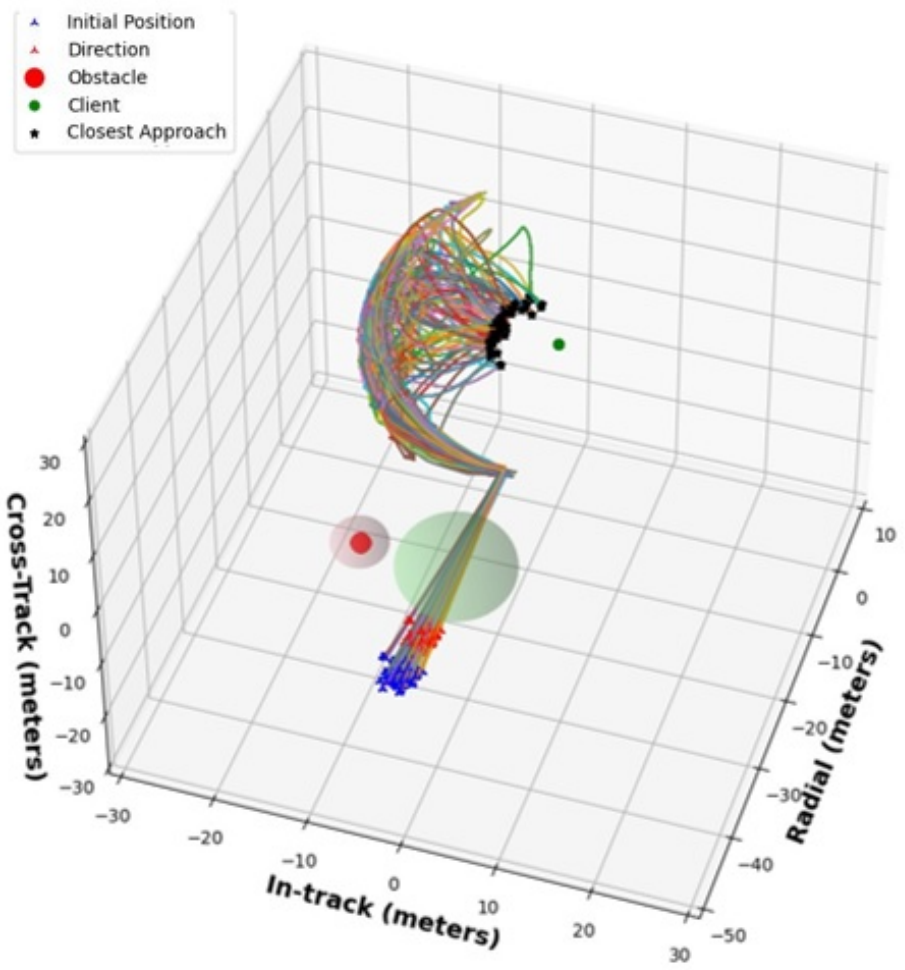

Figure 4-10: 1000 trajectories of Servicer in relative motion with respect to Client and IQC-worst case uncertainty bound (green sphere) at TCA to obstacle.

Table 4.4: Final Position's best/worst coordinates from mean-Truth and Cartesian distances for 1000 MC runs. The MC and IQC runs considered initial condition, sensor noise, and orbital parameters uncertainties.

Metric	Radial (meters)	In-track (meters)	Cross-track (meters)	Cartesian distance (meters)
Best distance	-0	-0.77	0.9	9.1
Worst distance	-13	1	-1.5	8.2
IQC bound [+/−] from mean	[-10, -14]	[-1.5, 1.5]	[0.5,2]	[7,13]

Table 4.5: Final Position's best/worst coordinates from mean-Truth and Cartesian distances for 1000 MC runs. The MC and IQC runs considered initial conditions, sensor noise orbital parameters, and thruster output uncertainties.

Metric	Radial (meters)	In-track (meters)	Cross-track (meters)	Cartesian distance (meters)
Best distance	-10	-0.99	0.9	11
Worst distance	-13	1	-1.5	9
IQC bound [+/−] from mean	[-10, -14]	[-1.5, 1.5]	[0.5,2]	[7,13]

The worst values of MC runs can be compared with the IQC bounds as shown in Figure 4-13. Figure 4-14 shows the time of closest approach, the distance of closest approach to the obstacle, and Monte Carlo run

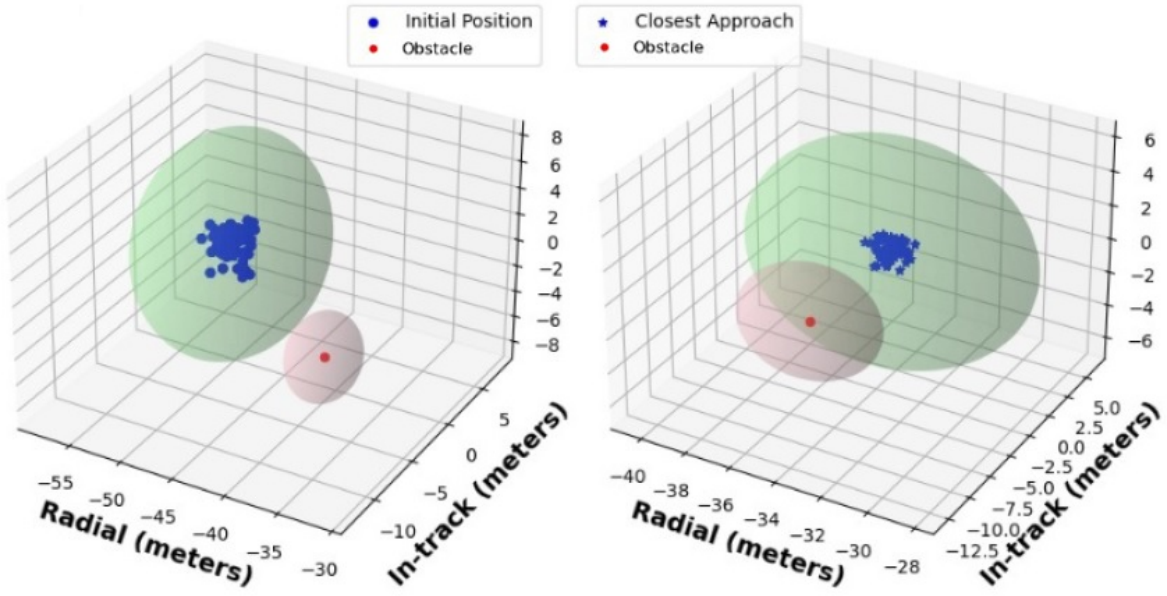

Figure 4-11: Variation of initial conditions and TCA to obstacle during the direct approach phase. 1000 trajectories were generated for this dispersion analysis.

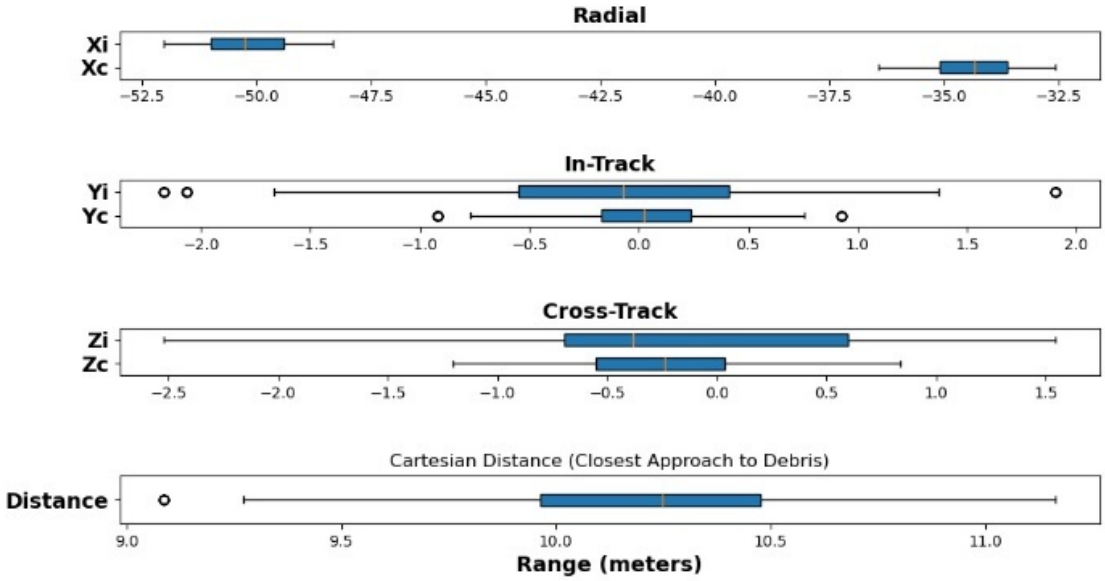

Figure 4-12: Dispersion analysis of uncertain initial and closest positions to obstacle during 1000 MC runs.

numbers associated with each trajectory. The figure shows that the closest approach trajectories vary from 9 meters to 11 meters and TCAs vary from 500 seconds to 600 seconds. The Monte Carlo runs considered uncertainties in the initial condition, sensor noise, state parameter, and actuation devices as shown in Table 4.2.

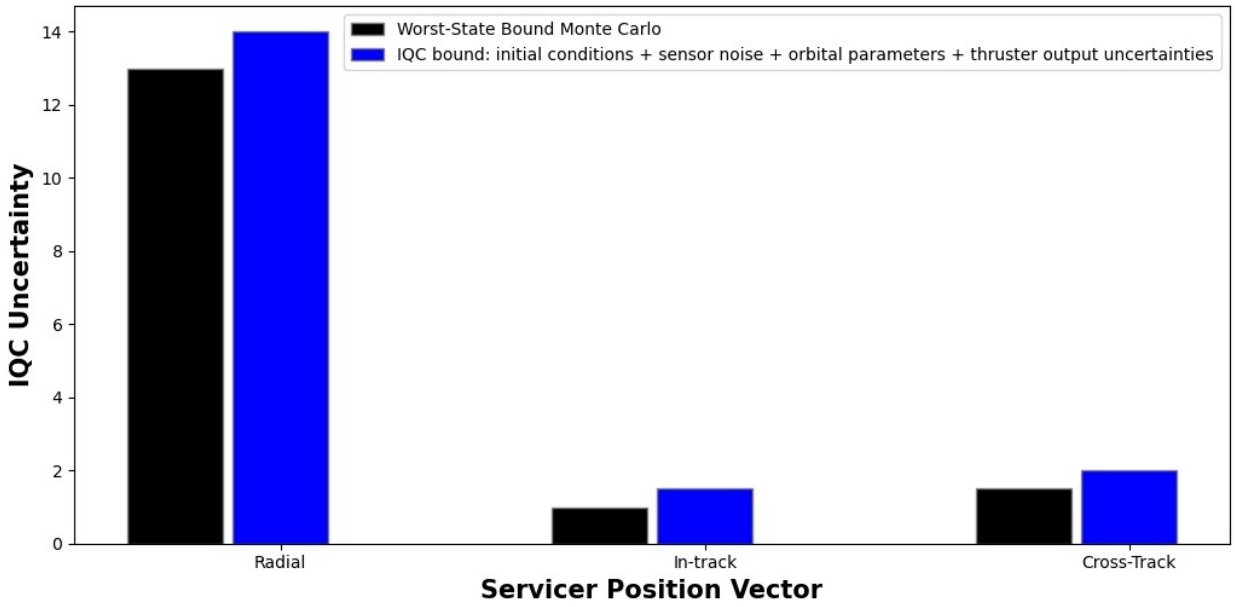

Figure 4-13: Comparison of MC runs vs. IQC bounds capturing all uncertainties and nonlinearities.

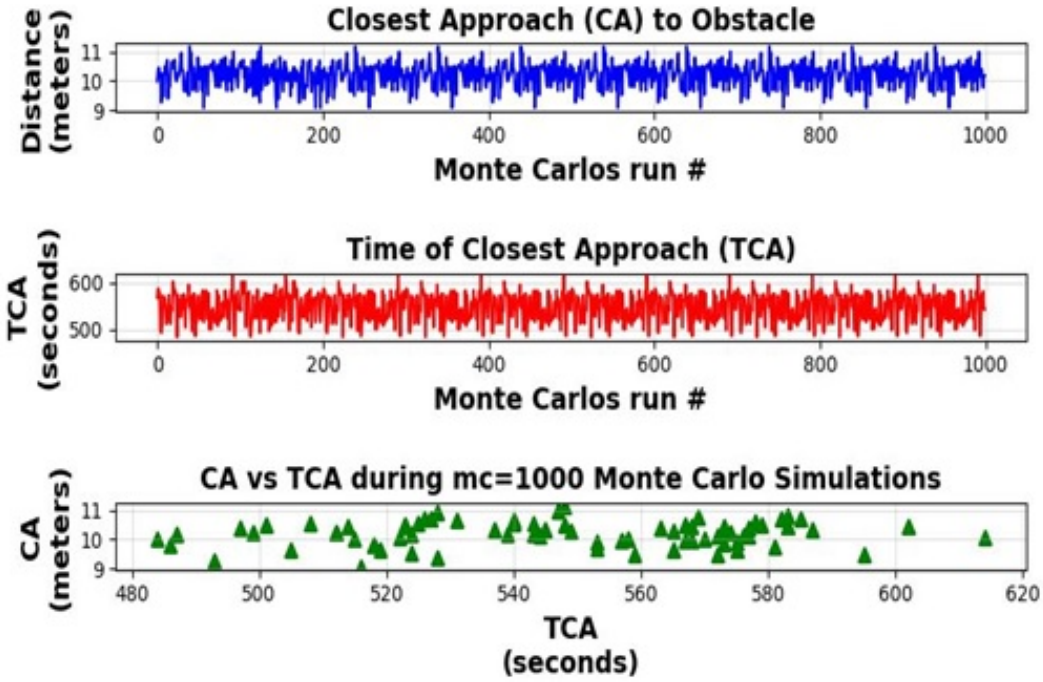

Figure 4-14: Analysis of Servicer closest approach to obstacle object for mc=1000 Monte Carlo simulations.

The IQC generated the worst-state uncertainty bound at TCA to obstacle object and can be seen more closely in a 2D-projection as shown in Figure 4-15. IQC bounds show a more conservative result than MC runs but they guarantee that the bound at a TCA will not be violated over time.

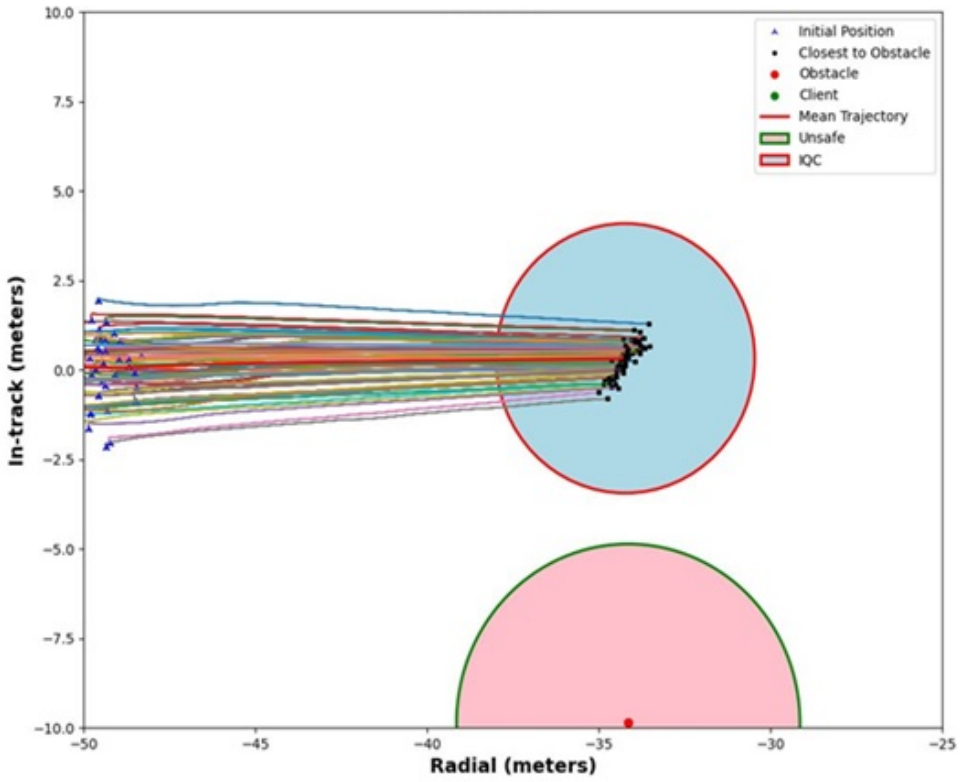

Figure 4-15: Analysis of Servicer during closest approach to obstacle for mc=1000 Monte Carlo simulations and IQC bound at TCA to obstacle.

The same 1000 trajectories are broken down into three components and analyzed via the IQC reachability method. The radial, in-track, and cross-track coordinates are shown with the worst-case uncertainties for the entire duration of the RPO mission: Figure 4-16 shows the radial component, 4-17 shows the in-track component, and 4-18 shows the cross-track component. The three plots show the IQC uncertainty bounds throughout the mission.

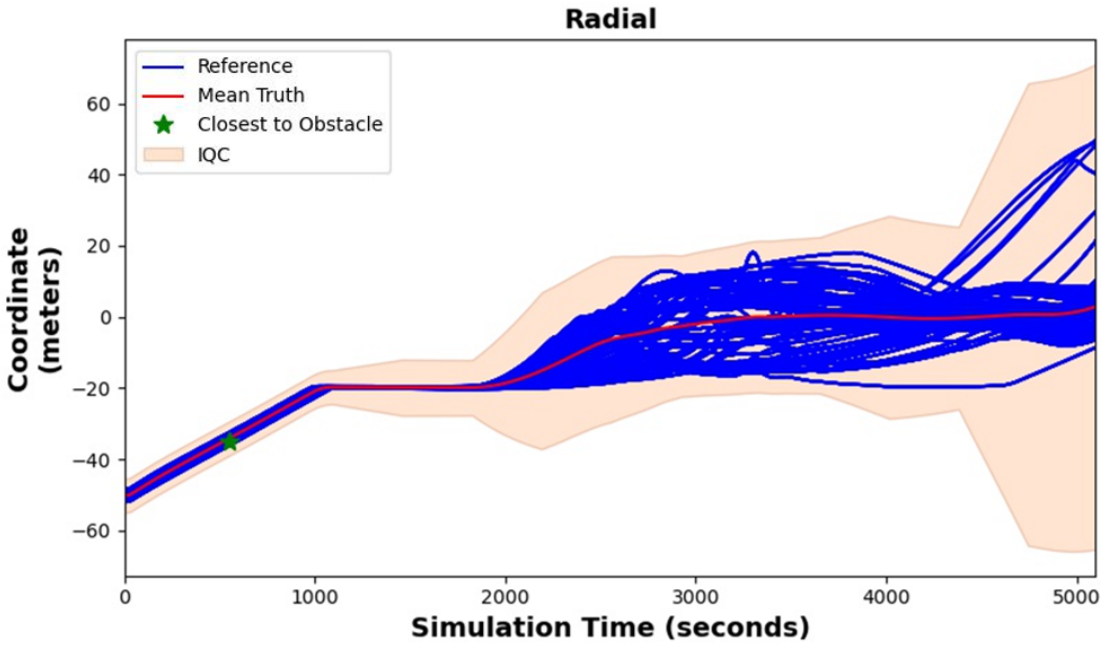

Figure 4-16: Radial component with IQC bounds for the whole duration of the simulation.

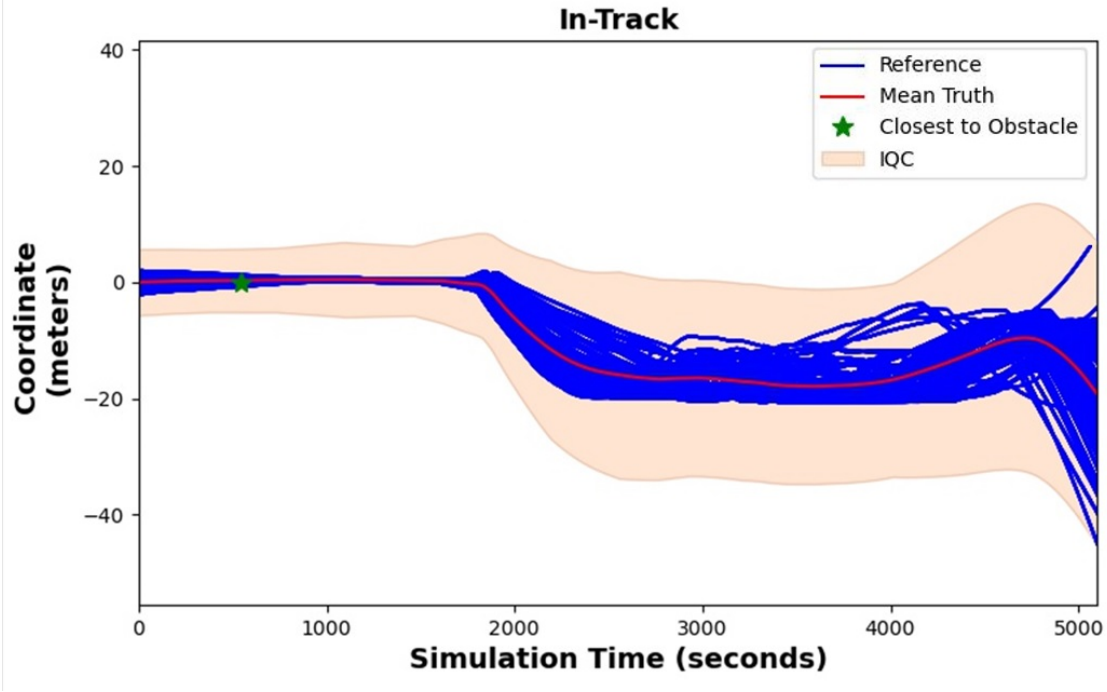

Figure 4-17: In-track with IQC bounds for the whole duration of the simulation.

These plots confirm that IQC bounds can generate worst-state case output for each component while capturing various sources of uncertainty and nonlinearities of current RPO GN&C systems. Table 4.6 shows Monte Carlo results for the worst coordinates on each axis and confirmed that Cartesian distances do not

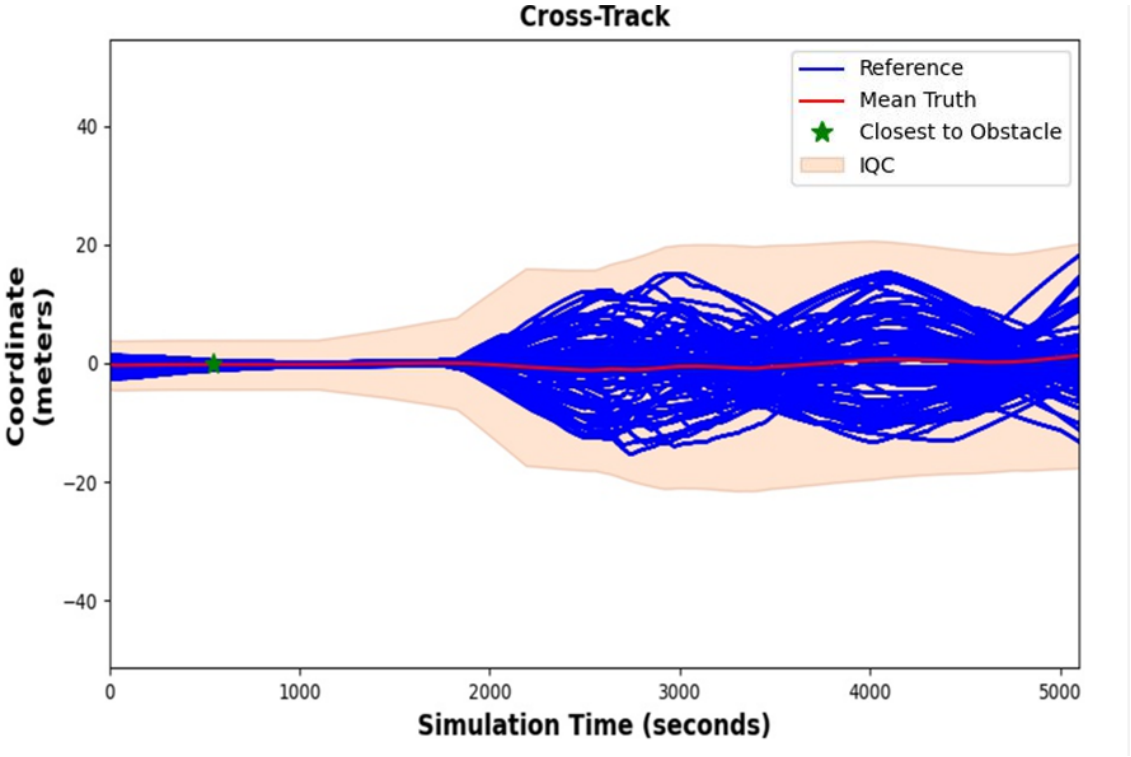

Figure 4-18: Cross-track with IQC bounds for the whole duration of the simulation.

exceed the bounds found by the IQC reachability method. In addition, the IQC enables the calculation of worst-state performance much faster than Monte Carlo runs. This table also shows IQC-bounds for various uncertainty groups and compares computational time of two reachability methods: IQC and MC. A desktop computer with an iCore I7-11700k and 3.4 GHz speed was used to generate these results.

Table 4.6: Comparison of IQC uncertainty groups for Servicer position and computational times (IQC-reachability and MC runs.)

Uncertainty Type	MC Computational Time	MC IQC Computational Time
Noise and initial condition (IC)	1w 1d 15h 12m 45s 240ms	2d 0h 33m 24s
Noise, IC, and orbital parameters (OP)	1w 1d 17h 26m 17s 240ms	2d 3h 5m 5s
Noise, IC, OP, and thruster output	1w 1d 19h 12m 15s 120ms	2d 3h 12m 1s

As a result, IQC bounds generation takes less time to compute than Monte Carlo runs (less than 5 days of computational time difference). This is because IQC bounds the uncertainties as integral quadratic constraints while solving for the worst-state magnitudes through Ricatti equations. Monte Carlo runs stochastically sample the whole trade-space without any guarantee of computational efficiency or robustness. The next subsection will show the analysis conducted for the inspection phase of this RPO mission.

4.2.3 Case Study 2: IQC-based Reachability during Inspection Phase (Closest Approach/Attitude Pointing Requirements to Client)

This second case study includes an analysis of the Servicer getting closer to the Client with the goal of performing an inspection. The closest approach is examined as well as Servicer pointing requirements with respect to the Client. Figure 4-19 shows the inspection phase in the In-track, Radial (IR)-plane. The research goal of this inspection phase is to characterize the position of the Servicer as well as its attitude pointing along the trajectory with respect to the Client during the maneuvers phases of this RPO mission. The IQC-reachability method is validated with MC runs as shown in Figure 4-20.

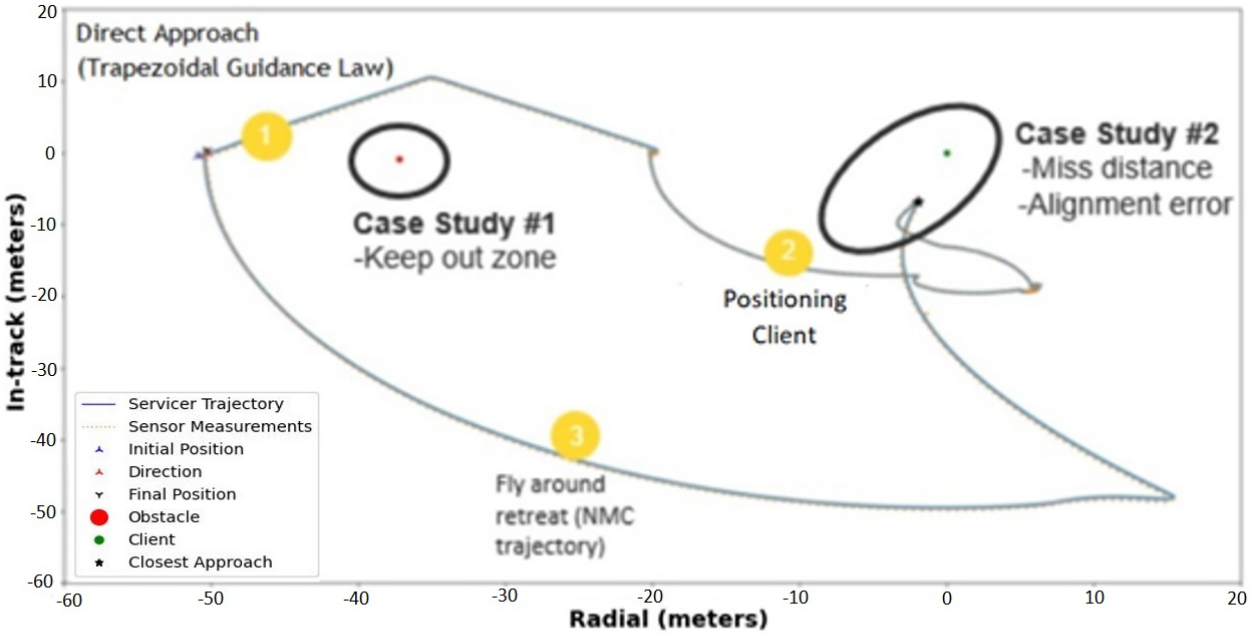

Figure 4-19: Inspection of Client. Trajectory of Servicer in relative motion with respect to Client. MC=1 run.

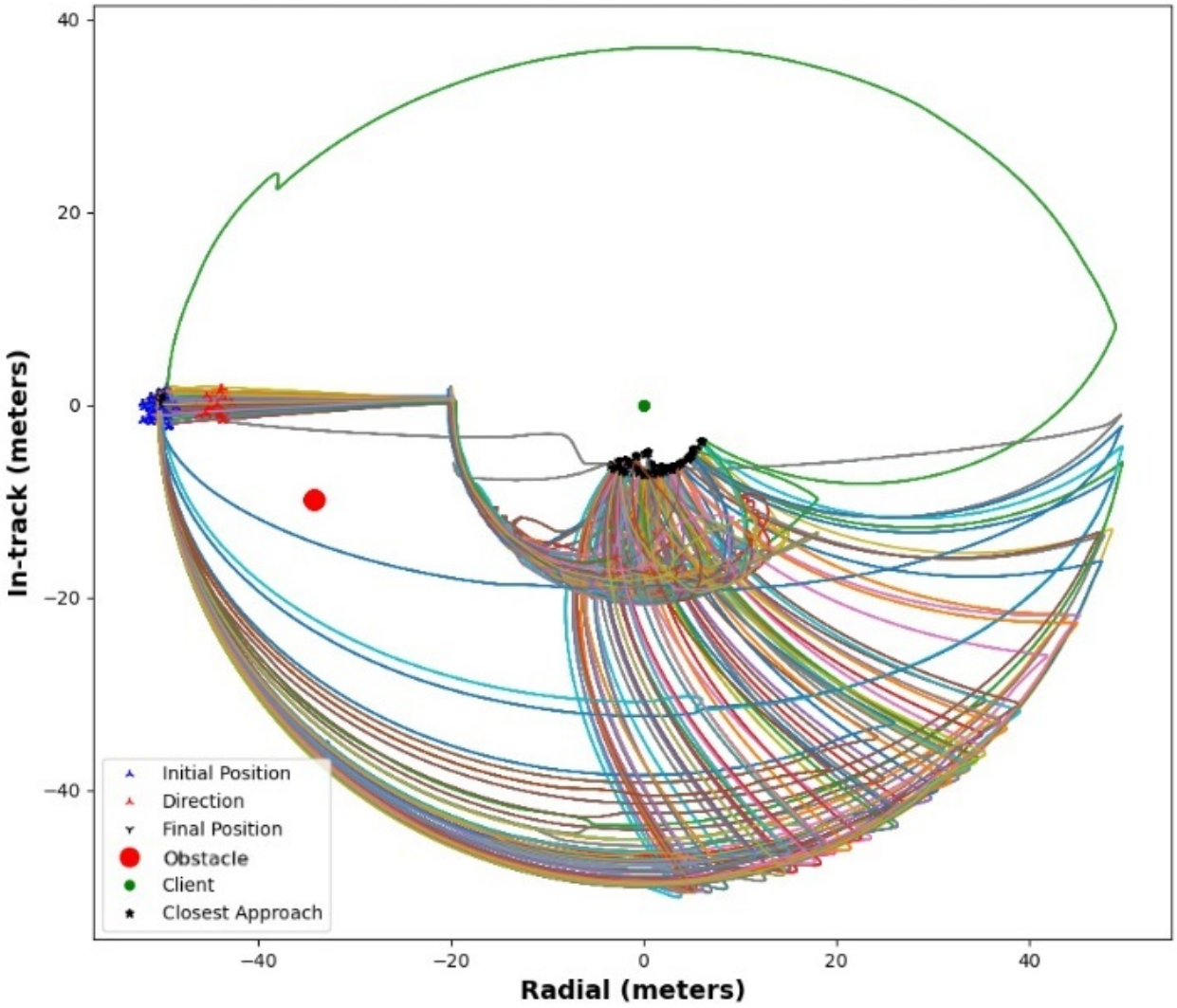

Figure 4-20: Inspection of Client. Trajectory of Servicer in relative motion with respect to the Client. MC=1000 runs.

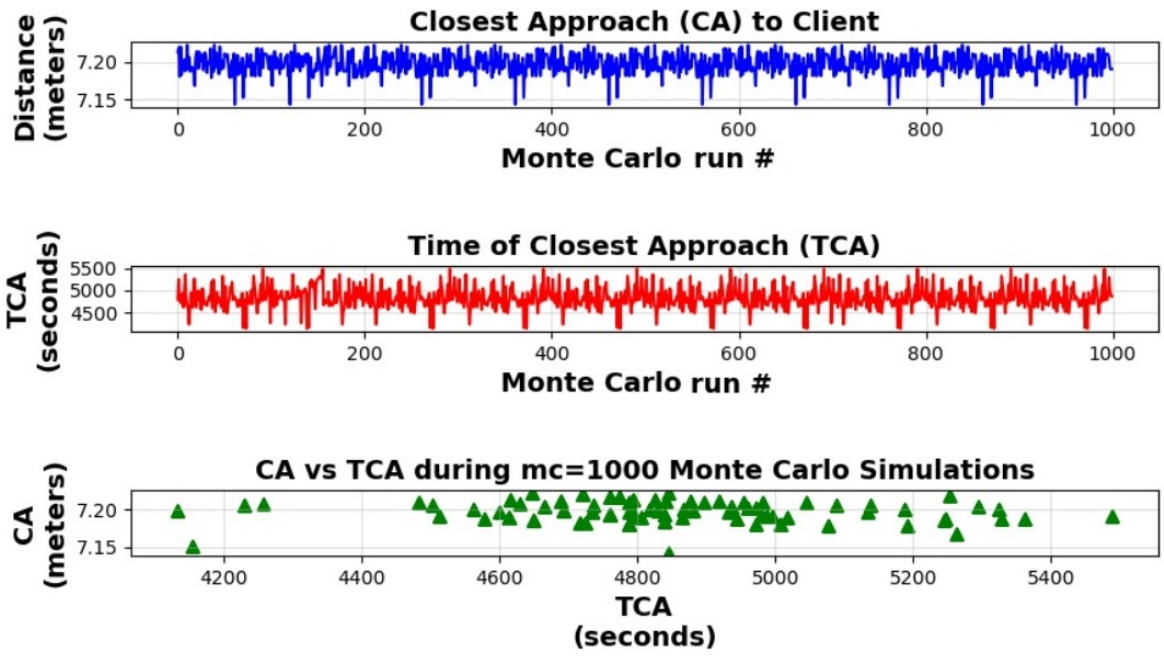

Figure 4-21: Analysis of Servicer closest approach to Client object for MC=1000 Monte Carlo simulations.

The position uncertainty was already characterized in the previous section. Consequently, Figure 4-21 shows the closest approach trajectories to the Client, TCA, and associated Monte Carlo run numbers. As shown in the figure above, the closest approach varies from 7.15 *meters* to 7.20 *meters* and the TCA varies from 4500 *seconds* to 5,500 *seconds*. The variation of the initial conditions and the closest approach trajectories can be seen in Figure 4-22.

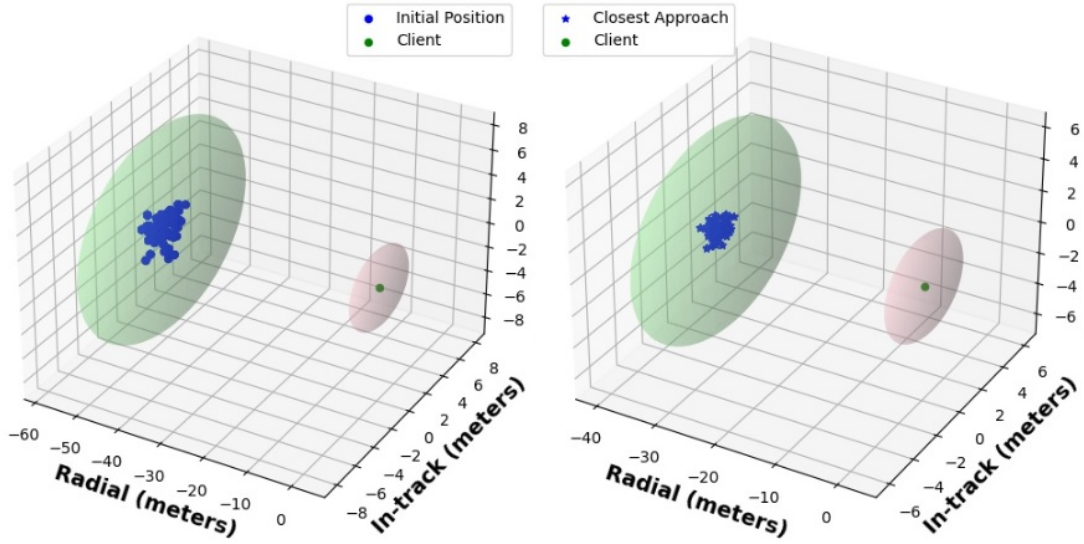

Figure 4-22: Variation of initial conditions and TCA to the Client object during the direct approach phase. 1000 trajectories were generated for this dispersion analysis.

The distance variation of the initial condition and closest approach to Client object can be seen in Figure 4-23 below:

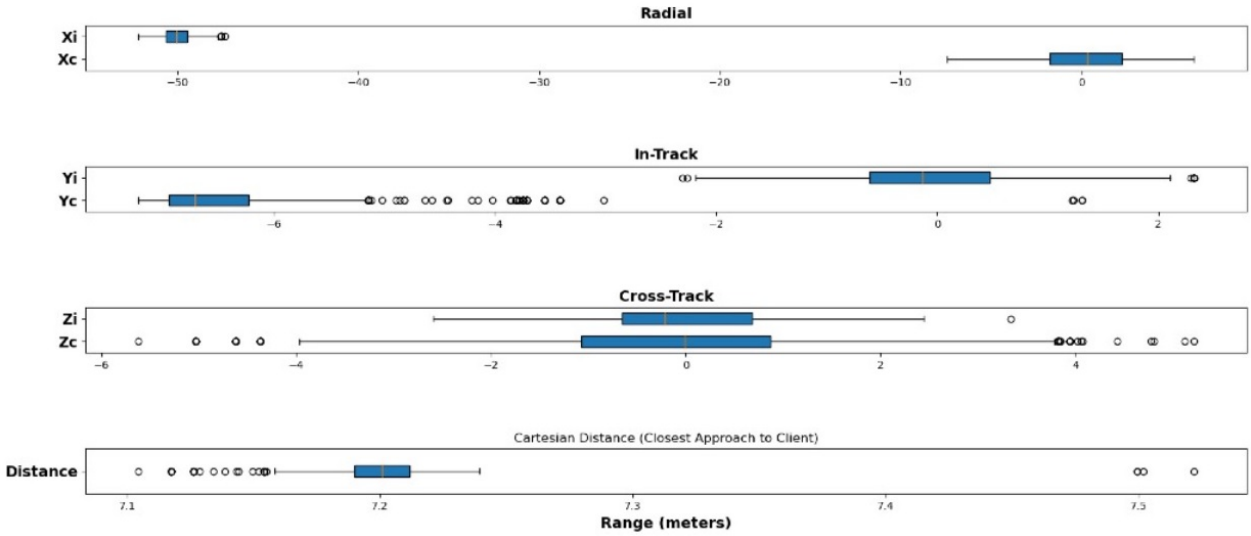

Figure 4-23: Dispersion analysis of uncertain initial and closest positions to the Client during 1000 MC runs.

Table 4.7: Phases of RPO Mission for MC=1 run. Total Duration:1.94 hrs [143].

Phases	Time Duration (seconds)
Direct Approach	[0-1000]
Inspection Mode	[1200-1700]
Positioning	[1700-4100]
Closest Approach	[4100-5700]
Retreat	[5700-7000]

The attitude pointing will be divided among maneuver phases, and each phase will be characterized as shown in Table 4.7. The IQC reachability framework was also used to propagate attitude dynamics using quaternions, which are used to represent a system that extends the real number into a four-dimensional domain and used to describe rotations of coordinate systems. The purpose of using this system is to remove singularities such as the loss of a degree of freedom in a rotation system (e.g., gimbal lock [56]).

4.2.4 Feedback Proportional Derivative (PD) for Attitude Control

The desired attitude maneuver is a combination of a Client pointing together with a slewing maneuver, to continuously reorient the Servicer to be able to follow the Client. The desired pointing is achieved when the Servicer body frame is aligned with the LVLH reference frame with respect to the Client body. The control law to model the actuators that produce the requested torque is based on a quaternion proportional and derivative control law, as shown in Equation (4.10).

$$u_{id} = -k_p \frac{dH(q_0)}{dq_0} - k_d \omega_{BT} \tag{4.10}$$

where q_e represents the quaternions error vector, q_0 is the scalar component of the quaternion vector, $H(q_0)$ is a function that satisfies the Lyapunov stability theorem, whereas k_p and k_d are the proportional and derivative gains, respectively. These quantities are selected to satisfy the time requirement and the pointing accuracy of the RPO mission. Reaction wheel modeling is outside the scope of this thesis.

The control solution of the quaternion output is then transformed into roll, pitch, and yaw Euler angles. The conversion from small roll-pitch-yaw Euler angles to the vector part of the corresponding error quaternion is described in Equation (4.11)

$$(q_1, q_2, q_3)^T = \frac{1}{2} \begin{bmatrix} 0 & 0 & 1 \\ 0 & 1 & 0 \\ 1 & 0 & 0 \end{bmatrix} [\theta_{roll}, \theta_{pitch}, \theta_{yaw}]^T \tag{4.11}$$

where θ_{roll}, θ_{pitch}, and θ_{yaw} represent the roll, pitch, and yaw angles. The body frame of this rotation can be seen in Figure 4-24. Consequently, the IQC-worst angle uncertainties are compared with dispersed results from Monte Carlo runs throughout the RPO mission phases.

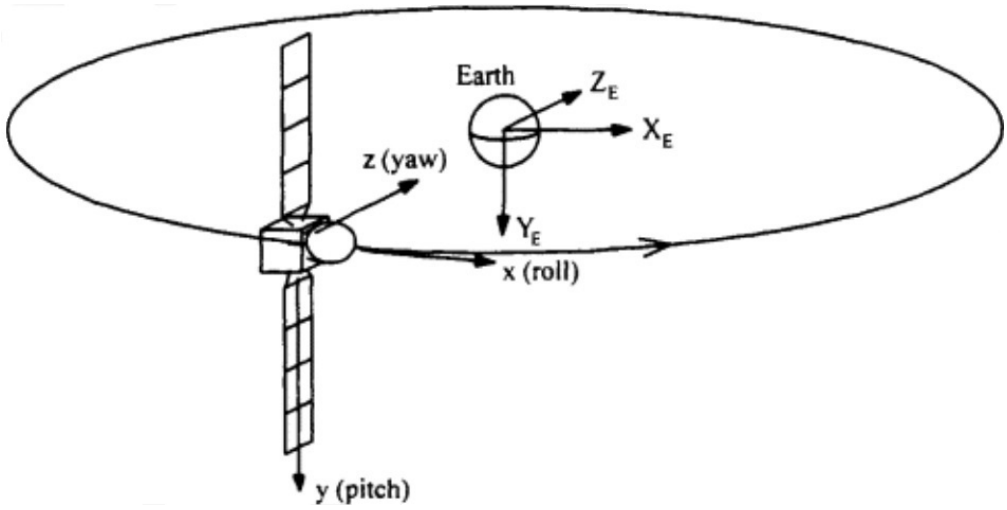

Figure 4-24: Spacecraft attitude in body frame

Figure 4-25, Figure 4-26, and Figure 4-27 below show the attitude pointing for the direct approach maneuver for each Euler angle. In this phase, attitude is controlled in all axes to maintain pointing towards a Client in LVLH frame. For the roll angle during the direct approach maneuver, see Figure 4-25.

For pitch angle during the direct approach maneuver, see Figure 4-26. For yaw angle during the direct approach maneuver, Figure 4-27. Similarly, Figure 4-28, Figure 4-29, and Figure 4-30 show the attitude pointing during the inspection phase. All angles are controlled to point directly at the Client in LVLH frame. For roll angle during the inspection maneuver, see Figure 4-28.

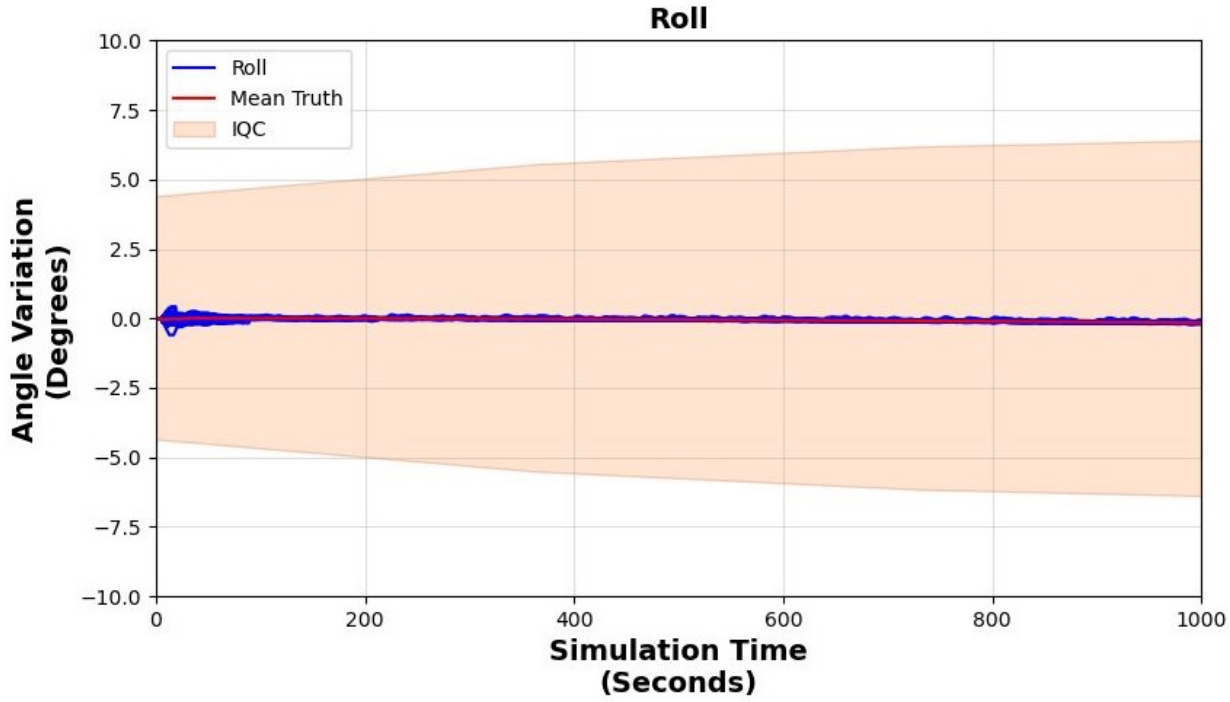

Figure 4-25: Servicer Roll Angle alignment with respect to Client during phase 1: direct approach (t=0s to 100s) for MC=1000 runs.

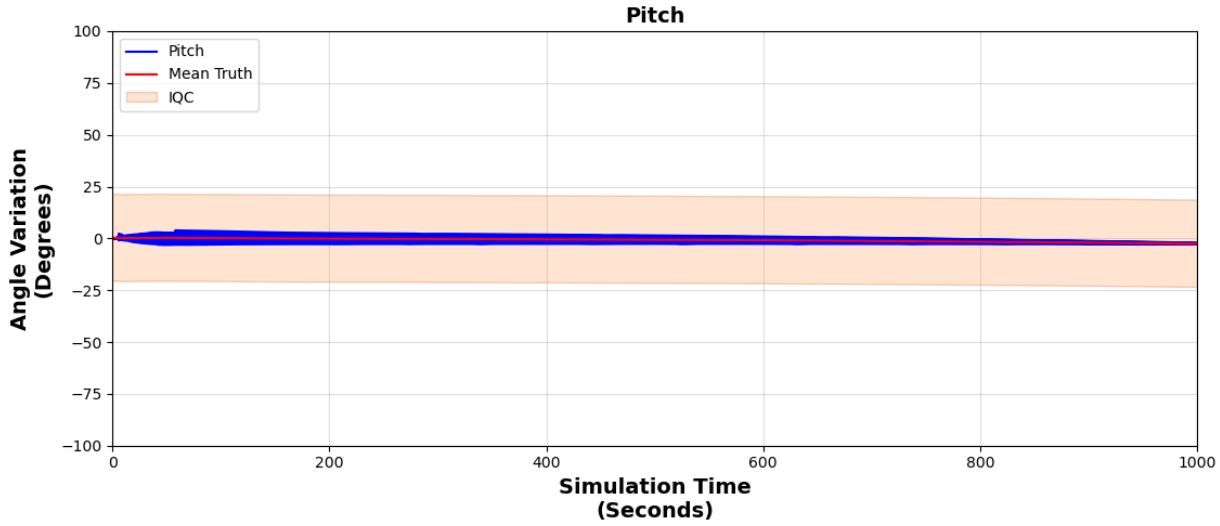

Figure 4-26: Servicer Pitch Angle alignment with respect to Client during phase 1: direct approach (t=0s to 100s) for MC=1000 runs.

For pitch angle during the inspection maneuver, see Figure 4-29. For yaw angle during the inspection maneuver, see Figure 4-30. During the positioning phase, only the pitch angle is controlled, pointing to the Client in the spacecraft body frame. The roll and yaw angles are free to vary and for that reason, IQC bounds

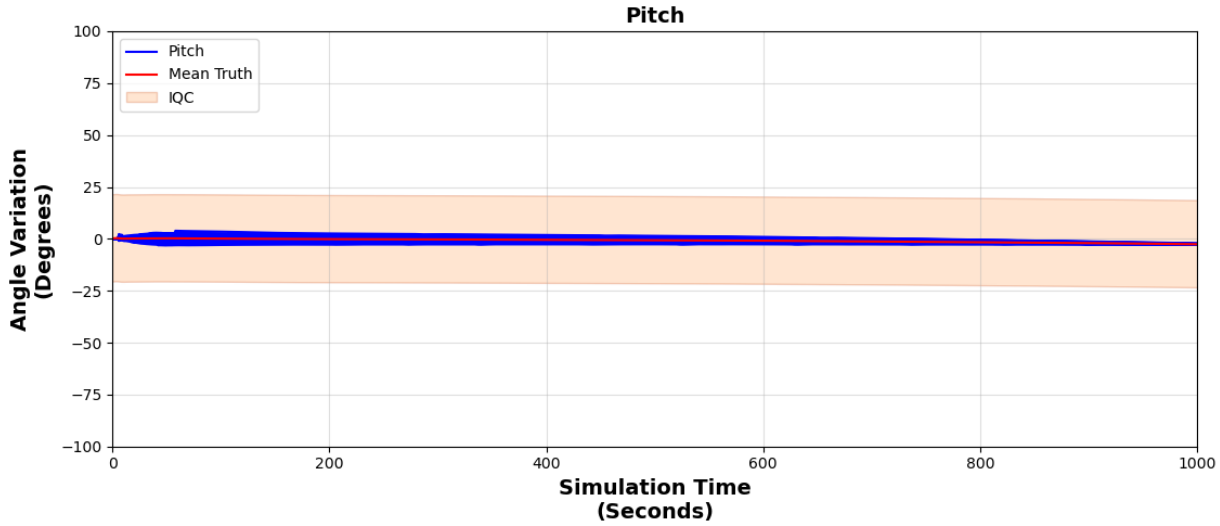

Figure 4-27: Servicer Yaw angle alignment with respect to Client during phase 1: direct approach (t=0s to 100s) for MC=1000 runs.

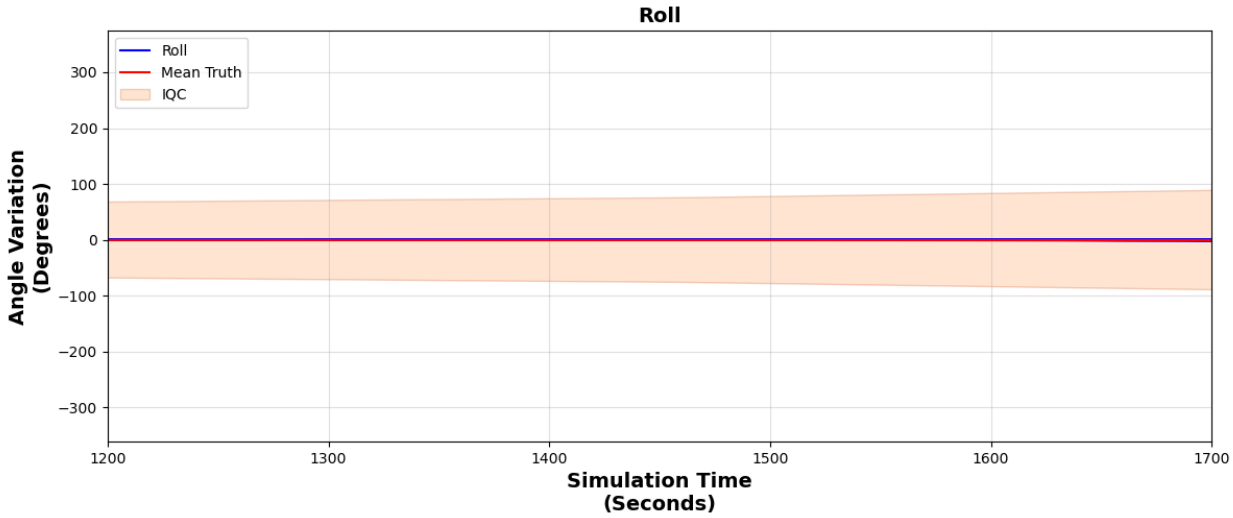

Figure 4-28: Servicer Roll alignment with respect to Client during phase 2: inspection mode (t=1200s to 1700s) for MC=1000 runs.

are not calculated as shown in Figure 4-31 and Figure 4-33. For roll angle during the positioning maneuver, see Figure 4-31.

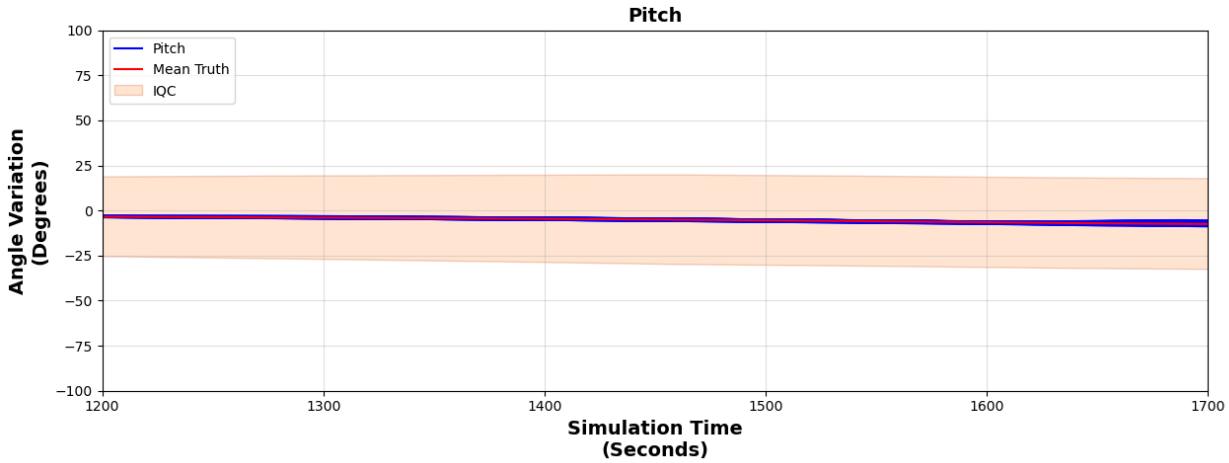

Figure 4-29: Servicer Yaw alignment with respect to Client during phase 2: inspection mode (t=1200s to 1700s) for MC=1000 runs..

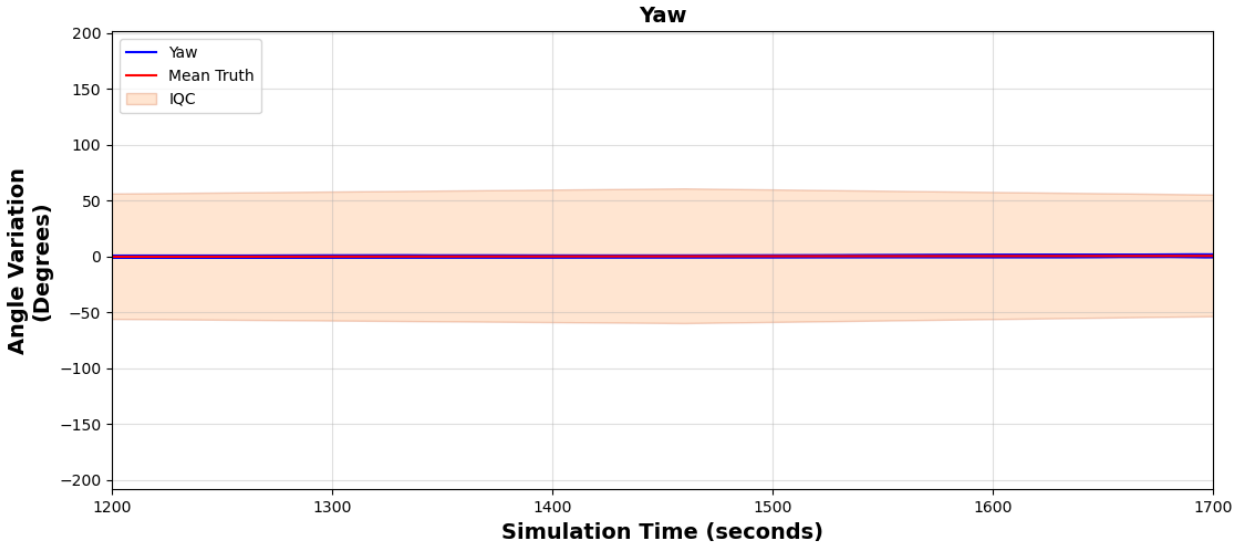

Figure 4-30: Servicer Yaw alignment with respect to Client during phase 2: inspection mode (t=1200s to 1700s) for MC=1000 runs.

For pitch angle during the positioning maneuver, see Figure 4-32. For yaw angle during the positioning maneuver, see Figure 4-33. Similarly, during the closest approach phase, only the pitch angle is controlled pointing, to the Client in the spacecraft body frame. The yaw angle is free to vary and for that reason, IQC bounds are not calculated for that component as shown in Figure 4-36. For roll angle during the closest approach maneuver, see Figure 4-34.

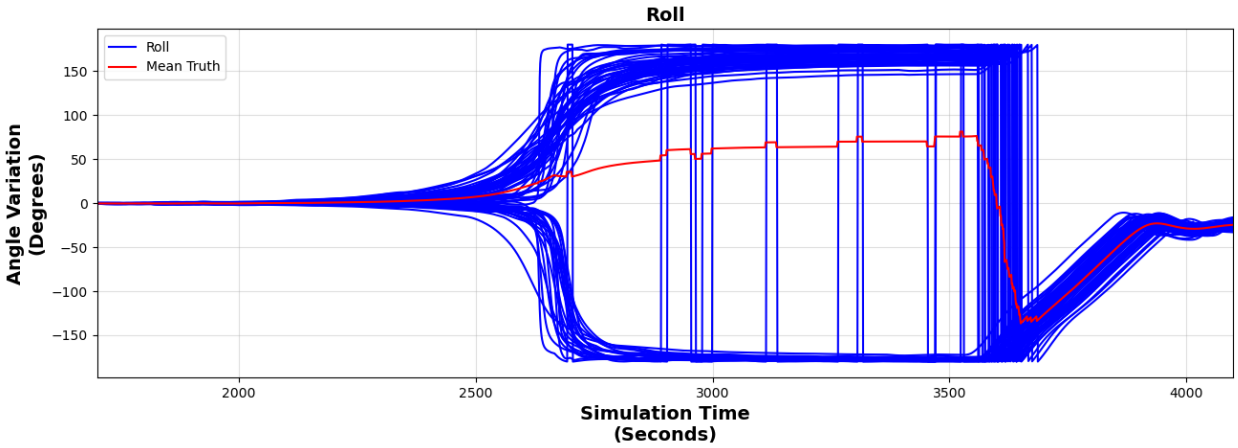

Figure 4-31: Servicer Roll alignment with respect to Client during phase 3: positioning mode (t=1700s to 4100s) for MC=1000 runs.

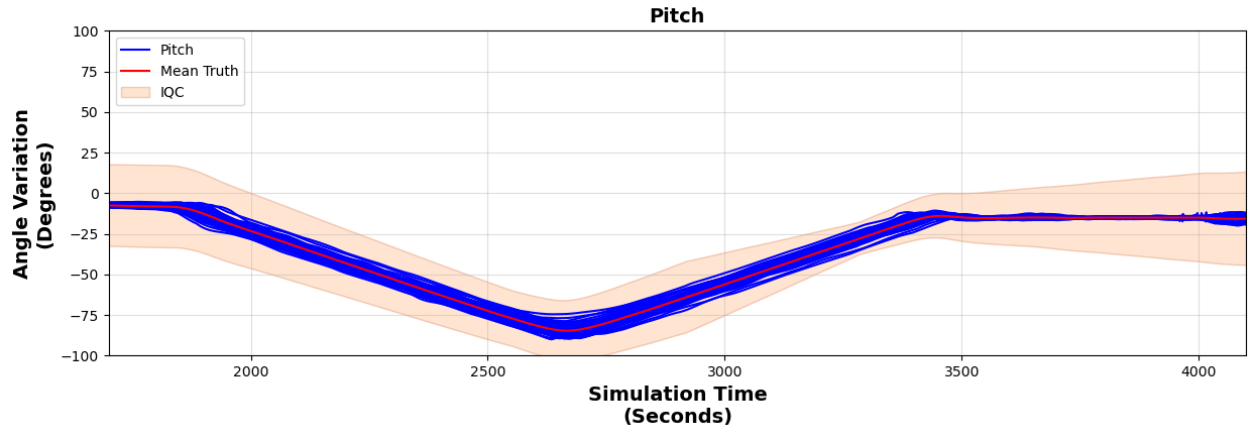

Figure 4-32: Servicer Pitch alignment with respect to Client during phase 3: positioning mode (t=1700s to 4100s) for MC=1000 runs.

For pitch angle during the closest approach maneuver, see Figure 4-35. For yaw angle during the closest approach maneuver, see Figure 4-36. The last phase is the retreat maneuver. The frame is switched to LVLH frame and as in the closest approach maneuver, the yaw angle is free to vary as shown in Figure 4-39. For roll angle during the retreat maneuver, see Figure 4-37.

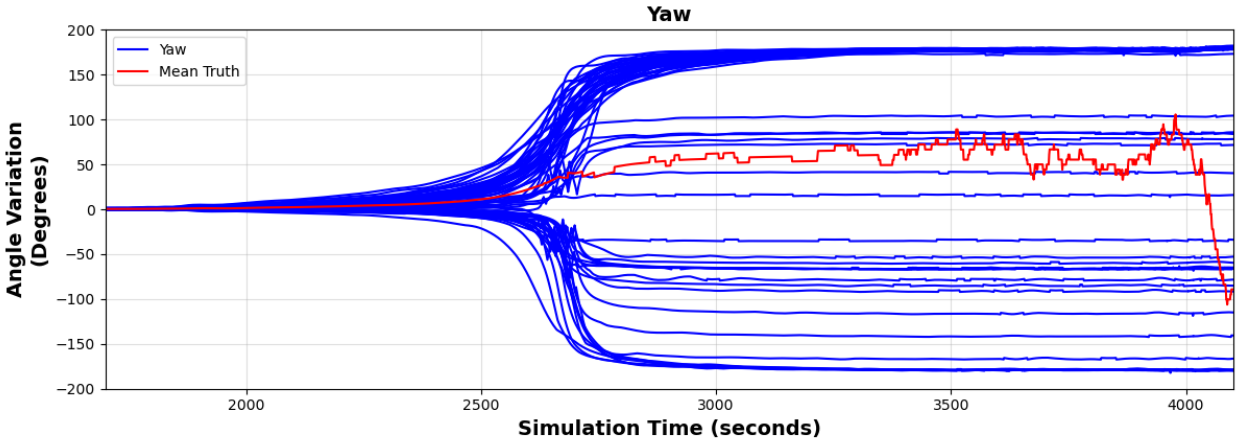

Figure 4-33: Servicer Yaw alignment with respect to Client during phase 3: positioning mode (t=1700s to 4100s) for MC=1000 runs.

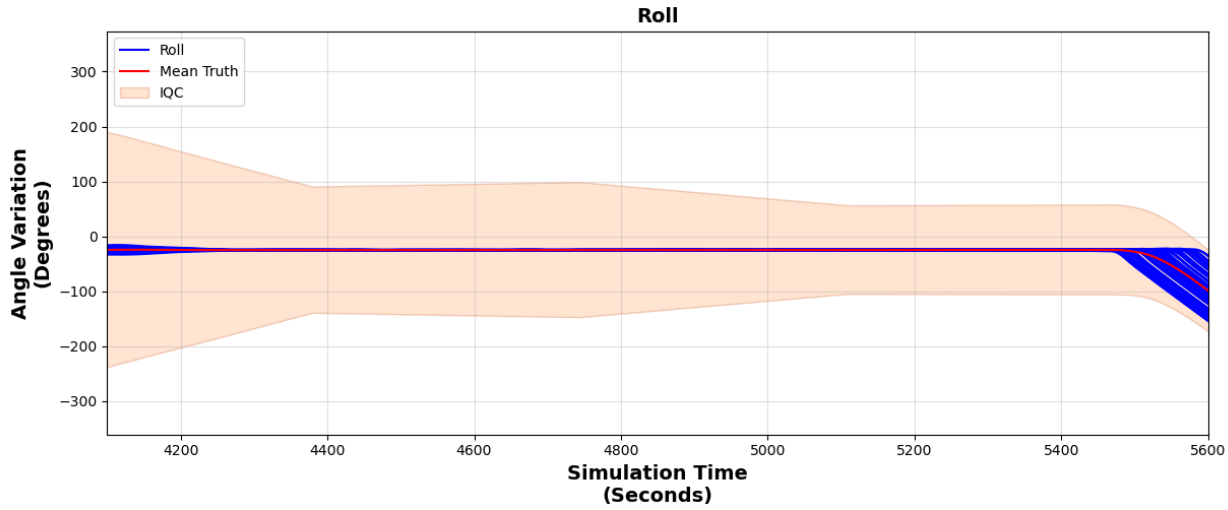

Figure 4-34: Servicer roll alignment with respect to Client during phase 4: closest approach (t=4100s to 5600s) for MC=1000 runs.

For pitch angle during the retreat maneuver, see Figure 4-38. For yaw angle during the retreat maneuver, see Figure 4-39. The variation of these angles during closest approach to the Client (phase 4) and obstacle (phase 5) can be interpreted in the following figures and tables. In both cases, yaw angles are free to vary as the inspection is only being controlled with the roll and pitch angles. Furthermore, yaw values oscillate from -180 *degrees* to 180 *degrees*, which is a common problem in this numerical propagation. These two values are identical in a unit circle but processing the data requires an innovative filtering technique, which is outside the scope of this thesis (i.e., yaw angle is not bounded by the IQC framework). Table 4.8 below shows the range of worst (farthest from mean) and best (closest to mean) angles and IQC bounds at TCA for these ranges.

Table 4.9 shows the range of worst (farthest from the mean) and best (closest to mean) angles and

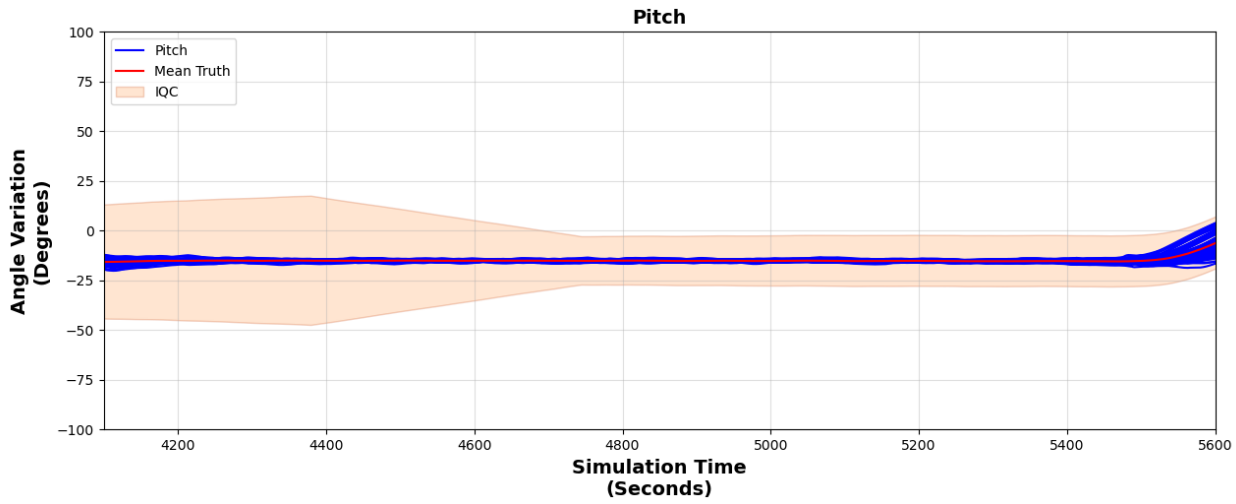

Figure 4-35: Servicer pitch alignment with respect to Client during phase 4: closest approach (t=4100s to 5600s) for MC=1000 runs.

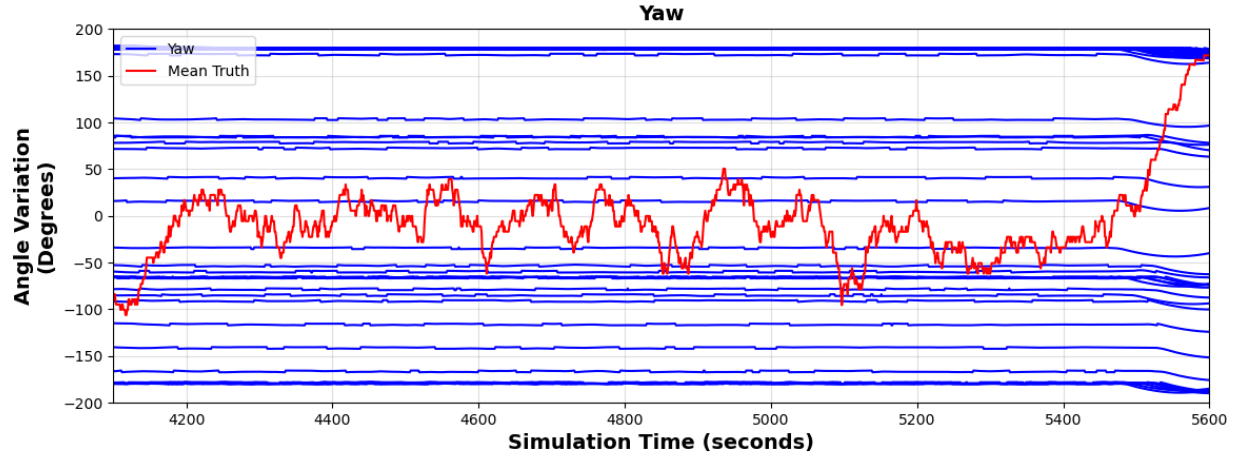

Figure 4-36: Servicer yaw alignment with respect to Client during phase 4: closest approach (t=4100s to 5600s) for MC=1000 runs.

Table 4.8: Final Position's best/worst angles from mean-Truth during phase 4: closest approach. Runs considered initial conditions, sensor noise orbital parameters, thruster output uncertainties, and alignment error bias.

Metric	Roll (angles)	Pitch (angles)	Yaw (angles)
Best angle	-24.80	-14.85	-179.97
Worst angle	-27.50	-17.89	179.99
IQC bound [+/−] from mean	[-27.50, -22.50]	[-18.50, -13.10]	Not Applicable

IQC bounds at TCA for these ranges. In addition, Table 4.10 shows uncertainty groups captured by the IQC-reachability framework and compares the computational loads of two reachability methods: IQC and MC. A desktop computer with an iCore I7, 8 processors, and 3.4 GHz speed was used to generate these results.

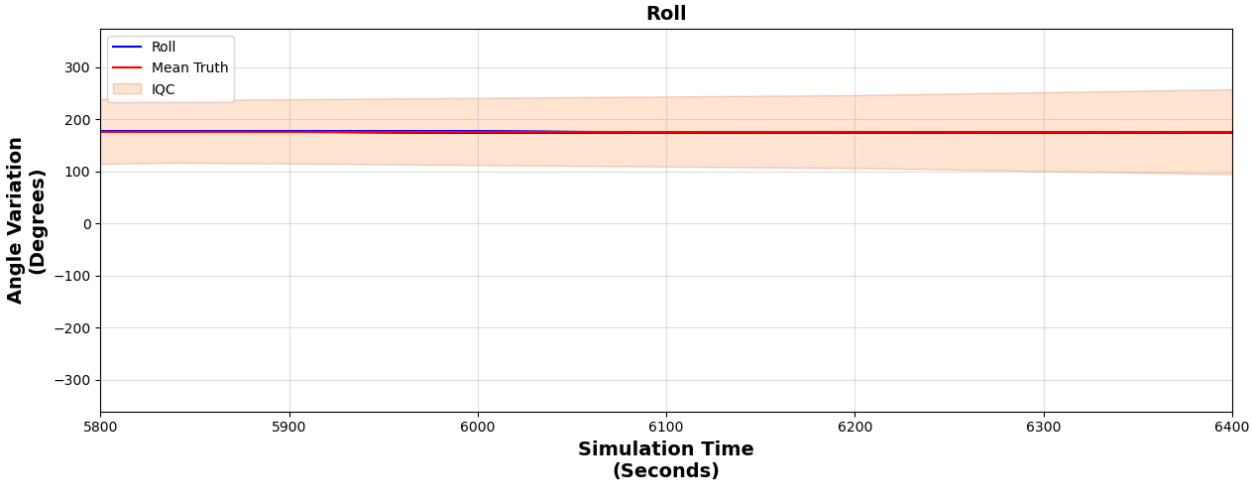

Figure 4-37: Servicer roll alignment with respect to Client during phase 5: retreat phase (t=5800s to 6400s) for MC=1000 runs.

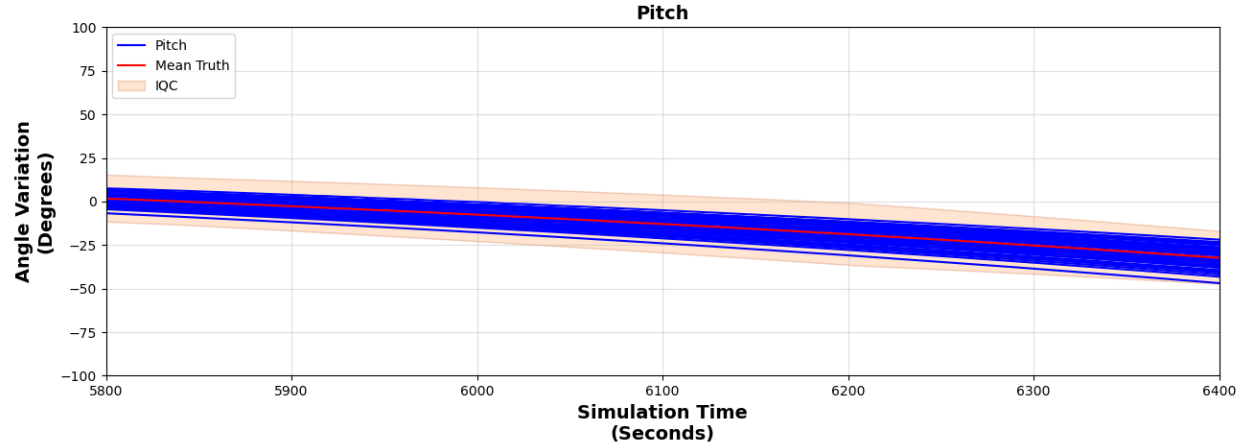

Figure 4-38: Servicer pitch alignment with respect to Client during phase 5: retreat phase (t=5800s to 6400s) for MC=1000 runs.

Table 4.9: Final Position's best/worst angles from mean-Truth during phase 5: retreat phase (TCA to Obstacle). Runs considered initial conditions, sensor noise orbital parameters, thruster output uncertainties, and alignment error bias.

Metric	Roll (angles)	Pitch (angles)	Yaw (angles)
Best angle	-175.20	-25.10	172.42
Worst angle	175.27	-8.30	-179.45
IQC bound [+/−] from mean	[174.50, 175.76]	[-30.0, -5.0]	Not Applicable

Table 4.10: Comparison of IQC uncertainty groups for Euler angles and computational times (IQC-reachability vs. Monte Carlo runs).

Uncertainty Group	MC Time Time	IQC Time
Sensor noise, initial condition, orbital parameter, and thruster	1w 1d 17h 12m 15s 120ms	2d 3h 12m 1s
Sensor noise, initial cond., orbital param., thruster, and alignment bias	1w 1d 22h 14m 3s	2d 19h 20m 8s

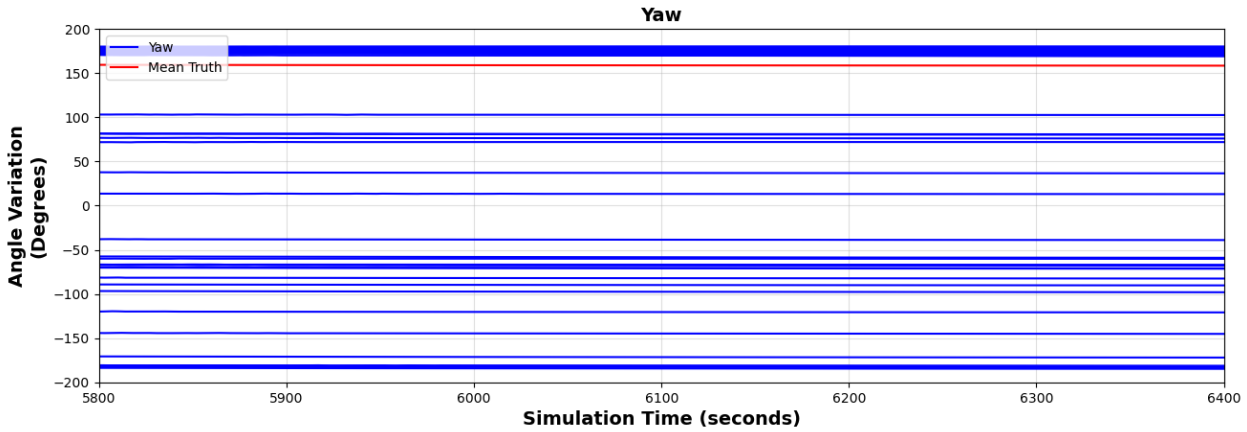

Figure 4-39: Servicer yaw alignment with respect to Client during phase 5: retreat phase (t=5800s to 6400s) for MC=1000 runs.

These results demonstrate the efficiency of using the proposed IQC reachability method to examine safety in a closed-loop feedback control law. This improvement consists of speeding up computation and improving robustness when solving for the worst-state uncertainty through an RPO mission. In the next section, the results of safety-aware filters applied to an optimal model predictive control, designed for an RPO mission, are presented. The IQC reachability framework is also used as a validation technique for the proposed safety framework using control barrier/Lyapunov functions. The results of this innovative filtering scheme are compared with dispersed results via Monte Carlo simulations as well.

4.3 Control Lyapunov/Barrier Functions on RPO GN&C Platforms

This section shows the results of novel approaches that combine the stability criteria from Lyapunov certificates and the safety component of barrier functions to synthesize control Lyapunov and barrier functions, and the combination of the two (i.e., CLFs/CBFs/CLBFs). This concept encapsulates properties of both CLF and CBF, and enforces stability of a controller towards a specific region while filtering the control output to stay within some safety bounds specified by the control designer. Earlier sections showed five main phases of the RPO mission: direct approach, inspection mode, positioning, closest approach, and retreat. The first and last phases (i.e., direct approach and retreat) are trajectories designed to pass by an obstacle, so the third case study presented in this section focuses on applying a neural CBF to these two phases. On the other hand, the fourth case study focuses on filtering the controller output used for the inspection-related phases (i.e., inspection mode, positioning and closest approach) by applying a neural CLBF. The CLBF is chosen as the filtering scheme, as the intent for the designed trajectories is to arrive to a specific point while assuring that all trajectories stay within a safety region. The switching safety-aware filtering function is shown in Figure 4-40.

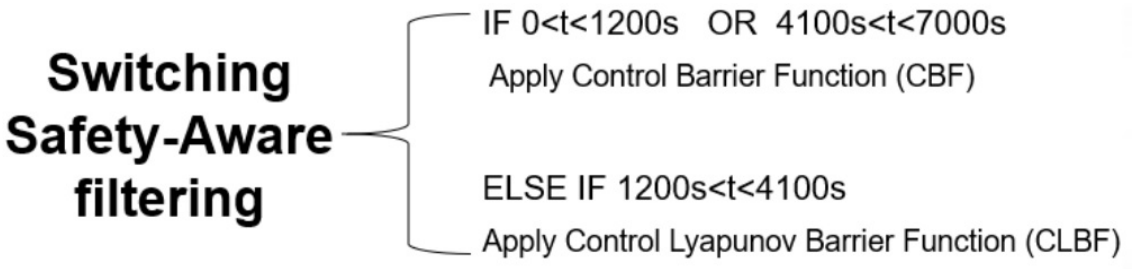

Figure 4-40: Safety-aware filtering technique for RPO missions (i.e., CBFs are applied to the first and fifth phases and CLBFs are applied to the second, third and fourth phases).

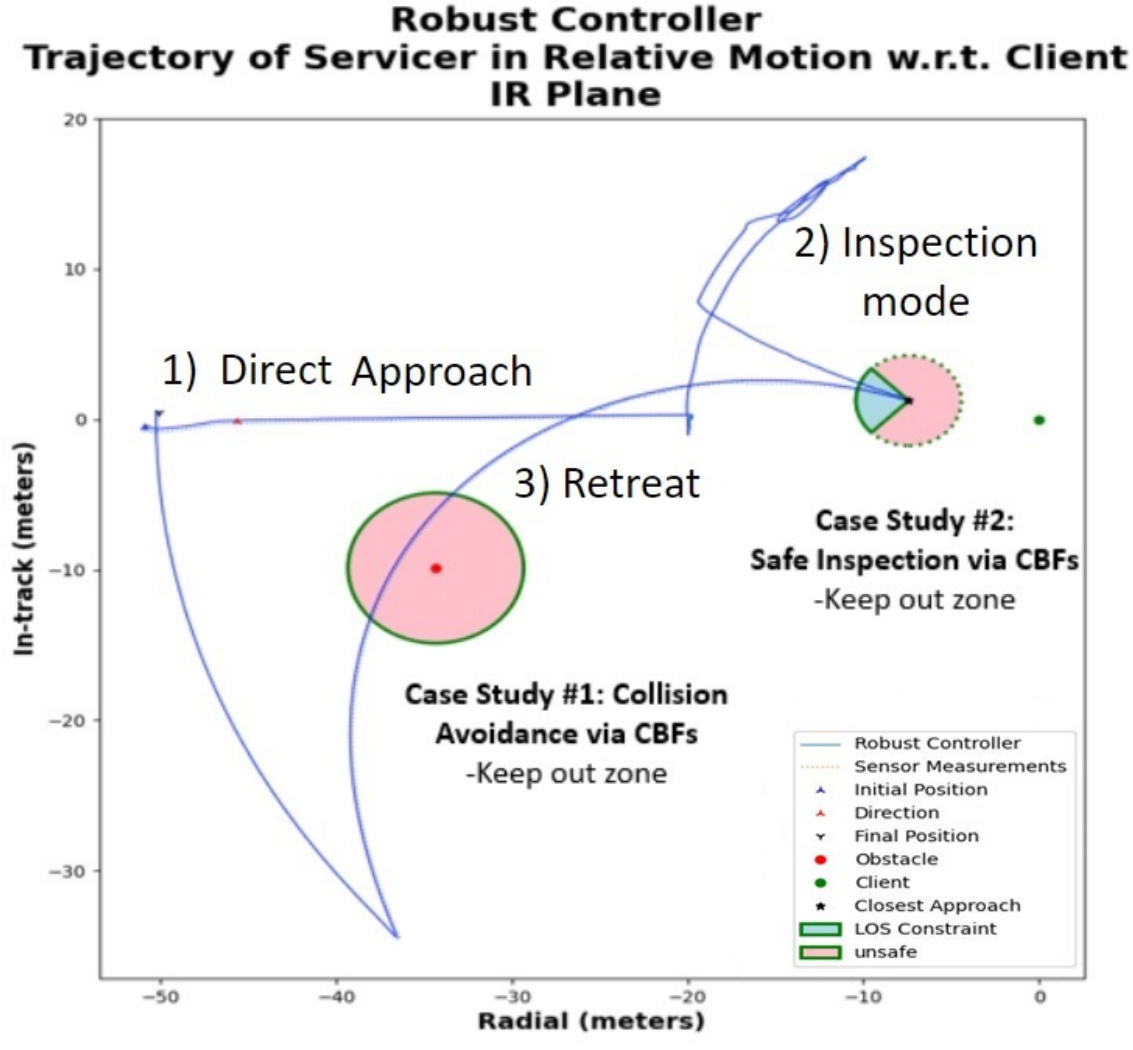

Figure 4-41: Summary of case studies: safety-aware filtering technique for RPO missions (i.e., CBFs are applied to the first and fifth phases and CLBFs are applied to the second, third and fourth phases).

A simulation of the neural Lyapunov MPC trajectories with the detailed phases can be seen in Figure 4-41. The uncertain output is caused by disturbances affecting actuation, unmodeled effects in relative motion

dynamics, and unanticipated maneuvers by Client/obstacle, which are not captured by current onboard GN&C platforms. Figure 4-42 shows an illustration of the worst and best scenarios in RPO controllers.

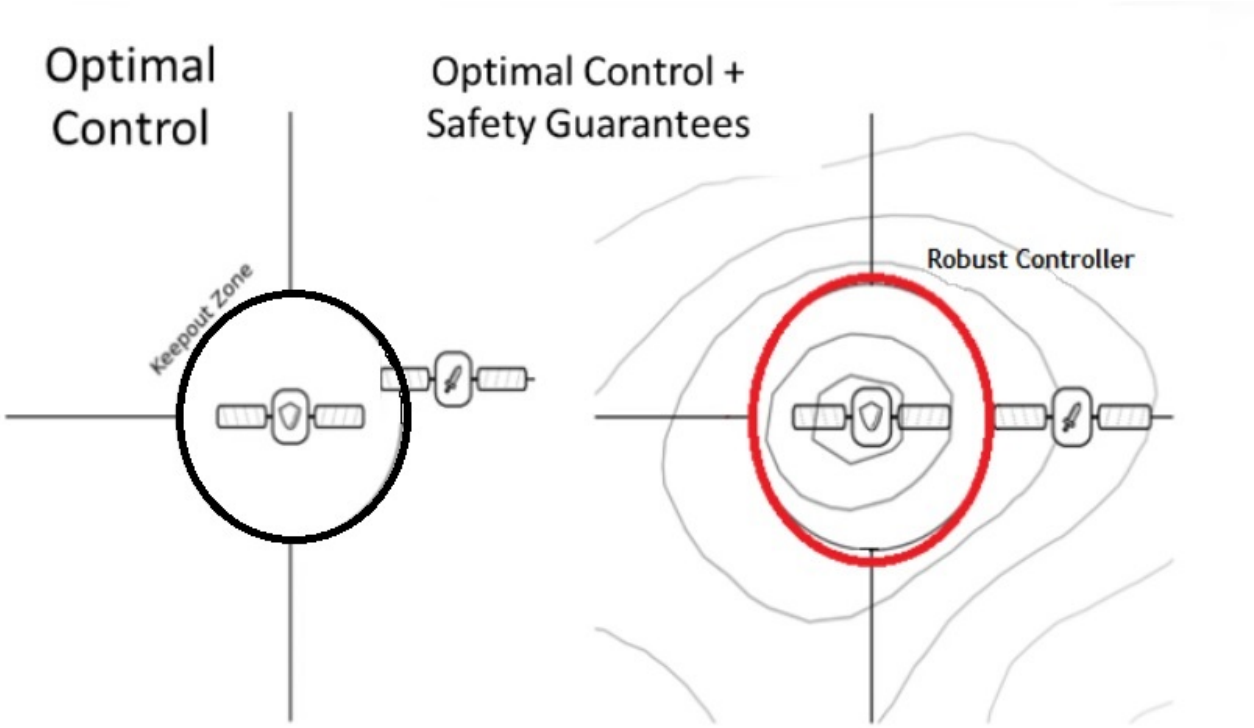

Figure 4-42: Illustration of best- and worst-case scenarios for RPO GN&C design.

4.3.1 Model Predictive Control Applied to RPO Mission

As shown in the MPC implementation from [66], the constraint on the maximum impulsive velocity change is considered as a limit on the ∞-norm of the control. Using the ∞-norm implies that thrusters are used in all body-fixed frame directions and limit the maximum thrust for each body axis individually as shown in Equation 4.12.

$$|u_k|_\infty \leq u_{max} \tag{4.12}$$

where u_{max} is a result of the finite-thrust capability of the Servicer. Alternative norms for impulsive control were considered, but they changed the computational complexity of the problem. For a single thruster, the 2-norm could be used, requiring that the Servicer slews for each impulse. During a rendezvous maneuver, the Servicer is typically desired to be aligned with the Client body or payload frame. An LOS cone constraint is usually implemented to maintain trajectories within a "keep-in zone" for a successful inspection of a Client. To keep the MPC controller in a quadratic program (QP) formulation, the method in [12] treats the LOS constraint as an inner polyhedral approximation given by Equation 4.13.

$$A_{cone} x_k \leq b_{cone} \tag{4.13}$$

This constraint is considered "soft" [12], which means that the states are allowed to violate the conditions and added as a penalty to the cost function. The penalty augmented to the cost function in [12] is given by Equation 4.14:

$$\sum_{i=1}^{N} \lambda_k 1^T (A_{cone} x_k - b_{cone})_+ \tag{4.14}$$

where λ is the weight on the penalty, and the subscript $+$ denotes that only positive components are considered (i.e., if the constraint is violated, negative values are set to zero so as not to contribute to that penalty).

In addition, to ensure that the Servicer does not overshoot the Client, a constraint is placed on the desired approach direction. For example, when considering a V-bar approach (along the Client's velocity direction or in-track), a constraint is placed on the in-track component of the state as stated in Equation 4.15.

$$y_k \geq 0 \tag{4.15}$$

As previously mentioned in the introduction of this subsection, the RPO mission scenario has been split into five phases. The phases have different sample times between control inputs for the MPC solution. The direct approach phase has the longest sample rate since it occurs when the relative distance is large (i.e., $2km$-$10km$) compared to the next four phases. Upon entering the close range or inspection phase (i.e., less than $10m$), the sample time decreases for faster Servicer control in response to disturbances. The fastest

sample rate is in the closest approach phase, where the Servicer and Client are closest, so that the Servicer can react quickly to perturbations in order to avoid collisions.

The LOS and overshoot constraints are added to the MPC formulation. Adding in the LOS cone constraint ensures that the Servicer will begin to approach the Client from a desired inspection direction. Equation 4.16 below describes the optimization problem in the R-bar approach rendezvous:

$$\begin{aligned} min \quad & J = \sum_{i=1}^{N-1} x_k^T Q x_k + u_k^T R u_k + x_N^T Q_f x_N + \sum_{i=1}^{N} \lambda_k 1^T (A_{cone} x_k - b_{cone})_+ \\ \text{s.t.} \quad & x_{k+1} = A x_k + B u_k \\ & |u_k|_\infty \leq u_{max} \\ & x_k \geq 0 \end{aligned} \tag{4.16}$$

The next subsection explains the assumptions and methodology behind the CBF and CLBF synthesis, and the filtering methodology applied to the MPC scheme.

4.3.2 Neural Lyapunov Synthesis for an RPO Mission

Verifying that a Servicer controller satisfies this safety constraint is challenging for a number of reasons:

1. The LVLH frame is convenient for expressing the safety constraints, but the relative equation of motion relies on a linearization of orbital dynamics and thus does not capture higher-order nonlinear effects and actuation uncertainties. The safety verification process should account for these effects.

2. The Client or obstacle region may not be static; each will often have its own control policy, which may not be known ahead of time (or at all). The safety verification process should be robust to some (bounded) maneuvering by the Client and obstacle objects.

3. Designing a Servicer controller is challenging, so the safety verification process should allow maximum flexibility in designing the controller.

A safety verification strategy that meets all three requirements is that of robust Control Barrier Functions (CBFs) or Control Lyapunov Barrier Functions (CLBFs). As discussed in chapter 3, a CBF is a scalar function of state $h : \mathbb{R}^n \mapsto \mathbb{R}$ such that $h(\mathbf{x}) < 0$ in the safe region, $h(\mathbf{x}) > 0$ in the unsafe region, and the time derivative of h satisfies the inequality

$$\inf_u \left[\frac{dh}{dt}\right] = \inf_u \left[\nabla h \mathbf{f}(x) + \nabla h \mathbf{g}(\mathbf{x})\mathbf{u}\right] \leq -\lambda h(\mathbf{x}) \tag{4.17}$$

for control-affine dynamics, $\dot{\mathbf{x}} = \mathbf{f}(\mathbf{x}) + \mathbf{g}(\mathbf{x})\mathbf{u}$. If h satisfies these requirements, then established results in control theory imply that there exists a family of feedback control policies that cause the state to remain in the safe region for all future time [9]. Even if these conditions are violated in some regions, as long as they hold throughout the region where $h < 0$ the safety guarantees hold, and safe controllers are guaranteed to exist. In particular, this family of safe controllers is all Lipschitz continuous control policies taking values

from the set $K_{CBF} = \{\nabla h\mathbf{f}(x) + \nabla h\mathbf{g}(\mathbf{x})\mathbf{u} \leq -\lambda h(\mathbf{x})\}$. An arbitrary Lipschitz controller $\pi_{baseline}$ can be projected onto this safe set by solving the CBF quadratic program (CBF-QP).

$$\min_u ||u - \pi_{baseline}||^2 \tag{4.18}$$

$$\text{s.t. } \nabla h\mathbf{f}(x) + \nabla h\mathbf{g}(\mathbf{x})\mathbf{u} \leq -\lambda h(\mathbf{x}) \tag{4.19}$$

The CLBF holds the same criteria but adds enforcement of the stability of a controller towards a specific location, as shown in Equation (3.27). This CBF/CLBF-QPs can act as safety filters, satisfying requirement (1) by allowing the system designers to choose any desirable $\pi_{baseline}$, so long as it is filtered to a safe policy by solving Equation (4.18). However, to meet requirements (2) and (3), the synthesis of CBF/CLBF should be robust to uncertainty and adversarial disturbances in the inputs. To do this, a robust certificate is implemented as discussed in [31].

The safety analysis must be robust to three sources of disturbance: higher-order effects, (ignored in the linearized LPE dynamics), actuation uncertainty, and worst-case movement from the Client/obstacle objects. The worst-case disturbance is assumed from the sum of these three effects, which are bounded along each axis, i.e. $d_x, d_y, d_z \in [d_{min}, d_{max}]$. For the following analysis, we take $d_{max} = -d_{min} = 0.01$. By exploiting the fact that condition (4.17) is affine in these uncertain disturbances, if (4.17) holds for all worst-case scenarios $\mathbf{d} = (d_x, d_y, d_z) \in \{d_{min}, d_{max}\}^3$ then it is guaranteed to hold for any scenario in the convex hull of those extreme points [31]. Using this fact, the CBF/CLBF-QPs in (4.18) can be expanded to construct a robust version, which is sufficient to enforce safety despite perturbations from nonlinear effects and actuation devices, and potentially adversarial actions by the Servicer and obstacle region.

$$\min_u ||u - \pi_{baseline}||^2 \tag{4.20}$$

$$\text{s.t. } \nabla h(\mathbf{f}(x) + \mathbf{d}_i) + \nabla h\mathbf{g}(\mathbf{x})\mathbf{u} \leq -\lambda h(\mathbf{x}) \qquad i = 1, 2, \ldots 8 \tag{4.21}$$

These robust CBF/CLBF-QPs can be used as safety filters, guaranteeing that the system remains safe despite perturbations. The safety-aware filter is shown in Figure 4-43: the CBF/CLBF-QPs project the baseline control policy onto the set of safe controllers, allowing it to be used with baseline controllers that are difficult to rigorously verify (such as MPC controllers). This innovative method provides flexibility and robustness, satisfying our three requirements for safety verification; however, there are three notable drawbacks.

First, this architecture shifts the responsibility for safety to an online monitor in the form of robust CBF/CLBF-QPs. Instead of using a more accurate perturbation model and propagating the dynamics forward in time, the CBF/CLBF-QPs assume that an accurate state estimate will allow it to adapt to disturbances online. The feasibility of the CBF/CLBF-QPs can be verified offline, but the need for an accurate, high-frequency state estimate is a hard requirement for this approach.

Second, the CBF/CLBF-QPs safety filters have no intrinsic notion of optimality (other than closeness to the baseline controller). By design, the CBF/CLBF-QPs are concerned only with maintaining safety. If a mission requires optimal use of resources or positioning relative to the Client, those considerations are delegated to the baseline controller. For example, an MPC controller may be used to ensure low propellant use, while a CBF-QP is used to filter the output of the MPC algorithm.

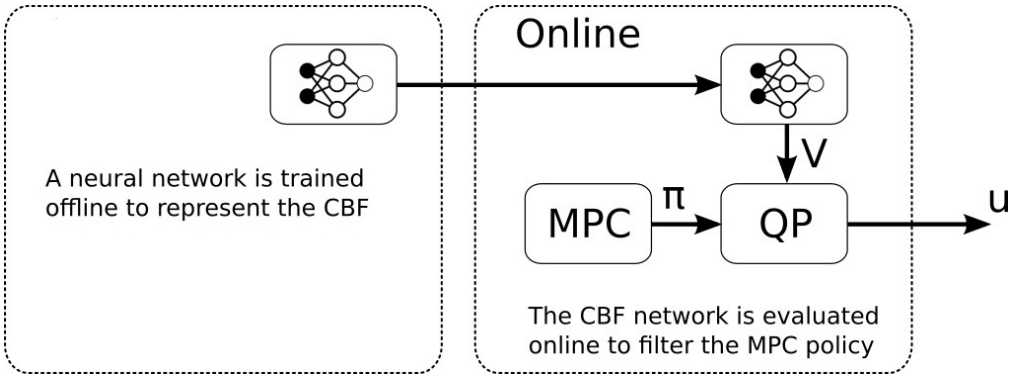

Figure 4-43: Control barrier/Lyapunov functions (CBFs/CLBFs) can act filters for any control policy $\pi(x)$ (in our case, MPC), endowing the combined controller with guarantees on long-term safety.

Finally, robust certificate functions such as CBFs and CLFs are notoriously difficult to synthesize by hand [45]. In this thesis, an approach from [31] is adapted for improving GN&C platforms in RPO missions. The Lyapunov functions are synthesized by training neural networks with 4 hidden layers of 128 tanh activation units each, using stochastic gradient descent to minimize the violation of the constraints in Equation (4.21) in the robust CBF/CLBF-QPs. As a result, the next subsection uses the designed MPC to execute the maneuvers during the various mission phases described in this thesis. Two synthesized neural Lyapunov functions (CBF and CLBF) are used to filter the output of the MPC to achieve fuel-optimal trajectories with safety guarantees.

4.3.3 Case Study 3: Collision Avoidance (Servicer/obstacle) via Neural CBF

This case study applies a CBF to an MPC scheme for robust safety guarantees during the direct approach and retreat phases at 550 km in LEO. For guaranteeing safety in proximity operations, it is important that the Servicer spacecraft avoids any obstacle object to prevent a collision from happening. Table 4.11 shows the Servicer specifications and acceleration disturbances considered in this case study.

It is assumed that the Servicer has perfect state knowledge of itself. The CBF network is trained on 100,000 data points sampled uniformly from $[x, y, z, \dot{x}, \dot{y}, \dot{z}] \in [-3, 3]^3 \times [-1, 1]^3$, considering disturbances as shown in Table 4.11. The violation of the constraints in Equation (4.21) is computed on each data point. Since some flexibility is needed in determining the shape of the robust CBF, the safety constraints were modified in Figure 4-58 to specify safe and unsafe regions of state space, leaving some separation between these sets (states in this buffer zone may be either safe or unsafe).

Table 4.11: Servicer specifications and disturbances considered in the CBF synthesis.

Specifications	Values
Altitude	550 km
Initial Conditions (Cartesian/LVLH frame)	[0.0 m, -50.0 m, 0.0 m]
Drag Coefficient	2.2
Mass	160 kg
Thruster Uncertainty	[-5% m/s^2 to 5% m/s^2]
State Uncertainty (x, y, z, $\dot{x}$, $\dot{y}$, $\dot{z}$)	[-3 m, 3 m]$^3\times$ [-1 m/s, 1 m/s]^3
Uncertainty in obstacle motion	[-0.01 m/s^2, 0.01 m/s^2]
Additive Disturbance (Due to geopotential uncertainty	[-0.001 cm/s^2, 0.001 cm/s^2]

A contour plot of the trained CBF network is shown in Figure 4-44. Trajectories starting at states within this 0.95-sublevel set are guaranteed to remain within that set when controlled using the robust CBF-QP. The conditions in Equation (4.21) were found to be satisfied at all points in Figure 4-44 within the 0.95-sublevel set; these conditions were checked on a uniform grid of points with maximum spacing 0.01 between points. The validity of this robust CBF was verified by checking that the conditions in Equation (4.21) were satisfiable at all points within the 0.95-sublevel set on a uniform grid with maximum spacing 0.01 between adjacent points. No violation was found of the CBF conditions on this set. Because the CBF conditions are satisfied throughout this dark purple set, this set is guaranteed to be invariant.

From Figure 4-44, a CBF certificate certifies an invariant region (red circle) that does not fully overlap with the specified safe region (green circle). By checking the certificate values on a uniform grid as described above, we find that our barrier certificate certifies 99.52% of the desired safe region as forward invariant, and the overlap between the certified invariant region and the specified unsafe region is 0%.

Figure 4-45 shows the derivative of the control barrier function. This figure shows the region where the synthesized function is valid (i.e., unsafe if $max(dV/dt, 0) > 0$ or safe if $max(dV/dt, 0)<0$). This means that if the derivative gradient is greater than 0, the CBF is not always valid for that region. On the other hand, if the derivative is less than 0 (or negative), the CBF is always valid for that region. Because the interest for safety is inside the keep-out zone, which represents the area inside the red circle, the CBF synthesis is valid for the direct approach and retreat mission phases. As a result, this CBF certificate will allow satisfaction of the obstacle KOZ constraint embedded in the MPC scheme.

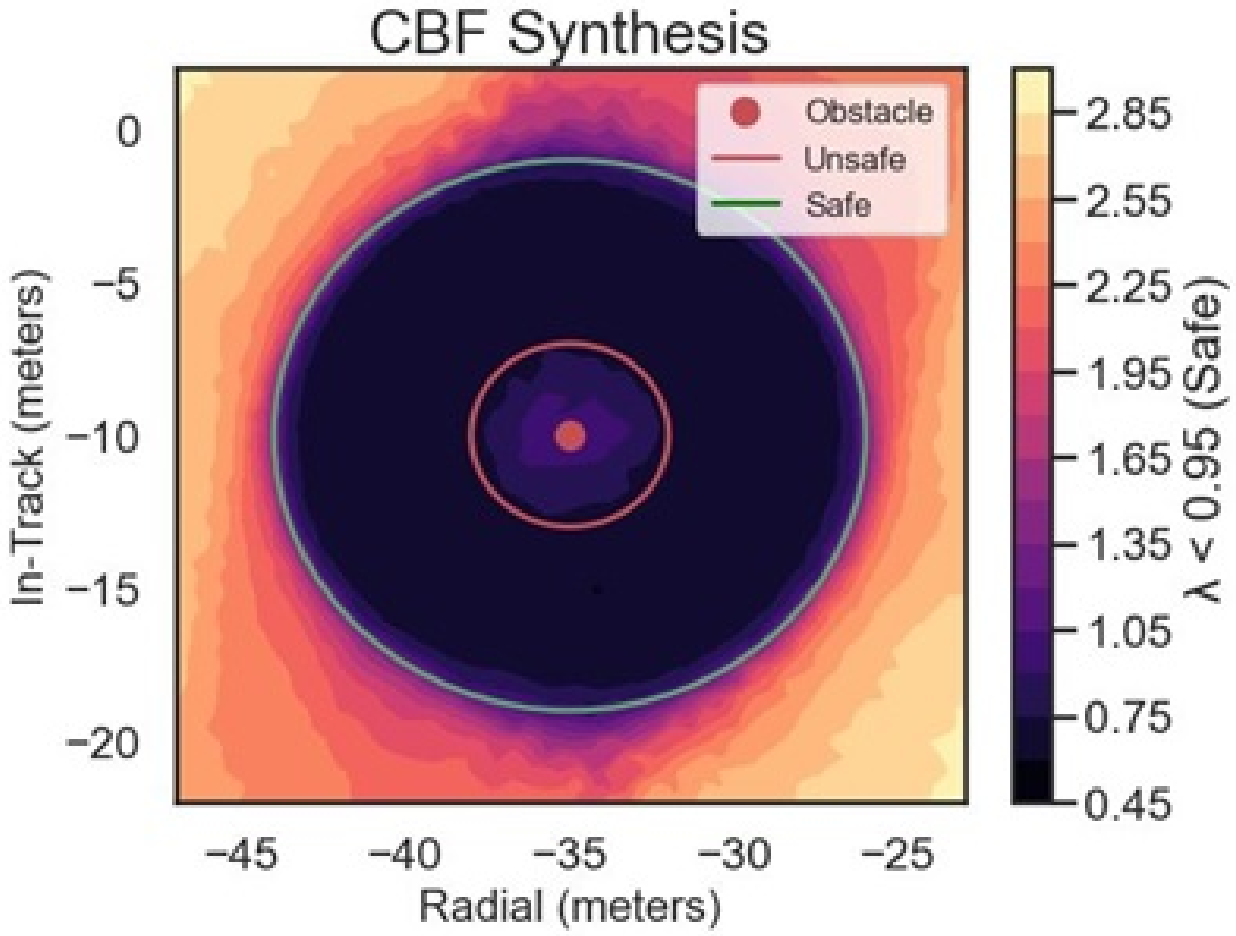

Figure 4-44: The robust neural CBF is synthesized using stochastic gradient descent to minimize the violation of the constraints. The 0.95 sub-level set (red circle) separates safe and unsafe states, guaranteeing safety.

One hundred trajectories were executed to compare the trajectories of the MPC vs. the CBF + MPC controllers as shown in Figure 4-46 and Figure 4-47. It is difficult to see which trajectories are passing through the obstacle in a 2D representation, and for that reason, Figure 4-48 shows the closest approach to Client in 3D space for the trajectories executed by the standalone MPC and the CBF+ MPC schemes.

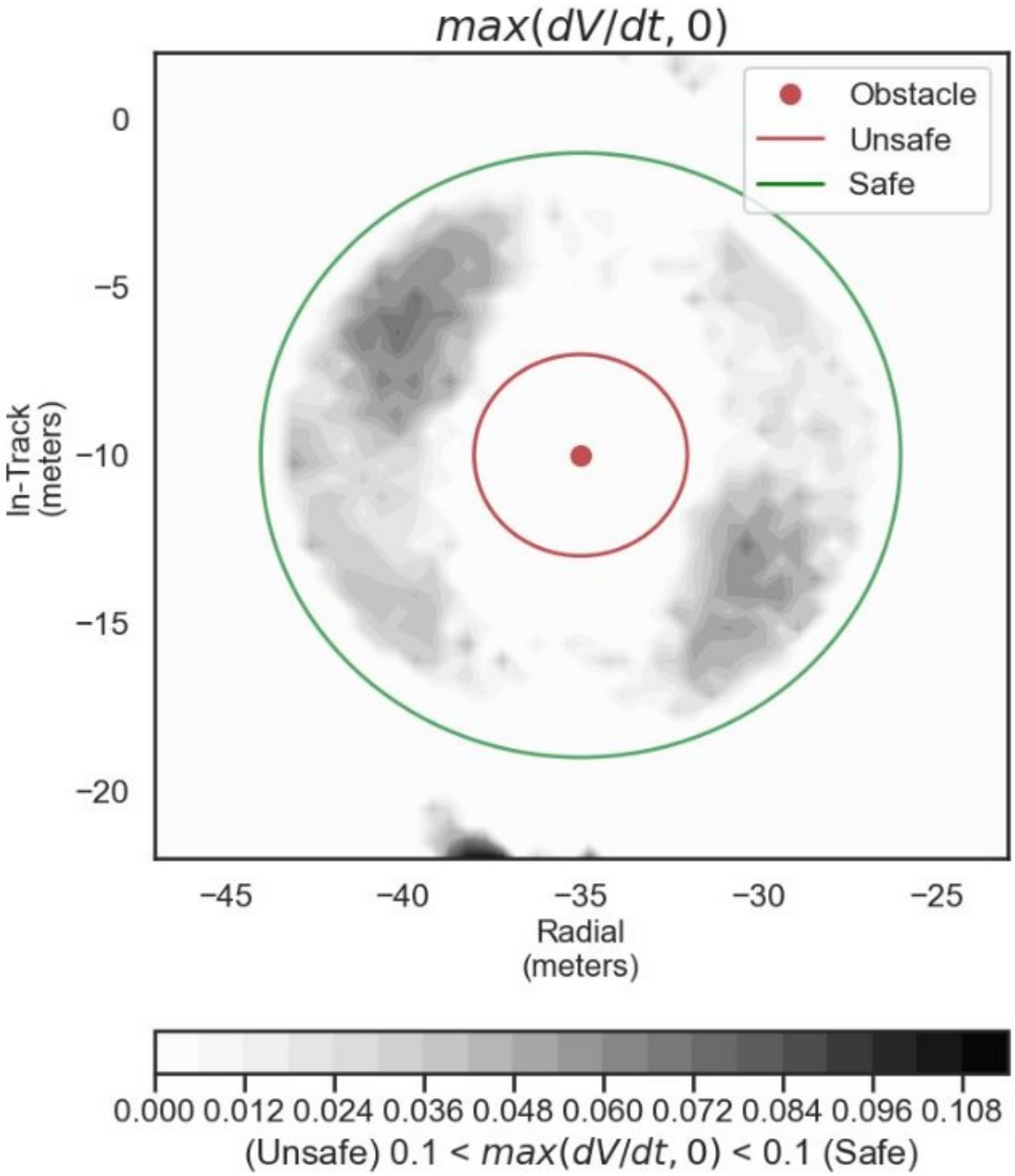

Figure 4-45: Derivative of the CBF using the point-wise maximum function (max). Trajectories starting at states within the invariant set of $\lambda < 0$ are guaranteed to remain within that set when controlled using the robust CBF-QP.

The left plot shows that the standalone MPC scheme will not always guarantee that trajectories remain outside the keep out zone. On the other hand, the right plot shows that the CBF embedded in the MPC scheme allows for a KOZ constraint satisfaction for the closest approach points to obstacle, despite the uncertainties and nonlinearities affecting the control output. In addition, in order to validate the robustness of CBF, Monte Carlo simulations were run and results were compared with the IQC bound at TCA. Figure 4-

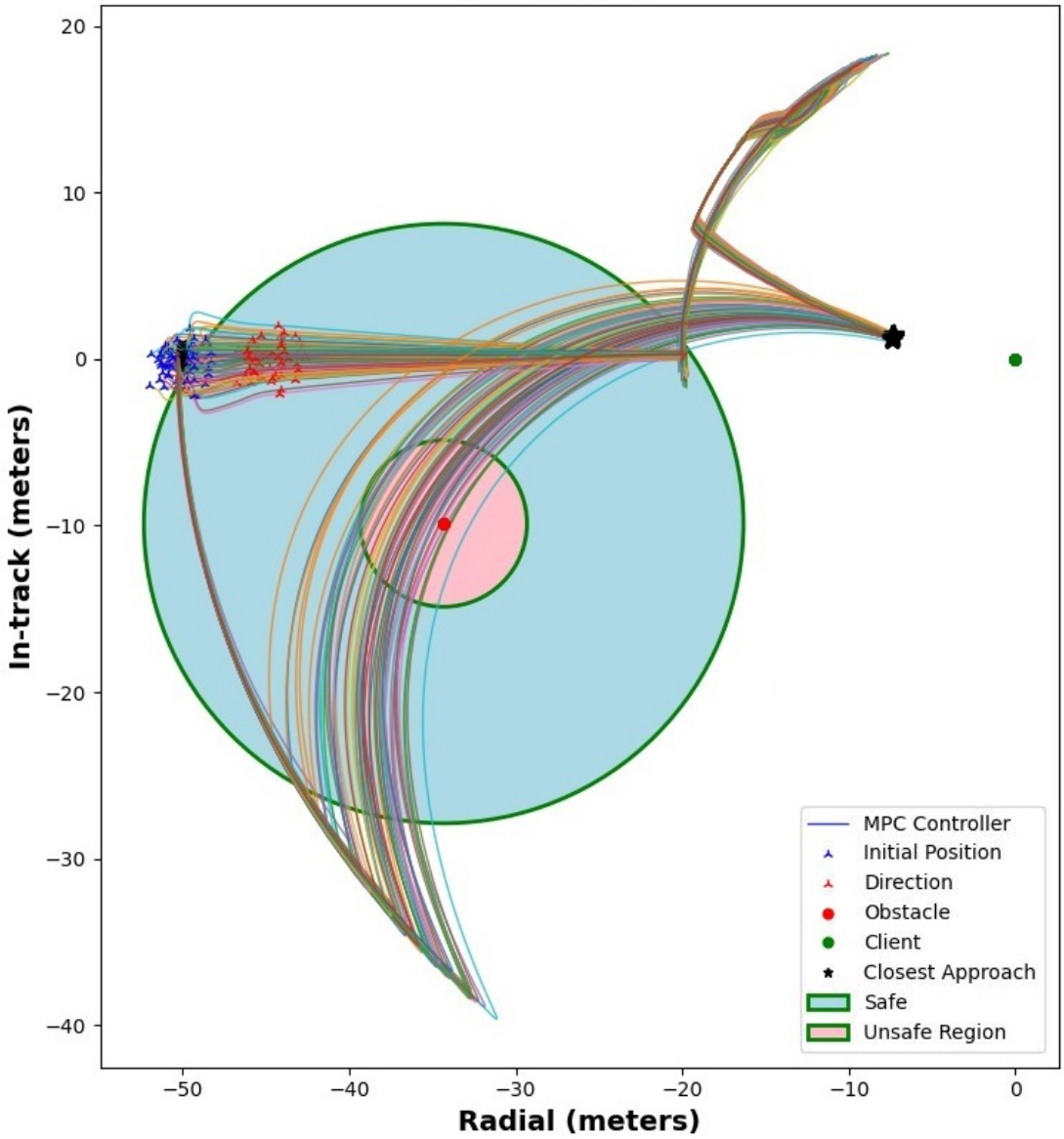

Figure 4-46: MPC trajectories of RPO phases while capturing uncertainties and nonlinearities (MC=100).

49 shows the worst-case uncertainty IQC bound at TCA to obstacle, during the direct approach phase, where the Servicer is passing by the obstacle.

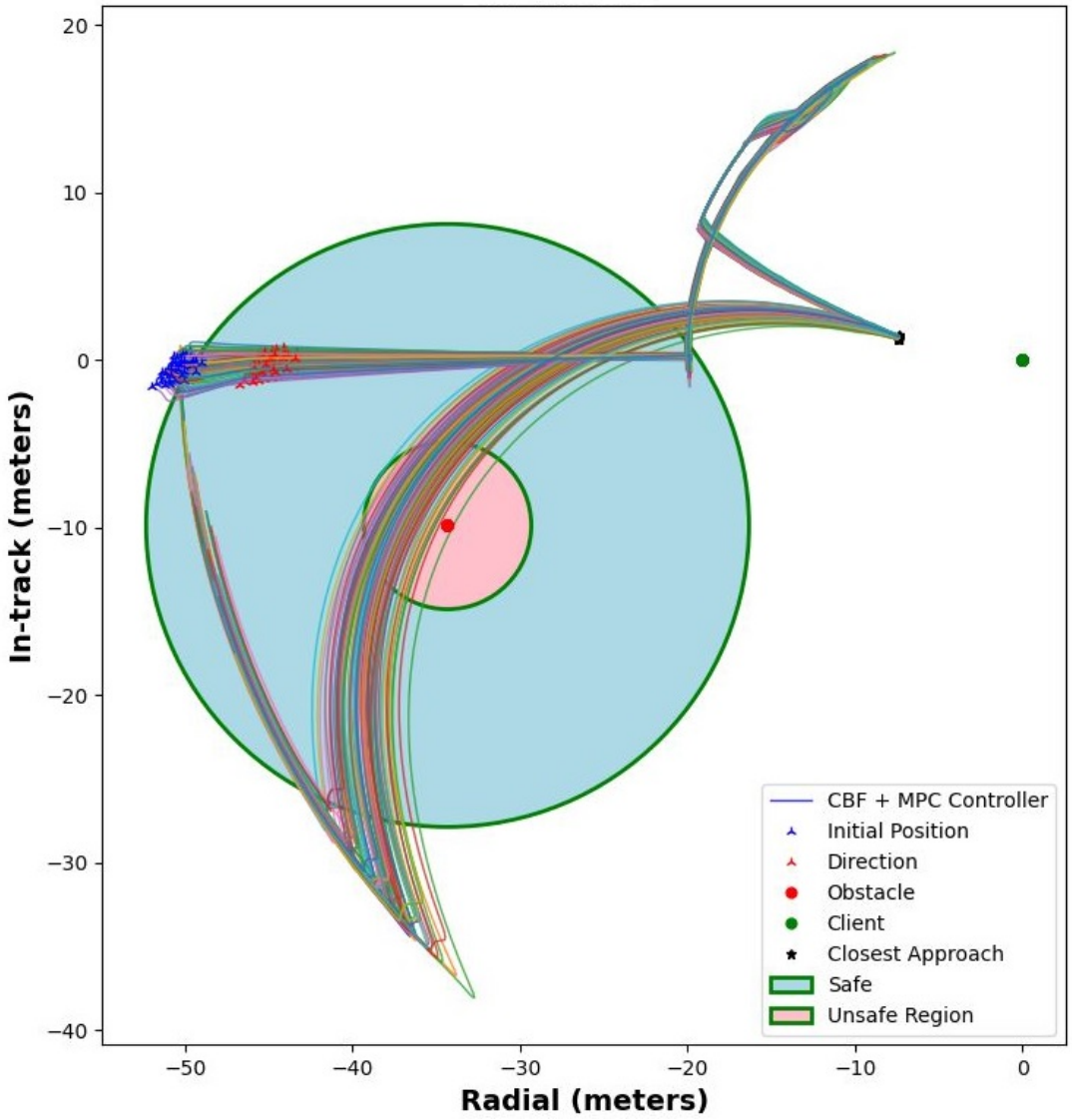

Figure 4-47: MPC+CBF RPO phases while capturing uncertainties and nonlinearities (MC=100).

Similarly, Figure 4-50 shows the same validation of Monte Carlo runs and IQC bound at TCA for the retreat phase. The actual time of the closest approach to the obstacle object occurs during the retreat phase. Because the bound generated by the IQC reachability method captures more uncertainties than the synthesis of the CBF (i.e., synthesis only captures disturbances in the form of accelerations (see Table 4.11) applied to the control-affine dynamics), the IQC uncertainty bound and the KOZ constraint are compared to determine the robustness of the synthesized CBF. As a result, as shown in Figure 4-51, the filtered-MPC via CBF only guarantees a safe keep-out distance of 2.5 *meters* instead of the 4 *meters* radius that was originally enforced during the CBF synthesis.

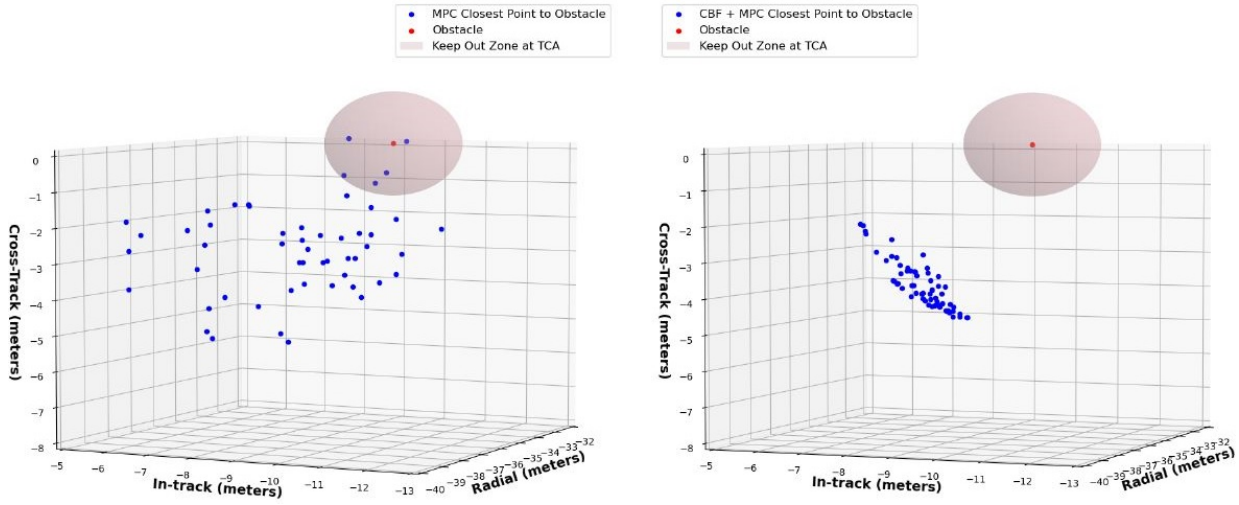

Figure 4-48: Trajectories satisfy the 4-*meter* radial keep out distance (KOZ constraint) to obstacle with the CBF+MPC Controller.

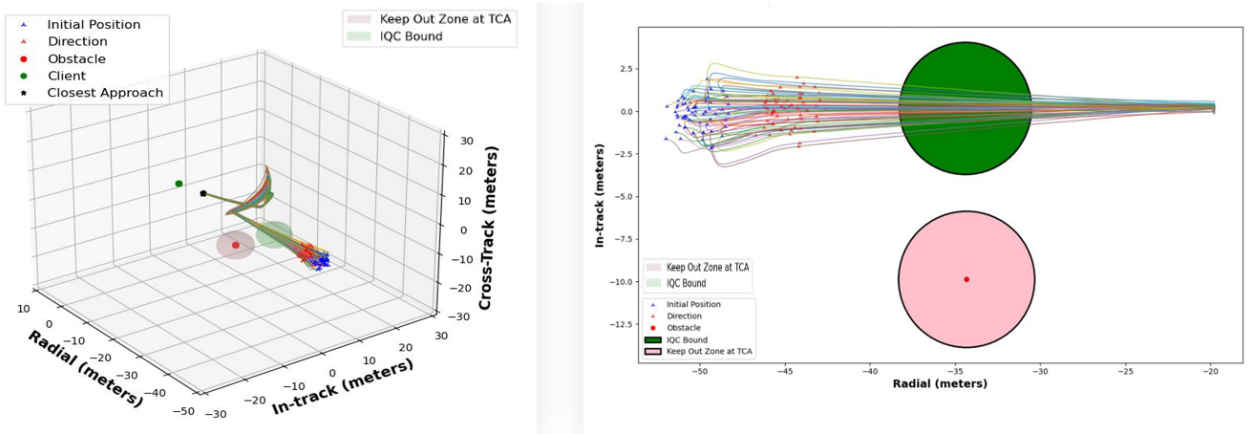

Figure 4-49: 3D vs. 2D plots. Direct approach trajectories ($0s$<t<$1200s$). Validation of CBF+MPC trajectories for MC=100.

When examining the behavior of these trajectories more closely, one can plot a chronological timeline of the times before and at the Time of Closest Approach (TCA) in Figure 4-53 and Figure 4-52. Figure 4-53 shows the behavior at the time of closest approach. A comparison of the averaged radial, in-track, and cross-track coordinates of the various RPO phases can be seen in Figure 4-54 for the standalone MPC and the MPC+CBF schemes. An average of the total fuel consumption during the direct and retreat phases (delta-v) output is also shown in Figure 4-55 below.

On average, the CBF+MPC scheme results in 8% more fuel-expensive trajectories than the standalone MPC. However, it provides the necessary safety guarantees for enforcing the full satisfaction of the KOZ constraint, which is critical for sustainable operations at these altitudes. Out of the 100 simulations run using the MPC scheme, only 33 resulted in safe trajectories. Therefore, to compare the actual fuel consumption when the CBF is used to enforce safety across all trajectories, a third line, representing the average of safe

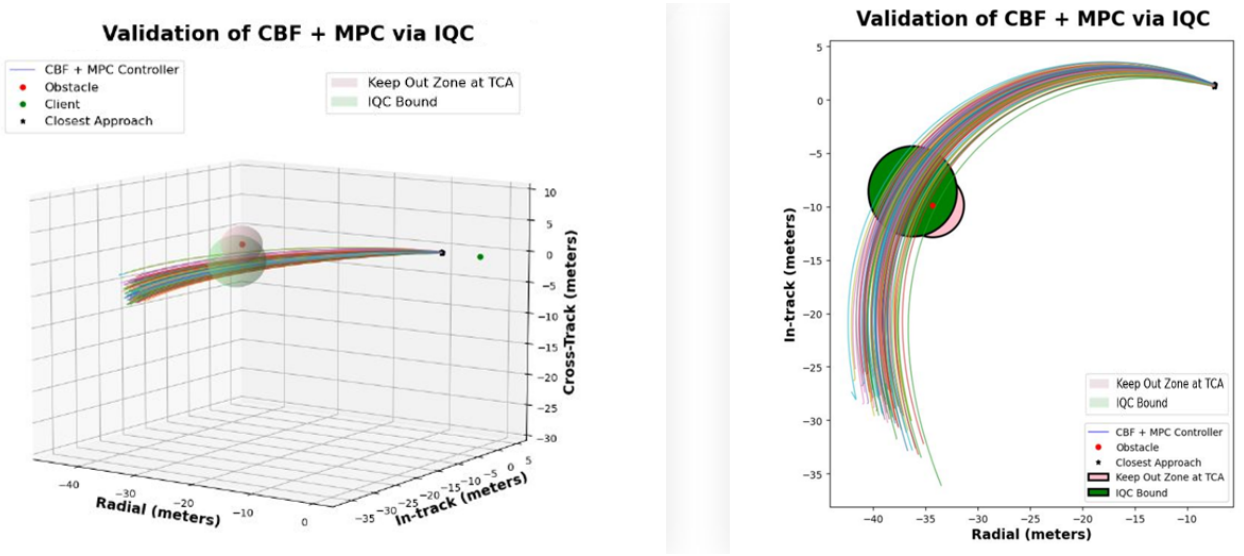

Figure 4-50: 3D vs. 2D plots. Retreat trajectories ($4500s$<t<$6000s$). Validation of CBF+MPC trajectories for MC=100.

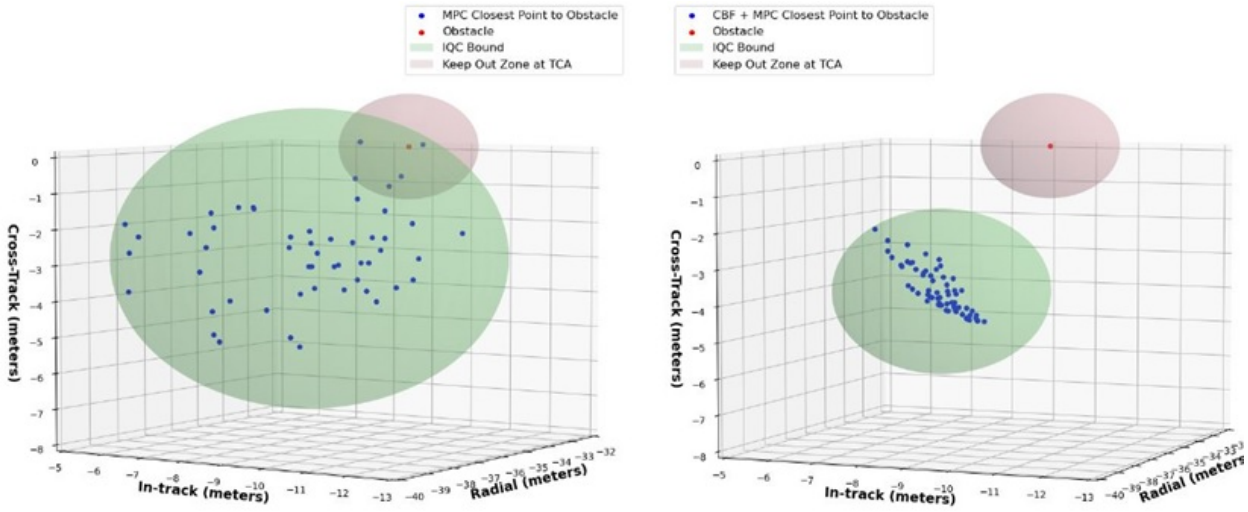

Figure 4-51: Validation of retreat trajectories via the IQC reachability method. IQC bounds (green sphere) considered sensor noise, initial position, state parameter and thruster uncertainties. CBF considered acceleration disturbances by thruster output and unknown motion from obstacle region.

MPC trajectories, was added to the fuel comparison plot shown in Figure 4-58, as seen in Figure 4-56.

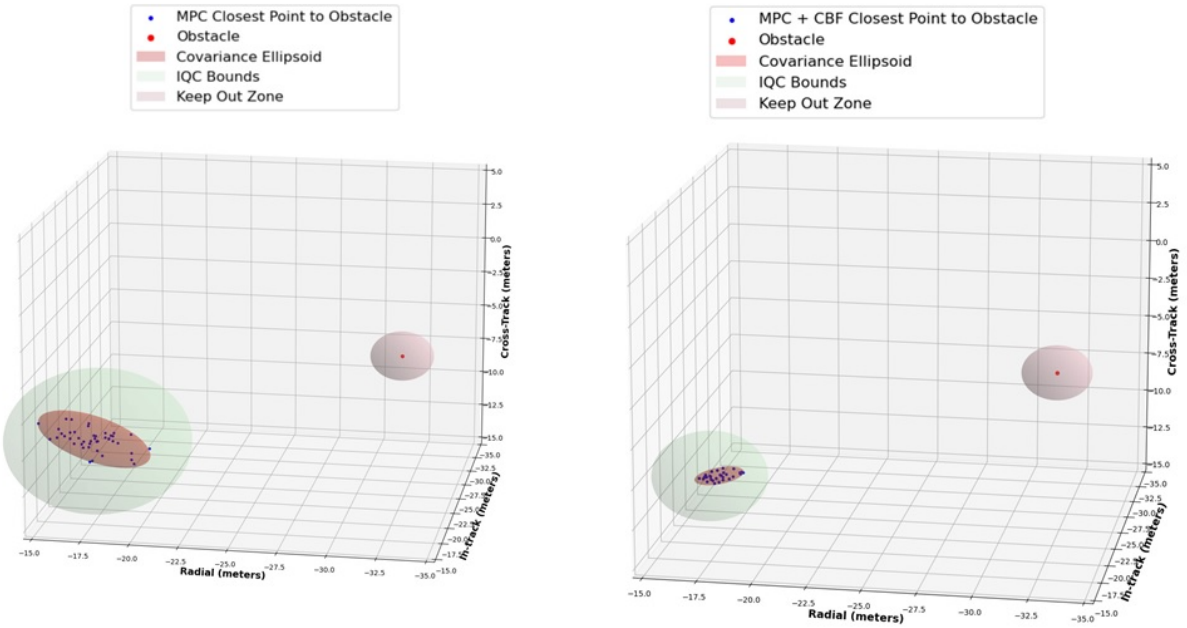

Figure 4-52: Before TCA.Validation of retreat trajectories via the IQC reachability method. IQC bounds (green sphere) considered sensor noise, initial position, state parameter and thruster uncertainties. CBF considered acceleration disturbances by thruster output and unknown motion from obstacle region.

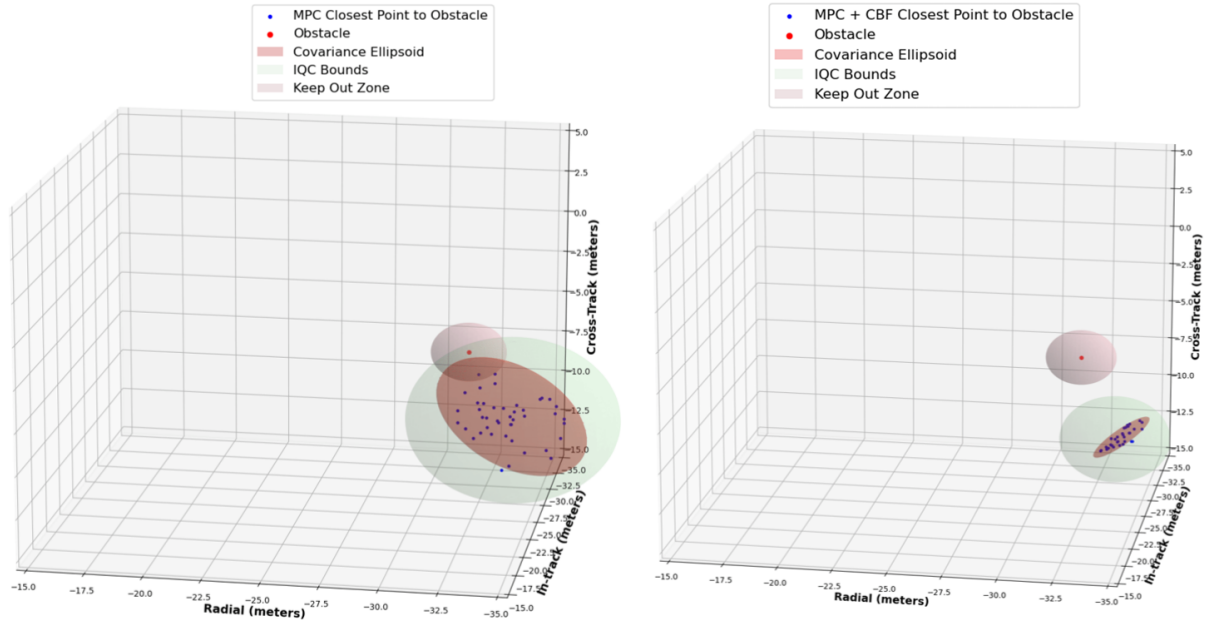

Figure 4-53: At TCA.Validation of retreat trajectories via the IQC reachability method. IQC bounds (green sphere) considered sensor noise, initial position, state parameter and thruster uncertainties. CBF considered acceleration disturbances by thruster output and unknown motion from obstacle region.

When the rocket equation is employed to convert the dV consumption of the Servicer into mass spent, expressed in kilograms, Figure 4-57 is obtained. As a result, the actual average trajectory of the safe MPC

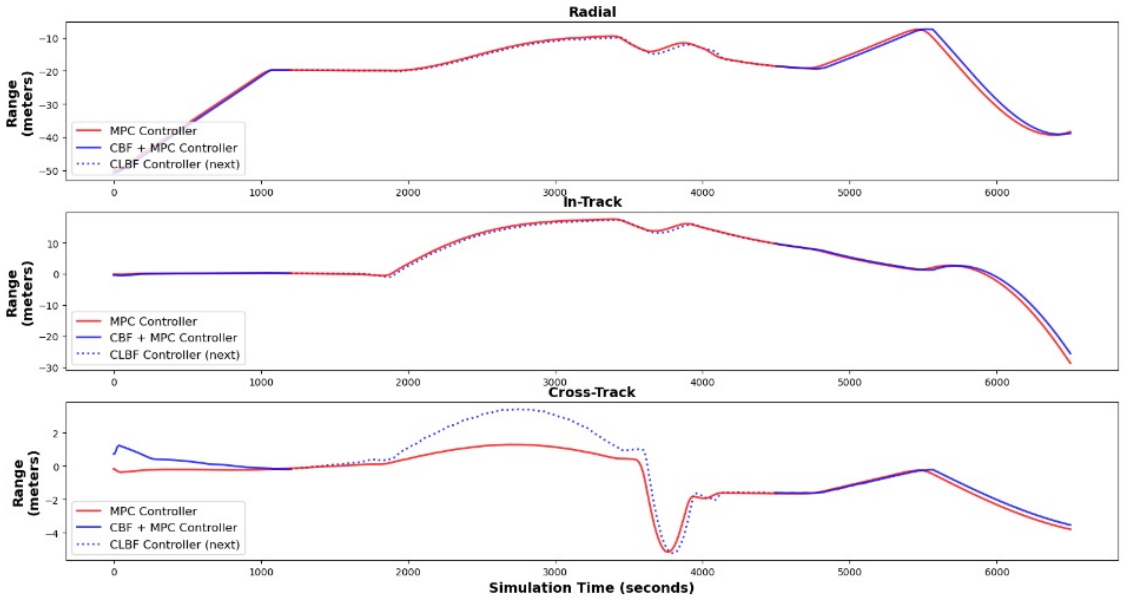

Figure 4-54: Servicer average trajectory: Robust CBF+MPC vs. standalone MPC for MC=100 Monte Carlo runs

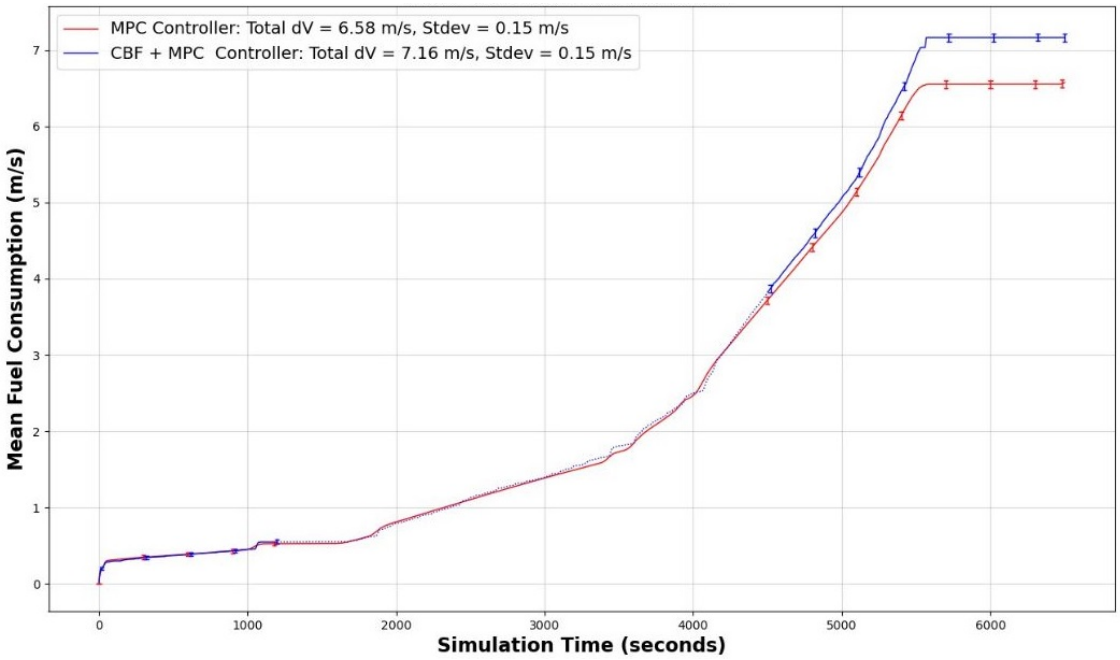

Figure 4-55: Fuel consumption comparison: Robust CBF+MPC vs. MPC standalone schemes for MC=100 Monte Carlo runs. 95% confidence interval.

resulted in a 6.1% more fuel-efficient trajectory than the average of the CBF+MPC trajectory. However, this framework provides robust guarantees for collision-free trajectories.

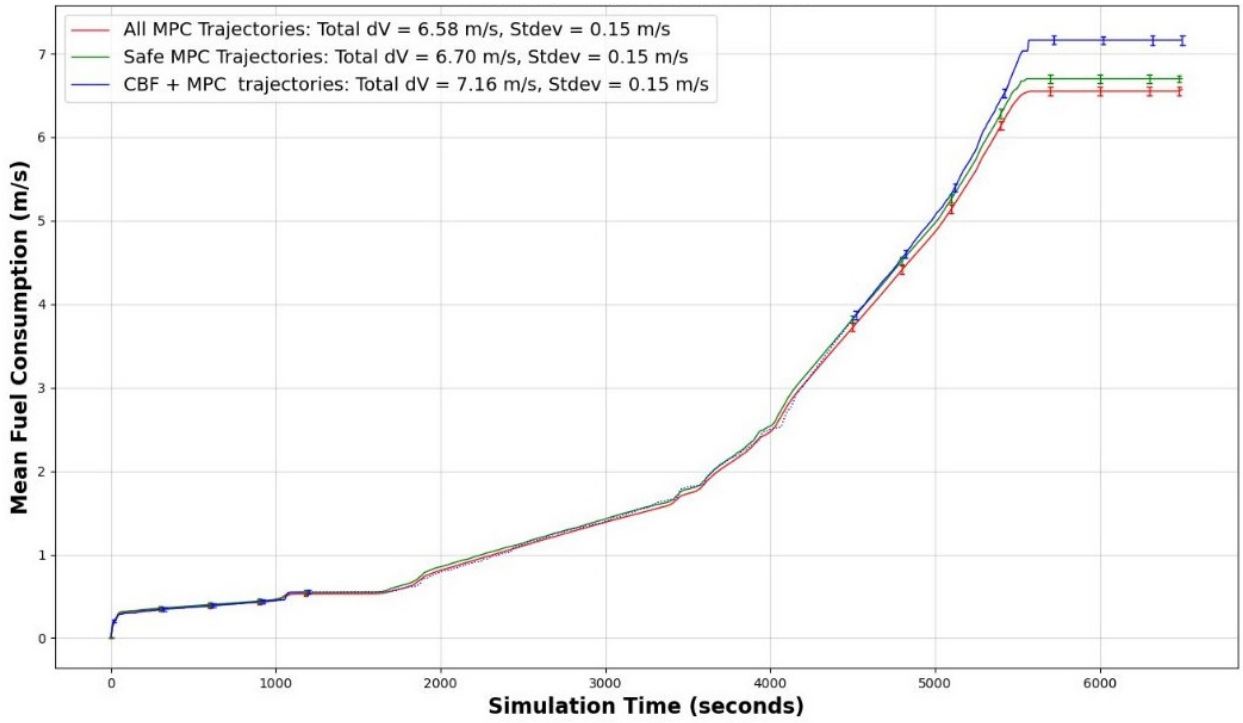

Figure 4-56: Fuel consumption comparison: Robust CBF+MPC vs. MPC standalone schemes for MC=100 Monte Carlo runs. 95% confidence interval

4.3.4 Case Study 4: Robust Inspection (Servicer/Client) via Neural CLBF

For safe proximity operations, it is important that the Servicer avoids the Client by guaranteeing a KOZ constraint to prevent collisions from happening while satisfying the sun-angle requirements (i.e., which is modeled by implementing a LOS constraint). In the LVLH frame, the Client is at the origin, and so the safety requirement can be expressed as a constraint on the state of the Client:

$$x_{min} \leq ||\mathbf{x}|| \leq x_{max} \tag{4.22}$$

for the state $\mathbf{x} = [x, y, z, \dot{x}, \dot{y}, \dot{z}]$, keep-away minimum norm x_{min} and keep-in maximum norm x_{max}. This constraint is illustrated in Figure 4-58.

The relative motion between the Servicer and the Client is transformed from Cartesian to spherical coordinates to capture safety requirements around the NMC. The states are transformed as $x = r\cos(\phi)\cos(\phi)$, $y = r\sin(\phi)\sin(\theta)$, and $z = r\cos(\theta)$ where θ represents the azimuth or inclination of the Servicer with respect to the Client (in degrees), and ϕ is the elevation, argument of latitude, or simply the sum of the argument of perigee (w) and true anomaly (v) (both in degrees). An example of the synthesized CLBF for the inspection mode, positioning, and closest approach RPO phases can be seen in Figure 4-59.

Table 4.12 shows the Client specifications and acceleration disturbances used to compute the neural CLBF for this case study. Servicer specifications were defined earlier in this chapter in Table 4.11. As shown

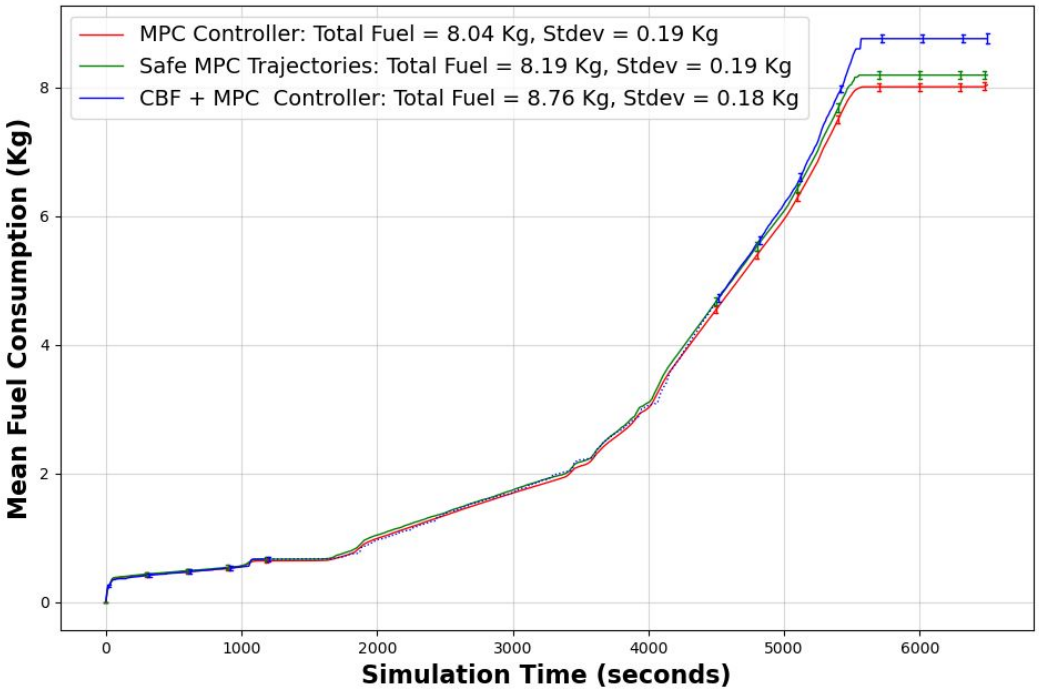

Figure 4-57: Fuel mass consumption comparison: Robust CBF+MPC vs. MPC standalone schemes for MC=100 Monte Carlo runs. 95% confidence interval

Table 4.12: Client specifications and disturbances considered in the CLBF synthesis.

Specifications	Values
Altitude	550 km
Client Location (Cartesian/LVLH frame)	[0.0 m, 0.0 m, 0.0 m]
Drag Coefficient	2.2
Mass	160 kg
Thruster Uncertainty	[-5% m/s^2 to 5% m/s^2]
State Uncertainty (x, y, z, $\dot{x}$, $\dot{y}$, $\dot{z}$)	[-3 m, 3 m]$^3\times$ [-1 m/s, 1 m/s]^3
Uncertainty in Client Motion	[-0.01 m/s^2, 0.01 m/s^2]
Additive Disturbance (Due to Geopotential Uncertainty)	[-0.001 cm/s^2, 0.001 cm/s^2]
Sun-Angle (LOS Constraint)	[135deg to 225deg]

in [31], a single safety certificate containing control Lyapunov functions (for stability) and control barrier functions (for safety) is synthesized. The goal here is to synthesize a CLBF that considers state constraints and the safety of the inspection with high eccentric NMC maneuvers. As shown earlier in this section, the Cartesian coordinates x, y, and z are transformed into spherical coordinates to describe the safety constraint as the azimuth and elevation angle of the Servicer with respect to the Client. Mathematically this is defined as $\theta = \arctan\left(\frac{y}{x}\right)$, and $\phi = \arcsin(\frac{z}{\sqrt{(x^2+y^2)}})$. Figure 4-60 shows the trajectory planner used to learn the data points on the way to the inspection region.

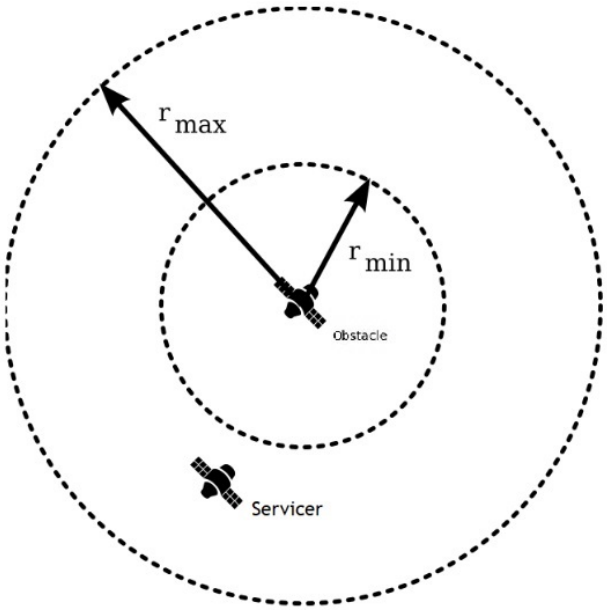

Figure 4-58: The Servicer must remain between a minimum and maximum distance from the Client.

The learning through optimization steps converged to a safety rate of 100% as shown in Figure 4-61. A contour plot of the trained CLBF network is shown in Figure 4-62. A neural network was trained with four hidden layers of 128 tanh activation units each, using stochastic gradient descent to minimize the violation of the constraints in the robust CLBF-QP. The CLBF network was trained on 100,000 data points sampled uniformly from $[x, y, z, \dot{x}, \dot{y}, \dot{z}] \in [-2.5, 2.5]^3 \times [-1, 1]^3$ and $[\theta, \phi] \in [-11 \times [-1.5\,\text{deg}, 1.5\,\text{deg}]$. The violation of constraints is computed on each data point. During the synthesis, no violation was found for the CLBF conditions on this set. Because the CLBF conditions are satisfied throughout the dark set, this region is guaranteed to be invariant.

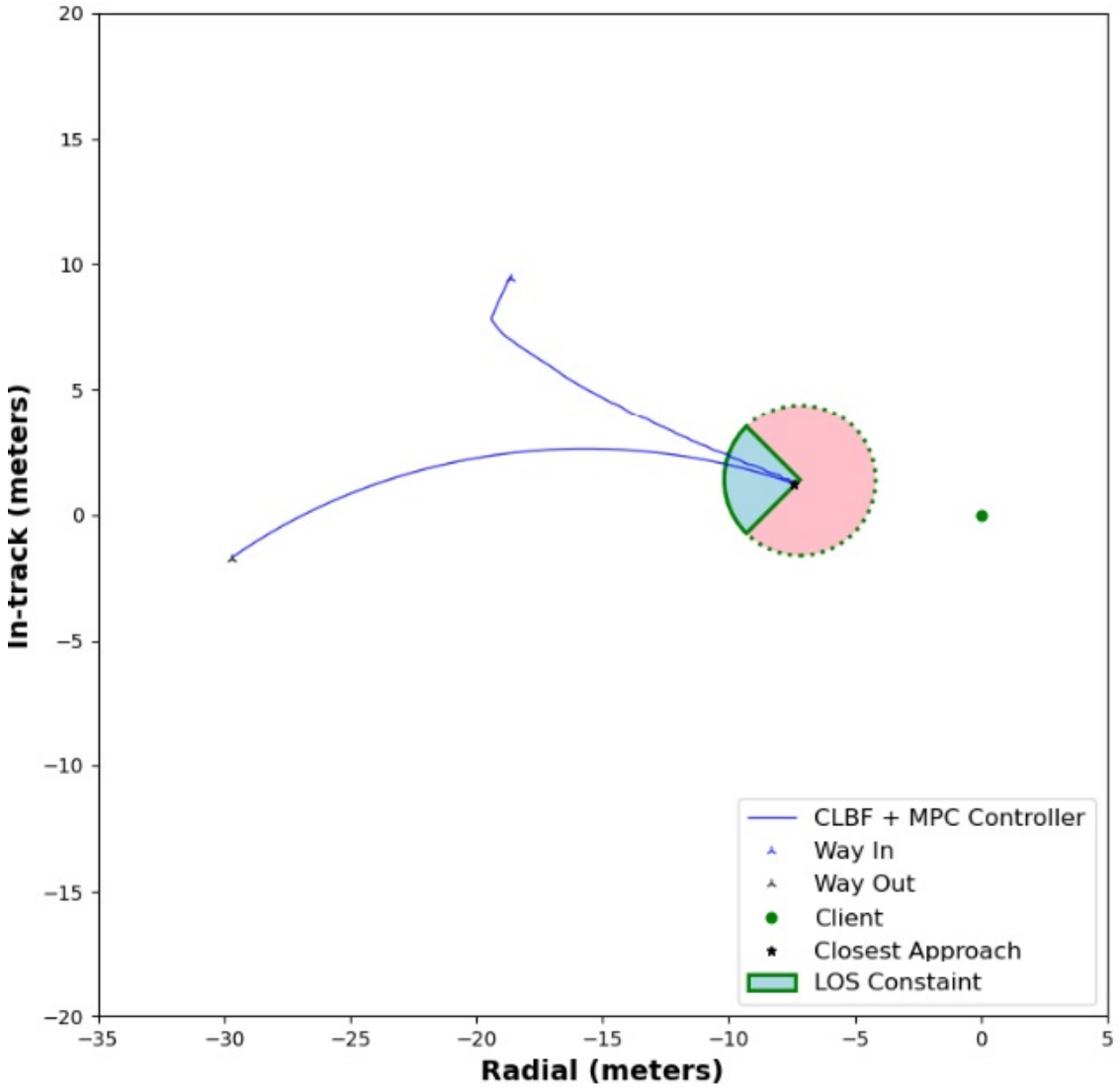

Figure 4-59: 2D example of robust CLBF synthesized for the inspection mode, positioning and closest approach RPO phases.

Figure 4-63 shows the derivative of the control Lyapunov barrier function. This figure shows the region where the synthesized function is valid (i.e., unsafe if $max(dV/dt, 0) > 0$ or safe if $max(dV/dt, 0)<0$). This means that if the derivative gradient is greater than 0, the CLBF is *not always* valid for that region. On the other hand, if the derivative is less than 0 (or negative), the CLBF *is always* valid in that region. Because the interest for safety is inside the LOS constraint, which represents the area inside the green cone, the CLBF synthesis is valid for the inspection mode, positioning, and closest approach RPO phases to satisfy sun-angle and keep-out zone requirements.

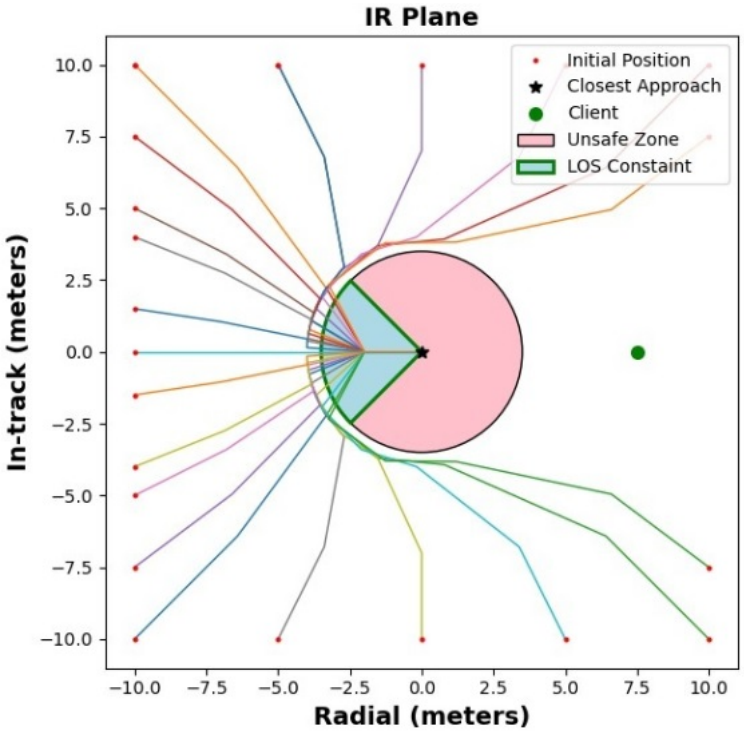

Figure 4-60: Trajectory planner for learning safe/unsafe sets. Inspection requirements from $135deg$ to $225deg$.

A comparison of the unsafe vs. safe inspection trajectories can be seen in Figure 4-64. The goal now is to validate CLBF+MPC scheme with MC runs and the IQC reachability method. As a result, one hundred trajectories were executed to validate the CBF + MPC scheme as shown in Figure 4-65. In order to validate that the CLBF+MPC scheme filtered the MPC output properly, a closer look of the LOS region can be seen in Figure 4-66. Adding the IQC bound at TCA to Client also validates the robustness of the CLBF filter to keep trajectories in this region as shown in Figure 4-67.

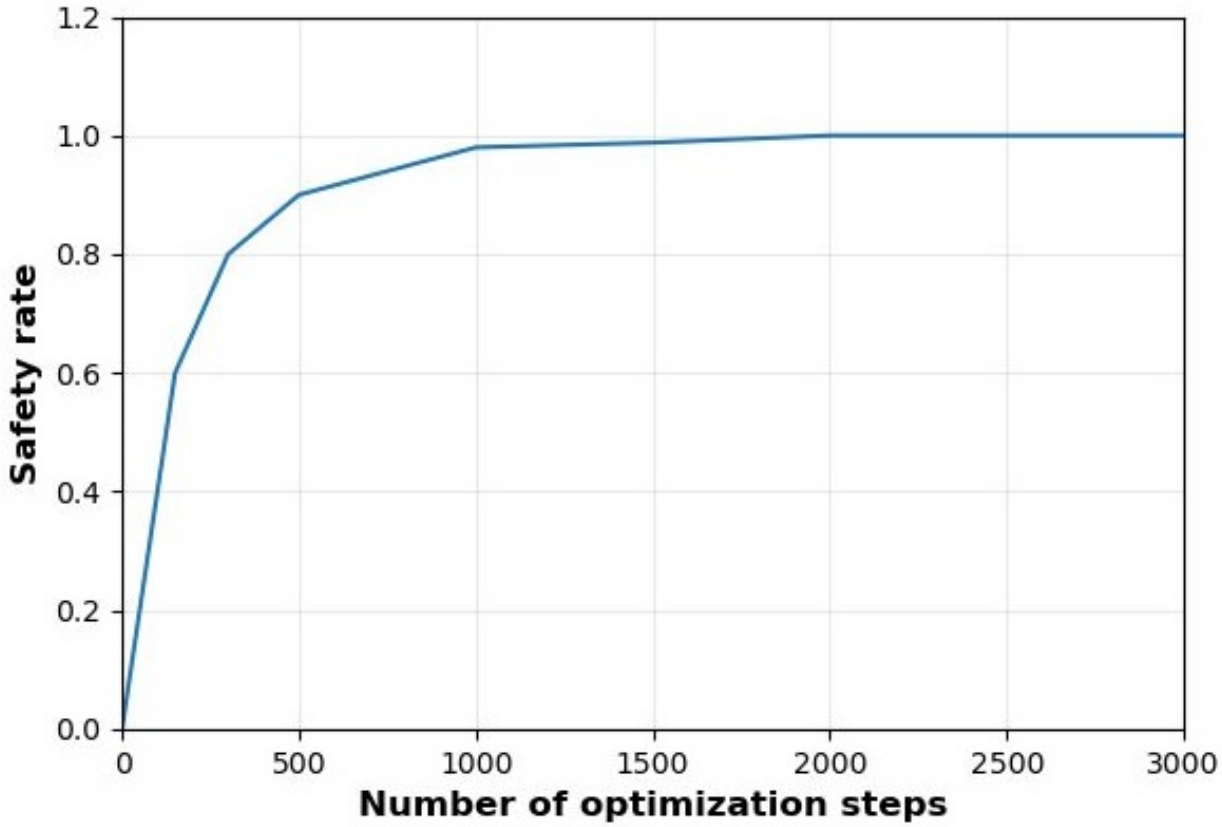

Figure 4-61: Running various simulations to obtain a CLBF safe region accuracy for the Servicer controller. Safety rate converges to 100% in less than 3000 optimization steps.

.

A comparison of the averaged radial, in-track, and cross-track coordinates of the inspection mode, positioning, and closest approach phases can be seen in Figure 4-68 for the standalone MPC and the MPC+CLBF schemes.

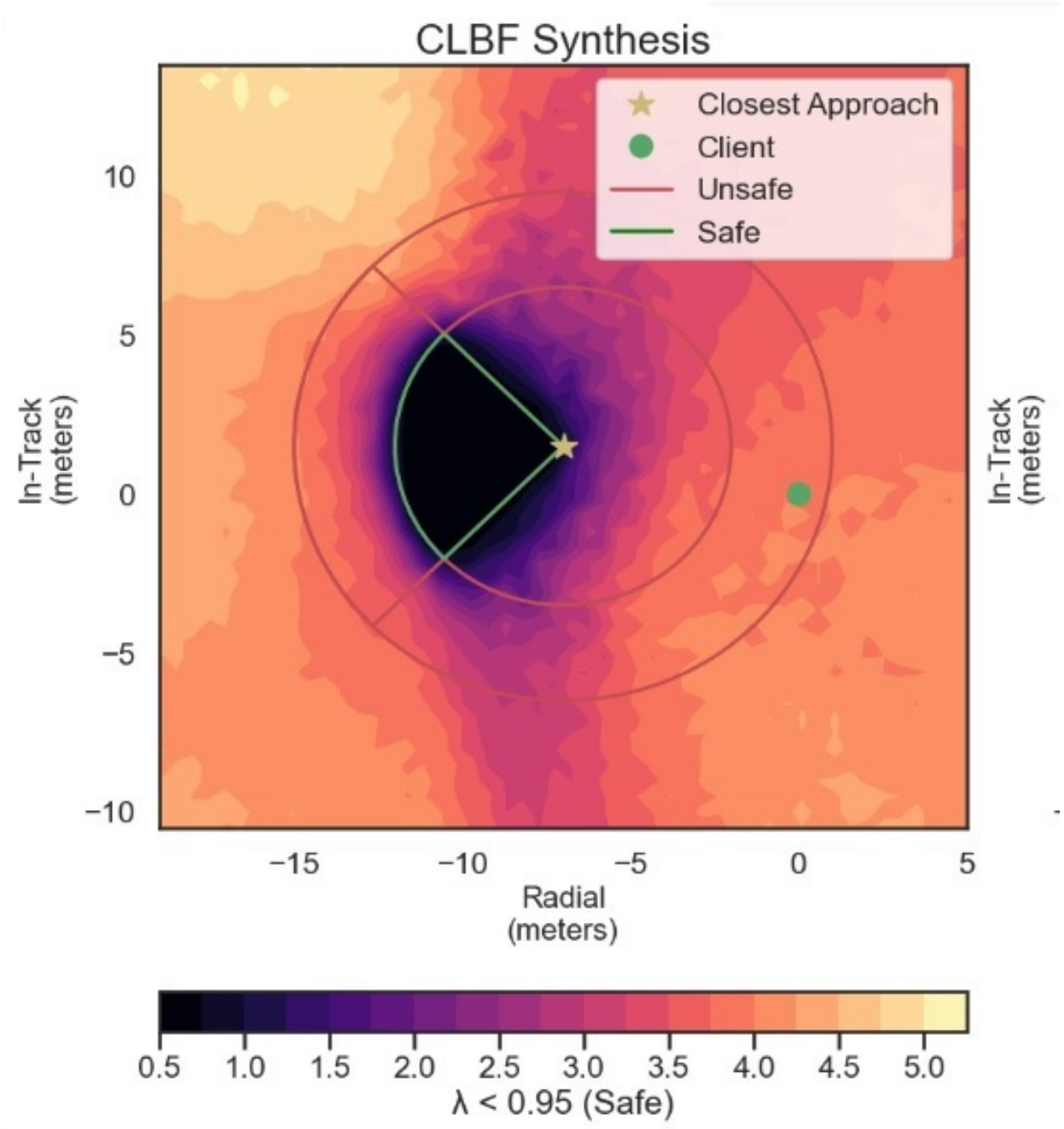

Figure 4-62: The robust CLBF synthesized using a neural network and stochastic gradient descent. The dark contour indicates the region that the CLBF guarantees to be forward invariant: all states starting between the green LOS constraint will remain within that region indefinitely.

An average of the total fuel consumption during the inspection mode, positioning, and closest approach phases (delta-v) output is also shown in Figure 4-69. On average, the CLBF+MPC scheme incurs a 2.4% higher fuel cost for executing trajectories during the inspection phase compared to the standalone MPC. However, it provides the necessary safety guarantees for fully enforcing the LOS constraint, which is critical

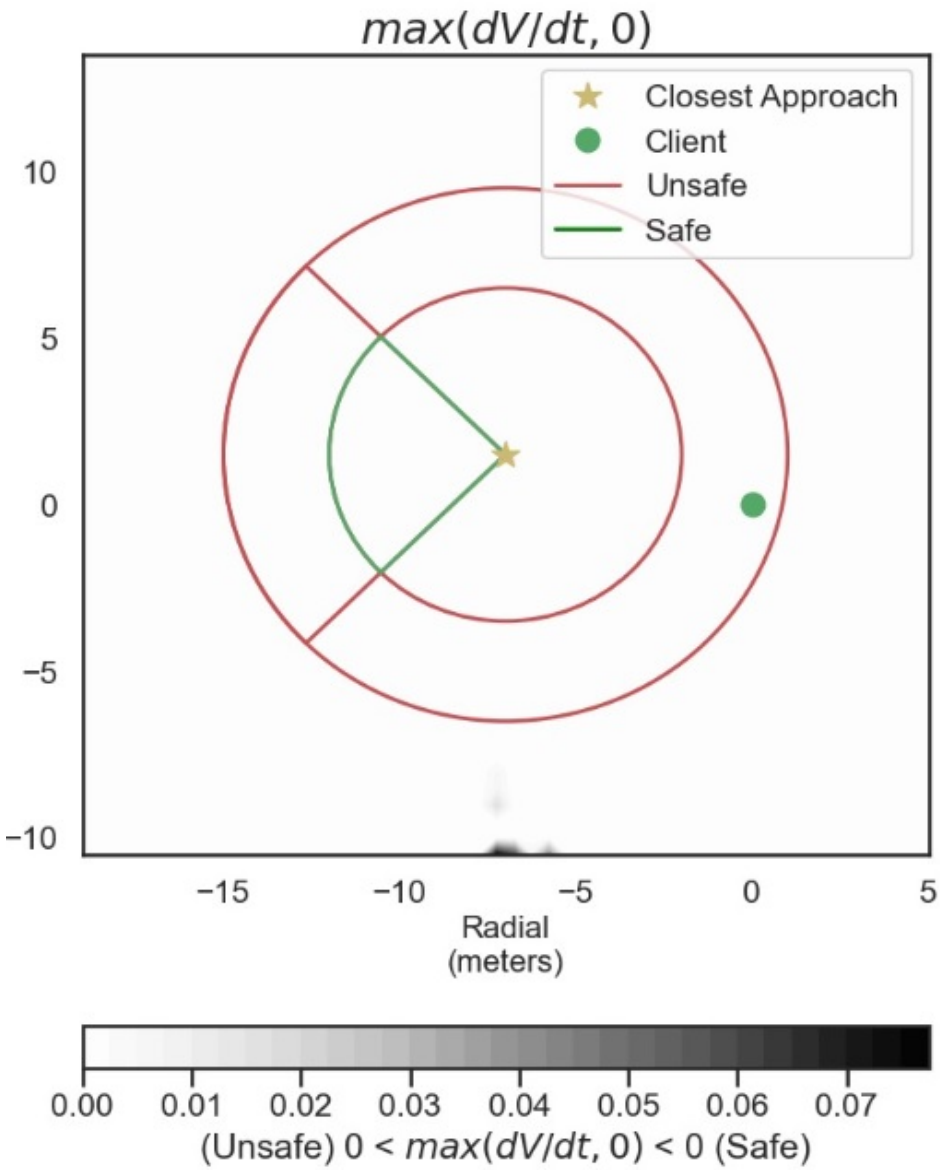

Figure 4-63: Derivative of the CLBF using the point-wise maximum function (max). Trajectories starting at states within the invariant set of $\lambda < 0$ are guaranteed to remain within that set when controlled using the robust CLBF-QP.

for sustainable operations at these altitudes. As mentioned in the previous section, out of the 100 simulations run using the MPC scheme, only 33 resulted in safe trajectories. Hence, a third line was added to the fuel comparison plot shown in Figure 4-69, to compare the actual fuel consumption when the CLBF is used to enforce the sun angle requirements across all trajectories. This comparison is in Figure 4-70.

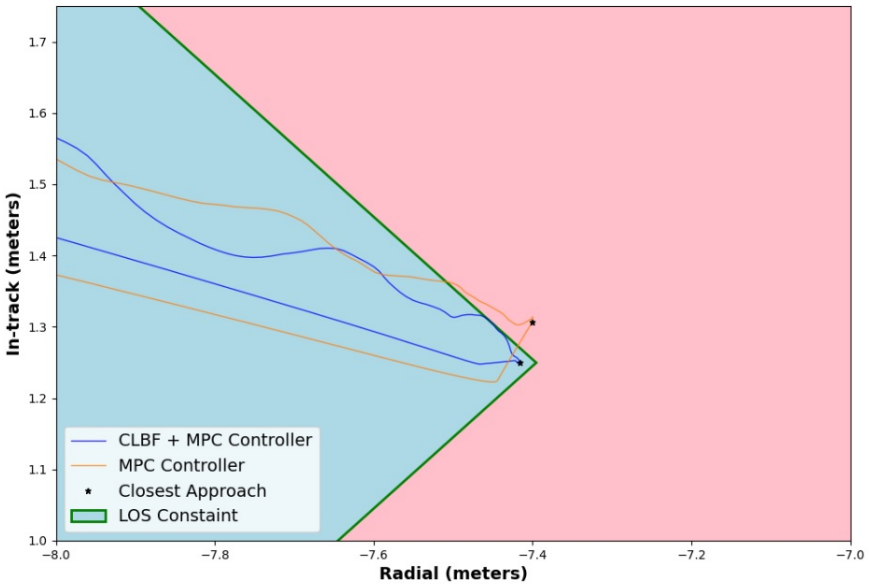

Figure 4-64: Comparison between robust CLBF+MPC and the standalone MPC schemes. IR-Plane

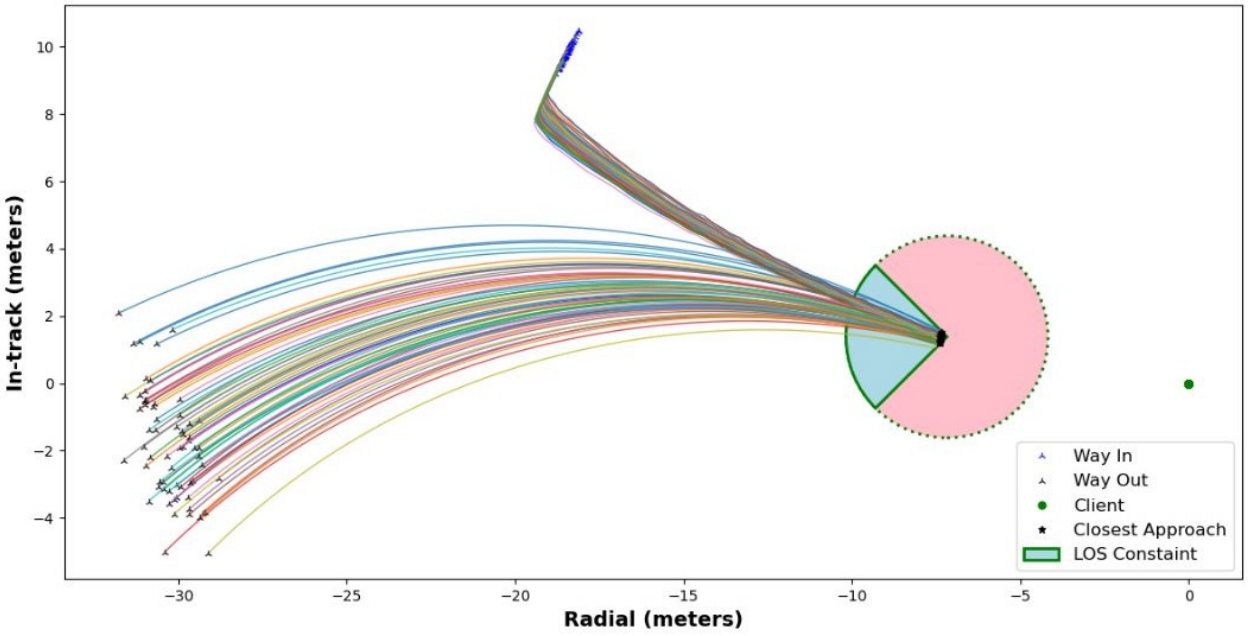

Figure 4-65: CLBF+MPC robust controller. The trajectory of Servicer in relative motion with Client for MC=100 Monte Carlo runs.

When the rocket equation is employed to convert the dV consumption of the Servicer into mass spent, expressed in kilograms, Figure 4-71 is obtained.

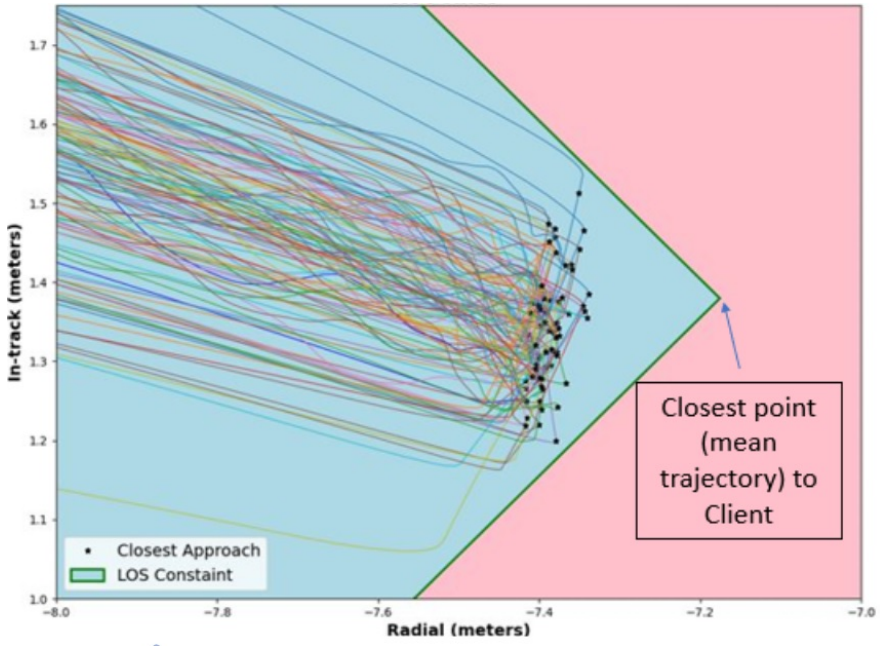

Figure 4-66: Closer inspection within the LOS region. Robust CLBF+MPC scheme for MC=100 Monte Carlo runs.

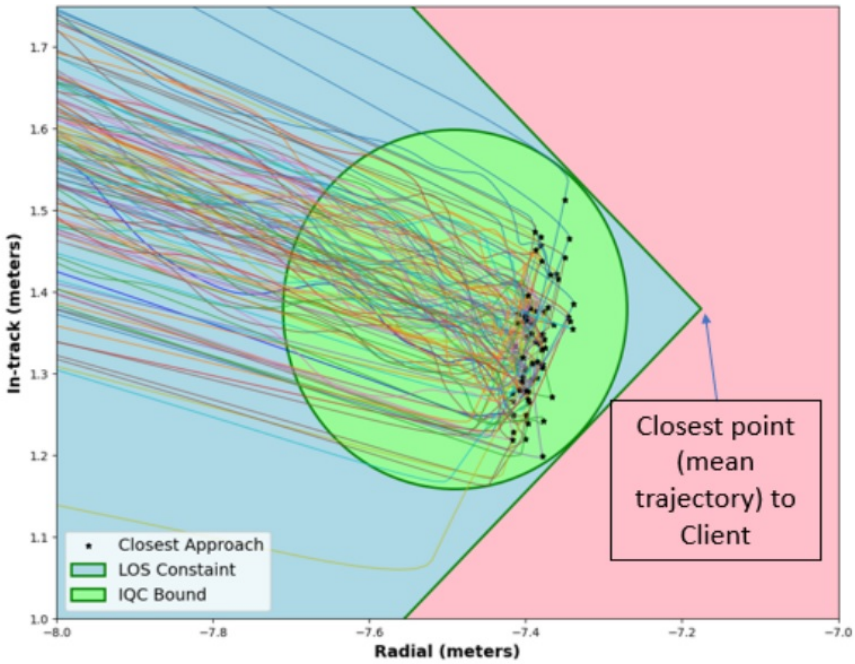

Figure 4-67: Zoom-in of the LOS region during the RPO inspection phase. Robust CLBF+MPC scheme for MC=100 Monte Carlo runs.

The safe MPC resulted in an actual average trajectory that was 1.8% more fuel efficient than the average trajectory of the CBF+MPC scheme. Despite this advantage, this safety framework ensures robust guarantees for satisfying mission requirements, such as sun-angle constraints.

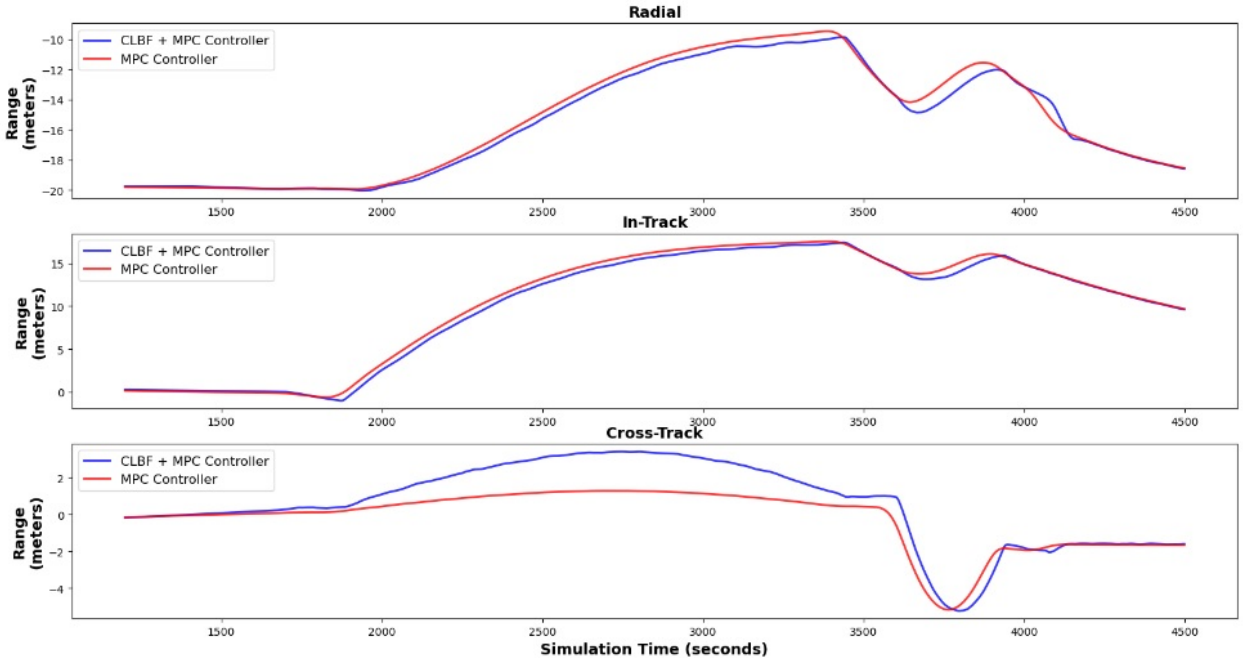

Figure 4-68: Servicer average trajectory: Robust CLBF+MPC vs. MPC standalone schemes for MC=100 Monte Carlo runs.

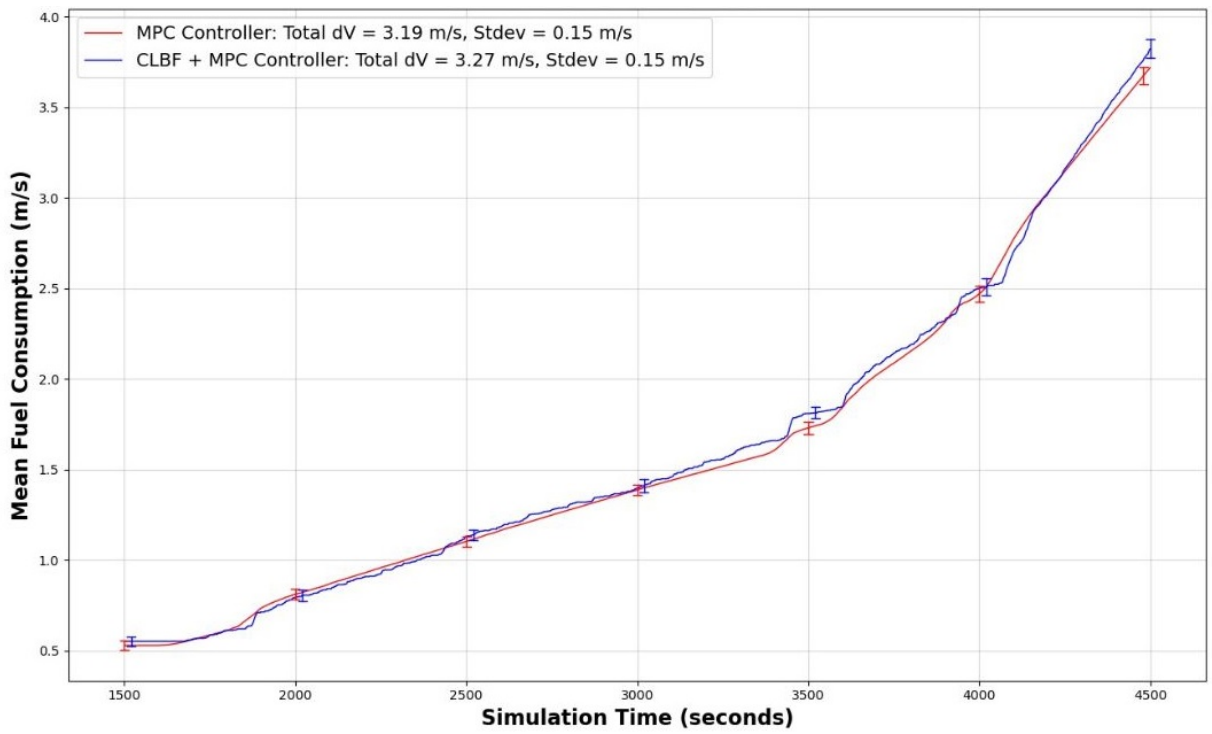

Figure 4-69: Fuel consumption comparison: robust CLBF+MPC vs. MPC standalone schemes for MC=100 Monte Carlo runs. 95% confidence interval.

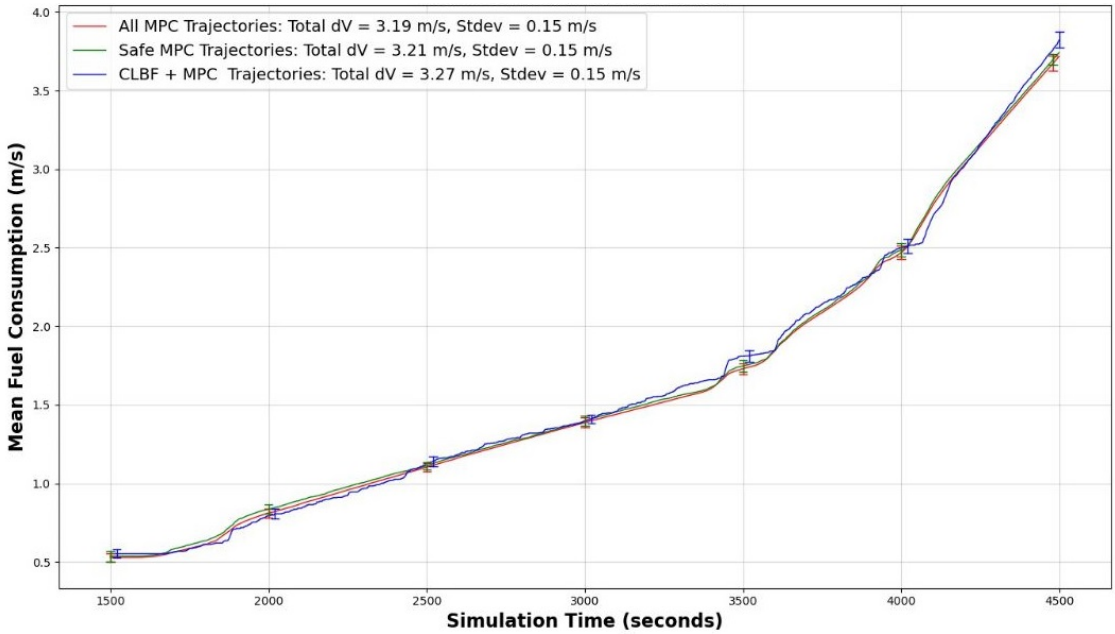

Figure 4-70: Fuel consumption comparison: Robust CBF+MPC, Safe MPC MPC standalone Trajectories for MC=100 Monte Carlo runs. 95% confidence interval

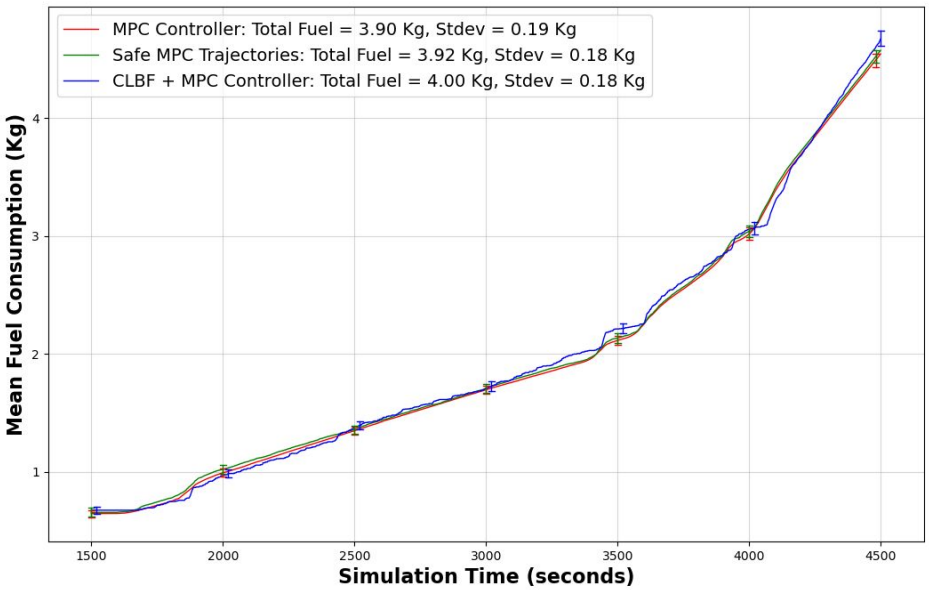

Figure 4-71: Fuel mass consumption comparison: Robust CBF+MPC vs. MPC standalone schemes for MC=100 Monte Carlo runs. 95% confidence interval

4.4 Collision Risk Mitigation

The proposed robust architecture for RPO activities was shown in Figure 3-3. For risk evaluation, three different metrics are used: miss distance, Mahalanobis distance in position space, and the PC metrics. As

shown earlier, the architecture indicates that if the IQC bounds exceed the safety threshold by these metrics, another initial guess for dV maneuver recommendation would be provided to minimize the collision risk. For faster computation, a two-dimensional (2D) PC is assumed where the three-dimensional Gaussian distribution of the relative position at the time of closest approach (TCA) is marginalized as a 2D Gaussian distribution on the encounter plane [5, 23]. The encounter plane is a plane perpendicular to the relative velocity at TCA. This thesis leverages relative velocity in the rotating Hill frame to construct the encounter plane. The PC is given by

$$p_c = \int_{A_{\text{hb}}} \frac{1}{2\pi\sqrt{|P_{\boldsymbol{dd}}|}} \exp\left(-\frac{1}{2}\boldsymbol{d}\cdot P_{\boldsymbol{dd}}^{-1}\cdot\boldsymbol{d}\right) dA \tag{4.23}$$

where $\boldsymbol{d}$ and $P_{\boldsymbol{dd}}$ are the relative position vector and its covariance mapped onto the encounter plane; A_{hb} is the area swept by the combined hard body. The study uses a circular area with a predefined hard body radius R_{hb}. The 2D PC computes a total collision probability for an isolated encounter, assuming the relative velocity is high enough that the relative motion is rectilinear. Another assumption is that relative covariance remains constant during an encounter. In general, 2D PC provides accurate collision probabilities for low Earth orbit conjunctions due to their high relative velocities. For RPO trajectories, the relative velocities are much smaller. However, assuming constant access to accurate navigation solutions, the time the spacecraft takes to travel a $1-\sigma$ position uncertainty could still be small, which motivates the use of the 2D PC. This thesis shows numerical computation to compute 2D PC formulation by NASA CARA[38, 5], miss distance, and Mahalanobis metrics. By definition, 2D PC is only applicable at TCA. However, this thesis computes 2D PC at any given time as it provides some insight into the risk trend. 2D PC computed at a point different from TCA is equivalent to 2D PC where the relative motion is approximated as a rectilinear motion with the position and velocity at that instance of time. Furthermore, expanding the collision risk mitigation framework to include 3D probability of collision validation [57] and examination of the dilution region [91] to determine robustness of probability of collision metric is future work.

4.4.1 Collision Risk Assessment (Prior to Neural Lyapunov/IQC bound)

The Figure 4-72 shows the values of the metrics used to determine the risk of the Servicer trajectory violating the obstacle KOZ constraint. Similarly, Figure 4-75 shows the same metrics applied to the Servicer trajectory at the closest approach to the Client during the inspection phase.

At NASA CARA, Pc values greater than 1E-07 merit operational attention, and values greater than 1E-04 require mitigation actions [3]. As a result, the Pc thresholds for the closest approach to the Client and obstacle exceeded the safety criteria specified by NASA standards.

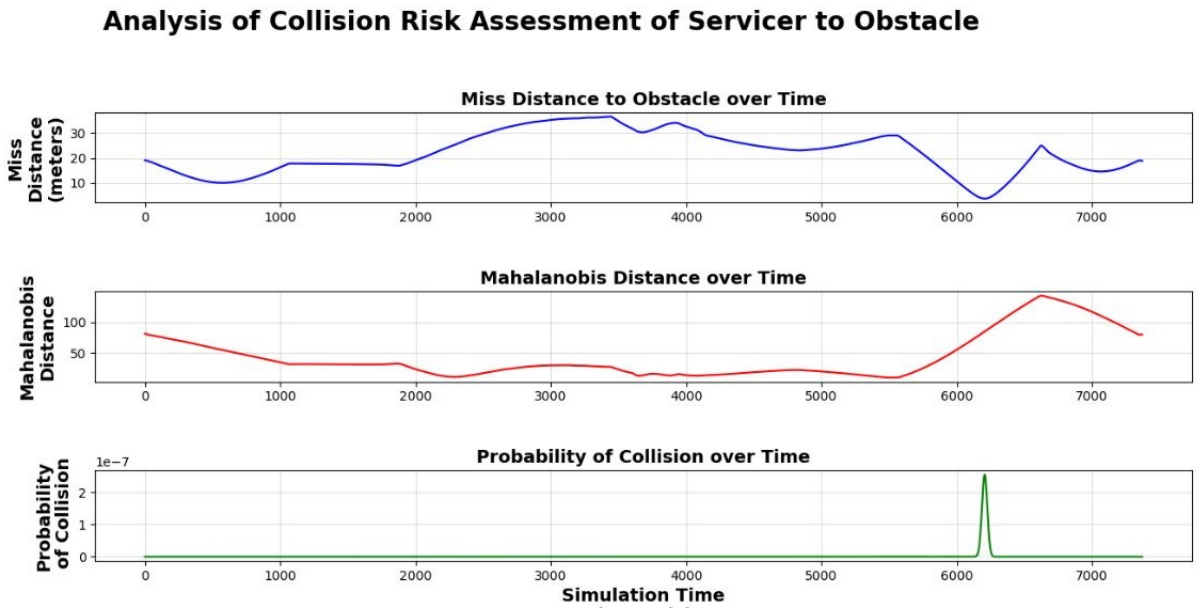

Figure 4-72: Collision risk assessment of Servicer during closest approach to obstacle (retreat phase). Values above 1E-07 merit operational attention (medium risk).

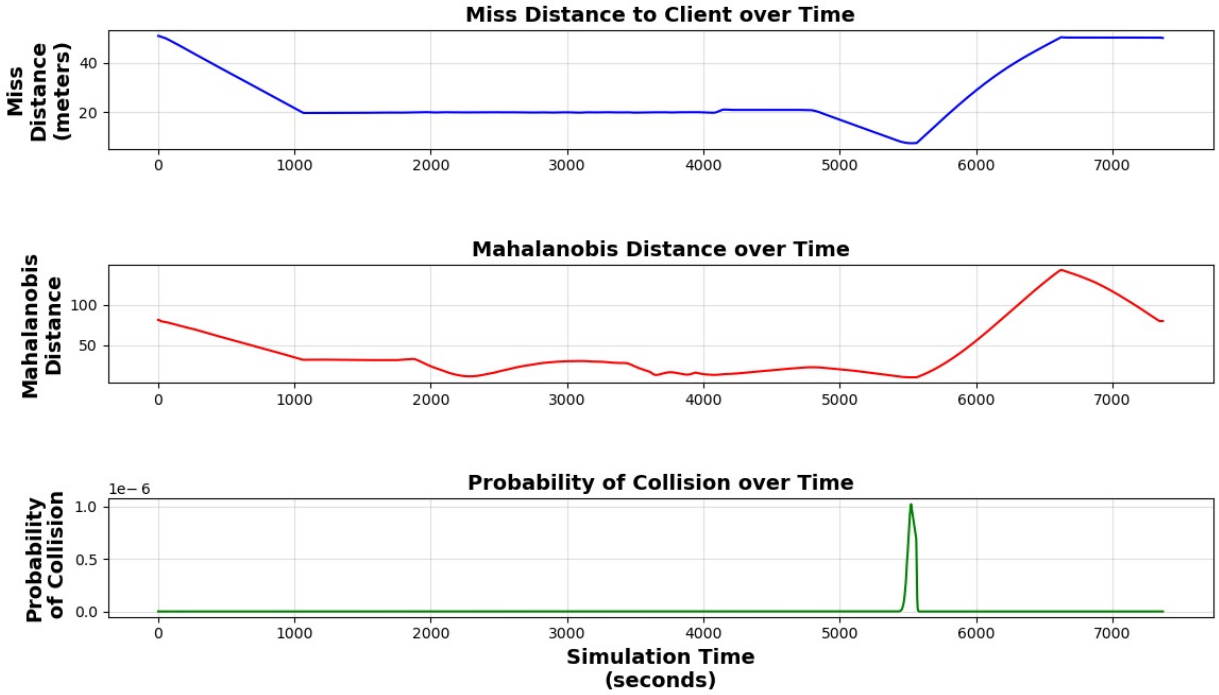

Figure 4-73: Collision risk Assessment of Servicer during closest approach to obstacle (retreat phase). Values greater than 1E-07 merit operational attention (medium risk).

4.4.2 Collision Risk Minimization (After applying Neural Lyapunov/IQC bound)

In order to minimize collision risk, it is crucial to examine how these metrics change as the Neural Lyapunov and IQC are applied to the GN&C of this RPO mission. For the 100 trajectories, the same metrics are

applied to conclude if this platform reduces the collision risk. Figure 4-74 shows the values of these metrics to determine the risk of the Servicer trajectory with respect to the obstacle object for MC=100 Monte Carlo runs. The PC values do not exceed 1E-07 which means that none of the trajectories require mitigation actions. The same analysis is applied in Figure 4-75, which shows the same metrics applied to the Servicer trajectory at the closest approach to the Client during the inspection phase for MC=100 Monte Carlo runs. Similarly, the PC values do not exceed 1E-07, which means that none of the trajectories require mitigation actions. As a result, this platform offers a new methodology for providing safety guarantees during RPO operations via robust optimization and formal methods techniques. The overall framework, which enables a robust GN&C platform, is shown in Figure 4-76.

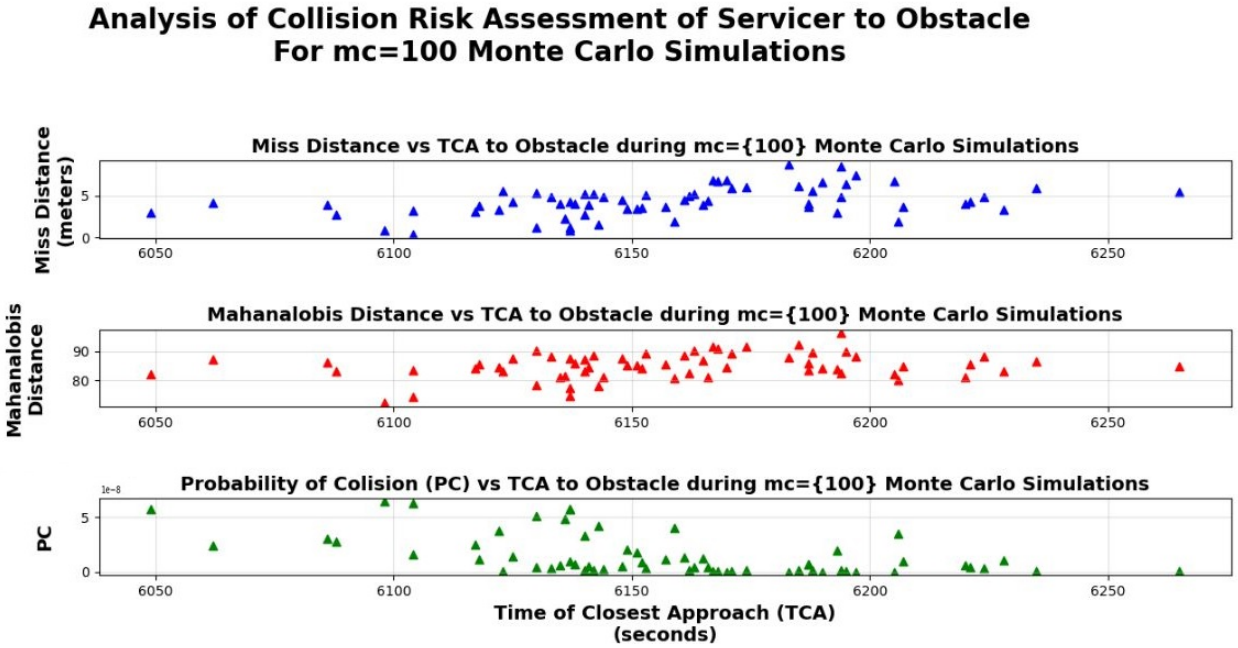

Figure 4-74: Collision risk minimization of Servicer during closest approach to obstacle (retreat phase) for MC=100 Monte Carlo Runs.

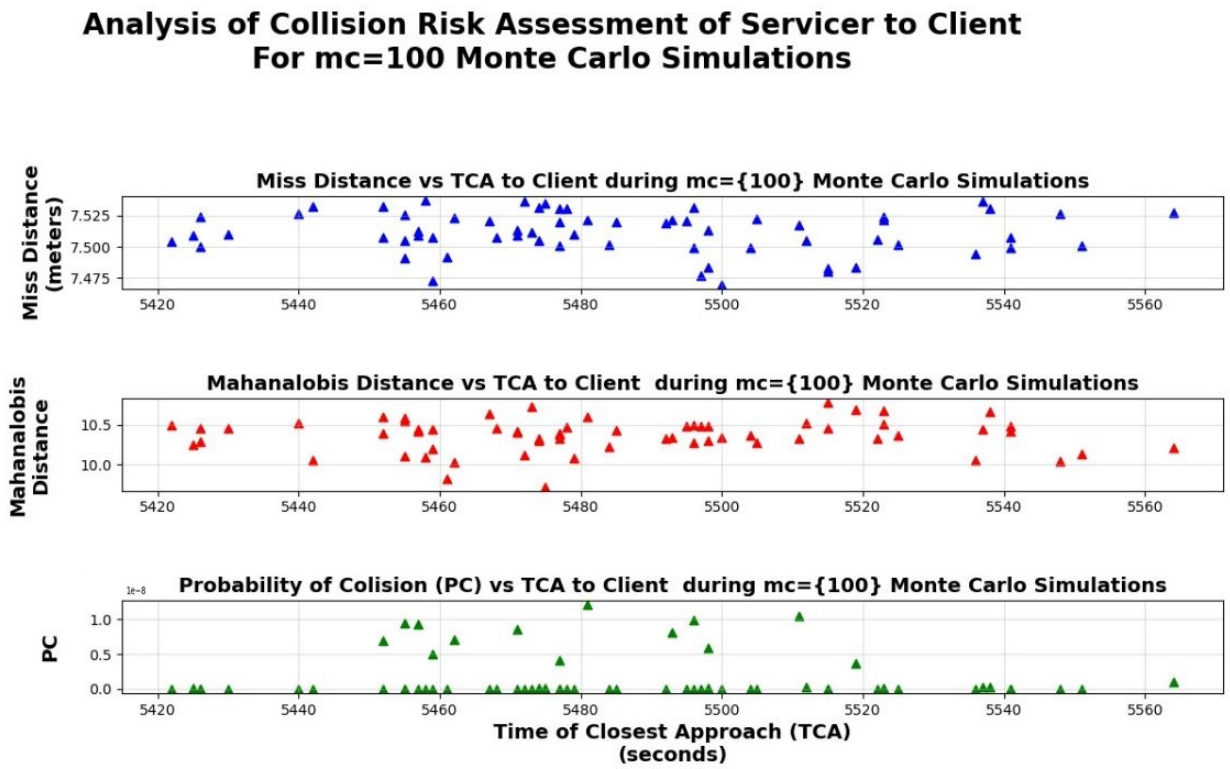

Figure 4-75: Collision Risk minimization of Servicer during closest approach to Client (inspection phase) for MC=100 Monte Carlo runs.

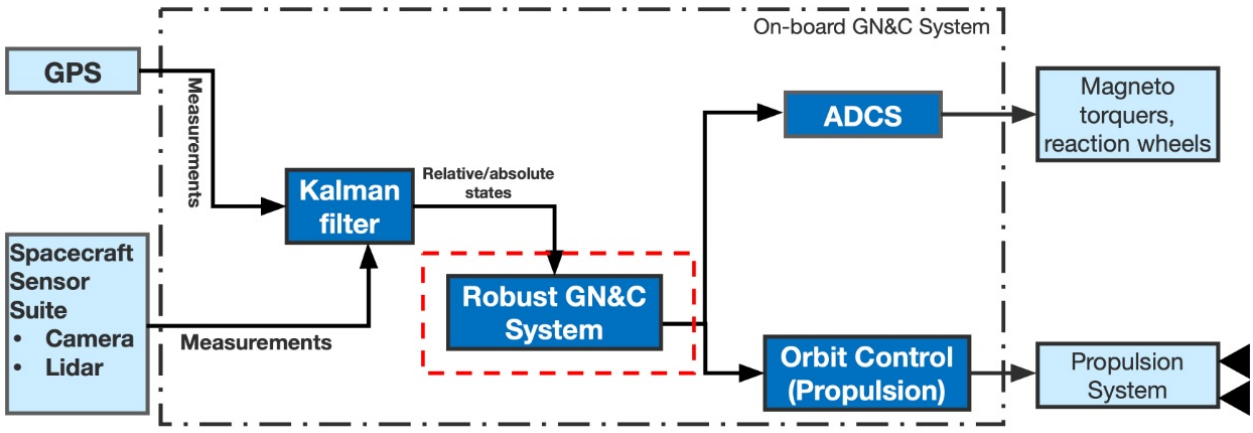

Figure 4-76: Robust GN&C Platform.

Chapter 5

Conclusion

5.1 Summary

The growth in space operations will require both increased spacecraft control autonomy and techniques to provide robust safety guarantees for satellite inspection, repair, debris retrieval/removal, and on-orbit assembly activities at various altitudes. Because of atmospheric drag, the Earth's non-uniform nature of gravity effects, and overall model uncertainties, performing these services becomes more challenging in LEO altitudes. The Reachability, control barrier functions, and integral quadratic constraints techniques presented in this thesis provide a method to obtain strong safety guarantees for complex systems featuring the interaction of multiple subsystems with significant complexity. These methods, if applied correctly, can provide safety guarantees for interaction between multiple spacecraft controlled by different satellite operators and offer insight into collision avoidance algorithm control performance under different levels of information sharing. The distinctive aspect of this approach, which sets it apart from other methods, lies in its deterministic methodology that employs mathematical assurances. This innovative technique is a departure from the more conventional stochastic approaches that have been widely used in the past. By utilizing deterministic principles, this method offers a more reliable and predictable foundation, in contrast to the uncertain nature of stochastic methods. In addition, this approach avoids many of the proprietary issues associated with screening operator interactions by using reachability-based and robust optimization methods, and does not require exquisitely accurate orbit propagation to ensure safety. It can be applied generically in a controller-agnostic manner without requiring extensive customization for each user or control algorithm. Nevertheless, this approach is reliant on the mutual sharing of timely, accurate decision-quality satellite ephemerides for relevant spacecraft.

These contributions enable safety verification of autonomous GN&C capabilities, which can reduce the cost and operational efforts of software testing. This thesis considers the analytical formulation of LPE relative motion dynamics, using the GA-STM method, with equinoctial element formulation, that can be applied to general Client's orbits under the assumption of J_2 perturbation. Different representations of the

relative state between the Client and Servicer, and transformation between them are explored to enable this robust GN&C architecture to satisfy mission requirements of RPO missions. The safety verification platform generates fuel-optimal maneuver commands while ensuring safety. The risk minimization is then performed by predicting the relative state-error covariance, and the result identifies key risk metrics such as miss distance, Mahalanobis distance, and probability of collision. The risk analysis and subsequent dispersion analysis also confirm that the trajectory generated by the control policy becomes safe when the proposed methodology is applied to the GN&C scheme. The LQR and MPC control laws are used for the case studies presented in this thesis. The navigation analyses are also performed, which demonstrates the capabilities to obtain an accurate navigation solution only using onboard measurements. The control commands from the proposed path planning policies are also evaluated running high-fidelity dispersion analyses via Orekit. The results confirm that the proposed methodology can enforce safety guarantees in proximity operations between satellites by applying slightly more fuel (6.1% for the first and last phases and 1.8% for the inspection phases), while achieving the required reconfiguration under the influence of unmodeled disturbances, uncertainties in actuation, exogenous disturbances, and nonlinearities due to the approximation of the first-order J_2 dynamics.

These contributions could enable mission assurance for commercial satellite operators by fulfilling a currently underserved niche relating to controller safety verification. The author envisions these algorithms being applied in two main ways: providing feedback during controller development and offering formal certification of controllers before operational use. During development, this technology complements traditional simulation-driven controller development, providing additional insight into controller robustness, optimality, and safety where traditional techniques face limitations. Once an operator decides on a final controller design, the platform proposed here could provide formal safety certification for that controller. Such certification could be used as part of an operator's internal validation and verification process, and externally as a reputational tool to signal the operator's commitment to space safety generally to insurers or to regulators (particularly for new entrants or high-altitude constellations). In the long run, this safety verification platform could become an industry best practice and would be adopted by civil regulators. A regulator might either mandate controller verification or provide expedited review and authorization for missions that demonstrate certification. As a result, as RPO companies demonstrate commercial feasibility to perform RPO operations in LEO, this platform can be used to create more robust GN&C platforms for the new era of on-orbit services across all orbits.

5.2 Contributions

The following is a list of contributions that this thesis provides to the field. The major numbered contributions align with the thesis objectives described in Section 1.4, while the subpoints go into more detail about the specific contributions.

1. Deterministic reachability technique to analyze robustness of GN&C systems. This contribution consists

of a framework capable of generating uncertainty bounds for state-related output (i.e., Servicer relative position/pointing attitude with Client) by performing reachability analysis deterministically for closed-loop controllers. The innovative reachability technique captures state and actuation uncertainties and nonlinearities, and attitude disturbances affecting the control output of the Servicer with respect to the Client.

   (a) Developed a novel IQC-reachability framework that captures uncertain initial conditions, sensor noise as white-signal IQC class, actuation uncertainty and exogenous disturbances with Δ IQC operators.

   (b) Integrated complex set of relative equations of motion that enables the analysis of the RPO mission across all orbits.

   (c) Implemented an LQR design method for the reachability analysis of the state uncertainty output, and implemented the PD control type for sensitivity analysis of the Servicer's attitude with respect to the Client.

   (d) Developed a collision risk minimization procedure that enforces safety during off-nominal RPO mission cases.

2. Methodology that combines deterministic reachability (contribution #1) and neural Lyapunov functions to increase safety in the design of autonomous GN&C systems. This contribution consists of developing fuel-optimal control methods with safety-aware filtering techniques (i.e., via control barrier/Lyapunov functions) that can handle nonlinear and time-varying dynamics and constraints, such as a Line-of-sight (LOS) cone constraint when the Servicer is at closest approach to Client for inspection, and a collision avoidance constraint (KOZ) in case the Servicer's planned trajectory intersect with obstacle region.

   (a) Developed a novel architecture that provides a robust filtering scheme to real-time controllers by capturing 1) LOS constraint when the Servicer is at closest approach to the Client for inspection, and 2) KOZ constraint when Debris intersects with the Servicer's planned trajectory.

   (b) Created a methodology to apply safety certificates of CBF and CLBF that guarantees robustness when planning under uncertainty during the RPO mission phases.

   (c) Implemented an MPC law for fuel-efficient maneuvers across RPO mission phases.

   (d) Integrated the IQC-reachability method with the filtering scheme that validates worst-case output uncertainty during RPO missions.

Figure 5-1 summarizes the PhD contributions towards closing the technical gap in the GN&C safety verification method of RPO missions.

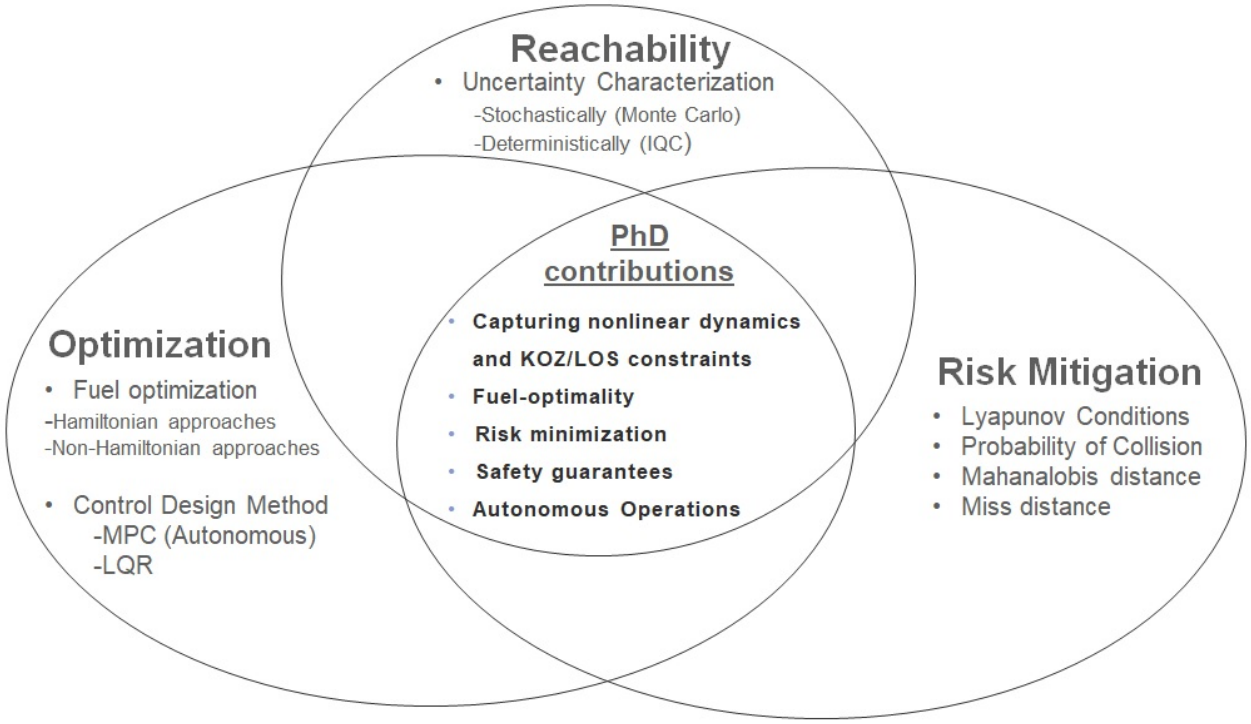

Figure 5-1: Summary of the PhD contributions.

5.3 Future Work

There are multiple areas that can be expanded to further improve the proposed safety verification platform.

Capturing More Uncertainties in Dynamical Models via IQCs

To characterize additional uncertainties caused by Servicer sensors, such as gyros, star trackers, and reaction wheel dynamical models, fidelity of the analytical dynamical models can be simulated, and worst-case uncertainties can be integrated into the IQC-reachability method for safety verification of RPO missions. If the RPO mission of interest would last longer than a few hours, the effects of atmospheric drag would significantly impact the worst-case outputs presented in this thesis. Although this platform considers this perturbation effect as an exogenous disturbance, it is possible to add the differential drag model as a dynamical IQC uncertainty in this innovative reachability method. Moreover, for RPO applications in the GEO regime, high-fidelity of the analytical dynamics models for differential solar radiation pressure (SRP) effects need to be captured with IQC classes as well. In addition, this platform can be extended to the acquisition and capture phases of an RPO mission. Future work will consist of implementing the dynamics of the combined stack of Servicer, Client or Debris and modeling the electrostatic force uncertainties, between

the Servicer and Client, and exogenous disturbances affecting the translation and rotational motions of the Servicer and Client spacecraft. Critical inclinations would also need to be studied for completeness of corner cases where additional dynamics might not work. For asteroid applications, two popular approximations of the dynamics could be implemented in control-affine form if the asteroid is assumed to be elliptical or if a full spherical-harmonics representation in the field [52] is used. Other approaches exist such as discretizing the asteroid into many small masses as shown in [142]. For applications in the cislunar domain, it is essential to characterize third-body effects to account for external disturbances that impact the GN&C system.

Increasing Robustness and Usage of Neural Lyapunov Functions

Neural Lyapunov synthesis can be extended to incorporate sensor measurements as part of the disturbance characterization as shown in [30]. With the advancement of tensor processing units, it would become relevant to test and emulate these algorithms in hardware-in-the-loop to examine computational loads in spaceborne computers. In addition, uncertainties, such as time delays in actuation, could be embedded in the Neural Lyapunov + MPC schemes with advanced IQC operators, such as ρ-hard IQCs, as defined by Algower [128].

Expanding Collision Risk Mitigation Framework

A complete validation of the current collision risk capabilities will require more accurate computation of the PC, such as Monte Carlo PC or Hall 3D PC. For off-nomial cases, it would be important to apply an adaptive feedback control scheme using QCQP with a single constraint, which is known to be solvable in a polynomial time by converting to an equivalent convex optimization problem. This thesis does not consider trajectory correction maneuvers, which are also relevant for mission planning test cases. For more practical applications, a state machine will need to be designed, with tolerance thresholds for guidance, navigation, and control errors, within the GN&C submodules to plan for emergency transfers and abort maneuvers during RPO mission phases.

Verification and Validation

The focus of this thesis was to prove the effectiveness of a novel methodology through extensive modeling. However, the thesis did not include any testing of these algorithms in hardware or real-time operations. Therefore, future work will involve testing these algorithms on astrobee hardware and performing various Zero-G experiments to validate the robustness of safety certificates in real-time operations. The aim of this future work is to validate the proposed methodology and ensure its practicality for use in real-world scenarios. By testing the algorithms on astrobee hardware and performing experiments in Zero-G environments, the author will be able to provide more concrete evidence of the usefulness and effectiveness of this new approach in the field of RPO.

Final Remarks

The safety verification GN&C platform that was developed in this study has significant implications for the future of space operations. As the number of active satellites increases and the demand for on-orbit services grows, the need for robust and reliable GN&C systems becomes increasingly important. The contributions made in this thesis provide a solid foundation for the development of such systems, offering a framework that takes into account critical factors such as computational complexity, safety in spaceflight, and fuel usage. By minimizing collision risk in proximity operations across all orbits, this work has the potential to improve the safety and success of autonomous space operations. Ultimately, this study provides valuable insights into the design and implementation of GN&C systems for satellite operations and lays the groundwork for future advancements in the field.

Appendix A

Appendix

A.1 Satellite Dynamics

The nearly nonsingular mean orbital elements of the reference (Client) orbit are defined as $\bar{\boldsymbol{e}} = \left[a, \lambda, i, q_1, q_2, \Omega\right]^{\mathrm{T}}$, where a is the semimajor axis, $\lambda = M + \omega$ is the mean argument of latitude, M is the mean anomaly, ω is the argument of perigee, i is the inclination, $q_1 = e\cos\omega$ and $q_2 = e\sin\omega$ are the orbital frame components of the eccentricity vector, e is the eccentricity, and Ω is the right ascension of the ascending node. This set of orbital elements is chosen instead of the classical orbital elements because it is not singular in the case of a circular orbit; however, it is still singular in an equatorial orbit. This set of coordinates is very suitable for low-Earth-orbit operations where equatorial orbits are vanishingly rare. Compared with fully nonsingular elements, such as the equinoctial elements, the associated mathematical formulations are greatly simplified. The unforced dynamics are given by a modified form of Lagrange's planetary equations (LPEs) for J_2:

$$\delta\dot{\bar{\boldsymbol{o}}}\bar{\boldsymbol{e}} = A\delta\bar{\boldsymbol{o}}\bar{\boldsymbol{e}} + Bu \tag{A.1}$$

$$\text{where } \mathrm{A}\delta\bar{\boldsymbol{o}}\bar{\boldsymbol{e}} = f(\bar{oe}) = \begin{bmatrix} 0 \\ n + \frac{3}{4}J_2(\frac{R_e}{p})^2 n[\eta(3cos^2(i) - 1) + (5cos^2(i) - 1)] \\ 0 \\ -\frac{3}{4}J_2(\frac{R_e}{p})^2 n(3cos^2(i) - 1)q_2 \\ -\frac{3}{4}J_2(\frac{R_e}{p})^2 n(3cos^2(i) - 1)q_1 \\ -\frac{3}{2}J_2(\frac{R_e}{p})^2 ncos(i) \end{bmatrix} \tag{A.2}$$

and B=

$$
\begin{aligned}
\dot{a} &= \frac{2a^2}{h} = [q_1 sin(\theta) - q_2 cos(\theta))u_r + \frac{p}{r}u_t] \\
\dot{\lambda} &= [\frac{-p}{h(1+\eta)}(q_1 cos(\theta) + q_2 sin(\theta) - \frac{2\eta r}{h}]u_r + (\frac{p+r}{h(1+\eta)}(q_1 sin(\theta) - q_2 cos(\theta))u_t - \frac{r sin(\theta) cos(i)}{h sin(i)})u_h \\
\dot{i} &= \frac{r cos(\theta)}{h}u_h \\
\dot{q_1} &= (\frac{p sin(\theta)}{h})u_r + \frac{1}{h}[(p+r)cos(\theta) + rq_1]u_t + \frac{rq_2 sin(\theta)cos(i)}{h sin(i)}u_h \\
\dot{q_2} &= (\frac{-p cos(\theta)}{h})u_r + \frac{1}{h}[(p+r)sin(\theta) + rq_2]u_t - \frac{rq_1 sin(\theta)cos(i)}{h sin(i)}u_h \\
\dot{\Omega} &= \frac{r sin(\theta)}{h sin(i)}u_h
\end{aligned}
\tag{A.3}
$$

where J_2 is the coefficient of the second zonal harmonic, R_e is the mean equatorial radius of the Earth, p is the semilatus rectum, i is the inclination, e is the eccentricity, q_1, q_2 are the eccentricity vector components, n is the mean motion, and $\eta = \sqrt{(}1 - e^2)$.

A feedback controller based on the equinoctial orbital elements (p, f, g, h, k, L) is implemented, instead of using classical orbital elements. This choice allows to avoid singularities for zero eccentricity and inclination angles [125]. The equinoctial orbital elements are expressed as:

$$
\begin{aligned}
a &= a \\
\Psi &= \Omega + \omega + f \\
q_1 &= e \sin(\omega + \Omega) \\
q_2 &= e \cos(\omega + \Omega) \\
p_1 &= \tan\left(\frac{i}{2}\right) \sin(\Omega) \\
p_2 &= \tan\left(\frac{i}{2}\right) \cos(\Omega)
\end{aligned}
\tag{A.4}
$$

where a is the semimajor axis, Ψ is the mean argument of latitude, Ω is the right ascension of the ascending node, ω is the argument of perigee, f is the true anomaly, e is the orbit eccentricity, p_1 and p_2 are the orbit inclination vector components,and q_1 and q_2 are the eccentricity vector components. This set of equinoctial variables was chosen for its benefits of avoiding the singularity for circular orbits (when $e = 0$), equatorial orbits (i.e., zero inclinations), as well as being extensively used throughout other bodies of work in the realm of relative spacecraft dynamics [47].

In modified equinoctial variables as:

$$
\begin{aligned}
p &= a(1-e^2) \\
f &= e\cos(\omega+\Omega) \\
g &= e\sin(\omega+\Omega) \\
h &= \tan\left(\frac{i}{2}\right)\cos(\Omega) \\
k &= \tan\left(\frac{i}{2}\right)\sin(\Omega) \\
L &= \Omega+\omega+\theta
\end{aligned}
\tag{A.5}
$$

where p is the semi-parameter, a the semi-major axis, e the orbital eccentricity, i the orbital inclination, ω the argument of perigee, Ω the right ascension of the ascending node, θ the true anomaly, and L the true longitude. The relationship between modified equinoctial and classical orbital element can be found in [137]. The system of first-order modified equinoctial equations of orbital motion are given by the following expressions:

$$
\begin{aligned}
\dot{p} &= \frac{dp}{dt} = \frac{2p}{w}\sqrt{\frac{p}{\mu}}\Delta_t \\
\dot{f} &= \frac{df}{dt} = \sqrt{\frac{p}{\mu}}\left[\Delta_r\sin L + [(w+1)\cos L + f]\,\frac{\Delta_t}{w} - (h\sin L - k\cos L)\frac{g\Delta_n}{w}\right] \\
\dot{g} &= \frac{dg}{dt} = \sqrt{\frac{p}{\mu}}\left[-\Delta_r\cos L + [(w+1)\sin L + g]\,\frac{\Delta_t}{w} + (h\sin L - k\cos L)\frac{g\Delta_n}{w}\right] \\
\dot{h} &= \frac{dh}{dt} = \sqrt{\frac{p}{\mu}}\frac{s^2\Delta_n}{2w}\cos L \\
\dot{k} &= \frac{dk}{dt} = \sqrt{\frac{p}{\mu}}\frac{s^2\Delta_n}{2w}\sin L \\
\dot{L} &= \frac{dL}{dt} = \sqrt{\mu p}\frac{w^2}{p^2} + \frac{1}{w}\sqrt{\frac{p}{\mu}}(h\sin L - k\cos L)\Delta_n \\
&\text{with} \quad w = 1 + f\cos L + g\sin L
\end{aligned}
\tag{A.6}
$$

where μ is the standard gravitational parameter, and $\Delta_{r,t,n}$ are the orbital perturbations in the radial, along-track and cross-track directions, respectively [137]. In vector form the equations of motion can be expressed as follows:

$$
\dot{\vec{y}} = \frac{d\vec{y}}{dt} = A + B(\vec{y})[\vec{P} + \vec{u}] \tag{A.7}
$$

$$
A = \begin{bmatrix} 0 & 0 & 0 & 0 & 0 & \sqrt{\mu p}\frac{w^2}{p^2} \end{bmatrix}^T \tag{A.8}
$$

$$B = \begin{bmatrix} 0 & \frac{2p}{w}\sqrt{\frac{p}{\mu}} & 0 \\ \sqrt{\frac{p}{\mu}}\sin L & \sqrt{\frac{p}{\mu}}\left[(w+1)\cos L + f\right]\frac{1}{w} & -\sqrt{\frac{p}{\mu}}\left[(h\sin L - k\cos L)\frac{g}{w}\right] \\ -\sqrt{\frac{p}{\mu}}\cos L & \sqrt{\frac{p}{\mu}}\left[(w+1)\sin L + g\right] & -\sqrt{\frac{p}{\mu}}\left[(h\sin L - k\cos L)\frac{f}{w}\right] \\ 0 & 0 & \sqrt{\frac{p}{\mu}}\frac{s^2}{2w}\cos L \\ 0 & 0 & \sqrt{\frac{p}{\mu}}\frac{s^2}{2w}\sin L \\ 0 & 0 & \frac{1}{w}\sqrt{\frac{p}{\mu}}(h\sin L - k\cos L) \end{bmatrix} \tag{A.9}$$

with $\vec{P}$ the orbital perturbations acceleration vector, and $\vec{u}$ the control acceleration vector. The orbital perturbations considered in the analysis are the atmospheric drag and J2 perturbation. Details about the mathematical formulations can be found in [137]. A feedback controller is implemented in a closed-loop fashion aiming to reduce the error between the spacecraft current state and the desired state. The desired state is the space debris state for the first part of the mission, followed by the space station state for the second part of the mission.

By employing the geometric approach, a state transition matrix (STM) has been taken from [47] to depict the relative motion of adjacent satellites in the context of an elliptical Client orbit, while taking into account the gravitational perturbation J_2. The STM has been derived in closed-form for both mean and osculating orbital elements.

Appendix B

Appendix

B.1 Code

B.1.1 Truth Trajectories

```
// Values used for truth trajectory

{
  "CelestialBody": {
    "Earth": {
      "mu": 3.986004415e14,// standard gravitational parameter [m^3/s^2]
      "radius": 6378.137e3,// radius of Earth [m]
      "omega": 7.2921159e-5,// rotation rate of Earth [rad/s]
      "J2": 1.0826359e-3,// oblateness term of Earth
      "h0": 500e3,// reference altitude for air drag [m]
      "rho0": 6.967e-13,// density of atmosphere at ref alt [kg/m^3]
      "H": 63.822e3,// scale height of atmosphere [m]
      "gravf_deg": [10, 10]// degree and order of the gravity field model
    }
  },
```

Figure B-1: Parameters for generating Truth Trajectories.

B.1.2 Sensor Noise

Parameters used for Sensor Noise of lidar sensor

```
/Sensor Noise Lidar
"LiDARMMN": {
  "cov": [
    [0.0025, 0, 0],
    [0, 0.0025, 0],
    [0, 0, 0.0025]
  ],// random error of LiDAR readout [m]
  "bias": [0.05, 0.05, 0.05],// constant bias of LiDAR readout [m]
  "HFOV": 60, // [deg]
  "VFOV": 22, // [deg]
  "delay_time": 0,// sensor output delay [sec]
  "realistic": false,// legacy boolean
  "dcm_CamCSBD": [
    [1, 0, 0],
    [0, 1, 0],
    [0, 0, 1]
```

Figure B-2: Parameters for generating Truth Trajectories.

Appendix C

Appendix

C.1 IQC White Class

Sensor noise can be characterized as a white noise IQC Class. This IQC class can be represented as L_2 signals with flat spectrum over a suitable large frequency range [111]. For the scalar case, a signal $\omega \in L_2$ (-∞, ∞) is white over the frequency range -b $\leq \omega \leq$ b if

$$|\widehat{w}(j\omega)|^2 = \left\{ \begin{array}{ll} \frac{\pi}{b}||\omega||^2, & \omega \in [-b, b] \\ 0, & |\omega| \geq b \end{array} \right\} \tag{C.1}$$

This situation ins less trivial in higher dimensions. Moreover, $\omega \in L_2^n$(-∞, ∞) is white over the frequency range -b $\leq \omega <$b if

$$\widehat{w}(j\omega)\widehat{w}(j\omega)^* = \left\{ \begin{array}{ll} \frac{\pi}{bn}||\omega||^2 I, & \omega \in [-b, b] \\ 0, & |\omega| \geq b \end{array} \right\} \tag{C.2}$$

This is not possible since the left hand side is a rank one matrix. To overcome this problem, the following class of white signals is defined.

Definition C.1.1. In the class of $W_{white} = \{ \omega : \omega = \{\omega_1,...,\omega_N\}, \omega_i \in L_2^n$ (-∞, ∞)$\}$, each family satisfies

$$\frac{1}{N}\sum_{i=1}^{\infty}(\widehat{w}(j\omega) = \left\{ \begin{array}{ll} \frac{\pi}{bn}||\omega||^2 I, & \omega \in [-b, b] \\ 0, & |\omega| \geq b \end{array} \right\} \tag{C.3}$$

where $c = \frac{\pi}{(bnN)}\ \frac{1}{N}\ \sum_{i=1}^{\infty}|\omega_i||^2$

This means that each family in the class has an average spectrum which is flat over the bandwidth [-b,b]. The energy is concentrated to the interval [-b,b] with equal distribution between the components of the signals and there is no cross correlation between the components. Note that it is possible to find n signals ω_1, ..., ω_n such that the average satisfies the property (C.2). If if we let $\omega_1 = \omega_i$, where e_i is the i^{th} unit

vector and ω is a scalar signal satisfying condition in (C.1).

The next proposition gives an exact characterization of the class $||W_{white}||$.

Proposition 1. The IQCs defined by the multipliers

$$\psi_{white} = \psi \in S_{\infty}^{nxn} : \int_{-b}^{b} (tr(\psi(j\omega))d\omega \geq 0 \tag{C.4}$$

gives an exact characterization of W_{white}.

Proof. Is is necessary to prove two things

1. For every $\psi \in \psi_{white}$, the following holds

$$\frac{1}{N}\sum_{i=1}^{\infty}\int_{-\infty}^{\infty} \widehat{w}^{*}\psi\widehat{w_i}^{*}d\omega \geq 0, \tag{C.5}$$

   for any family w=ω_1,...,$\omega_N \in W_{white}$

2. if ω_1,...,$\omega_N \in L_2^n$ (-∞,∞) violates (C.2), then there exists $\psi \in \psi_{white}$ such that

$$\frac{1}{N}\sum_{i=1}^{\infty}\int_{-\infty}^{\infty} \widehat{w}^{*}\psi\widehat{w_i}^{*}d\omega < 0, \tag{C.6}$$

To prove (1) we just note that

$$\frac{1}{N}\sum_{i=1}^{\infty}\int_{-\infty}^{\infty} \widehat{w}^{*}\psi\widehat{w_i}^{*}d\omega = \int_{-\infty}^{\infty} tr(\psi\sum_{i=1}^{N}\widehat{w}\widehat{w}^{*})d\omega = \frac{\pi}{bN}(\frac{1}{N}\sum_{i=1}^{N}||\omega_i||^2)\int_{-b}^{b} tr(\psi)d\omega \geq 0. \tag{C.7}$$

For the proof of (2) we define the function

$$Z_0(\omega) = \left\{ \begin{array}{ll} bI, & \omega \geq b \\ \omega I, & |\omega| \leq b \\ bI, & |\omega| < -b \end{array} \right\} \tag{C.8}$$

This is a function of bounded variation and it belongs to the dual space of S_{∞}^{nxn} in terms of the Stieltjes integral

$$< \psi, Z_0 >= \int_{-\infty}^{\infty} (tr(\psi(j\omega))dZ_0(\omega)). \tag{C.9}$$

We note that

$$< \psi, Z_0 >= \int_{-b}^{b} (tr(\psi(j\omega))d\omega(\omega)) \geq 0. \tag{C.10}$$

which shows that ψ_{white} is the half space $\psi_{white}= \psi \in S_{\infty}^{nxn}$ $<\psi, Z_0> 0$. Now let ω_1,...,$\omega_N \in L_2^n$ (-∞, ∞) be a set of signals that does not satisfy condition (C.2) and define

$$Z(\omega) = \frac{1}{N} \sum_{i=1}^{N} \int_0^{\omega} \widehat{w}^* \widehat{w_i}^* dv, \tag{C.11}$$

This is a function of bounded variation that is different from Z_0 and it thus defines another half space. It follows that there exists $\psi \in \psi_{white}$ such that $< \psi, Z > 0$. □

Bibliography

[1] *Ion and Hall Thruster Plumes*, chapter 8, pages 393–428. John Wiley Sons, Ltd, 2008.

[2] Alessandro Abate, Daniele Ahmed, Mirco Giacobbe, and Andrea Peruffo. Formal synthesis of lyapunov neural networks. *IEEE Control Systems Letters*, 5(3):773–778, Jul 2021.

[3] National Aeronautics, Space Administration National Aeronautics, and Space Administration. Nasa spacecraft conjunction assessment and collision avoidance. best practices handbook. 2020.

[4] Yunus M. Agamawi and Anil V. Rao. Cgpops: A c++ software for solving multiple-phase optimal control problems using adaptive gaussian quadrature collocation and sparse nonlinear programming, 2019.

[5] Maruthi R Akella and Kyle T Alfriend. Probability of collision between space objects. *Journal of Guidance, Control, and Dynamics*, 23(5):769–772, 2000.

[6] KT Alfriend and H Yan. Evaluation and comparison of relative motion theories. *Journal of Guidance, Control, and Dynamics*, 28(2):254–261, 2005.

[7] Kyle T Alfriend, Srinivas R Vadali, Pini Gurfil, Jonathan P How, and Louis Breger. *Spacecraft formation flying: Dynamics, control and navigation*, volume 2. Elsevier, 2009.

[8] M Althoff. An Introduction to CORA 2015. In *Proc. of the Workshop on Applied Verification for Continuous and Hybrid Systems*, 2015.

[9] Aaron D. Ames, Samuel Coogan, Magnus Egerstedt, Gennaro Notomista, Koushil Sreenath, and Paulo Tabuada. Control barrier functions: Theory and applications. In *2019 18th European Control Conference, ECC 2019*, pages 3420–3431. Institute of Electrical and Electronics Engineers Inc., jun 2019.

[10] Dale Arney, John Mulvaney, Christina Williams, Richard Sutherland, and Christopher Stockdale. In-space servicing, assembly, and manufacturing (isam) state of play. AAS/AIAA Astrodynamics Specialist Conference, Portland, ME, February 2-8, 2023.

[11] Michael Asbury. Monte carlo simulation at nasa., Pubicly released in 11. Aug. 2017 <https://www.nasa.gov/centers/ivv/jstar>.

[12] Courtney Bashnick and Steve Ulrich. Fast model predictive control for spacecraft rendezvous and docking with obstacle avoidance. *Journal of Guidance, Control, and Dynamics*, 0(0):1–10, 0.

[13] Alberto Bemporad and Manfred Morari. Robust model predictive control: A survey. In *Robustness in Identification and Control*, 1998.

[14] Andrew Berning, Ethan Burnett, and Bieniawski Stefan. Chance-constrained, drift safe guidance for spacecraft rendezvous. 02 45th Annual Rocky Mountain AAS/GNC Conference 2023.

[15] Chaize M. Delpy P. Strandmoe S Berthelier, D. *Automated Transfer Vehicle (atv) Nominal Software Gnc Numerical Validation Overview*, pages 31.8–21.12. 2006.

[16] J.T. Betts. Practical methods for optimal control and estimation using nonlinear programming. *SIAM Press*, 2009.

[17] Chris Blackerby, Akira Okamoto, Kohei Fujimoto, Nobu Okada, Jason L Forshaw, and John Auburn. Elsa-d: An in-orbit end-of-life demonstration mission. In *Proc. Int. Astronaut. Congr. IAC*, volume 6, page 43644, 2018.

[18] John R. Brophy, Charles E. Garner, and Steven C. Mikes. Dawn ion propulsion system: Initial checkout after launch. *Journal of Propulsion and Power*, 25(6):1189–1202, 2009.

[19] Dirk Brouwer. Solution of the problem of artificial satellite theory without drag. *The Astronomical Journal*, 64:378–397, 1959.

[20] Sonja Caldwell. 5.0 guidance, navigation, and control." nasa.

[21] Fernando Castañeda, Jason J. Choi, Bike Zhang, Claire J. Tomlin, and Koushil Sreenath. Gaussian process-based min-norm stabilizing controller for control-affine systems with uncertain input effects and dynamics, 2021.

[22] Damiana Catanoso, Florian Kempf, Klaus Schilling, and Simone D'Amico. Networked model predictive control for satellite formation flying. 07 2019.

[23] F Kenneth Chan et al. *Spacecraft collision probability*. Aerospace Press El Segundo, CA, 2008.

[24] Xin Chen, Sriram Sankaranarayanan, and Erika Ábrahám. Flow* 1.2: More Effective to Play with Hybrid Systems. In *ARCH14-15. 1st and 2nd International Workshop on Applied veRication for Continuous and Hybrid Systems / Goran Frehse and Matthias Althoff (editors)*, volume 34 of *EPiC Series in Computer Science*, pages 152–159, Manchester, apr 2015. 1st and 2nd Int. Workshop on Applied veRification for Continuous and Hybrid Systems, Seattle, WA (USA), 13 Apr 2015 - 17 Apr 2015.

[25] Raphael Cohen, Eric Feron, and Pierre-Loïc Garoche. Verification and validation of convex optimization algorithms for model predictive control. *Journal of Aerospace Information Systems*, 17(5):257–270, 2020.

[26] McKinsey & Company. New space: Accelerating innovation and investment. https://www.mckinsey.com/industries/aerospace-and-defense/our-insights/new-space-accelerating-innovation-and-investment, 2018.

[27] Hongkai Dai, Benoit Landry, Marco Pavone, and Russ Tedrake. Counter-example guided synthesis of neural network lyapunov functions for piecewise linear systems. In *2020 59th IEEE Conference on Decision and Control (CDC)*, pages 1274–1281, 2020.

[28] Simone D'Amico and Oliver Montenbruck. Proximity operations of formation-flying spacecraft using an eccentricity/inclination vector separation. *Journal of Guidance, Control, and Dynamics*, 29, 05 2006.

[29] Charles Dawson, Sicun Gao, and Chuchu Fan. Safe control with learned certificates: A survey of neural lyapunov, barrier, and contraction methods for robotics and control. *IEEE Transactions on Robotics*, pages 1–19, 2023.

[30] Charles Dawson, Bethany Lowenkamp, Dylan Goff, and Chuchu Fan. Learning safe, generalizable perception-based hybrid control with certificates. *IEEE Robotics and Automation Letters*, 7(2):1904–1911, 2022.

[31] Charles Dawson, Zengyi Qin, Sicun Gao, and Chuchu Fan. Safe nonlinear control using robust neural lyapunov-barrier functions, 2021; Submitted for review.

[32] Nathaniel Demmons, Vlad Hruby, Douglas Spence, Thomas Roy, Eric Ehrbar, Jurg Zwahlen, Roy Martin, John Ziemer, and Thomas Randolph. *ST7-DRS Mission Colloid Thruster Development*.

[33] Delia Desiderio, Marco Lovera, Stephane Pautonnier, and Remi Drai. Magnetic momentum management for a geostationary satellite platform. In *2008 47th IEEE Conference on Decision and Control*, pages 1243–1248, 2008.

[34] Wayne H. Yu Donald J. Dichmann, Cassandra M. Alberding. Station keeping monte carlo simulation for the james webb space telescope.

[35] Parasara Sridhar Duggirala, Sayan Mitra, Mahesh Viswanathan, and Matthew Potok. C2E2: A verification tool for stateflow models. *Lecture Notes in Computer Science (including subseries Lecture Notes in Artificial Intelligence and Lecture Notes in Bioinformatics)*, 9035:68–82, 2015.

[36] Hui Fang and Panos J. Antsaklis. Distributed control with integral quadratic constraints. *IFAC Proceedings Volumes*, 41(2):574–580, 2008. 17th IFAC World Congress.

[37] Z.J. Folcik. Accurate low-thrust orbit transfer solutions in equinoctial elements using an analytic representation of the geopotential. In *www.anilvrao.com/Publications/ConferencePublications/trajectorySurveyAAS.pdf.*, pages 19–770. AAS/AIAA Astrodynamics Specialist Conference, Portland, ME, August 11-15, 2019, 2019.

[38] James Lee Foster and Herbert S Estes. *A parametric analysis of orbital debris collision probability and maneuver rate for space vehicles*. NASA, National Aeronautics and Space Administration, 1992.

[39] Jedediah Micah Fry. *On Integral Quadratic Constraint Theory and Robust Control of Unmanned Aircraft Systems*. PhD thesis, 07 2019.

[40] Micah Fry. Iqc toolbox found on <https://github.com/iqctoolbox/iqctoolbox>, Pubicly released in 2021.

[41] Li Fu, Lingling Wang, Jianghai Hu, and Xiaohong Liu. Stability analysis of inertial navigation system-aided phase-lock-loop via an integral quadratic constraint approach. *IET radar, sonar navigation*, 8(9):1100–1108, 2014.

[42] Axel Garcia, Miles lifson Dawson, Charles, and Linares Richard. Model predictive control and safety analysis for satellite collision avoidance. *AAS*, 08 2021.

[43] Ignacio García-Fernández, José Martín-Guerrero, Emilio Olivas, Rafael Martínez, Silvia Rueda, and Rafael Magdalena. A neural network approach for real-time collision detection. volume 5, page 5 pp. vol.5, 11 2002.

[44] Clarence R Gates. A simplified model of midcourse maneuver execution errors. Technical report, NASA, 1963. JPL Technical Report No. 32-504.

[45] Peter Giesl and Sigurdur Hafstein. Review on computational methods for Lyapunov functions. *Discrete and Continuous Dynamical Systems - Series B*, 20(8):2291–2331, oct 2015.

[46] Dong-Woo Gim and Kyle T. Alfriend. State transition matrix of relative motion for the perturbed noncircular reference orbit. *Journal of Guidance, Control, and Dynamics*, 26(6):956–971, 2003.

[47] DW. Gim and K.T. Alfriend. *Satellite Relative Motion Using Differential Equinoctial Elements*, pages 295–336. Springer International Publishing, 2005.

[48] Andrew J. Fear Glenn Lightsey. Cubesat autonomous rendezvous simulation. 02 45th Annual Rocky Mountain AAS/GNC Conference 2023.

[49] Tamas Gombosi, Gábor Tóth, Igor Sokolov, Ward Manchester, Aaron Ridley, Ilia Roussev, Darren Zeeuw, Kenneth Hansen, and Q. Stout. *Halloween Storm Simulations with the Space Weather Modeling Framework*, pages AIAA–2006. 01 2006.

[50] David J. Gondelach and Roberto Armellin. Element sets for high-order poincaré mapping of perturbed keplerian motion. *Celestial Mechanics and Dynamical Astronomy*, 130(65), 2018.

[51] CAPD Group. Computer assisted proofs in dynamics group, a c++ package for rigorous numerics (2019). 10 2019.

[52] Mauricio Guelman. Closed-loop control of close orbits around asteroids. *Journal of Guidance, Control, and Dynamics*, 38(5):854–860, 2015.

[53] Bochmann. G.v. *Finite State Description of Communication Protocols, Computer Networks*, pages 361–372. 1978.

[54] Doyle T. Hall. Expected collision rates for tracked satellites. *Journal of Spacecraft and Rockets*, 58(3):715–728, 2021.

[55] Harris, Andrew T. and Petersen, Christopher D. and Schaub, Hanspeter. Linear coupled attitude–orbit control through aerodynamic drag. *Journal of Guidance, Control, and Dynamics*, 43(1):122–131, 2020.

[56] Evan Hemingway and Oliver O'Reilly. Perspectives on euler angle singularities, gimbal lock, and the orthogonality of applied forces and applied moments. *Multibody System Dynamics*, 44, 09 2018.

[57] Richard Hofer, Ira Katz, Dan Goebel, Kristina Jameson, Regina Sullivan, Lee Johnson, and Ioannis Mikellides. *Efficacy of Electron Mobility Models in Hybrid-PIC Hall Thruster Simulations.*

[58] Marcus Holzinger and Daniel Scheeres. Applied Reachability for Space Situational Awareness and Safety in Spacecraft Proximity Operations. In *AIAA Guidance, Navigation, and Control Conference*, Guidance, Navigation, and Control and Co-located Conferences. American Institute of Aeronautics and Astronautics, aug 2009.

[59] Kyotaro Ida, Takashi Uchiyama, Yoshinori Kondoh, Masaharu Suzuki, and Yuki Ikejiri. Overview of h-ii transfer vehicle (htv) and htv-x safety design considering common-cause software failure. *Journal of Space Safety Engineering*, 10(1):7–12, 2023.

[60] Christopher Jewison and R. Scott Erwin. A spacecraft benchmark problem for hybrid control and estimation. In *2016 IEEE 55th Conference on Decision and Control (CDC)*, pages 3300–3305, 2016.

[61] Christopher Michael Jewison. *Guidance and control for multi-stage rendezvous and docking operations in the presence of uncertainty.* PhD thesis, 07 2017.

[62] Andrzej Jezierski, Jakub Mozaryn, and Damian Suski. A comparison of lqr and mpc control algorithms of an inverted pendulum. In *Trends in Advanced Intelligent Control, Optimization and Automation*, pages 65–76, Cham, 2017. Springer International Publishing.

[63] Ms Napasorn Jongjittanon and Victor Dos Santos Paulino. Contribution of in-orbit servicing on space sustainability.

[64] Lisa Jonsson. Simulations of satellite attitude maneuvers : Detumbling and pointing. 2019.

[65] Ulf Jonsson. Lecture notes on integral quadratic constraints. Technical report, Department of Mathematics Royal Institute of Technology SE-100 44 Stockholm, Sweden, 2009.

[66] Somasundar Kannan, Seyed Amin Sajadi Alamdari, Jan Dentler, Miguel Olivares-Mendez, and Holger Voos. Model predictive control for spacecraft rendezvous. pages 121–125, 12 2016.

[67] James Kapinski, Jyotirmoy V. Deshmukh, Sriram Sankaranarayanan, and Nikos Arechiga. Simulation-guided lyapunov analysis for hybrid dynamical systems. In *Proceedings of the 17th International Conference on Hybrid Systems: Computation and Control*, HSCC '14, page 133–142, New York, NY, USA, 2014. Association for Computing Machinery.

[68] S Kavitha, Prasanta Mula, Manamohan Kamat, S Nirmala, and Joel George Manathara. Extended kalman filter-based precise orbit estimation of leo satellites using gps range measurements. *IFAC-PapersOnLine*, 55(1):235–240, 2022. 7th International Conference on Advances in Control and Optimization of Dynamical Systems ACODS 2022.

[69] Shinichi Kimura, Eijiro Atarashi, Taro Kashiwayanagi, Kohei Fujimoto, and Ryan Proffitt. Low-cost and high-performance visual guidance and navigation system for space debris removal. *Advanced Robotics*, 35(21-22):1277–1285, 2021.

[70] Jan Kindracki, Karolina Tur, Przemysław Paszkiewicz, Łukasz Mężyk, Łukasz Boruc, and Piotr Wolański. Experimental research on low-cost cold gas propulsion for a space robot platform. *Aerospace Science and Technology*, 62:148–157, 2017.

[71] Pavel Kovář. Experiences with the gps in unstabilized cubesat. *International Journal of Aerospace Engineering*, 2020:1–12, 09 2020.

[72] Erik Kulu. Satellite constellations-2021 industry survey and trends. 2021.

[73] L. Lamport. How to make a correct multiprocess program execute correctly on a multiprocessor. *IEEE Transactions on Computers*, 46(7):779–782, 1997.

[74] Christopher M. Lane and Penina Axelrad. Analysis of formation flying in eccentric orbits using linearized equations of relative motion. 2004.

[75] Giovanni Lavezzi, Mariusz Eivind Grøttey, and Marco Ciarcià. Attitude control strategies for an imaging cubesat. In *2019 IEEE International Conference on Electro Information Technology (EIT)*, pages 149–155, 2019.

[76] Hannu Leppinen. Current use of linux in spacecraft flight software. *IEEE Aerospace and Electronic Systems Magazine*, 32:4–13, 10 2017.

[77] Hannu Leppinen. *Enabling technologies and practices for low-cost nanosatellite missions*. Doctoral thesis, School of Electrical Engineering, 2018.

[78] W. S. Levine and S. V. Rakovic. Handbook of model predictive control. In *https://doi.org/10.1007/978-3-319-77489-3*.

[79] Johan Löfberg. Approximations of closed-loop minimax mpc. 2003.

[80] James M. Longuski, Felix R. Hoots, and George E. Pollock IV. *The Lagrange Planetary Equations for a General Perturbing Force*, pages 99–123. Springer International Publishing, Cham, 2022.

[81] J. Schwartz M. Milam M. J. Holzinger, J. DiMatteo. Passively safe receeding horizon control for satellite proximity operations. *IEEE Conference on Decision and Control*, 5(3), December 2008.

[82] Maisonobe, Luke, and Pommier-Maurussane, Veronique. Orekit: an open-source library for operational flight dynamics applications, proceedings of the 4th international conference of astrodynamics tools and technique. *International Conference of Astrodynamics Tools and Technique*, April 2010.

[83] M. Mammarella, E. Capello, H. Park, G. Guglieri, and M. Romano. Tube-based robust model predictive control for spacecraft proximity operations in the presence of persistent disturbance. *Aerospace Science and Technology*, 77:585–594, 2018.

[84] Robert Marks. *History of Monte Carlo*, pages 1–4. 01 2016.

[85] Joseph Frisbee Matthew Duncan, Joshua Wysack. Collision probability forecasting using a monte carlo simulation. In *AMOS tech*.

[86] T. Soler M. W. Cline G. L. Mader M.C. Eckl, R. A. Snay. Accuracy of gps-derived relative positions as a function of interstation distance and observing-session duration.

[87] Megretski. Integral quadratic constraints. Technical report, MIT Lectures 6.245, 2009 http://web.mit.edu/6.245/www/schedule.html, 2009.

[88] Megretski. Iqc toolbox found on <https://github.com/iqcbeta/iqc-toolbox>, Pubicly released in 2021.

[89] J.H. Meub and H. Pernicka. Spacecraft proximity operations using continuous low thrust. *Advances in the Astronautical Sciences*, 140:545–564, 01 2011.

[90] Pierre-Jean Meyer, Alex Devonport, and Murat Arcak. Tira. *Proceedings of the 22nd ACM International Conference on Hybrid Systems: Computation and Control*, Apr 2019.

[91] Colin Miller. Efforts in solving the dilution problem for orbital collisions, 2022.

[92] Oliver Montenbruck and Eberhard Gill. *Force Model*, pages 53–116. Springer Berlin Heidelberg, Berlin, Heidelberg, 2000.

[93] Rafael M. Morales and William P. Heath. The robustness and design of constrained cross-directional control via integral quadratic constraints. *IEEE Transactions on Control Systems Technology*, 19(6):1421–1432, 2011.

[94] Joseph B. Mueller. Onboard planning of collision avoidance maneuvers using robust optimization. In *American Institute of Aeronautics and Astronautics (AIAA) Scitech Forum. 2009.*

[95] Mitio Nagumo. Über die lage der integralkurven gewöhnlicher differentialgleichungen. 1942.

[96] Nedialko S. Nedialkov. *Implementing a Rigorous ODE Solver Through Literate Programming*, pages 3–19. Springer Berlin Heidelberg, Berlin, Heidelberg, 2011.

[97] Ajie Nayaka Nikicio, Weiqi Tu, Edwin Chen, Sha Luo, and Cher-Hiang Goh. Gps and sgp4 based orbit propagation onboard the galassia-2 nanosatellite. 05 2018.

[98] Onera. Smac-iqc toolbox found on found <https://w3.onera.fr/smac/analysis>, Pubicly released in 2013.

[99] F. Paganini. A set-based approach for white noise modeling. *IEEE Transactions on Automatic Control*, 41(10):1453–1465, 1996.

[100] Mark C. Palframan, J. Micah Fry, and Mazen Farhood. Robustness analysis of flight controllers for fixed-wing unmanned aircraft systems using integral quadratic constraints. *IEEE Transactions on Control Systems Technology*, 27(1):86–102, 2019.

[101] Parv Patel and Bogdan Udrea. Optimal guidance trajectories for a nanosat docking with a non-cooperative resident space object. In *2020 IEEE Aerospace Conference*, pages 1–16. IEEE, 2020.

[102] Richard Pates and Glenn Vinnicombe. Scalable design of heterogeneous networks. *IEEE Transactions on Automatic Control*, 62(5):2318–2333, 2017.

[103] Michael A. Patterson and Anil V. Rao. Gpops-ii: A matlab software for solving multiple-phase optimal control problems using hp-adaptive gaussian quadrature collocation methods and sparse nonlinear programming. *ACM Trans. Math. Softw.*, 41(1), oct 2014.

[104] Caleb Peck, Ian Down, and Majji Manoranjan. Constrained optimal reconfiguration of distributed satellite servicing modules. 02 45th Annual Rocky Mountain AAS/GNC Conference 2023.

[105] J. M. Picone, A. E. Hedin, D. P. Drob, and A. C. Aikin. Nrlmsise-00 empirical model of the atmosphere: Statistical comparisons and scientific issues. *Journal of Geophysical Research: Space Physics*, 107(A12):SIA 15–1–SIA 15–16, 2002.

[106] Valentin Preda, Jérôme Cieslak, David Henry, Samir Bennani, and Alexandre Falcoz. Robust microvibration mitigation and pointing performance analysis for high stability spacecraft. *International Journal of Robust and Nonlinear Control*, 28(18):5688–5716, 2018.

[107] Austin Probe, Matthew Ruschman, and Woodbury Tim. Onboard autonomy for redenzvous and proximity operations and collision avoidance. 02 45th Annual Rocky Mountain AAS/GNC Conference 2023.

[108] Zengyi Qin, Kaiqing Zhang, Yuxiao Chen, Jingkai Chen, and Chuchu Fan. Learning safe multi-agent control with decentralized neural barrier certificates, 2021.

[109] Kendra Lesser R. Scott Erwin, Meeko Oishi. Stochastic reachability for control of spacecraft relative motion. In *52nd IEEE Conference on Decision and Control.*

[110] D.M. Raimondo, D. Limon, Mircea Lazar, Lalo Magni, and Eduardo Camacho. Min-max model predictive control of nonlinear systems: A unifying overview on stability. *European Journal of Control*, 15, 12 2009.

[111] Anders Rantzer and Alexandre Megretski. System analysis via integral quadratic constraints. volume 3, pages 3062 – 3067 vol.3, 01 1997.

[112] Satellite Market & Research. Nsr in-orbit services report projects us$ 14.3 billion in revenues as non-geo constellations grow demand. 2022.

[113] Andrew S. Rivkin, Nancy L. Chabot, Angela M. Stickle, Cristina A. Thomas, Derek C. Richardson, Olivier Barnouin, Eugene G. Fahnestock, Carolyn M. Ernst, Andrew F. Cheng, Steven Chesley, Shantanu Naidu, Thomas S. Statler, Brent Barbee, Harrison Agrusa, Nicholas Moskovitz, R. Terik Daly, Petr Pravec, Petr Scheirich, Elisabetta Dotto, Vincenzo Della Corte, Patrick Michel, Michael Küppers, Justin Atchison, and Masatoshi Hirabayashi. The double asteroid redirection test (dart): Planetary defense investigations and requirements. *The Planetary Science Journal*, 2(5):173, aug 2021.

[114] Aureliano Rivolta, Paolo Lunghi, and Michèle Lavagna. Gnc robotics for on orbit servicing with simulated vision in the loop. *Acta Astronautica*, 162:327–335, 2019.

[115] Alexander Robey, Haimin Hu, Lars Lindemann, Hanwen Zhang, Dimos V. Dimarogonas, Stephen Tu, and Nikolai Matni. Learning control barrier functions from expert demonstrations, 2020.

[116] Stephanie Thomas Björn Jakobsson Per Bodin Robin Larsson, Joseph Mueller. Orbit constellation safety on the prisma in-orbit formation flying test beds. 01 2001.

[117] Muhammad Zakiyullah Romdlony and Bayu Jayawardhana. Uniting control lyapunov and control barrier functions. *53rd IEEE Conference on Decision and Control*, pages 2293–2298, 2014.

[118] Christopher W. T. Roscoe, Jason J. Westphal, Jacob D. Griesbach, and Hanspeter Schaub. Formation establishment and reconfiguration using differential elements in j2-perturbed orbits. In *2014 IEEE Aerospace Conference*, pages 1–19, 2014.

[119] Christopher W. T. Roscoe, Jason J. Westphal, Jacob D. Griesbach, and Hanspeter Schaub. Formation establishment and reconfiguration using differential elements in j2-perturbed orbits. *Journal of Guidance, Control, and Dynamics*, 38(9):1725–1740, 2015.

[120] Tomasz Rybus, Karol Seweryn, and Jurek Z Sasiadek. Control system for free-floating space manipulator based on nonlinear model predictive control (nmpc). *Journal of Intelligent & Robotic Systems*, 85(3-4):491–509, 2017.

[121] Nuno Ricardo Salgueiro Filipe. *Nonlinear pose control and estimation for space proximity operations: An approach based on dual quaternions.* PhD thesis, Georgia Institute of Technology, 2014.

[122] Julien Alexandre Dit Sandretto and Alexandre Chapoutot. Validated explicit and implicit runge-kutta methods. *Reliable Computing electronic edition*, 22, 2016.

[123] Subrata K Sarker, Faisal R Badal, Purnima Das, and Sajal K Das. Multivariable integral linear quadratic gaussian robust control of islanded microgrid to mitigate voltage oscillation for improving transient response. *Asian journal of control*, 21(4):2114–2125, 2019.

[124] H. Schaub and J. L. Junkins. *Analytical Mechanics of Space Systems.* AIAA Education Series, Reston, VA, 4th edition, 2018.

[125] Hanspeter Schaub and John L. Junkins. *Analytical Mechanics of Space Systems.* AIAA Education Series, Reston, VA, October 2003.

[126] Peter Z. Schulte and David A. Spencer. State machine fault protection architecture for aerospace vehicle guidance, navigation, and control. *Journal of Aerospace Information Systems*, 17(2):70–85, 2020.

[127] Bob Schutz, Byron Tapley, and George H Born. *Statistical orbit determination*. Elsevier, 2004.

[128] Lukas Schwenkel, Johannes Köhler, Matthias A. Müller, and Frank Allgöwer. Dynamic uncertainties in model predictive control: guaranteed stability for constrained linear systems. In *2020 59th IEEE Conference on Decision and Control (CDC)*, pages 1235–1241, 2020.

[129] Lukas Schwenkel, Johannes Köhler, Matthias A. Müller, and Frank Allgöwer. Model predictive control for linear uncertain systems using integral quadratic constraints, 2021.

[130] Erik Seedhouse. *The Dragon has landed: Picking up where NASA left off*, pages 85–109. Springer New York, New York, NY, 2013.

[131] Peter Seiler, Mrdjan Jankovic, and Erik Hellstrom. Control barrier functions with unmodeled input dynamics using integral quadratic constraints. *IEEE Control Systems Letters*, 6:1664–1669, 2022.

[132] Fabrizio Stesina. Tracking model predictive control for docking maneuvers of a cubesat with a big spacecraft. *Aerospace*, 8(8), 2021.

[133] Dawei Sun, Susmit Jha, and Chuchu Fan. Learning certified control using contraction metric, 2020.

[134] Shota Takahashi Siamak Hesar Mark Muktoyuk Axel Garcia Sunderland, Benjamin. Autonomous onboard risk mitigation for spacecraft proximity operations; a zero swap flight software enhancement. AAS/AIAA Astrodynamics Specialist Conference, Portland, ME, February 2-8, 2023, 2023.

[135] MM Tavakoli and N Assadian. Model predictive orbit control of a low earth orbit satellite using gauss's variational equations. *Proceedings of the Institution of Mechanical Engineers, Part G: Journal of Aerospace Engineering*, 228(13):2385–2398, 2014.

[136] David Vallado and John Seago. Covariance realism. *Advances in the Astronautical Sciences*, 135, 01 2010.

[137] David A Vallado. "long-term numerical propagation for earth orbiting satellites. In *American Astronautical Society (AAS)*.

[138] Joost Veenman, Carsten W. Scherer, and Hakan Köroğlu. Robust stability and performance analysis based on integral quadratic constraints. *European Journal of Control*, 31:1–32, 2016.

[139] Oskar Von Stryk and Roland Bulirsch. Direct and indirect methods for trajectory optimization. *Annals of Operations Research*, 37:357–373, 12 1992.

[140] Maximilian Wang and Jin Wang. Removing the inherent paradox of the buffon's needle monte carlo simulation using fixed-point iteration method. volume 2015, 12 2014.

[141] Shengli Wang, Q. Wang, W. Gao, and S. Pan. Analysis and valuation of ill-condition in baseline solution of gnss multi-system. *Dongnan Daxue Xuebao (Ziran Kexue Ban). Journal of Southeast University (Natural Science Edition)*, 43:753–757, 07 2013.

[142] R.A. Werner and D.J. Scheeres. Exterior gravitation of a polyhedron derived and compared with harmonic and mascon gravitation representations of asteroid 4769 castalia. *Celestial Mechanics and Dynamical Astronomy*, 65:313–344, 1996.

[143] Lijun Wu, Weichao Zhong, Wenlong Li, Haiyong Yu, and Hao Zhang. The modular relative orbit design method for spacecraft proximity motion. 2252(1), April 2022. Publisher Copyright: © Published under licence by IOP Publishing Ltd.; Conference date: 18-02-2022 Through 20-02-2022.

[144] Lijun Wu, Weichao Zhong, Wenlong Li, Haiyong Yu, and Hao Zhang. The modular relative orbit design method for spacecraft proximity motion. *Journal of Physics: Conference Series*, 2252(1):012032, apr 2022.

[145] Dan Xue, Junfeng Li, Hexi Baoyin, and Fanghua Jiang. Reachable Domain for Spacecraft with a Single Impulse. *Journal of Guidance, Control, and Dynamics*, 33(3):934–942, may 2010.

[146] Zhen Yang, Yazhong Luo, Vaios Lappas, and Antonios Tsourdos. Nonlinear analytical uncertainty propagation for relative motion near j2-perturbed elliptic orbits. *Journal of Guidance, Control, and Dynamics*, 41:1–16, 10 2017.

[147] Lvyang Ye, Yikang Yang, Xiaolun Jing, Hengnian Li, Haifeng Yang, and Yunxia Xia. Altimeter + ins/giant leo constellation dual-satellite integrated navigation and positioning algorithm based on similar ellipsoid model and ukf. *Remote Sensing*, 13(20), 2021.